THÈSE

présentée par

Bruno Lenzi

pour obtenir le grade de

Docteur ès sciences de l'Université Paris Sud Orsay

Spécialité: Particule, Noyaux, Cosmos (ED 517)

Recherche du boson de Higgs se désintégrant en quatre leptons dans l'expérience ATLAS auprès du LHC et études de l'isolation et de la perte d'énergie des muons

Soutenue le 17 septembre 2010 devant le jury composé de:

M.	A.	Djouadi	Examinateur
M.	C.	Guyot	Directeur de thèse
Mme.	R.	Nikolaidou	Membre invitée (encadrante)
M.	L.	Pontecorvo	Examinateur
Mme.	V.	Ruhlmann-Kleider	Rapporteur
M.	A.	Stocchi	Président du Jury
M.	G.	Unal	Rapporteur

Thèse préparée au Service de Physiques des Particules du CEA de Saclay

THESIS

presented by

Bruno Lenzi

to obtain the degree of

Doctor of sciences of the Université Paris Sud Orsay

Search for the Higgs boson decaying to four leptons in the ATLAS detector at LHC and studies of muon isolation and energy loss.

September 17, 2010. Committee:

A.	Djouadi	
C.	Guyot	Thesis advisor
R.	Nikolaidou	Thesis advisor
L.	Pontecorvo	
V.	Ruhlmann-Kleider	
A.	Stocchi	
G.	Unal	

Thesis prepared at IRFU / SPP / CEA - Saclay

Abstract

The central subject of this thesis is the evaluation of the discovery potential of the Higgs boson through its decay into four leptons (electrons and muons) in the ATLAS experiment installed at the Large Hadron Collider (LHC). The LHC was designed to accelerate proton beams at a center of mass energy of 14 TeV and started its physics program with 7 TeV collisions in the beginning of 2010.

An inclusive analysis involving all the production modes and an exclusive one aiming at production through vector boson fusion (VBF), studied for the first time in the collaboration, are presented. Both are capable of discovering the Higgs boson after a few years of LHC operation, with integrated luminosities of 30 fb^{-1}. The first one covers most part of a Higgs mass window from 130 to 500 GeV. The second one concentrates on masses around 180 GeV and above, exploiting the presence of high energy jets with large separations in pseudo-rapidity to increase the signal over background ratio.

An important part of the document is devoted to the reconstruction of muon isolation and energy loss in the ATLAS calorimeters. A software package that optimized the way of treating the energy deposits was developed and tested on simulated data and cosmic-ray events, leading to improvements in the muon momentum resolution and the distinction between muons from heavy quark and vector boson decays. As a consequence of the last result, one of the dominant backgrounds to the $H \to 4\mu$ channel, $Zb\bar{b}$, is expected to be reduced by almost a factor of two.

Résumé

Cette thèse porte sur l'évaluation du potentiel de découverte du boson de Higgs par sa désintégration en quatre leptons (électrons et muons) dans l'expérience ATLAS auprès du LHC. Le LHC a été construit pour accélérer des faisceaux de protons à une énergie dans le centre de masse de 14 TeV. Son programme de physique a commencé avec des collisions à 7 TeV au début de l'année 2010.

Deux analyses sont présentées: une analyse inclusive visant tous les modes de production du boson Higgs et une analyse exclusive spécifique à la production par fusion de bosons vecteurs (VBF), étudiée pour la première fois dans la collaboration. Toutes deux permettent la découverte du boson de Higgs après quelques années de fonctionnement du LHC, avec une luminosité intégrée de 30 fb^{-1}. La première couvre la plus grande partie d'une fenêtre en masse du Higgs allant de 130 à 500 GeV. La deuxième est focalisée sur des masses de 180 GeV ou plus et utilise la présence de jets de grande énergie et relativement séparés en pseudo-rapidité pour augmenter le rapport signal sur bruit.

Une partie importante de ce document est consacrée à la reconstruction de l'isolation et de la perte d'énergie des muons dans les calorimètres d'ATLAS. Un outil pour l'identification des dépôts d'énergie a été développé et testé avec des données simulées et des muons cosmiques. Ceci a conduit à une amélioration de la résolution en impulsion des muons et de la séparation entre muons provenant de la désintégration des quarks lourds et des bosons vecteurs. Le dernier résultat devrait aboutir à une réduction proche d'un facteur deux du bruit de fond $Zb\bar{b}$, l'un des fonds dominants pour le canal $H \to 4\mu$.

Contents

Introduction

The study of the fundamental constituents of matter and their interactions has intrigued scientists over many centuries. The 20th century witnessed the division of the atomic nucleus and the subsequent birth of particle physics.

Developments in this field have always been closely related to the observation of high energy collisions between particles, at first using cosmic rays as a natural source. Technical progress and interest to reproduce collisions in a controlled environment motivated the construction of particle accelerators: devices with increasing size, capable of attaining higher energies built throughout the last decades.

Once again the eyes of the scientific community have turned to the European Organization of Nuclear Research (CERN) in the French - Swiss border, near Geneva. The year of 2010 marked the beginning of the physics program of the largest and most powerful particle accelerator ever operated: the Large Hadron Collider (LHC). Its main objective is to probe the modern theory of particle physics at a new energy frontier and find evidence for new phenomena predicted by other models.

This theory is the well-known Standard Model of particle physics. It summarizes our current understanding of three out of the four fundamental interactions involving all the known elementary constituents of matter. Extensive tests of this model were performed over the last decades with high-precision measurements carried out at collider experiments at the Large Electron Positron Collider (LEP) at CERN, the Tevatron at Fermi National Accelerator Laboratory in the United States, and elsewhere. Remarkable agreement with respect to its predictions promoted it to one of the most successful achievements in modern physics. It remains, nevertheless, an incomplete description of the elementary phenomena. The origin of the mass of the particles, the existence of dark matter and extra dimensions are some of the open questions that will be addressed by the LHC program.

A key objective is the elucidation of the mechanism of electroweak symmetry breaking that gives mass to the particles and foresees the existence of the only unobserved particle of the Standard Model: the Higgs boson. One of the most promising signatures on Higgs boson searches are the detection of final states involving four

leptons issued from the decay of a pair of Z bosons.

The central subject of this thesis is exactly the Higgs search through this particular decay in the ATLAS experiment installed at LHC. It relies on the very efficient detection of muons and electrons and requires the distinction between the Higgs decay products and other processes that generate such particles. The study of the phenomena associated to one of the main discriminants used in the analysis – muon isolation and energy loss in the calorimeters – constitutes the first part of the present document. In summary, it is organized as following:

- The first part of the thesis is devoted to studies of muon isolation and energy loss in the ATLAS calorimeters. Descriptions of the LHC and the ATLAS experiment are given in chapters 1 and 2. The software developed for such studies, its capabilities and the improvements related to muon reconstruction and Higgs analyses are the object of chapter 3. In a second step, the results obtained with Monte Carlo simulations were compared to cosmic-ray events recorded in ATLAS before the startup of the LHC. Chapter 4 discusses these results.

- The second part is related to Higgs searches. A brief description of the Standard Model is presented in chapter 5 together with the current situation and prospects for the near future in Higgs boson physics. The definition of the strategy and the expected sensitivity for the searches involving four lepton final states in the ATLAS experiment is reviewed in chapter 6. Finally, a search mode that was never explored in ATLAS – the vector boson fusion associated to decays to four leptons – is studied in chapter 7.

- Concluding remarks and perspectives are discussed in chapter 7.6.

Part I

Studies of muon isolation and energy loss

Chapter 1

The Large Hadron Collider

The Large Hadron Collider (LHC) [1] is the world's newest and most powerful tool for research in particle physics. It is a 26.7 km two-ring superconducting collider capable of accelerating counter-rotating proton beams to a center of mass energy ($\sqrt{s}$) of 14 TeV, and lead ions (Pb) to 2.8 TeV per nucleon.

The tunnel that previously hosted the LEP accelerator is now used by the LHC machine. It comprises eight straight sectors and eight arcs and lies between 45 m and 170 m below the surface. LEP operated from 1989 to 2000, colliding electrons and positrons at ~ 90 GeV in its initial phase, reaching $\sqrt{s} = 209$ GeV in the end of its operations.

Center of mass energies achievable at the LHC are seven times higher than the previous record, detained by the Tevatron. This is only possible through several steps that take place in the CERN accelerator complex before the beam injection at the LHC. The chain is illustrated in fig. 1.1. A hydrogen bottle is the beginning of the process, from where the protons are extracted. A linear accelerator (LINAC 2) bring their energy to 50 MeV and is followed by a circular booster (PSB) where the beams reach 1.4 GeV. The Proton Synchrotron (PS) and the Super Proton Synchrotron (SPS) are the last two steps, where the particles attain 26 GeV and then 450 GeV before being transferred to the LHC. The beams are injected in bunches with a length corresponding to 1.71 ns (reduced to 1.06 ns for collisions) and nominally spaced by 25 ns. Consequently, the bunch crossing occurs at a frequency of 40 MHz to induce the collisions.

Being a particle – particle collider (as opposed to particle – anti-particle), the LHC is composed of two separate beam-lines where the protons and ions are deflected by opposite magnetic fields to follow circular trajectories. A "two-in-one" magnet design was adopted to cope with restrictions in the tunnel diameter, with two coils sharing the same cooling infrastructure. Superconducting dipole magnets are the

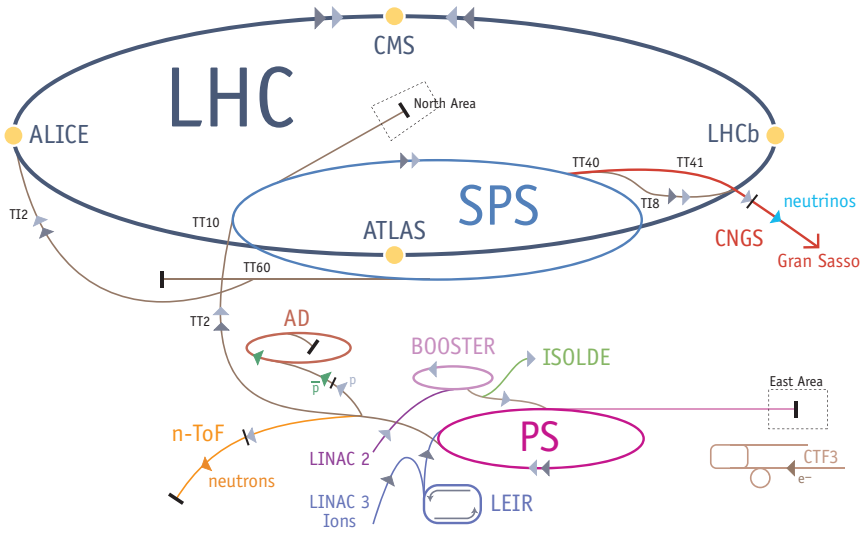

Figure 1.1: Illustration of the LHC injector complex. The LHC experiments are indicated with yellow circles.

key elements of the machine, responsible for bending the beams with magnetic fields above 8 T. The 1 232 dipoles, and the 392 quadrupoles responsible for focusing the beam operate at temperatures below 2 K maintained by superfluid helium.

The acceleration is performed by radio-frequency (RF) cavities. A 400 MHz superconducting system increases the beam energy by 485 keV at each turn until it reaches 7 TeV. The limiting factor for the LHC is not the acceleration itself but the bending power of the dipole magnets.

1.1 Luminosity

A particle accelerator should aim at producing collisions at the maximum rate with the highest possible center of mass energy. The number of events per second generated in the collisions is given by:

$$N_{events} = L \cdot \sigma_{event} \,, \tag{1.1}$$

where σ_{event} is the event cross section and L is the machine luminosity. The luminosity depends only on parameters of the beam through the equation:

$$L = \frac{N_b^2 n_b f_r \gamma_r}{4\pi \epsilon_n \beta^*} F \,, \tag{1.2}$$

where (the nominal parameters for the LHC are given in parenthesis):

- N_b is the number of particles per bunch ($\sim 10^{10} - 10^{11}$),
- n_b is the number of bunches per beam (2808),
- f_r is the revolution frequency (11 245 Hz),
- γ_r the relativistic gamma factor (~ 7000),
- ϵ_n the normalized transverse beam emittance (3.75 μm), related to its size,
- β^* is the beta function at the collision point (0.55 m), related to the beam focusing,
- F is the geometric luminosity reduction factor if the beams do not collide head-on. A crossing angle of 285 μrad will be introduced to prevent collisions outside the nominal interaction points, leading to $F = 0.84$.

As a result, the LHC should operate at 10^{33} cm^{-2} s^{-1} in a low-luminosity phase and 10^{34} cm^{-2} s^{-1} at high luminosity, depending on the number of particles per bunch. The expected beam lifetime is $\sim$ 22 h, with losses caused mainly by the collisions. The luminosity decreases by a factor of 2 within 10h, after which a new injection into LHC takes place. Assuming the machine can be run for 200 days per year, integrated luminosities of $\mathscr{L} = 10$ fb^{-1} and $\mathscr{L} = 100$ fb^{-1} per year are achievable in the low and high-luminosity phases, respectively. The duration of each phase is currently being re-evaluated. During approximately one month per year, the LHC should operate with lead ion beams, with a peak luminosity of $L = 10^{27}$ cm^{-2} s^{-1}.

1.2 Startup and first physics run

The first beams circulated in the LHC by September 10, 2008 [2]. At that time, almost all the elements of the accelerator were only tested to reach a center of mass energy of 10 TeV. Nine days later an incident was caused by a faulty electrical connection between two magnets during powering tests of the main dipole circuit. Helium leakage into the tunnel and serious mechanical damage delayed the operations by about a year.

Repairs and consolidation work allowed the accelerator to resume its program in the end of 2009. The first collisions were achieved in November 23 and the

world energy record was set one week later, with 1.18 TeV beams colliding at $\sqrt{s} = 2.36$ TeV.

After a Christmas break, the LHC beams were ramped to 3.5 TeV and the research program started in March 30, 2010. This first run at $\sqrt{s} = 7$ TeV is scheduled to last until the end of 2011 and provide an integrated luminosity of 1 fb^{-1} for physics studies. A long shutdown will follow to prepare the machine for a 14 TeV run.

1.3 The LHC experiments and physics reach

The LHC beams can collide in four different points, all instrumented with large experiments: ATLAS (A Toroidal LHC ApparatuS), CMS (Compact Muon Solenoid), ALICE (A Large Ion Collider Experiment) and LHCb.

ATLAS and CMS are general purpose detectors with broad physics programs. Studies of the Standard Model and searches for evidences of new physics are among their main objectives. Both were designed to operate at the highest luminosity achievable at the LHC. A more detailed description of ATLAS will be given in the next chapter.

ALICE is specialized in heavy-ion physics and is devoted to the characterization of quark-gluon plasma, a phase that should have existed in the early universe when extremely high temperature and/or densities were found. Although the other experiments also foresee studies with heavy ions, ALICE is the only one dedicated to the subject.

LHCb will focus on b-quark physics and precise CP violation measurements, addressing the question of apparent violations of the symmetry between matter and antimatter in the universe. It is designed to operate at a luminosity almost two orders of magnitude lower than the nominal one.

The study of the Standard Model and the search for new phenomena in proton-proton collisions involve the detection of very rare processes. The associated cross sections are many orders of magnitude below the total cross section, dominated by Quantum Chromodynamics effects. Their dependence with the center of mass energy is shown in fig. 1.2. The figure highlights some of the interesting processes in the collisions, mentioned below:

- B-physics studies will probe the CP violation in systems involving the b-quark.
- Detection of electroweak bosons W and Z and precise measurement of the W boson mass constitute a powerful consistency test of the Standard Model.

- Studies with top quarks include precise measurements of its mass and production cross section, detection of single top events and searches for top – anti-top ($t\bar{t}$) resonances. The top is the heaviest known particle and plays a major role in constraining new physics phenomena. The LHC will be a top-factory with millions of particles produced per year.

- Higgs boson searches are the central goal of ATLAS and CMS and the main subject of this thesis. Its existence is behind the mechanism that originates the mass of the other particles in the Standard Model. The Higgs mass itself is a free parameter and will have to be determined if this particle is discovered.

- Physics beyond the Standard Model is expected in the energy regime probed by LHC collisions. Supersymmetric extensions of the SM foresee the production of dark matter that would escape the detection but induce large amounts of missing energy. Models based on extra-dimensions usually include heavy gauge bosons (W' and Z') with masses in the TeV range. A wide variety of phenomena and models will be tested at the LHC.

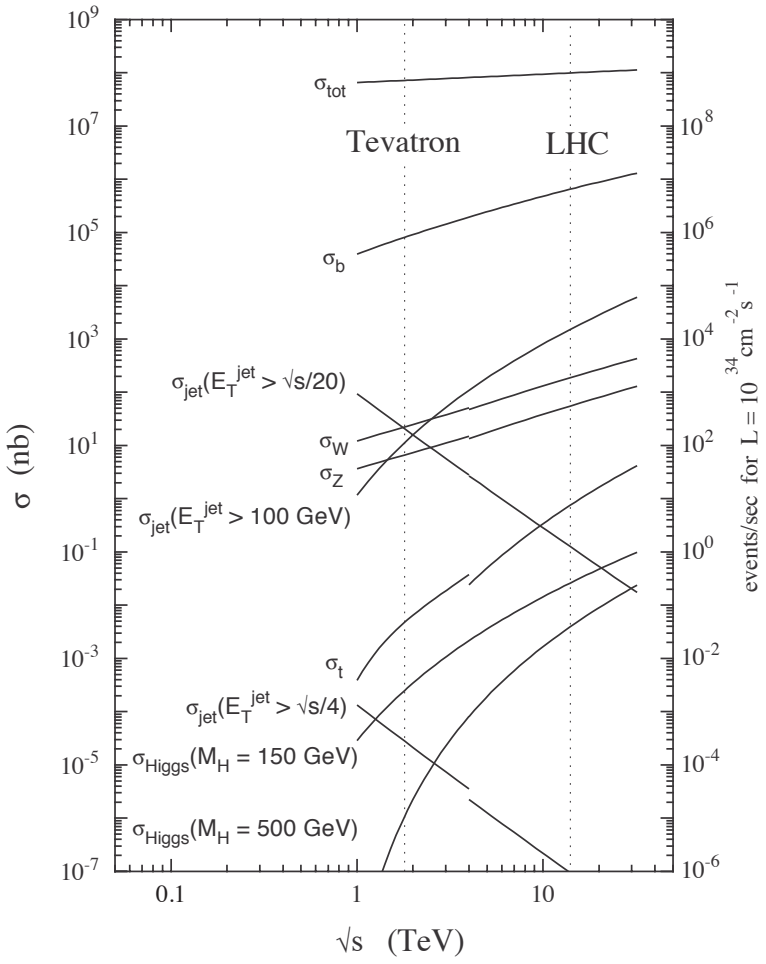

Figure 1.2: Cross sections of various physics processes in proton-proton (or proton anti-proton) collisions as a function of the center of mass energy $\sqrt{s}$. The scale on the right-hand side show the event rate with the design LHC luminosity. The vertical bands correspond to the center of mass energies at the Tevatron and the LHC.

Chapter 2

The ATLAS experiment

A collaboration of more than 2800 physicists from 32 countries composes the largest experiment installed at the LHC, ATLAS - A Toroidal LHC ApparatuS. Together with CMS, ATLAS is a general purpose detector, designed to explore a wide range of physical processes and take advantage of the full LHC program.

The detection of rare processes produced in the LHC collisions imposes stringent demands on the capabilities of the experiment. To provide sensitivity to basically any evidence of new physics beyond the Standard Model, ATLAS had to meet the following requirements:

- Full azimuthal coverage and large geometrical acceptance.
- Excellent tracking capability with precise momentum determination over a wide range of momenta – from hundreds of MeV to a few TeV.
- Vertexing detectors close to the beam line, to identify b-quark jets and tau-leptons.
- Hermetical calorimetry for missing transverse energy measurements, and fine segmentation, for the measurement of photons, electrons and jets.
- Good muon identification and momentum measurement up to a few TeV.
- Fast triggering systems, to spot interesting events and reduce background levels for efficient storage.
- Radiation hardness to tolerate the large particle fluxes provided by the LHC without loss of performance or important ageing effects.

Those demands were achieved with an Inner Detector (ID) immersed in a 2 T solenoidal magnetic field, followed by electromagnetic and hadronic calorimeters,

and a large Muon Spectrometer (MS) mounted inside air-core toroids. The configuration of the magnet systems has driven the design of the rest of the detector, illustrated in figure 2.1.

In what follows, the details of the sub-systems are given, including the trigger and software framework. But before, it is useful to present a few definitions and conventions which will be used throughout the text.

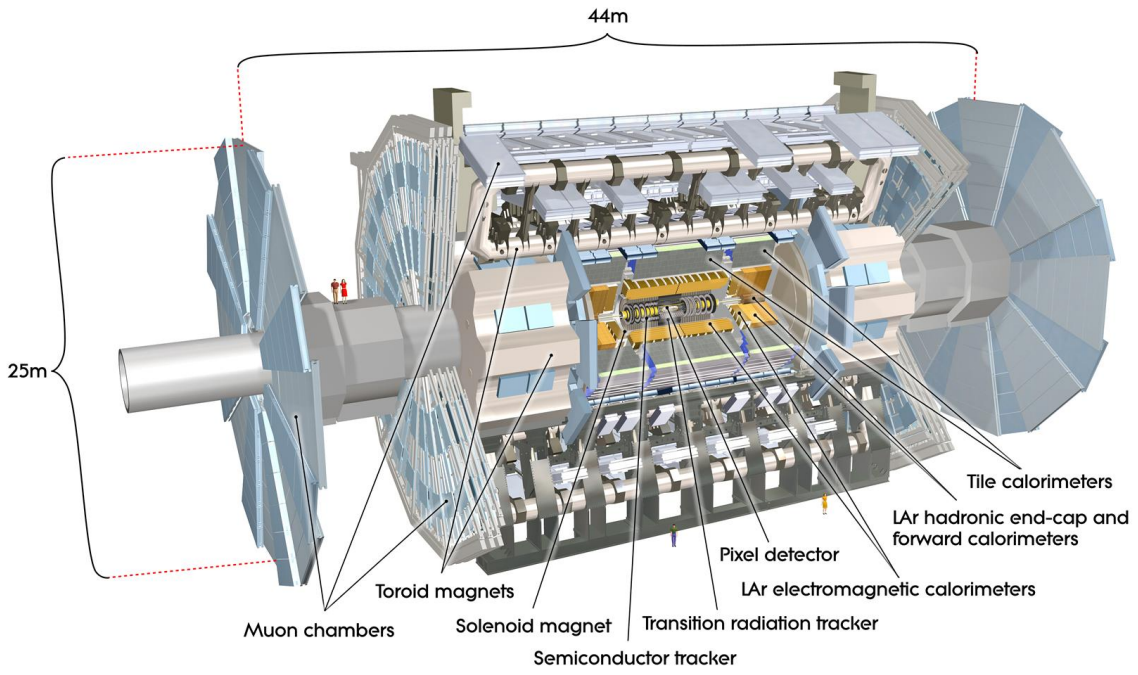

Figure 2.1: Cut-away view of the ATLAS detector, with the different sub-systems identified.

Geometry and coordinate system

ATLAS has cylindrical shape, with 25 m height, 44 m length and weights 7000 tonnes. The center of the detector corresponds to the interaction point (I.P.) and defines the origin of the coordinate system.

A right-handed Cartesian system, illustrated in fig. 2.2, is used. The z-axis is defined by the beam direction, while the x-axis points towards the center of LHC and the y-axis points upwards in the vertical direction. A polar system is frequently used, and defined by the radial vector R, the azimuthal angle ϕ, and the polar angle θ. R starts at the origin of the system, ϕ is measured from the x-axis, and runs from $-\pi$ to π, while θ is comprised between 0 and π.

The transverse plane, perpendicular to the beam line, is the $x-y$ plane. Several quantities are expressed in this plane, such as the transverse momentum (P_T) and the transverse energy (E_T), and can be defined as:

$$P_T = P \sin(\theta) \ . \tag{2.1}$$

A convenient way of expressing the polar angle is the pseudo-rapidity, η, defined by:

$$\eta \equiv -\log\left(\tan\frac{\theta}{2}\right) \ . \tag{2.2}$$

For highly relativistic particles, η is an approximation of the rapidity $y = \frac{1}{2}\ln\left[(E+P_Z)/(E-P_Z)\right]$, which transforms additively under boosts in the z direction. As a consequence of the last statement, differences in rapidity Δy , and the shape of the rapidity distribution in particle collisions dN/dy are Lorentz invariants [3]. This shape is also flat in the central region up to a few units in rapidity. To determine y, one must know the energy or mass of the particle, while the pseudo-rapidity depends only on the polar angle of the track.

Boosts along the beam axis also do not affect the ϕ angle, and thus it is useful to measure distances in the azimuthal – pseudo-rapidity plane. The distance ΔR is defined as:

$$\Delta R = \sqrt{(\Delta\eta)^2 + (\Delta\phi)^2} \, . \tag{2.3}$$

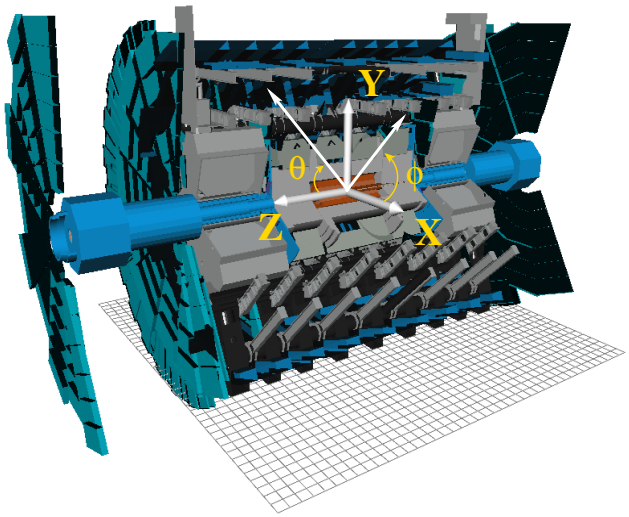

Figure 2.2: Illustration of the coordinate system used in ATLAS.

2.1 The Inner Detector

Precise tracking is achieved by the combination of high bending power and fine-granularity position measurements for charged particles. The Inner Detector offers pattern recognition, momentum and vertex measurements, and electron identification capabilities.

Three independent and complementary systems help fulfilling these requirements. The inner part of the tracking volume is composed of precision silicon detectors – pixels and strips – while the outer part comprises straw-tube trackers with the capability to generate and detect transition radiation. The layout of the sub-system is illustrated in figure 2.3 and details can be found in ref. [4].

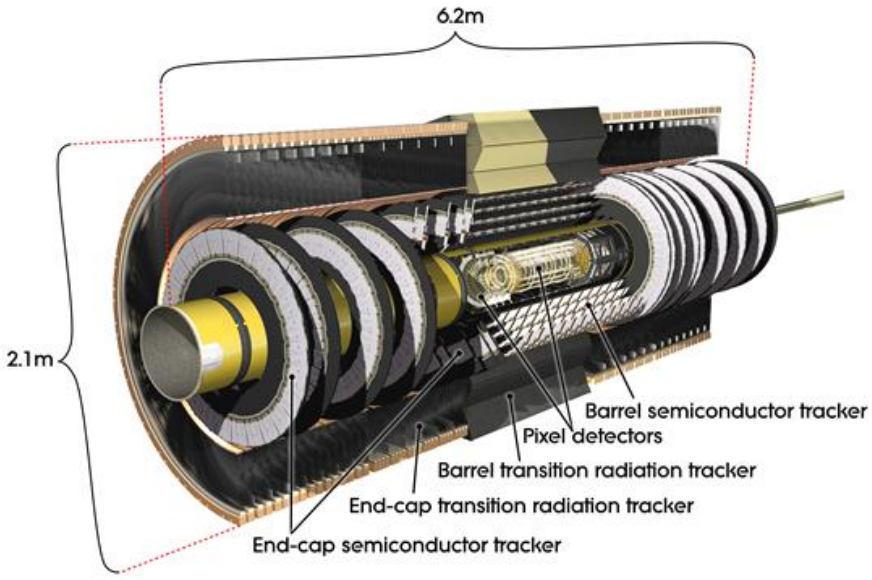

Figure 2.3: Cut-away view of the ATLAS Inner Detector.

The high-radiation environment was a major consideration for the design of the Inner Detector sensors, on-detector electronics, mechanical structure and services. The silicon detectors are kept at low temperatures (approximately -5 to -10°C) to minimize the noise after radiation damage. Nonetheless, the innermost layer of the pixels needs to be replaced after three years of operation at full luminosity. The straw-tubes, on the contrary, can operate safely at room-temperature.

The material budget was also minimized, to avoid deterioration of the resolution of both tracking and calorimetry. Still, mainly due to the services and supports it varies from 0.5 to 2.5 radiation lengths (X_0) depending on η (fig. 2.4). As a consequence, 40% of the photons convert into electron-pairs and electrons lose a great fraction of their energy through bremsstrahlung before reaching the electromagnetic

calorimeter.

The system is surrounded by a central solenoid that generates a rather uniform axial magnetic field with a strength of 2 T in the center. The solenoid extends over a length of 5.3 m with a diameter of 2.5 m. The operating temperature of 4.5 K is maintained by a cryostat shared with the barrel electromagnetic calorimeter.

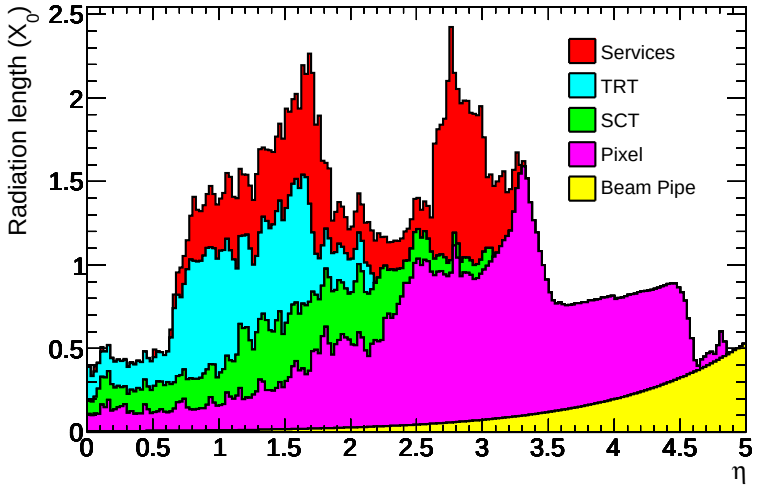

Figure 2.4: Material distribution at the exit of the Inner Detector envelope as a function of $|\eta|$ (averaged over ϕ).

2.1.1 The pixel detectors and the silicon micro-strip trackers (SCT)

The precision tracking detectors (pixel and SCT) extend up to $|\eta| < 2.5$. They are arranged in concentric cylinders around the beam axis in the barrel, and disks perpendicular to this axis in the end-cap regions. Typically three pixel layers and four SCT strips are crossed by each track, as illustrated in fig.2.5.

The pixel layers are positioned at radial distances of 50.5 mm, 88.5 mm and 122.5 mm in the barrel, and 49.5 mm, 58.0 mm and 65.0 mm in the end-caps. All pixel sensors are identical, segmented in $R-\phi$ and z, with intrinsic accuracies of 10 μm in $R-\phi$ and 115 μm in z (R) in the barrel (end-cap). Approximately 80.4 million readout channels are used. The high-precision space point measurements allow the reconstruction of short lived particles and the associated production vertices. This is of fundamental importance in the identification of b-quark jets.

Following the pixel detectors, eight layers of silicon strips are placed in 2-by-2 structures, providing four space point measurements for each track. The intrinsic

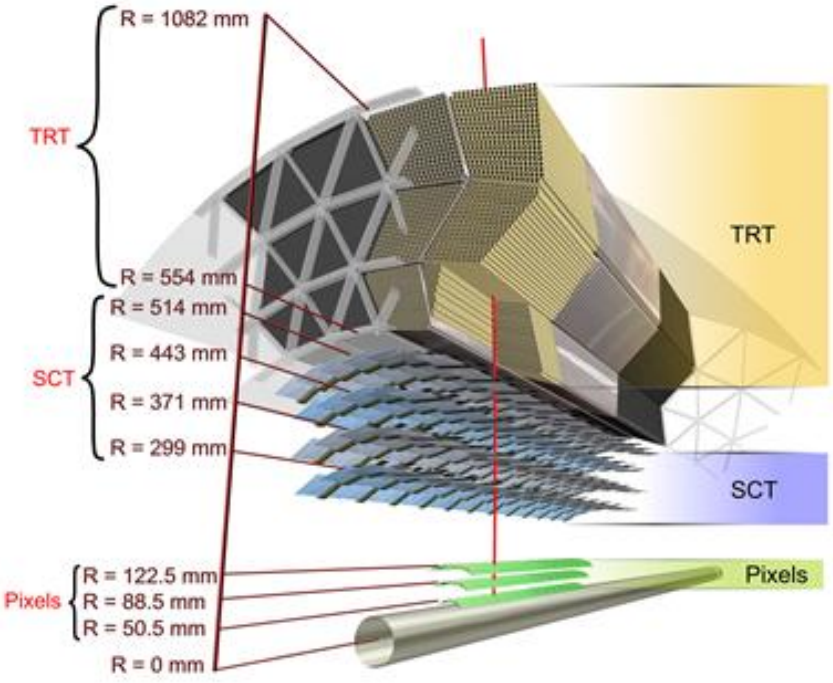

Figure 2.5: Illustration of the structural elements and sensors with their respective position, traversed by a track in the barrel region of the Inner Detector.

accuracy per module is 17 μm in $R-\phi$ and 580 μm in z (R) in the barrel (end-cap), with a total of 6.3 million readout channels.

2.1.2 The transition radiation tracker

The outer part of the Inner Detector is composed of layers of gaseous straw tubes inserted in transition radiation material. With an average of 30 hits per charged particle track, the transition radiation tracker (TRT) provides continuous tracking and electron identification complementary to that of the calorimeter over a wide range of energies. Enhanced pattern recognition and significant improvement of the momentum resolution are achieved with this detector, which extends radially from 56 to 107 cm over $|\eta| < 2.0$.

The TRT only provides $R-\phi$ information in the barrel and $z-\phi$ in the end-cap, for which it has an intrinsic accuracy of 130 μm per straw. In the barrel region, straws with a diameter of 4 mm and 144 cm long are disposed parallel to the beam axis, with their wires divided around $\eta = 0$. In the end-cap region, the 37 cm long straws are arranged radially in wheels. The total number of TRT readout channels is approximately 351 000.

The tubes are filled with a non-flammable xenon-based gas mixture of 70% Xe, 20% CO_2 and 10% CF_4. This ensures high efficiency in the detection of ionization signals and transition radiation photons, produced in the polypropylene fibres that surround the straws. Typically, seven to ten high-threshold hits from transition radiation are expected for electrons with energies above 2 GeV. This capability is illustrated in figure 2.6.

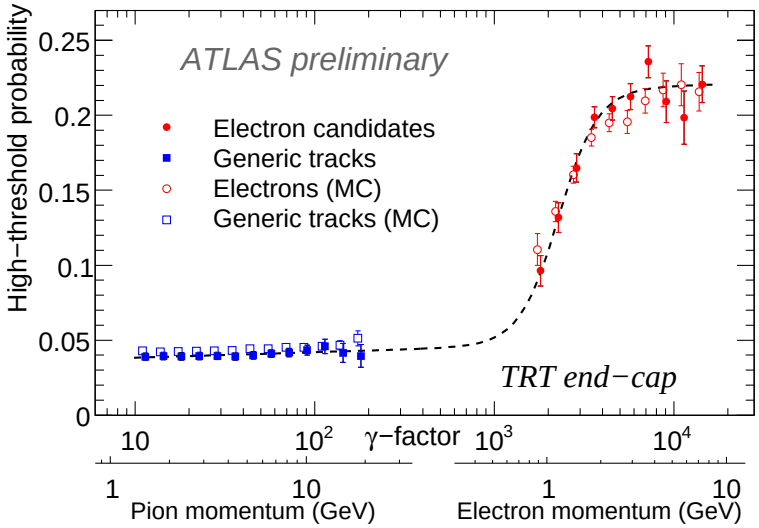

Figure 2.6: Probability of a transition radiation high-threshold hit in the TRT end-caps as a function of the Lorentz Factor. Measurements from 2009 LHC collision events are compared to predictions from Monte Carlo simulations.

2.1.3 Inner Detector tracking performance

The Inner Detector offers robust pattern recognition and high performance tracking in both $R-\phi$ and z coordinates. Precision silicon trackers close to the beam line are complemented by straw tubes providing many space point measurements with a longer lever arm. As a result, a reconstruction efficiency above 99% is obtained for muons with transverse momenta above 5 GeV for all pseudo-rapidities, as shown in in fig. 2.7a. The efficiency for reconstructing pions and electrons around 5 GeV is expected to go down to $\sim 80\%$ at large rapidities, becoming larger and more uniform as a function of $|\eta|$ at higher momenta. Multiple scattering, hadronic interactions in the case of pions and bremsstrahlung effects in the case of electrons are behind such inefficiencies.

Overall, the momentum resolution can be approximated by the formula: $\sigma_{P_T}/Pt = 0.05\%\, P_T(\text{GeV}) \oplus 1\%$. Low-$P_T$ tracking is limited by the amount of mate-

rial in the detector, while for large pseudo-rapidities the absence of the TRT implies a degradation of the momentum resolution. The expected momentum resolution for muons as a function of η is given in fig. 2.7b.

In addition, the impact parameter at the perigee, i.e. the point of closest approach with respect to the beam line, is determined accurately. The expected resolution on the modified longitudinal impact parameter ($z_0 \times \sin\theta$) is of a few hundred microns, while in the transverse plane (d_0) it goes down to 10 μm for high momentum tracks. Low momentum particles are more subject to multiple scattering effects, which limits the resolution. The results obtained with full simulations for pions of $P_T = 1$ GeV, 5 GeV and 100 GeV are shown in fig. 2.8.

Although these results were evaluated for single particles, the performance is essentially unchanged in the presence of additional tracks [5]. The fine granularity of the silicon detectors ensures low occupancy rates ($< 4\%$) for up 100 collisions occurring per bunch crossing at the LHC, which corresponds to a luminosity of 4×10^{34} cm^{-2} s^{-1}. Only the momentum resolution may be worsen due to the high occupancy of the TRT (up to 60%), with degradations up to a factor of two.

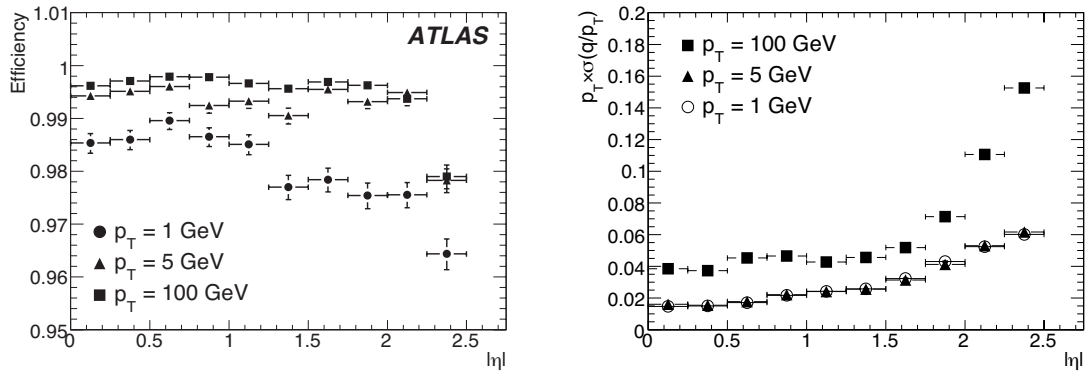

(a) (b)

Figure 2.7: Expected tracking performance in terms of (a) reconstruction efficiency and (b) relative transverse momentum resolution as a function of $|\eta|$ for muons of $P_T = 1$ GeV, 5 GeV and 100 GeV.

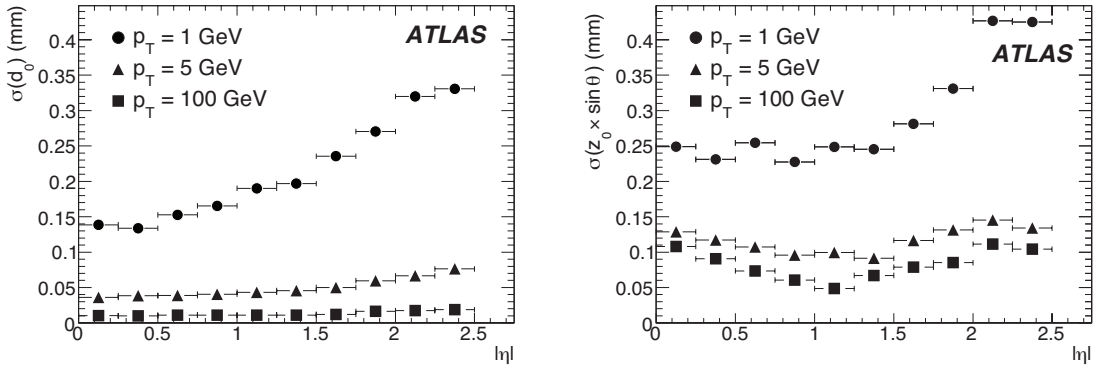

(a) (b)

Figure 2.8: Expected resolution on (a) transverse and (b) modified longitudinal impact parameters (d_0 and $z_0 \times \sin\theta$, respectively) as a function of $|\eta|$ for pions of $P_T = 1$ GeV, 5 GeV and 100 GeV.

2.2 The Calorimeters

The calorimetric system is located between the Inner Detector and the Muon Spectrometer, covering the pseudo-rapidity range $|\eta| < 5$. Different techniques are used in the barrel and end-cap regions, according to the demands of a wide range of physics process and radiation environment. Measurements of electrons, photons and jets and information about missing transverse energy are provided, given the full azimuthal coverage and good hermeticity of the detectors.

In the region covered by the inner tracker, showers produced by electrons and photons are contained in the finely segmented liquid argon (LAr) electromagnetic calorimeters (EM), with excellent performance in terms of energy and position resolution. Liquid argon technology is also applied in the detection of hadronic activity in the end-cap and forward regions, instrumented by a Hadronic End-cap Calorimeter (HEC) and a Forward Calorimeter (FCal). Chosen for its intrinsic linear behavior, its stability of response over time and its intrinsic radiation-hardness, the LAr detectors require an operating temperature around 88 K. The barrel EM calorimeter shares the cryostat with the central solenoid, eliminating two vacuum walls. The end-caps are hosted in their own cryostats, used for the EM, the HEC and the FCal.

Hadronic calorimetry is complemented by a scintillator-tile detector of easier assembling and lower cost, extending up to $|\eta| < 1.7$. A layout of the ATLAS calorimeters is presented in fig. 2.9 and the segmentation of each part is summarized in table 2.1. Each sub-calorimeter is described in the following subsections and their performance is also discussed. The strategies for reconstructing electrons are reviewed in 2.2.5.

An additional function of the calorimeters is to limit the rate of particles escaping to the muon system. The total depth of the EM calorimeter exceeds 22 radiation lengths (X_0) in the barrel and 24 in the end-cap. The hadronic part comprises 9.7 interaction lengths (λ) in the barrel and 10 in the end-caps. This ensures good resolution on high-energy jets and punch-through into the MS well below the irreducible level of prompt muons or the ones from pion and kaon decays. The material budget of the calorimeters as a function of pseudo-rapidity is presented in fig. 2.10.

2.2.1 The electromagnetic calorimeter

The precision electromagnetic calorimeters are lead - liquid argon detectors with accordion shape absorbers and electrodes. This geometry, represented in figure 2.11, provides full azimuthal coverage without cracks, allows fast signal extraction and segmentation of the active layers in depth. The total calorimetric depth

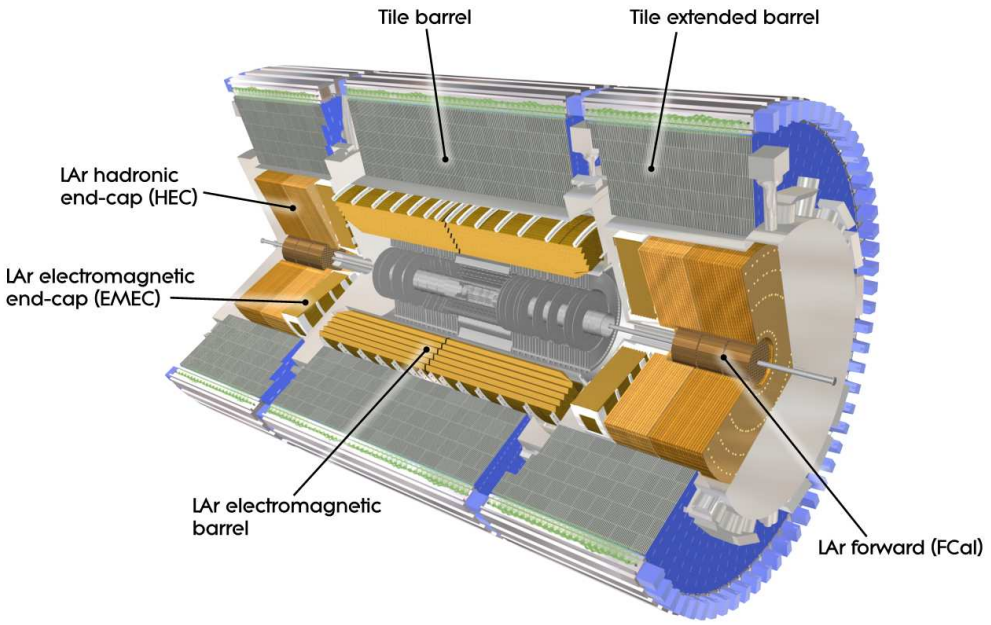

Figure 2.9: Cut-away view of the ATLAS calorimeter system.

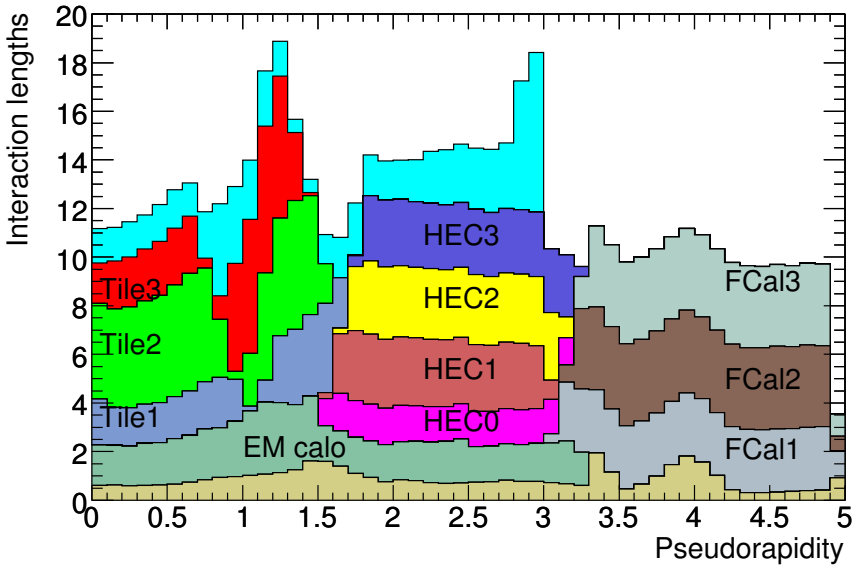

Figure 2.10: Cumulative amount of material, in units of interaction length, in front of and after the calorimeters as a function of $|\eta|$. Also shown for completeness is the total amount of material in front of the first active layer of the Muon Spectrometer (light blue). The peaks at $|\eta| \sim 1.3$ and $|\eta| \sim 3$ correspond to the TileCal extended barrel and a shielding disk, respectively. Details can be found in ref. [4].

is approximately constant over η, although three layers are used in the region covered by the Inner Detector ($0 < |\eta| < 2.5$), and two both in the higher-η region

Table 2.1: Pseudo-rapidity coverage, longitudinal segmentation and granularity of the ATLAS calorimeters. The full numbers can be found in ref. [6].

Calorimeter	**Coverage**		**Granularity** ($\Delta\eta \times \Delta\phi$)
EM calorimeter	**barrel**	**end-cap**	
Presampler	$\lvert\eta\rvert < 1.54$	$1.5 < \lvert\eta\rvert < 1.8$	0.025×0.1
Sampling 1	$\lvert\eta\rvert < 1.475$	$1.375 < \lvert\eta\rvert < 3.2$	0.003×0.1[a] 0.025×0.025[b] 0.003 - 0.025×0.1[c] 0.1×0.1[d]
Sampling 2	$\lvert\eta\rvert < 1.475$	$1.375 < \lvert\eta\rvert < 3.2$	0.025×0.025 0.075×0.025[b] 0.1×0.1[d]
Sampling 3	$\lvert\eta\rvert < 1.35$	$1.5 < \lvert\eta\rvert < 2.5$	0.05×0.025
Tile calorimeter	**barrel**	**extended barrel**	
Sampling 1 Sampling 2	$\lvert\eta\rvert < 1.0$	$0.8 < \lvert\eta\rvert < 1.7$	0.1×0.1
Sampling 3			0.2×0.1
Hadronic end-cap calorimeter			
Samplings 1-4	$1.5 < \lvert\eta\rvert < 3.2$		0.1×0.1[e] 0.2×0.2[d]
Forward calorimeter			
Samplings 1-3	$3.1 < \lvert\eta\rvert < 4.9$		0.2×0.2

[a] $\lvert\eta\rvert < 1.4$, [b] $1.4 < \lvert\eta\rvert < 1.475$, [c] $1.375 < \lvert\eta\rvert < 2.5$, [d] $2.5 < \lvert\eta\rvert < 3.2$, [e] $1.5 < \lvert\eta\rvert < 2.5$

($2.5 < \lvert\eta\rvert < 3.2$) and in the overlap region between the barrel ($\lvert\eta\rvert < 1.475$) and the end-caps ($\lvert\eta\rvert > 1.375$). Geometrical limitations and simplicity of construction justify this layout.

Up to $\lvert\eta\rvert = 2.5$, accurate position measurements are obtained by finely segmenting the first layer, with narrow strips of 4 mm pitch. The cell granularity in the barrel is $\Delta\eta \times \Delta\phi = 0.003 \times 0.1$ and varies with η in the end-cap. The middle layer has a constant cell size of $\Delta\eta \times \Delta\phi = 0.025 \times 0.025$ and is the thickest of the three compartments, providing good positioning of photon clusters and precise energy measurement. A back compartment with a granularity of $\Delta\eta \times \Delta\phi = 0.05 \times 0.025$ ensures the shower containment in the EM volume. The higher eta region ($2.5 < \lvert\eta\rvert < 3.2$) exhibits coarser granularity, with the two layer segmented at $\Delta\eta \times \Delta\phi = 0.1 \times 0.1$.

Energy losses by particles crossing the material in front of the calorimeters introduce an uncertainty in the energy measurements. To overcome this difficulty, the EM is complemented by presamplers – thin layers of liquid argon – in the regions

up to $|\eta| < 1.8$. The performance of the system is reviewed in section 2.2.4.

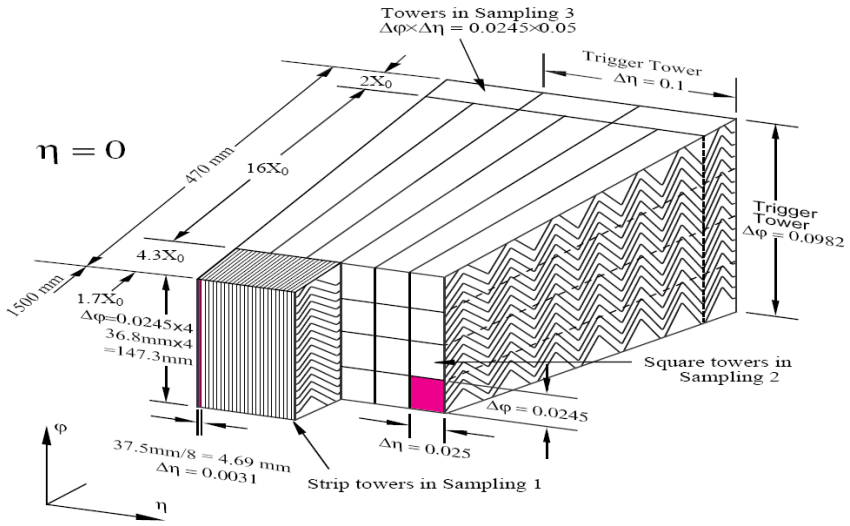

Figure 2.11: Sketch of a barrel module of the electromagnetic calorimeter.

2.2.2 The hadronic calorimeters

Two different systems are used as hadronic calorimeters, the one in the end-caps using the radiation hard LAr technology and the barrel one made of scintillating tiles. Their main features are presented here, and their performance is compared in 2.2.4.

The hadronic end-cap calorimeter (HEC) is a parallel plate copper - liquid argon sampling calorimeter. It provides coverage for hadronic showers in the range $1.5 < |\eta| < 3.2$, sitting right behind the electromagnetic end-caps.

Radiation hardness and cost effectiveness drove the choice for this technology and the calorimeter geometry. The HEC is formed by two wheels divided into two segments in depth, with a total of four compartments per end-cap. Each wheel is built from 32 identical wedge-shaped modules, providing projective geometry in the ϕ direction but only "pseudo-projectivity" in η, as illustrated in figure 2.12. The size of the HEC cells is $\Delta\eta \times \Delta\phi = 0.1 \times 0.1$ up to $|\eta| < 2.5$ with twice those values in the rest of the coverage.

In the central region, hadronic activity is measured by the tile calorimeter (TileCal), placed directly outside the EM calorimeter envelope. Steel absorbers and scintillating tiles as active material are employed. The two sides of the scintillators are connected to wavelength shifting fibres, and read out by photomultiplier tubes.

The TileCal is divided into a 5.8 m long barrel, covering the region up to $|\eta| < 1.0$ and two extended barrels in the range $0.8 < |\eta| < 1.7$ with 2.6 m in length. It is segmented in depth in three layers, with approximately 1.5, 4.1 and 1.8 interaction lengths (λ) for the barrel and 1.5, 2.6, and 3.3 λ for the extended barrel. This provides maximum radial depth at a minimum cost, with an inner radius of 2.28 m and an outer radius of 4.25 m.

Cables and services from the detectors placed before the tile calorimeter occupy the 60 cm gap between the barrel and the extended barrel. In this region, scintillating tiles assembled in the so called Intermediate Tile Calorimeter complement the energy measurement.

The geometry of TileCal is sketched in figure 2.13, with the layers in depth noted as A, BC and D. The orientation of the scintillator tiles radially and normal to the beam line allows for full projective azimuthal coverage. On the other hand, the grouping of the readout fibres imply a "pseudo-projective" geometry in η. A particle crossing the calorimeter eventually leaves signal in more than one cell per layer, which have granularities of $\Delta\eta \times \Delta\phi = 0.1 \times 0.1$ in in the first two samplings and 0.2×0.1 in the third.

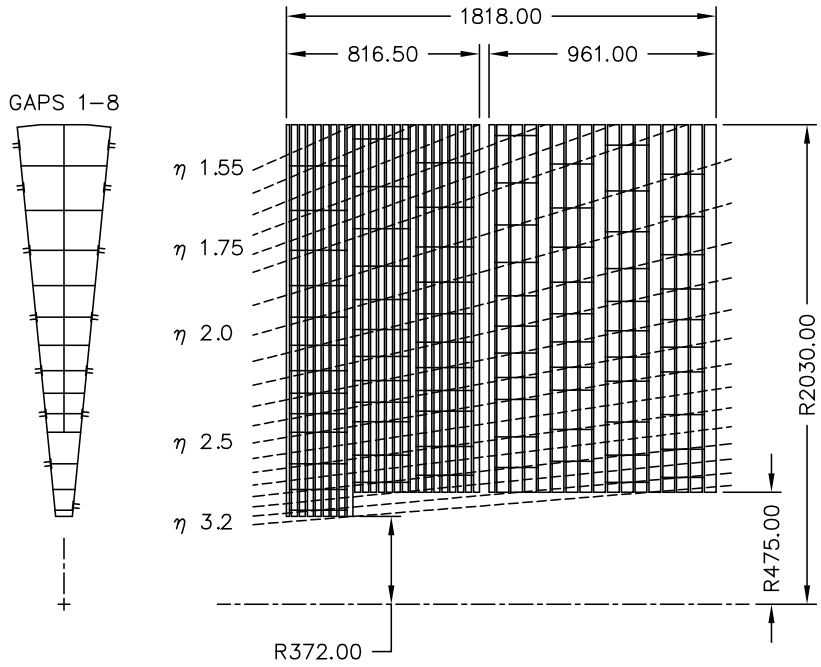

Figure 2.12: Schematic views of the hadronic end-cap calorimeter in $R - \phi$ (left) and $R - z$ (right). The semi-pointing layout of the readout electrodes is indicated by the dashed lines. Dimensions are in mm.

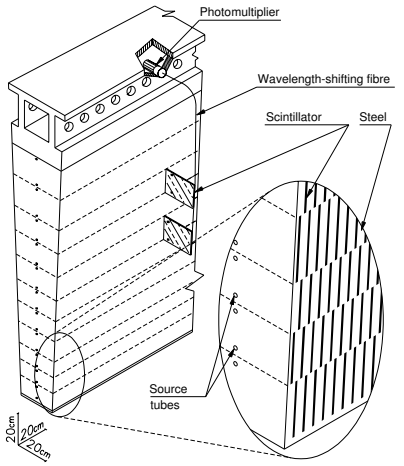

(a) Illustration of the components in a module of the tile calorimeter.

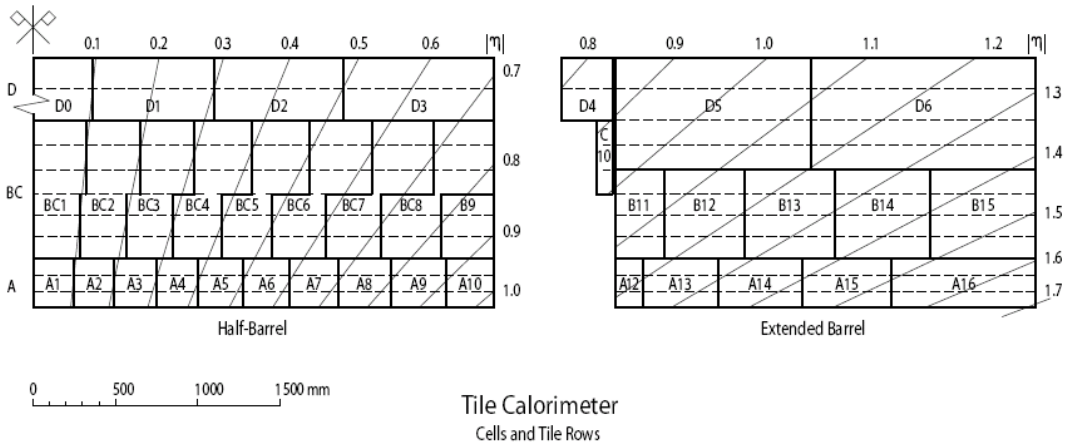

(b) $R-z$ view of the tile calorimeter. The diagonal lines indicate the semi-projective layout of the cells.

Figure 2.13: Schematic views of (a) a module and (b) the full tile calorimeter geometry in the $R-z$ plane.

2.2.3 The forward calorimeter

The forward calorimeter (FCal) provides both electromagnetic and hadronic energy measurements, and extend the pseudo-rapidity coverage of the calorimetric system from $|\eta| = 3.1$ to $|\eta| = 4.9$. Although the system is not used for precision measurements, it provides valuable information for missing transverse energy determination and reconstruction of very forward jets.

Radiation tolerance is extremely important in this region, where high particle fluxes are expected. This has resulted in a design with very small liquid-argon gaps, separated by copper absorbers in the first compartment, and tungsten absorbers in

the last two. Overall, the thickness of the FCal is of the order of 10 interaction lengths.

2.2.4 Performance of the calorimeters

The energy resolution of each sub-calorimeter was evaluated with beams of electrons and pions before their insertion in the ATLAS detector. The experimental measurements, after noise subtraction, have been fitted with the expression:

$$\frac{\sigma(E)}{E} = \frac{a}{\sqrt{E(\mathrm{GeV})}} \oplus b, \tag{2.4}$$

where a is the stochastic term and b the constant term reflecting local non-uniformities in the response of the calorimeter. The design parameters, specified in ref. [7] were fulfilled, and the obtained performance is summarized in table 2.2.

In what concerns the electronic noise, updated information was extracted during the cosmic-ray data taking periods, from 2007 to 2010. The noise was measured in intervals when no track was recorded in ATLAS. During LHC runs this is done in time windows when no collisions should happen. The results correspond to the expectations for both the LAr and Tile calorimeters and are shown in figures 2.14 and 2.15 respectively. No major impacts on jet reconstruction above ~ 5 GeV or electron identification above ~ 0.5 GeV are expected from these noise levels.

Table 2.2: Resolution of the different calorimeters for pions and electrons evaluated with test beam data, given by the stochastic term a and the constant term b as in equation 2.4. The constant term for the full electromagnetic calorimeter is expected to be around 1%.

Calorimeter	**Particle**	**Energy Resolution**	
		a (% $\sqrt{\mathrm{GeV}}$)	b (%)
Electromagnetic	electrons	10.0 ± 0.4	0.4 ± 0.1
Hadronic End-Cap	pions	70.6 ± 1.5	5.8 ± 0.2
Forward	electrons	28.5 ± 1.0	3.5 ± 0.1
	pions	94.2 ± 1.6	7.5 ± 0.4
Tile	pions	56.4 ± 0.4	5.5 ± 0.1

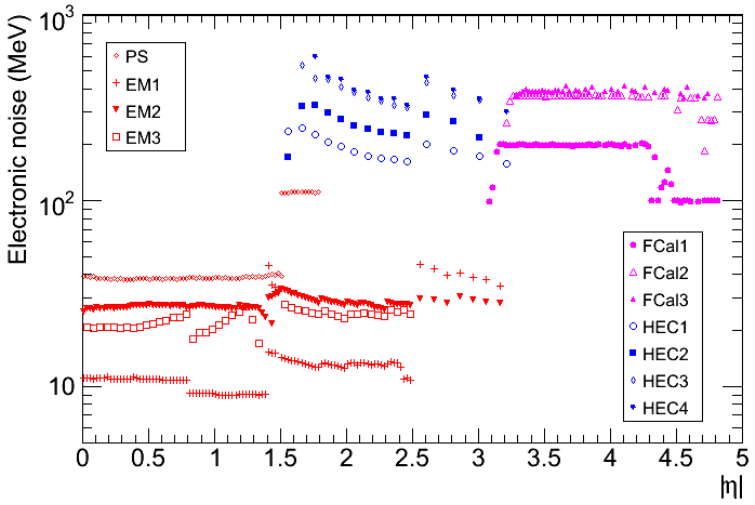

Figure 2.14: Electronic noise in the cells of the liquid argon calorimeters as a function of $|\eta|$.

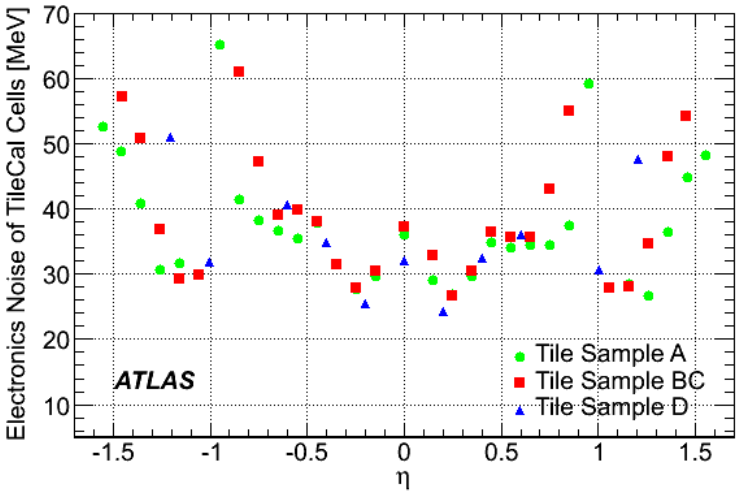

Figure 2.15: Electronic noise in the cells of the tile calorimeter as a function of η.

2.2.5 Electron reconstruction and associated performance

The EM calorimeter was designed to provide good photon and electron identification over a broad energy range, from a few GeV up to ~ 5 TeV. Electrons with such P_T are expected from physics channels of prime interest at the LHC, while hadronic collisions at LHC energies produce mainly QCD jets. The rate of isolated electrons compared with the abundance of jets in the P_T range between 20 and 50 GeV is below 10^{-5}. Excellent jet rejection factors are therefore required with reconstruction efficiencies satisfying the needs of different physics channels. The strategies adopted to achieve this goal are briefly discussed here.

Electrons are reconstructed using information from both the calorimeter and the

Inner Detector. The standard algorithm starts from ensembles of cells (clusters), defined in the EM calorimeter and then builds the identification variables based on information from both systems. A second algorithm, which is seeded from the Inner Detector tracks, is optimized for electrons with energies as low as a few GeV, and selects good-quality tracks matching a relatively isolated deposition of energy in the EM.

A *sliding window algorithm* with fixed size [8, 9] is used for cluster reconstruction. It looks for regions of approximately 0.1×0.1 in $\Delta\eta \times \Delta\phi$ where the deposits exceed 2.5 GeV and defines the cluster position such that the energy inside the window is maximized. After the discrimination between electrons and photons (described below) the window size is redefined according to the region of the calorimeter and the particle being reconstructed. In the barrel, electrons need larger clusters than photons due to the bending in the magnetic field, which leads to soft photon radiation. In the end-cap, all the particles use the same window since the effect of the magnetic field is smaller. The window sizes were chosen as a compromise between the spread of the energy deposits and the noise (the inclusion of more cells increases the noise). The details can be found in ref. [9].

For each identified cluster, the reconstruction looks for a matching track within $\Delta\eta \times \Delta\phi = 0.05 \times 0.10$. If a suitable candidate is found the object is flagged as an electron and a classification of its reconstruction quality takes place. A cut-based selection is adopted, using 16 variables related to the shower shapes, tracking information and track-cluster matching. Groups of variables are used to introduce common criteria for physics analysis. Loose, medium and tight definitions are adopted and described below:

- **Loose cuts** perform a simple electron identification based only on limited information from the calorimeters. Hadronic leakage, i.e. the amount of energy that escapes to the hadronic calorimeter, and shower-shape variables only from the middle layer of the EM calorimeter are evaluated. This definition provides high identification efficiency $\mathcal{O}(90\%)$, but poor background rejection, around 600.

- **Medium cuts** improve the background rejection quality by a factor 3-4, adding cuts on the first layer of the EM calorimeter (strips) and on the tracking variables. The former are adequate for $e - \pi^0$ separation. The latter ones include requirements on the number of hits in silicon detectors (pixels and SCT) and the transverse impact parameter. As a result, the increase in purity is compensated by a drop in the identification efficiency around 10%.

- **Tight cuts** make use of all the particle-identification tools currently available for electrons. In addition to the *medium cuts*, they require hits on the first layer of the pixels to reject electrons from conversions, and hits in the TRTs. The total number of hits and the fraction of high-threshold hits are used to reject the dominant background from charged hadrons. Strict geometrical matching between the cluster and the extrapolated position of the track and compatibility between the track momentum and the energy deposit ($E/P < 10$) are also required. The last cut was applied in the baseline reconstruction until late 2008.

The isolation information, corresponding to the energy outside the cluster and within a cone of $\Delta R < 0.2$, can be applied to increase the purity of the electron sample. The efficiencies of each definition were evaluated with dedicated simulation samples of single electrons and physics processes [10]. The results for Higgs boson decays to four electrons are shown in figure 2.16, as a function of pseudo-rapidity and transverse energy.

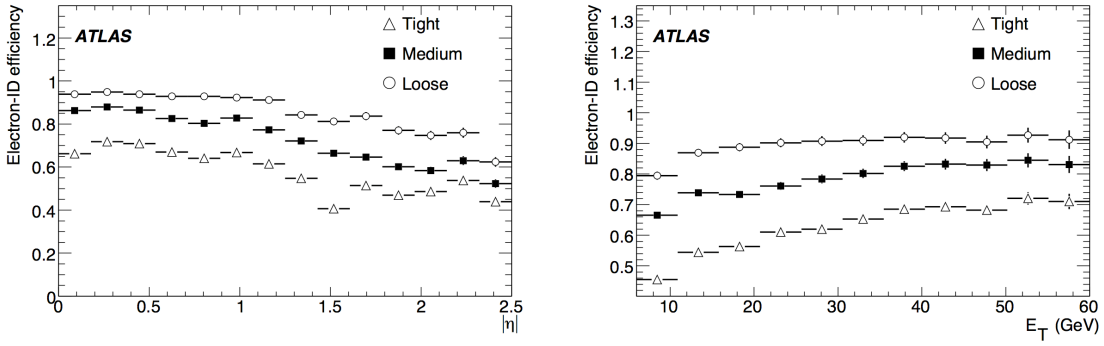

(a) (b)

Figure 2.16: Expected reconstruction efficiencies as a function of (a) pseudo-rapidity and (b) transverse energy for electrons originating from Higgs boson decays in the $H \to 4e$ channel. The different definitions described in the text are compared. Only electrons with $P_T > 5$ GeV are considered.

2.3 The Muon Spectrometer

The Muon Spectrometer is the outermost part of the ATLAS detector, defining its overall dimensions. It is a combination of large superconducting air-core toroid magnets, instrumented with separate trigger and high-precision tracking chambers, represented in figure 2.17. High-resolution momentum measurements independently of the Inner Detector are provided for $|\eta| < 2.7$, and triggering capabilities up to $|\eta| < 2.4$.

The driving performance goal is a stand-alone transverse momentum resolution of approximately 11% for 1 TeV tracks, with minimum charge misidentification. The associated sagitta of 500 μm for such tracks requires a resolution of 50 μm, obtained with precise knowledge of the magnetic field and chamber positioning. A brief description of the different components of the muon system and the obtained performance are given in the following subsections. The reader is referred to [4, 6, 10, 11] for more information.

2.3.1 The toroid magnets

The toroidal configuration provides a field which is mostly orthogonal to the muon trajectories over a large volume and little material in the measurement regions, minimizing the degradation of resolution due to multiple scattering. Over the range of $|\eta| < 1.4$, magnetic bending is provided by the large barrel toroid. Eight coils are arranged symmetrically around the beam axis, extending radially from 9.4 m to 22 m, with a length of 25.3 m. For $1.6 < |\eta| < 2.7$, muon tracks are deflected by two smaller end-cap magnets inserted into both ends of the barrel system. The end-cap toroids are rotated in azimuth by an angle of 22.5° with respect to the barrel coils to provide for radial overlap, and to optimize the bending power in the transition region ($1.4 < |\eta| < 1.6$). Nevertheless, due to the finite number of coils, the field configuration is not perfectly toroidal. Small regions with degraded momentum resolution exist due to the low field integral, represented in figure 2.19.

A picture of the system during the ATLAS installation period is shown in figure 2.18. The magnets are cooled down to 4.5 K by liquid helium and operate at a nominal current of 20.5 kA. The chambers, on the other hand, can operate at room temperature, and four different technologies are used according to the requirements of precision, timing and radiation hardness. Each one is briefly described in the following subsection.

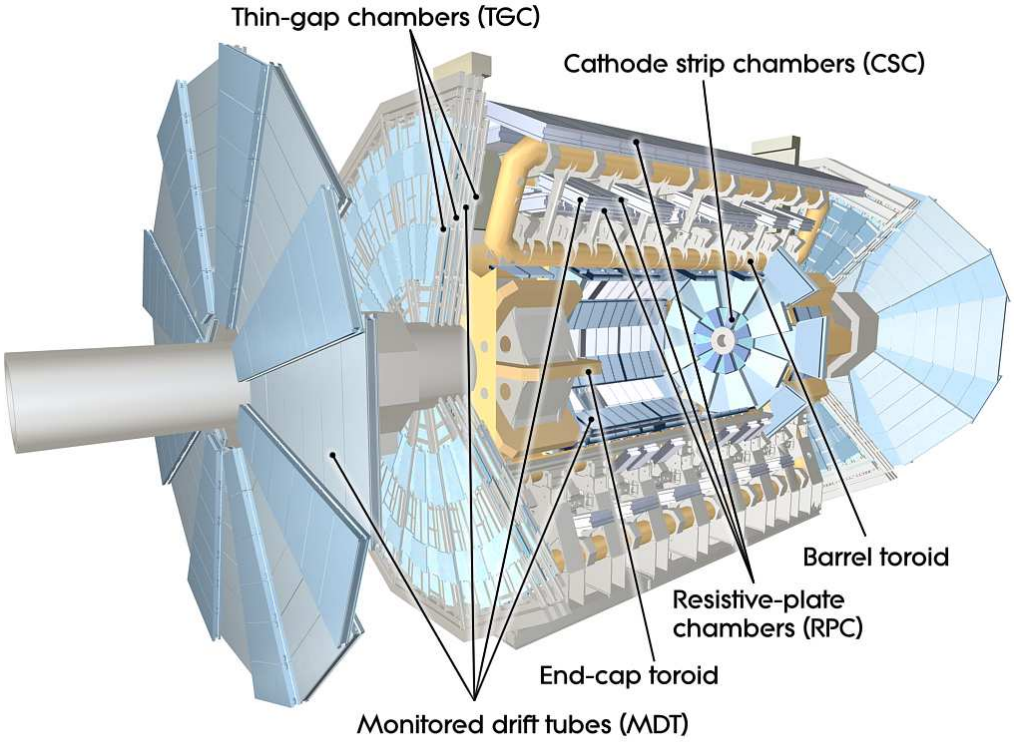

Figure 2.17: Cut-away view of the ATLAS muon system.

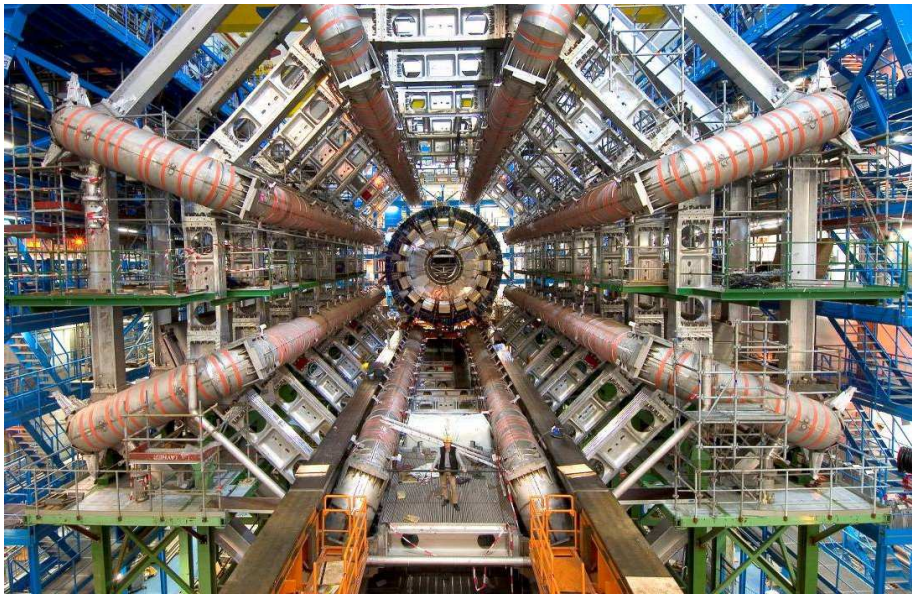

Figure 2.18: Picture of the barrel toroid magnet installed in the ATLAS cavern.

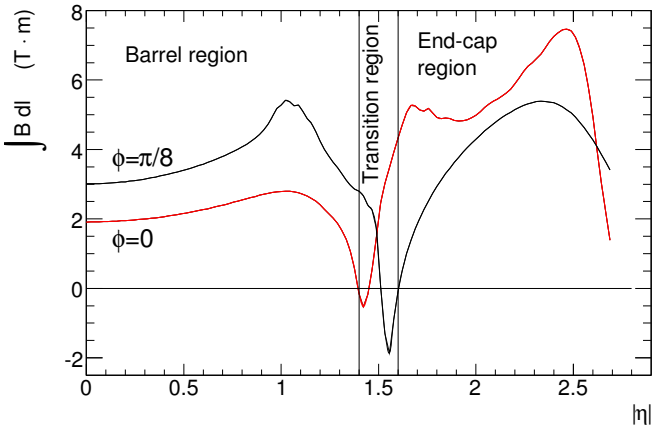

Figure 2.19: Predicted field integral as a function of $|\eta|$ inside the Muon Spectrometer.

2.3.2 Geometry and chamber types

The chamber geometry follows the eight-fold symmetry of the toroid magnets, as illustrated in figure 2.20. Each octant in the azimuthal direction is divided in a large and a small sector. The large chambers occupy the region between the barrel coils, while the small sectors are aligned with them. Overlaps in the boundaries of the sectors minimize gaps in detector coverage and also allow for the relative alignment of adjacent sectors using tracks recorded by both a large and a small chamber.

In the barrel region, tracks are measured in chambers arranged in three cylindrical layers around the beam axis, at radii of approximately 5 m, 7.5 m, and 10 m. In the transition and end-cap regions, the chambers are installed in planes perpendicular to the beam, also in three layers, located at distances of $|z| \approx 7.4$ m, 10.8 m, 14 m (transition region), and 21.5 m (end-cap) from the interaction point.

In the center of the detector ($\eta \approx 0$), a gap in chamber coverage has been left open to allow for services to the solenoid magnet, the calorimeters and the Inner Detector. The size of the gap varies from sector to sector depending on the service necessities, the biggest gaps of 1-2 m being located in the large sectors. This region extend up to $|\eta| = 0.08$ for large chambers and $|\eta| = 0.04$ for small sectors.

Precise momentum measurement is performed by determining the track coordinate in the bending plane. Monitored Drift Tubes (MDTs) were chosen for this task by their high measurement accuracy, predictability of mechanical deformations and simplicity of construction. In the forward region ($2.0 < |\eta| < 2.7$), the innermost layer is instead equipped with a radiation hard technology of Cathode Strip Cham-

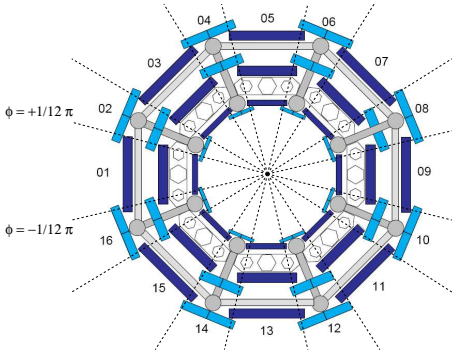

(a) $R - \phi$ view of the barrel Muon Spectrometer, illustrating large sectors (dark blue), small sectors (light blue) and the magnet coils (dark grey).

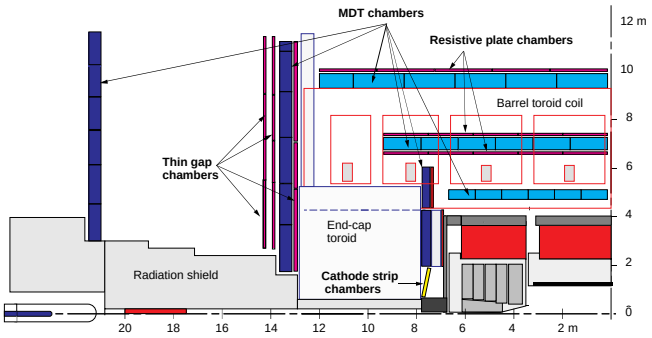

(b) $R - z$ view of the Muon Spectrometer showing the different technologies and stations.

Figure 2.20: Illustration of the muon system in $R - \phi$ and $R - z$ projections.

bers (CSCs), better suited for handling the expected particle fluxes. CSCs provide measurements of both coordinates and additionally good timing resolution. Fast triggering and second coordinate (ϕ) determination is provided by Resistive Plate Chambers (RPCs) in the barrel and Thin Gap Chambers (TGCs) in the end-caps. Both systems are able to separate beam crossings with intrinsic timing accuracies of a few nanoseconds and provide rough estimates of the track momentum. A summary of the expected resolution and number of elements of each technology is given in table 2.3. A brief description of the technologies follows.

Table 2.3: Parameters of the four chamber technologies used in the muon system: expected resolutions (not including alignment effects), maximum number of measurements per track, number of chambers and channels.

Type	**Chamber resolution**			**Measurements/track**		**Number of**	
	z/R	ϕ	time	barrel	end-cap	chambers	channels
MDT	35 μm	–	–	20	20	1150	354k
CSC	40 μm (R)	5 mm	7 ns	–	4	32	30.7k
RPC	10 mm (z)	10 mm	1.5 ns	6	–	606	373k
TGC	2-6 mm (R)	3-7 mm	4 ns	–	9	3588	318k

Monitored drift tubes (MDTs)

MDT chambers have a projective design, covering a total area of 5500 m^2. Their are formed of six or eight layers of pressurized drift tubes, with diameters of 29.970 mm. Illustrations of a tube and a chamber can be seen on figures 2.21a and

2.21b. The tubes operate with Ar/CO_2 gas (93% / 7%) at 3 bar, selected for its excellent ageing properties. In the center of each tube, a 50 μm tungsten-rhenium wire is kept at 3080 V, generating a radial electric field.

The passage of a charged particle ionizes the gas, and the liberated electrons drift towards the anode wire under the influence of the electric field. In the vicinity of the wire, an avalanche process takes place, inducing measurable signals which are read out by the on-chamber electronics. An amplifier / shaper / discriminator chip including a charge analog-to-digital converter (ADC) feeds the pulses to a time-to-digital converter (TDC). The charge information is used for noise discrimination.

The arrival time of the signal can be interpreted as a drift-radius, using a calibration function to correct for the non-linear drift velocity in the gas mixture. Single hit resolutions of the order of 80 μm are achieved, with an efficiency around 96%. The chamber resolutions are of the order of 35 μm. To fulfill the requirements for high-precision momentum determination, they are equipped with an optical monitoring system to calculate their deformations. Four alignment rays are used on most part of the chambers and only one in the center of the smallest chambers.

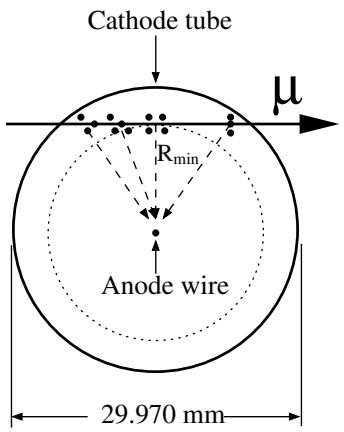

(a) Cross section of a MDT tube.

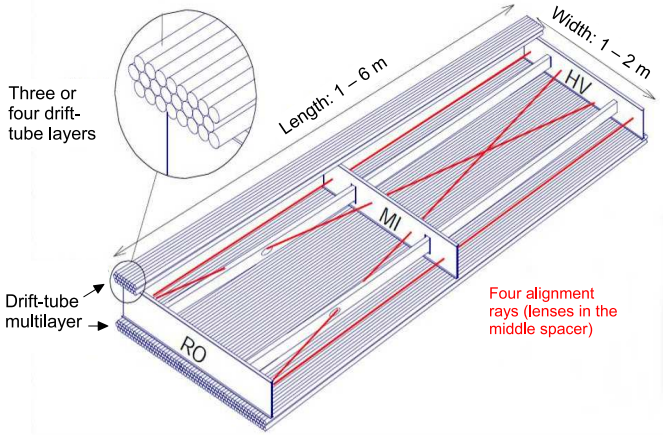

(b) Sketch of a MDT chamber. The alignment rays, shown in red, allow for the monitoring of chamber deformations.

Figure 2.21: Illustration of (a) a Monitored Drift Tube (MDT) and (b) the corresponding chamber.

Cathode Strip Chambers (CSCs)

The performance of MDTs is degraded at rates above 150 Hz/cm^2, which will be exceeded in the first layer of the forward region ($|\eta| > 2$). In this range up to $|\eta| < 2.7$, Cathode Strip Chambers provide high spatial and time resolutions with high-rate capability. CSCs are multiwire proportional chambers made of radial

anode wires and cathode planes segmented into orthogonal strips. Strips in the plane perpendicular to the wires provide the precision coordinate (η) and the ones parallel to the wire give the second coordinate (ϕ) information.

Each chamber is composed by 4 layers with 5 mm gaps filled with with Ar / CO_2 (80% / 20%). The wire plane is located at the center of each gap, with a wire pitch of 2.5 mm, equal to the anode-cathode spacing, as illustrated in figure 2.22. The wires are 30 μm in diameter and operate at 1900 V. This result in drift times of less than 40 ns, with an associated precision around 7 ns. The expected spatial resolutions are of the order of 40 μm in R and 5 mm in ϕ.

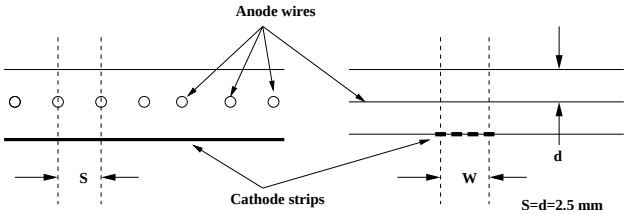

(a) Structure of the CSC cells looking down the wires. The wire pitch s is equal to the anode-cathode spacing $d = 2.5$ mm.

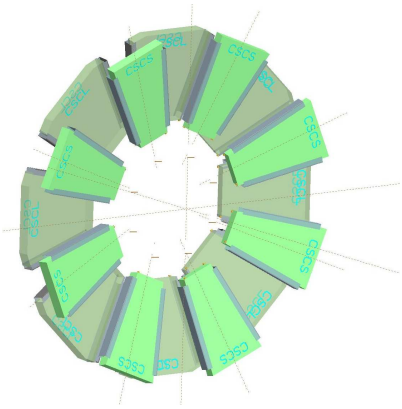

(b) Layout of a CSC end-cap with eight small and eight large chambers.

Figure 2.22: Illustration of (a) the structure and (b) the integration in the ATLAS detector of Cathode Strip Chambers (CSCs).

Resistive Plate Chambers (RPCs)

Three layers of Resistive Plate Chambers provide the trigger and second coordinate measurement in the barrel. Each station consists of two independent layers, each measuring η and ϕ, such that a track going through all three stations delivers six measurements per coordinate. The redundancy decreases fake rates from noise hits and increases the triggering efficiency.

RPCs are gaseous parallel-plate detectors, with a 2 mm gap created by insulating spacers between the electrodes. The gap is filled with a mixture of $C_2H_2F_4$ / Iso-C_4H_10/SF_6 (94.7/5/0.3), which allows relatively low operating voltage, non-flammability and low cost. The electric field between the plates of about 4.9 kV/mm creates avalanches in front of the anodes when an ionizing track crosses the chamber. Induced signals are read out via capacitive coupling to metallic strips, mounted on

the outer faces of the resistive plates. Spatial resolution around 10 mm is expected for both coordinates, with timing resolutions below 2 ns.

Thin Gap Chambers (TGCs)

TGCs have the same function as RPCs, providing trigger and second coordinate measurement in the end-cap. Each chamber is a multiwire proportional chamber filled with a highly quenching gas mixture of CO_2 and n-pentane. It operates in a quasi-saturated mode, preventing the occurrence of streamers in all operating conditions. Wire-to-cathode distance of 1.4 mm and wire-to-wire distance of 1.8 mm lead to very good time resolution.

Including the variation of the propagation time, signals arrive with 99% probability inside a time window of 25 ns. This corresponds exactly to the needs of the trigger system. The radial, bending coordinate is measured by the TGC wire groups, while the azimuthal coordinate is determined by the radial strips.

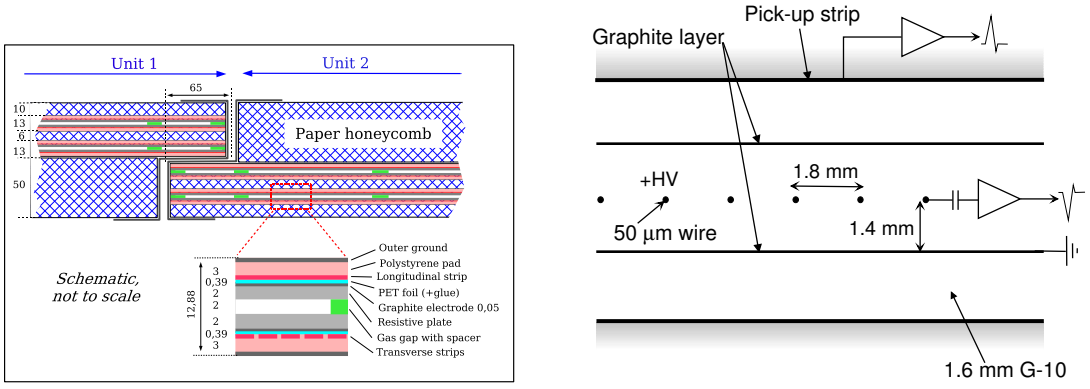

(a) (b)

Figure 2.23: Structure of (a) Resistive Plate Chambers (RPC) and (b) Thin Gap Chambers (TGC).

2.3.3 Alignment system

Although construction quality ensures a good precision for the chamber elements and the chambers as a whole, chamber positioning accuracy is limited to 5 mm, and additional deformations up to a few hundred microns due to thermal gradients and gravity are expected. This is two order of magnitude above the 50 μm resolution on sagitta measurements that are required for momentum determination to 10% at 1 TeV.

To reach this goal, a sophisticated optical alignment system was built to relate the position of each chamber to that of its neighbours within the same layer or tower continuously. In practice, the positions are measured and a new set of alignment constants are derived every 20 minutes. Given the present stability of the system, the measurements are only performed once per hour.

Three different technologies, described in [4] are applied for the more than 12 000 lines, based on optoelectronic image sensors that monitor an illuminated target. The different alignment lines are presented in figure 2.24. In the barrel, a row of MDT chambers are referenced to each other by praxial and axial systems, while the projective system links inner, middle and outer stations. Additional reference lines connect chambers with the barrel toroid, or small to large sectors. In the end-cap, polar lines and azimuthal lines linked to a grid of alignment bars are also used, extending the coverage to CSC chambers.

The global position determination of the barrel and end-cap muon-chamber systems with respect to each other and to the Inner Detector are complemented by track-based alignment algorithms. The latter ones exploit the nearly straight trajectories of high-P_T muons, or eventually might use dedicated runs without toroidal field. Individually, both optical and track-based alignment can only reach a precision a few hundred microns. The desired accuracy in the sagitta measurement of 50 μm or below can only be achieved with their combination.

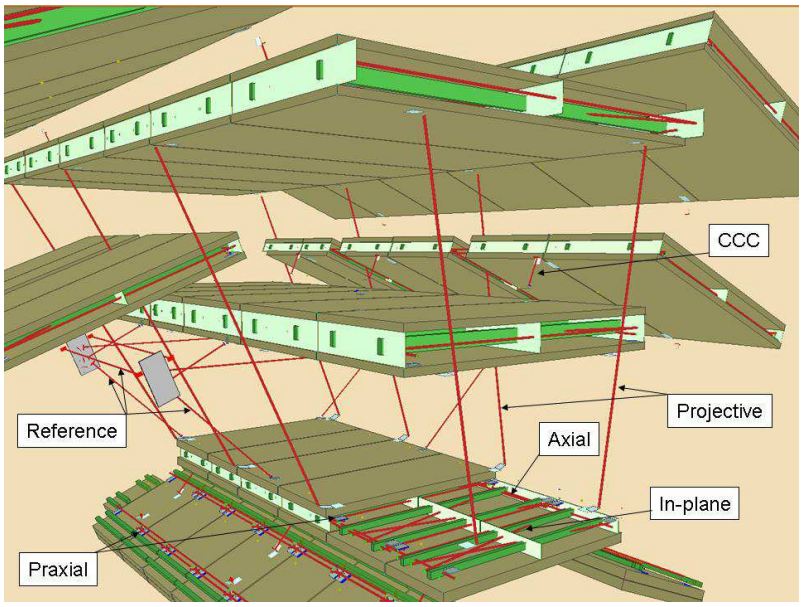

Figure 2.24: Layout of the optical-alignment lines (red) for three adjacent barrel sectors. The Chamber-to-Chamber Connector sensors (CCC) connect chambers in a small sector to those in an adjacent large sector.

2.3.4 Muon reconstruction and associated performance

The LHC will produce a broad spectrum of final-state muons, ranging from low momentum tracks inside b-jets, to high-momentum muons from the decays of W or Z-bosons, as shown in fig. 2.25. Eventually, new particles such as the Standard Model Higgs boson will decay to four-muons, while Z' or supersymmetric Higgs bosons may also decay to very energetic muon-pairs $\mathcal{O}(100\,\text{GeV} - 1\,\text{TeV})$, requiring the ultimate performance of the spectrometer. Muons are the only charged particles that can escape the calorimeter volume, and for those, a dedicated reconstruction fully independent of the Inner Detector can be performed in the Muon Spectrometer.

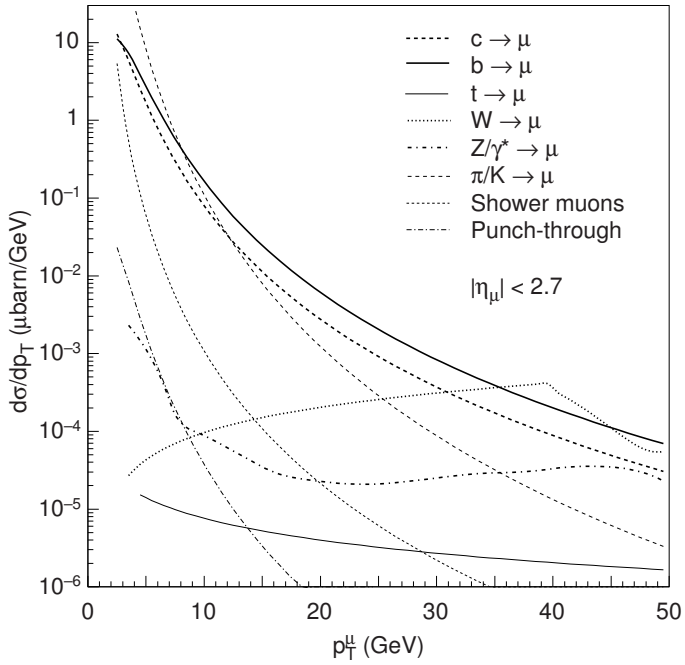

Figure 2.25: Components of the expected inclusive muon spectrum as a function of P_T. Extracted from ref. [11].

Three strategies resulting in three types of objects are applied, according to the use of information in the MS and ID:

- Stand-alone reconstruction: muon track reconstruction based solely on the Muon Spectrometer data over the range $|\eta| < 2.7$ (defined by the spectrometer acceptance).

- Combined reconstruction: combination of a Muon Spectrometer track with an Inner Detector track over the range $|\eta| < 2.5$ (defined by the inner-detector acceptance).

- Segment tag: combination of an inner-detector track with a Muon Spectrometer segment, i.e. a short straight-line track restricted to a station, typically in an inner muon station.

The combination of the MS and ID information improves the momentum resolution and ensures very low fake rates of the order of 10^{-3}/event on $t\bar{t}$ events. For the regions where the spectrometer coverage exceeds the Inner Detector one ($2.5 < |\eta| < 2.7$), standalone reconstruction is used. Below $P_T = 4$ GeV, muons in the barrel eventually do not reach the middle and outer stations, due to the energy loss upstream the MS and the bending in the toroidal field. Segment tagging recovers low-P_T muons and fills efficiency holes caused by gap regions in the muon system, at $\eta \approx 0$ and in the transition region ($|\eta| \approx 1.2$).

The expected efficiencies will be discussed in the end of this section. First, an overview of the reconstruction strategies is given. Different communities have followed slightly different approaches for dealing with the challenges involved in muon identification. The strategy adopted by the *Muonboy* reconstruction package is briefly described here and more information can be found in refs. [4, 12, 13].

For the standalone reconstruction, the main challenges involved in the pattern recognition are summarized by the following points:

- High background levels present in the ATLAS experimental hall if the LHC runs at design luminosity, inducing single tube occupancies and fake tracks.
- High inhomogeneity of the magnetic field.
- Large variety of the muon chambers with complex layouts.
- Large distances between the stations which induce significant extrapolation uncertainties.
- Need to combine measurements from precision and second-coordinate chambers to obtain a tri-dimensional information.

Muonboy starts the reconstruction by identifying regions of activity in the Muon Spectrometer through hits in both coordinates in the trigger systems (RPC / TGC). Around those regions ($\Delta\eta \times \Delta\phi = 0.4 \times 0.4$), straight track segments are formed by trying to combine hits in the precision chambers (MDT or CSC). The segments are required to point loosely to the interaction vertex, in order to suppress background tracks and random hit combinations. A quality factor determines if a segment is valid or not. It is based on a χ^2 distribution using the resolution of the associated hits and penalties for missing ones.

Tracks are seeded from segments, with a first rough estimate of the momentum deduced from the position and direction of the latter ones. Each segment is extrapolated to the other stations considering the effect of the magnetic field. The best matched combination is included in a track candidate. The final hits belonging to a track are not necessarily the ones selected by the segments, but are determined by a global fit procedure. This step filters the contribution of δ-rays and gamma or neutron backgrounds, removing hits which are too far away from the reconstructed path of the muon.

Finally, a fit including material effects is performed. The material distribution inside the Muon Spectrometer varies considerably due the presence of coils and support structures, and detailed information is given in [4, 11]. Chambers and dead matter traversed by the muon are discretized into a finite number of scatterings centers. A parametrization of the energy loss is considered, and scattering angles are included as Gaussian constraints to the track fit. The track quality factor is represented by a χ^2 estimator, which includes these constraints and the distance between the track and the associated hits.

The muon track parameters are expressed at the entrance of the spectrometer, and should be transported to the production point of the particle for physics analyses. A back-extrapolation procedure takes place, considering a parametrization of the material upstream of the MS and the knowledge about the magnetic field. Track parameters and associated errors are updated in this process, until the muon reaches the perigee. This is the convention adopted also by the Inner Detector.

The expected resolution of the muon system ranges from 3 to 11% in the P_T interval between 10 GeV and 1 TeV. The main components are the energy loss fluctuations at low momenta, followed by a multiple scattering term which is nearly constant, and finally the MDT tube resolution and alignment precision, which dominate at high momenta. An estimation of the contribution of each factor is given in figure 2.26.

Since a large fraction of the material upstream the MS is instrumented by the calorimeters, the use of the calorimeter measurement could reduce the importance of the energy loss fluctuations to the momentum resolution. This point will be discussed in detail in chapters 3 and 4.

With muon tracks expressed at the perigee, the *STACO* algorithm performs a statistical combination of the two independent measurements of the Muon Spectrometer and the Inner Detector. The parameters of the reconstructed tracks and their covariance matrices are used to select the best pair, improving the momentum determination as shown in figure 2.27a. The combination has an efficiency around

96% for prompt muons and allows the rejection of particles from secondary interactions that reach the MS, including muons from π/K decays in flight. Very low fake rates are obtained with this method. The rates for $t\bar{t}$ events were evaluated with dedicated simulation samples, and are shown in figure 2.27b. This process was chosen for containing at the same time muons from all the sources illustrated in fig. 2.25 and a large number of high-P_T hadrons due to the high jet multiplicity.

Muon identification is complemented by the *MuTag* algorithm. It tries to associate Inner Detector tracks not selected by *STACO* with segments in the Muon Spectrometer. Tracks with sufficient momentum are propagated up to the first MS stations (inner and eventually middle) and tagged as a muon if they match a segment. The main use of the algorithm is for low-P_T muons that do not reach the outer stations and for regions where a particle only traverses one station ($|\eta| \approx 1.2$).

The expected reconstruction efficiency, evaluated with single muon samples, as a function of transverse momentum and pseudo-rapidity are given in figures 2.28a and 2.28b. Typical values around 95% are expected. One observes the holes in the standalone and combined reconstruction efficiencies, which are partially filled by the tagging algorithm when considering all muons.

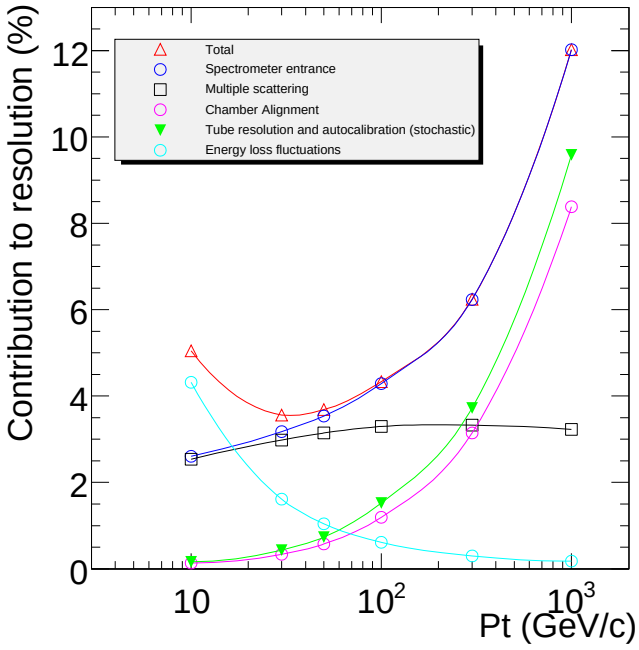

Figure 2.26: Contributions to the expected resolution of the muon system.

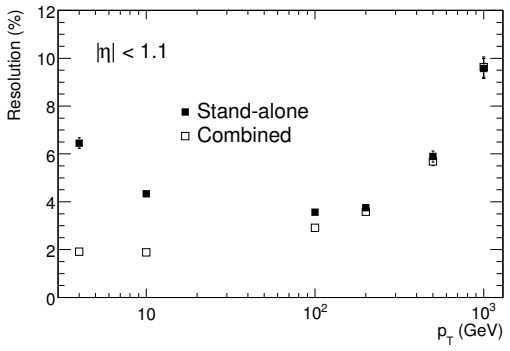

(a) Comparison of the expected momentum resolution for muons using the standalone and combined algorithms.

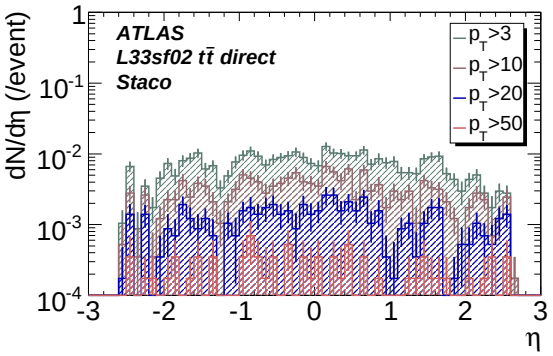

(b) Expected fake rates of muon combined reconstruction from simulated $t\bar{t}$ events.

Figure 2.27: (a) Expected resolution and (b) fake rates of the combined reconstruction for muons.

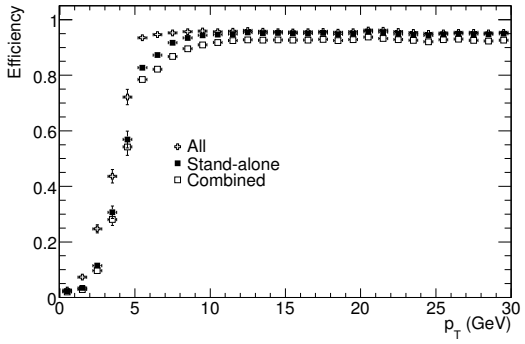

(a)

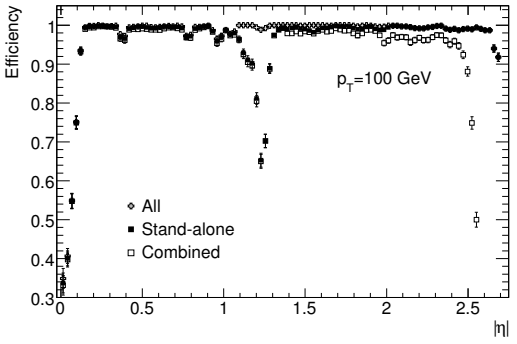

(b)

Figure 2.28: Expected efficiencies of the muon reconstruction algorithms for prompt muons as a function of (a) transverse momentum and (b) pseudo-rapidity. The label 'All' groups combined, stand-alone and tagged muons.

2.4 The trigger, data acquisition and detector control systems

One of the main challenges of the LHC experiments is to record interesting events given the huge amount of data produced and the high collision rate. The proton-proton interaction rate at the design luminosity of 10^{34} cm^{2}s^{-1} is approximately 1 GHz, while the event data recording, based on the available technology and resources, is limited to about 200 Hz. Therefore, a rejection factor above 10^6 must be achieved, with very efficient selection on physics processes of potential interest.

ATLAS has chosen a three level trigger system for this task, represented in

figure 2.29. A hardware based Level-1 (L1) precedes a software based High-Level Trigger (HLT), that includes Level-2 (L2) and Event Filter (EF). Level-1 receives data from the muon system (RPCs and TGCs) and the calorimeters at the bunch crossing rate of 40 MHz, reducing the output to 75 kHz (upgradeable to 100 kHz). The L1 decision must reach the front-end electronics within 2.5 μs and it is based on signatures like high-P_T muons, electromagnetic clusters, jets, hadronic decays of τ-leptons, E_T^{miss} and large total transverse energy.

The data corresponding to the regions of the detector where L1 decision has been taken are passed to Level-2. The L2 uses the information on these Regions-of-Interest (RoIs) and reduces the event rate below 3.5 kHz, with an average event processing time of approximately 40 ms. Special algorithms are run on this step that includes also tracking in the Inner Detector. Tracking and better information on energy deposition improve the threshold cuts and allow particle identification. One example is the distinction between photons and electrons.

The event filter uses the full granularity and precision of the detector to run some of the default reconstruction algorithms. The event rate is reduced to approximately 200 Hz, with an average event processing time around four seconds. Events selected in this stage are recorded and become available for offline analysis.

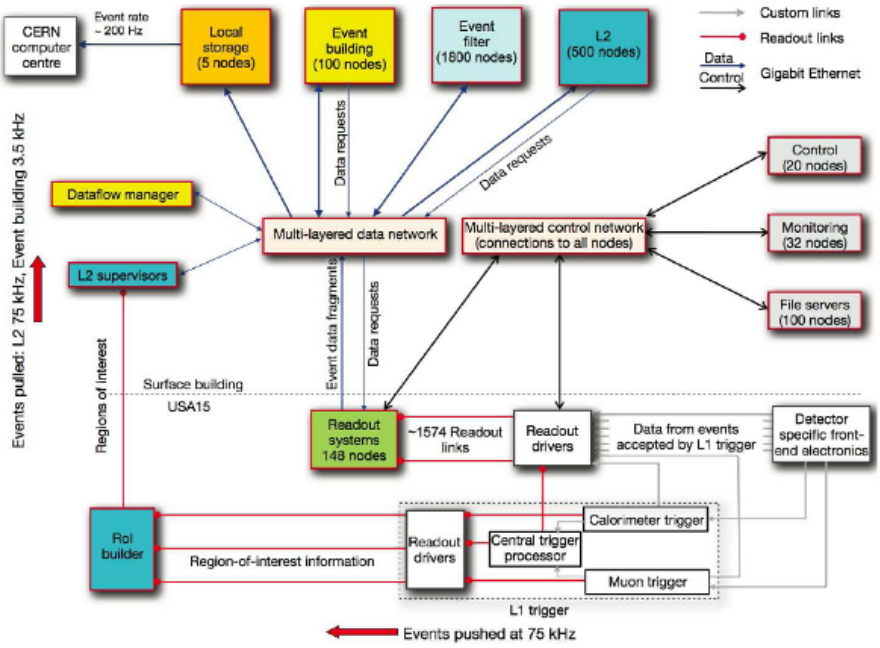

Figure 2.29: Block diagram of the ATLAS trigger and data acquisition. Details are given in ref. [4].

In parallel to the trigger, two independent, complementary and interacting systems are responsible for the data taking and control the experiment infrastructure:

the data acquisition system (DAQ), and the Detector Control System (DCS).

The former is charged with controlling the hardware and software elements of the detectors and the elements associated with High-Level-Trigger and data storage. This enables diagnostic and error recovery, with the capability of removing or re-enabling individual parts without stopping the full acquisition.

The DCS, on the other hand, ensures coherent and safe operation. It handles the control of the detector equipment and related infrastructure, monitoring the operational parameters such as temperature and power-supply voltages. Both systems are capable of taking corrective actions and additionally provide a human interface for the full control of ATLAS and its sub-detectors.

2.5 The ATLAS software framework

A common and robust analysis framework is a major requirement to deal with the huge amount of data produced by a large experiment like ATLAS. Moreover, combining the effort of different communities in a world-wide experiment with a few thousand collaborators requires the enforcement of a rather rigid structure for software development and the use of standard data formats. All that must be achieved combining flexibility and functionalities for common tasks.

A standard framework called `ATHENA` [14] is used by ATLAS for simulation, reconstruction and physics analyses. It is an implementation of the component-based architecture Gaudi, initially developed by the LHCb collaboration. `ATHENA` is responsible for handling the configuration and execution of several C++ packages through python scripts called *jobOptions*. It takes care of the execution order, data flow and storage (persistification). Some basic design principles under which `ATHENA` is developed are:

- Use of abstract software interfaces, making easy to handle groups of components.
- Clear separation between data and algorithms. Clients of the data should not be exposed to the machinery of the algorithms that created it. In this way, changes are transparent to the client.
- Classification of data with respect to their lifetime. Persistent data are stored on disk while transient data reside on memory.

In practice, the framework is composed by a multitude of components that take care of different tasks in the simulation, reconstruction and analysis chain. Some of

them are described below. This subset correspond to the components typically used in analyses, and their definition will be useful for the next chapter. A simplified scheme of their relations in the ATHENA framework is presented in figure 2.30.

- *Algorithm:* application building block, visible and controlled by the framework, performing a well-defined configurable operation. Runs once per event, calling *tools* and *services*, reading and usually producing data.
- *Service:* globally available software, for common tasks such as data access and message printing.
- *Tool:* lightweight piece of code to execute a specific task once or multiple times per event. Shared and owned by *algorithms* or *services*.
- *Data object:* object-oriented representation of particles (muon, electron) or detector information (cells).

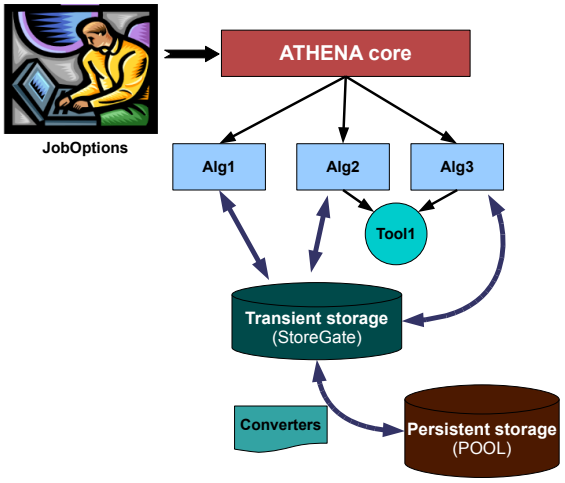

Figure 2.30: Simplified scheme of the ATHENA framework and relations between components.

2.5.1 Data management and data formats

The yearly data volume of $\mathcal{O}(10$ PB) is used by data processing and analysis activities spread around the world. High degree of decentralisation and sharing of computing resources was promoted and met with the Grid paradigm. A three level Tier structure was implemented, in order to use all the available resources efficiently:

- One Tier-0 (CERN) is responsible for the primary event processing, storage of the RAW data and distribution of the data to Tier-1s.
- Approximately 10 Tier-1 facilities archive a copy of the RAW data, provide the reprocessing capacity, access to the various processed versions and allow scheduled analysis of the processed data by physics analysis groups.
- Several Tier-2 centers store analysis data and provide resources for calibration, simulation and analysis.

Some details about the several data formats handled in the framework, and foreseen in the ATLAS Event Data Model are given below. They correspond to different steps in the event processing and filtering, meeting the capabilities of the data storage centers and the needs of the end-users to perform physics analyses. The following types are available:

- **RAW** data: contains the output of the ATLAS detector, produced by real or simulated events after the High-Level Trigger. It comes in the "bytestream" format as they are delivered from the detector, rather than object-oriented format. The size of each event is approximately 1.6 MB.
- **Event Summary Data (ESD)**: holds the output of the reconstruction process. Both detector information and combined reconstruction objects like muons, electrons and jets are stored at this stage. An object-oriented format is adopted, and the typical event size is 1 MB.
- **Analysis Object Data (AOD)**: a subset of the ESD, with the physical objects used in analysis and few detector objects to allow track-refitting, isolation studies and others. Also stored in object oriented format, the nominal event size is of the order of 100 KB.
- **Derived Physics Data (DPD):** contains a small subset derived from the AOD / ESD, specific for an analysis or performance group. More than one derivation is possible, in which the data is reduced by removing unnecessary containers, selecting objects and dropping information from those objects. User-data can be added in the process, and in the final stage of derivation a flat ROOT tuple can be produced.
- **TAG**: event-level meta-data containing a minimum set of information for fast event selection. Can be either ROOT [15] files or databases which are replicated and can be accessed online. Advanced queries can be made and ROOT files, histograms and tables can be produced. The event size is $\mathcal{O}(1\text{ kB})$.

The availability of Event Summary Data is reduced, being restricted to basic studies on detector performance, specially in the initial phase of the experiment. Physics analyses are performed using Analysis Object Data and Derived Physics Data. Lightweight data formats like TAGs are used for efficient event selection. Tools for their production are provided in the context of the Physics Analysis Tools working group [16].

Coherent development, integration and operation of the distributed database and data management software and infrastructure are essential for this scheme. A complex system of replicated databases is used to control technical aspects of the detector construction, installation and survey, together with the detector geometry, data acquisition conditions, offline processing configuration and data management services.

This whole structure was successfully exercised in the commissioning phase and initial collision data taking. However, the first tests of the framework and Event Data Model were done with simulated data, with the chain described in the following.

2.5.2 The simulation chain

The same data formats described above are used when dealing with simulated data. Instead of starting from signals measured in the detector, the input now is a list of the four momenta of final-state particles, as given by an event generator. The response of the ATLAS detector is simulated by `GEANT4` [17] using a detailed model of the detector geometry and the underlying physics. Each particle is propagated through the detector, generating hits which are then digitized, reproducing the RAW data coming from ATLAS. Reconstruction is done using the same algorithms than run in collision events, including the trigger. The output files contain information about the generated and reconstructed particles and can be analysed using the offline software.

This chain is very CPU-time consuming and the need for great quantities of Monte Carlo in some studies obliges the use of fast simulation. `Atlfast` or its second generation version `Atlfast II` are adopted in such cases. Although less precise than the full simulation, they still contain a realistic model of the detector and physics processes. These chains are illustrated in fig. 2.31, and detailed descriptions can be found in ref. [14].

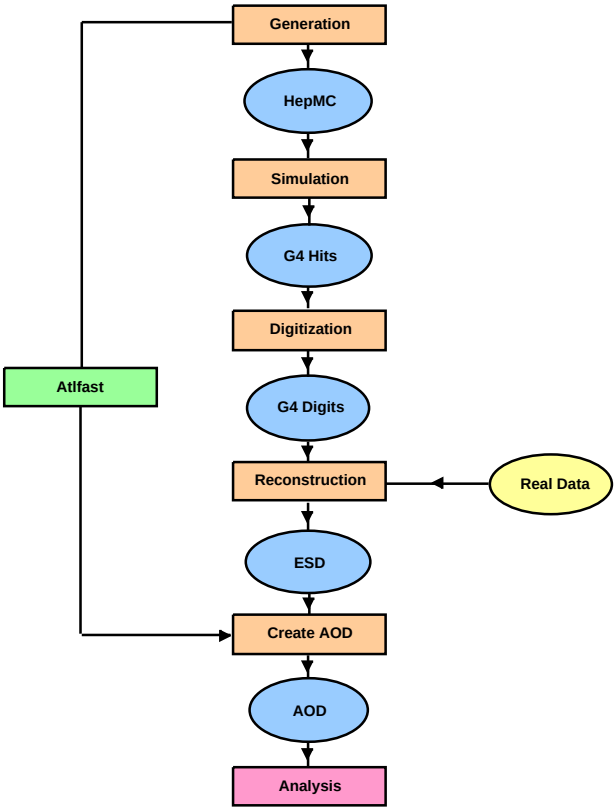

Figure 2.31: Schematic representation of the generation / simulation / reconstruction chain for Monte Carlo and real data in ATLAS. Extracted from ref. [18].

Chapter 3

Calorimetric isolation and energy loss measurements for muons in ATLAS

Muons are typically the only charged particles that can traverse the 100 radiation lengths (X0) of material that separate the ATLAS Inner Detector (ID) and the Muon Spectrometer (MS). Part of their energy is deposited in inert material, but most part of the losses occur inside the region instrumented by the calorimeters.

The proper account for multiple scattering and energy loss is essential for muon reconstruction. As it was mentioned in the previous chapter, a parametrization of the material effects is normally used for transporting the track measured at the spectrometer to the perigee. This approach is clearly insufficient in the cases where high energy deposits take place. In those situations, the use of the calorimeter information can improve the transverse momentum resolution.

On the other hand, muons usually do not reach the calorimeters alone. The activity around them, or conversely the isolation, is one of the most powerful features to identify their origin. Distinction between W and Z decays from semi-leptonic decays of heavy flavour mesons (containing b and c quarks) are among the main applications, which is vital for several physics analyses. The Higgs searches in the four lepton channel, presented in chapter 6, are one of the most prominent examples.

In this chapter, the problematic behind the calculations of muon isolation and energy losses in the calorimeters are discussed. The software package developed to perform these tasks, called *TrackInCaloTools*, is described in section 3.1. The latest optimizations and their implications are reviewed in sections 3.2 and 3.3.

3.1 The software package *TrackInCaloTools*

TrackInCaloTools [19–21] is the package that provides isolation and energy loss measurements for muons in ATLAS. It is integrated in the ATLAS software framework `ATHENA` as part of the standard event reconstruction, performing two complementary tasks:

- Estimation of the energy deposits related to a muon candidate by following its trajectory in the calorimeters.
- Selection of the calorimeter cells around the muon to determine its isolation, defined by the sum of the transverse energy of the cells. This calculation includes the subtraction of the energy loss contribution.

In the `ATHENA` scope, *TrackInCaloTools* can be called by algorithms and other tools many times per event. Its working principle is illustrated in figure 3.1, and described below:

(a) For each muon candidate, *TrackInCaloTools* takes the associated track parameters expressed at the point of closest approach with respect to the beam line – the perigee – and relies on the ATLAS extrapolator [22] to define the position where the particle crossed each calorimeter layer. This task is actually performed by a sub-tool of the package called *TrackExtrapolatorToCalo*.

(b) To estimate the energy around the muon, the calorimeter cells around the extrapolation point on each compartment are collected. Only cells whose center is inside a given cone in ΔR (defined in eq. 2.3) are kept. A noise cut is applied, comparing the ratio between the cell energy and the RMS noise, with the noise threshold defined by the user.

(c) To calculate the isolation, the sum of the transverse energy recorded in the cells that lie within the given cone is taken, excluding the ones associated with the muon energy loss (core energy, illustrated in fig. 3.1).

The extrapolation takes into account the bending in the magnetic field and a simplified description of the material effects from the ATLAS Tracking Geometry [23] to update the parameters of the track from one layer to another. The position and momentum are calculated together with the associated errors at each step, allowing an estimation of the most probable value of the muon energy loss. *TrackExtrapolatorToCalo* can provide, apart from this parametrized energy loss, the

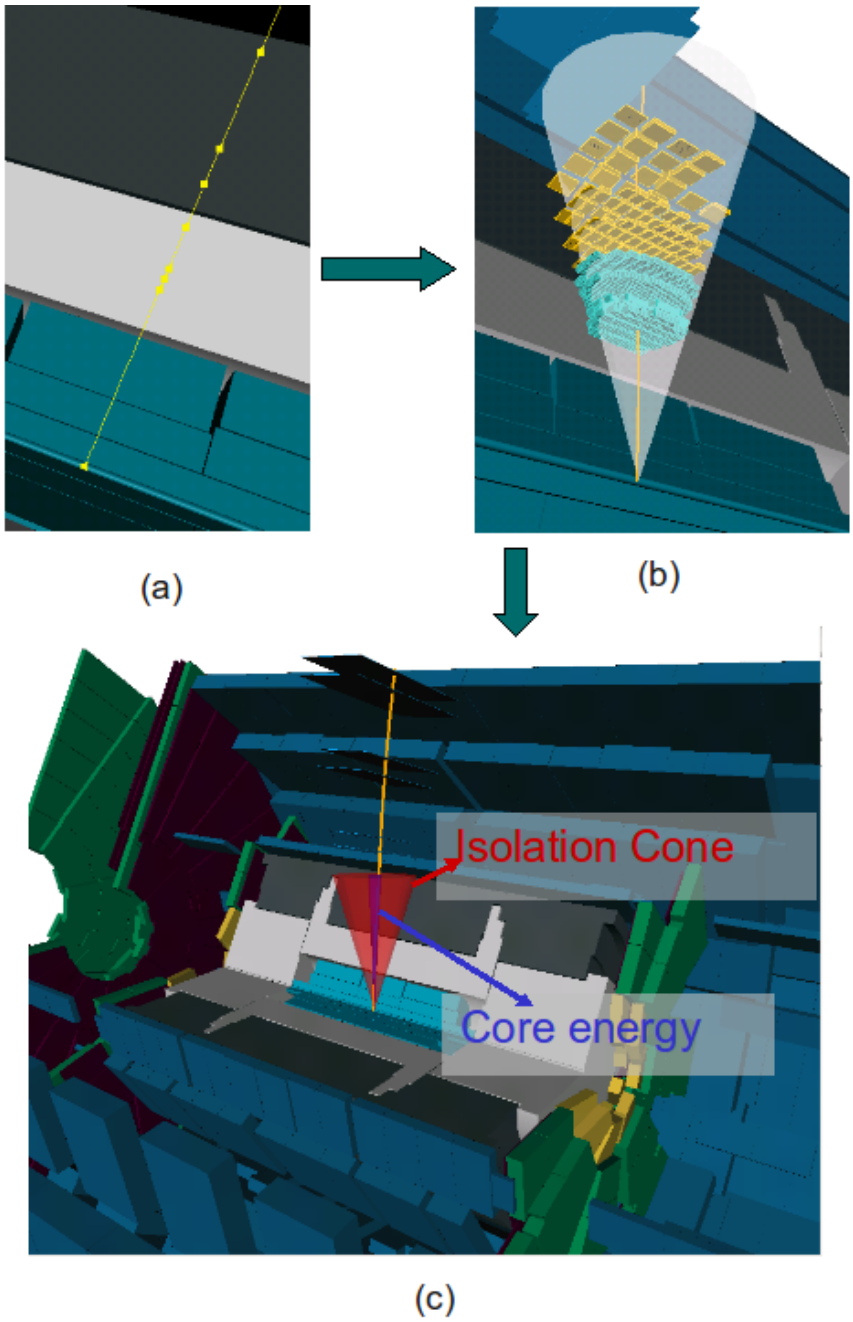

Figure 3.1: Illustration of the working principle of *TrackInCaloTools*: (a) a muon track is extrapolated from the perigee to each layer of the electromagnetic and hadronic calorimeters, represented in light grey and dark grey. (b) The cells around the extrapolated points, above a noise threshold, are collected on each compartment. (c) An internal region denoted as core energy (or E_T^{core}) is used to define the muon energy loss while an isolation cone quantifies the activity around the muon.

parameters at the entrance and exit of each layer, so that the cells crossed by the track can be identified. This also allows the calculation of the path length of the

track inside the calorimeter and the positions at the middle of each layer, which are used for the cell collection.

The extrapolation process starts from the perigee and stops when each surface, corresponding to the entrance or exit of each calorimeter layer, is reached by the track propagation. It goes on until the end of the last layer, taking the parameters at the previous step in case an extrapolation fails. To save computational resources, the mid-point between the entrance and the exit points determined in each layer is taken for the cell collection. This avoids an additional extrapolation step to the middle of each layer. The extrapolation and the cell collection procedures are illustrated in figure 3.2.

TrackInCaloTools then selects the cells around the track, merging calorimeter compartments from different regions within the same technology if needed: LAr EM barrel and end-cap, Tile barrel and extended barrel. This is done in order to get a continuous picture as a function of pseudo-rapidity. The absolute value of the energy of each cell is required to be above a threshold t with respect to the RMS noise:

$$|E_{cell}| > t \cdot (\text{cell noise}),\ t = 3.4 \text{ by default.} \tag{3.1}$$

This determination can be done considering or not cells with negative energies, which arise from noise fluctuations after the calorimeter calibration. Those cells are kept to minimize biases in the energy measurement and do not influence significantly the isolation performance, as will be discussed in section 3.3. A brief description of the energy calibration of the calorimeters is given in appendix A and detailed information can be found in refs. [10, 24, 25].

Given its importance for physics analyses, isolation information is attached to every muon object in the reconstruction. The isolation variables (*etcone*10, *etcone*20, *etcone*30, *etcone*40) are calculated for cones of $\Delta R = 0.1$, 0.2, 0.3 and 0.4, respectively, subtracting the energy loss component, noted as E_T^{core}, according to:

$$etconeY = \sum_{cells} E_T^{\Delta R=Y/100},\ \text{cell} \notin E_T^{core}. \tag{3.2}$$

The definition of the cells belonging to E_T^{core} takes into account the features and the geometry of each calorimeter layer. The tool provides the possibility of choosing them independently for each layer, either using a cone in ΔR corresponding to circular regions in the $\eta - \phi$ plane, a rectangle with different values for $\Delta\eta$ and $\Delta\phi$, a fixed number of cells in $\eta \times \phi$ around the track, or only the cells crossed by the track. This subject is discussed in detail in section 3.2.

Apart from the *etcone* variables, the tool gives a list of the cells crossed by each muon candidate and the cells around the track (within $\Delta R = 0.45$) collected using a loose noise cut ($t = 2.0$ by default). Both are kept in Analysis Object Data (AOD), and allow the isolation variables to be recalculated if a user wishes to do so.

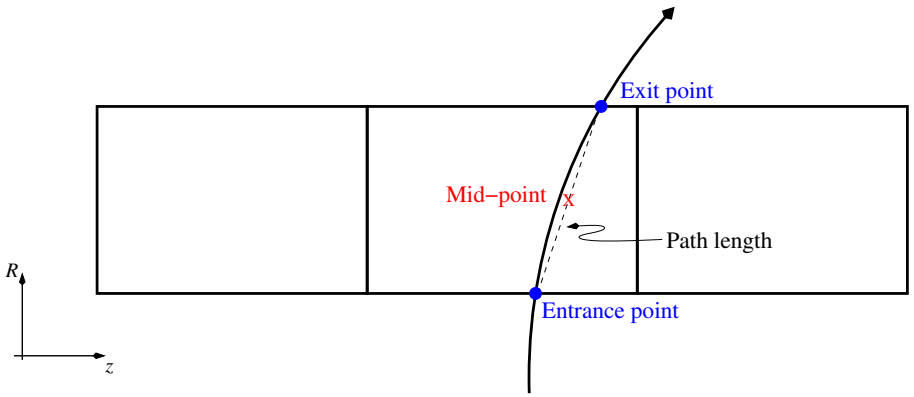

(a) Sketch of a track extrapolation through a calorimeter layer in the $R - z$ plane, showing the outputs from *TrackExtrapolatorToCalo*. The rectangles indicate the cells. The mid-point between the entrance and exit points, marked with an `X`, is used for the cell collection.

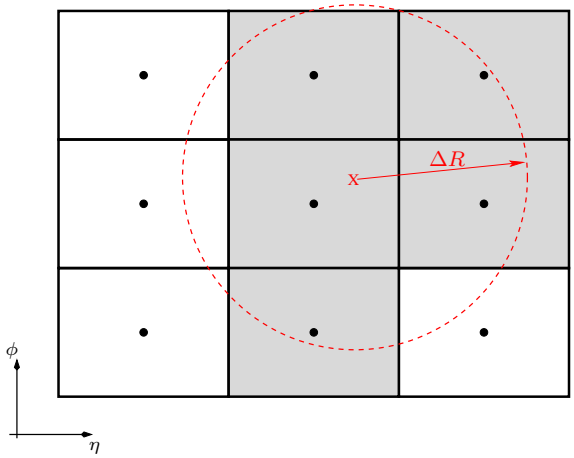

(b) Illustration of the cell collection in the $\eta - \phi$ plane for a given cone in ΔR. Only the cells whose center is inside the cone with respect to the extrapolation point (marked with an `X`) are selected (in grey).

Figure 3.2: Illustration of (a) the extrapolation and (b) the cell collection in *TrackInCaloTools*.

3.1.1 Framework and functionalities

As mentioned above, *TrackInCaloTools* is used in the standard event reconstruction. It actually feeds a tool that handles both calorimetric and track-based isolation: *MuonIsolationTools*. An illustration of how the package is inserted in the ATHENA framework is given in figure 3.3.

TrackInCaloTools uses a few other packages from the ATLAS software: its subtool *TrackExtrapolatorToCalo* relies on the *AtlasExtrapolator* and on the *CaloSurfaceBuilder* to take care of the extrapolation process, while *TrackInCaloTools* itself selects calorimeter cells and calculates the isolation. The cell selection requires the detector geometry, given by the *Detector Description* module and involves applying noise cuts with the help of *CaloNoiseTool*. The functionalities provided by the package can be summarized in the following list:

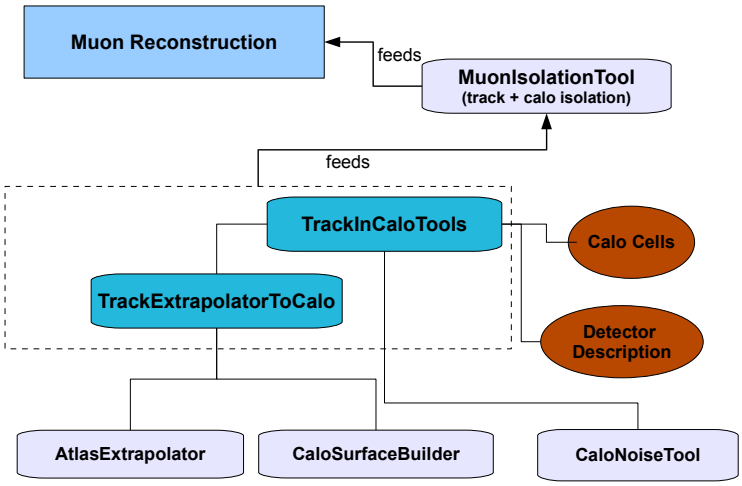

Figure 3.3: Illustration of the integration of *TrackInCaloTools* in the ATHENA framework.

- Input:
  - Track parameters expressed at the perigee.
  - Muon track, from which the parameters at the perigee are extracted.
- Outputs from *TrackExtrapolatorToCalo*:
  - Parameters of the track at the entrance and exit of each calorimeter layer.
  - Position of the track extrapolation in the middle of each layer.

  - Path length traversed by the track on each layer.
  - Parametrized energy loss.

- Outputs from *TrackInCaloTools*:
  - Cells around the track for a given cone in ΔR, rectangle in $\Delta\eta \times \Delta\phi$ or a fixed number of cells in $\eta \times \phi$.
  - Cells crossed by the track on each layer.
  - Measured energy loss (core energy), according to the definition set by the user.
  - Isolation energy, corresponding to the transverse energy around the track per layer for a given cone in ΔR, excluding the cells inside the core region.

- Configurable parameters:
  - Noise threshold used to collect cells, defined as the minimum ratio of the energy of the cell to the RMS noise.
  - Whether to use or not cells with negative energy values, which are caused by noise fluctuations.
  - Whether to use the extrapolation to follow the track bending in the magnetic field, or a straight track approximation.
  - Definition of the core energy on each layer. The user can choose between a cone, a rectangle, the cells crossed by the track, a given number of cells in $\eta \times \phi$ and the parametrized energy loss.

Although the default usage of the tools is related to muons, they are suitable to handle any kind of particle with an associated track. More than providing the standard isolation variables, the package is configurable and flexible to handle isolation and energy loss measurements as the needs of each analysis may differ when dealing with those quantities.

Despite the particularities of each physical process and the fact that the isolation information can be easily recalculated at the analysis stage, the *etcone* variables are attached to every muon object in the AODs, which is the baseline for physics analyses. Thus it is desirable to achieve a good separation between muons coming from vector bosons (W and Z) and muons coming from hadron decays using these quantities. A study for an optimal definition of E_T^{core} was carried out in view of this objective, and resulted in the improvement of calorimetric isolation performance. This is discussed in the next section.

3.2 Identification of muon energy deposits

When calculating the isolation variables, one has to subtract the muon activity in the calorimeter, which can be done in two ways: using a parametrization of the energy losses or identifying the cells associated to the muon deposits and excluding them from the isolation calculation, as shown in equation 3.2.

The first method gives a reasonable estimate of the energy loss and is used by some of the muon reconstruction algorithms, one of the reasons being the independence from the calorimeter calibration. Nevertheless, the fluctuations around the most probable value can be quite important and this can easily lead to a significant overestimation of the energy around the track[1]. On the other hand, subtracting the values given by the parametrization underestimates the isolation energy in cases when the muon induces signals below the noise threshold in some layer.

Therefore, the best approach is to exclude the cells associated to the muon activity from the isolation calculation. Originally, a cone of $\Delta R = 0.05$ was used for that purpose, as a compromise between the extension of the deposits and the calorimeter geometry. It was noted that this definition was not sufficient, and many of the developments described in the previous section were motivated by this limitation.

One should note that the deposits extend beyond the cells traversed by the track, for reasons that will be discussed shortly. Even this determination is limited by the cell description which usually assumes perfect projectivity. In the normal case, *TrackInCaloTools* only has access to the $\eta - \phi$ extension of the cells. This is sufficient for the cells of the electromagnetic calorimeter which are fully projective, but an approximation of the TileCal and HEC geometries. A special treatment for the non-projectivity of the TileCal was introduced recently in the package. Both rectangular cells and "ladder-shape" cells from the barrel BC layer are treated, using the complete information about the cell extension in $R - z$. The geometry of the HEC is more complex and the dimensions of the cells cannot be retrieved by the package. Thus, such treatment is not possible.

A detailed study was performed to redefine the so called E_T^{core} region. The strategy chosen to cope with the features of each calorimeter layer was to observe the extension of the deposits caused by fully isolated muons and compare the rejection power of the isolation variables in physical processes for different 'core' definitions. Using Monte Carlo simulated samples of muons with fixed transverse momenta at 10 and 100 GeV, some possibilities for the regions to be considered were chosen looking at the distance between the extrapolation point and the cells above the

[1]The calorimeter response to the passage of muons is discussed briefly in appendix A.

noise threshold for each layer.

In figure 3.4 one can observe the very different deposition patterns for the first layer of the electromagnetic calorimeter and the second layer of the TileCal. Although each contribution was not studied separately at this stage, the following aspects influence the obtained distributions and should be considered in the E_T^{core} determination:

- **Knowledge about the nature and the extension of the energy losses.** Although the ionization process dominates, leading to localized deposits, radiation might occur, affecting a larger region [26].
- **Tracking and extrapolation precision, associated to multiple scattering effects.** Poor estimation of the point where the muon entered each layer can lead to the selection of cells not crossed by the track.
- **Geometry and particularities of each calorimeter layer.** Significant differences between the granularity exist among the layers (table 2.1 and figure 3.5). Effects such as non-projectivity and charge sharing between adjacent cells require the selection of larger regions to account for the muon deposits.
  - **The electromagnetic calorimeter** has accordion shape electrodes (figure 2.11), which imply that a particle traversing its volume may leave signal on two adjacent cells in the azimuthal direction (ϕ). The fine segmentation can also contribute to the uncertainty in localizing the cells crossed.
  - **The hadronic calorimeters** do not have fully projective geometry in pseudo-rapidity (η). As a result, a straight track might traverse more than one cell. On the other hand, the coarse granularity limits the number of cells to be considered not to lose isolation performance.
- **Final state radiation (FSR) from W and Z bosons.** Photons with considerable energy, associated to the weak boson decays, are produced relatively often and close to the leptons. Figure 3.6 shows the energy of FSR photons and their distance with respect to the muons in $Z \rightarrow \mu\mu$ simulated events. `PYTHIA` [27] and `PHOTOS` [28] were used for the event generation and final-state radiation, respectively. If the shower produced by the radiated photon is decoupled from the muon activity in the calorimeter, significant decreases in the rejection against hadron decays are observed. Although the energy loss measurement might be overestimated, priority was given to the isolation performance in a first moment by including the photons in the E_T^{core} definition.

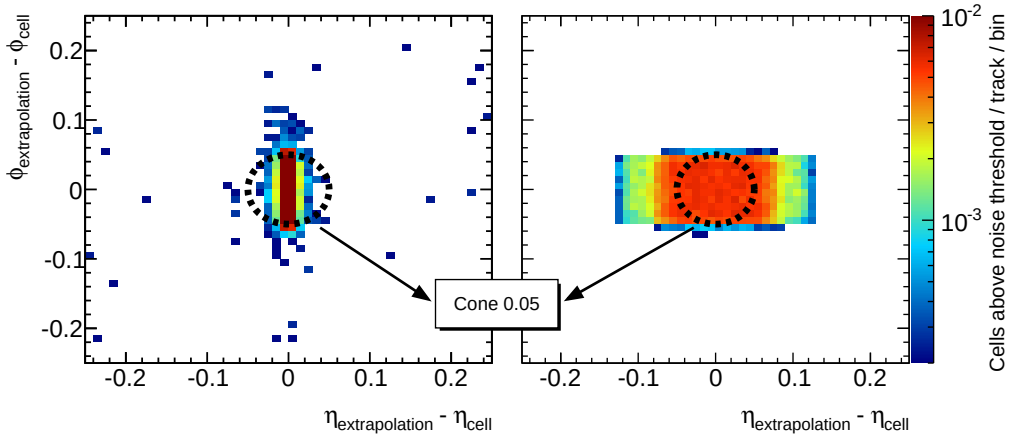

(a) First layer of the LArEM. (b) Second layer of the TileCal.

Figure 3.4: Distance in the $\eta - \phi$ plane between extrapolation and the center of the cells above the noise threshold (3.4σ) for simulated samples of single muons with $P_T = 100$ GeV. The colors indicate the probability of having a cell above the threshold in each bin. Also shown is the old E_T^{core} definition (cone 0.05).

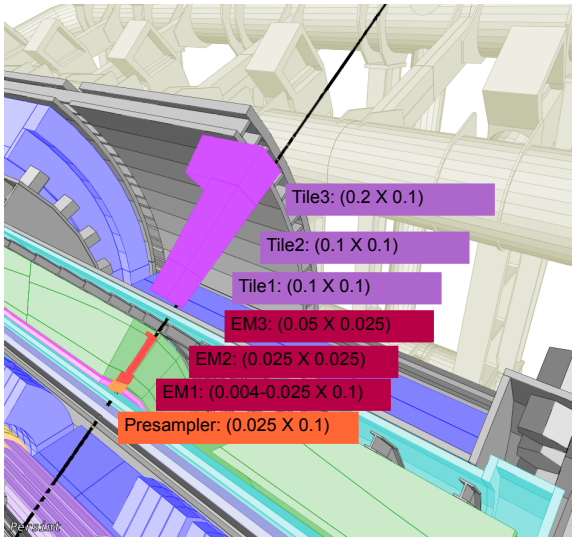

Figure 3.5: Segmentation of the calorimeter layers in the central region.

Using this information as a starting point, a new recipe for E_T^{core} was defined based on two quantities:

- The isolation performance, or the ability to separate muons coming from leptonic decays of vector bosons (W and Z) from the ones produced by hadron decays (heavy or light flavours).

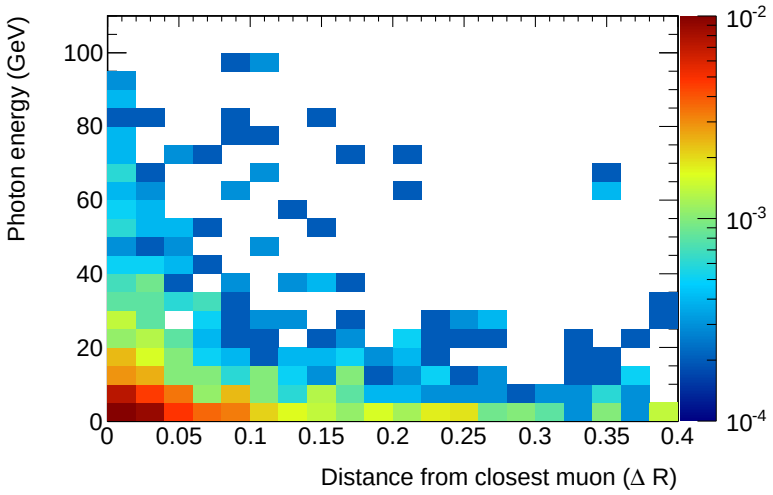

Figure 3.6: Presence of final-state radiation on simulated samples of Z boson decays to muon pairs. The colors indicate the emission probability as a function of the energy and distance from the closest muon for photons with $E > 1$ GeV (10 000 events, 1431 photons).

- The energy loss performance, quantified by the difference between the true energy loss in each calorimeter compartment and the reconstructed one for a given E_T^{core} definition.

Standard ATLAS simulation samples of top-quark pairs were used for the first item. They contain at the same time muons from W decays (including final-state radiation photons generated with `PHOTOS`) which are expected to be quite isolated, and muons from heavy quark (b or c) or light meson decays (such as kaons or pions), which are usually accompanied by several hadrons, thus having significant calorimeter activity around. Figure 3.7 illustrate this feature, comparing the location of the cells above the noise threshold with respect to the extrapolation position in the $\eta - \phi$ plane. The ability to separate reconstructed muons of the first kind, associated to leptonic decays of Ws, from muons from hadron decays was used as a discriminant to define E_T^{core}.

For the second aspect, special samples of muons with $P_T = 10$ and 100 GeV were generated, keeping the information corresponding to the true energy loss in the calorimeter volume. This allows one to compare the reconstructed energy on each layer for a given choice for E_T^{core}, with the actual deposits induced by the muon. It must be noted that other effects such as the calorimeter calibration and the noise suppression interfere with the energy loss scale. In this phase, only a reasonable agreement of $\mathcal{O}(10\%)$ between the quantities is requested.

The goal of the study was to select the minimal definition in terms of size or cell content that provided at the same time a good isolation performance and energy loss capability. All the possible characterizations of the energy loss including the features described in the previous section (cones, rectangles, crossed cells or fixed number of cells) were tested. The features and the results for each calorimeter technology: liquid-argon electromagnetic calorimeter (LArEM), liquid-argon hadronic end-cap (HEC) and tile hadronic (TileCal) are discussed in the following subsections. The forward calorimeters are not considered as their coverage ($3.1 < |\eta| < 4.9$) exceeds the acceptance region of the tracking detectors ($|\eta| < 2.7$).

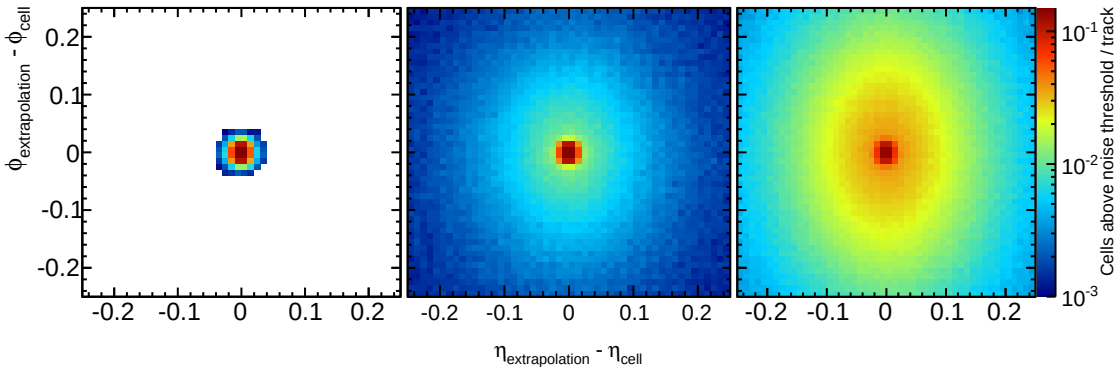

(a) Single muons with $P_T = 100$ GeV.

(b) Muons from W decays on $t\bar{t}$ events.

(c) Other muons from $t\bar{t}$ events.

Figure 3.7: Distance in the $\eta - \phi$ plane between extrapolation and cells touched on the second layer of the electromagnetic calorimeter for different simulation samples containing muons. The colors indicate the probability of having a cell above the threshold in each bin. For figures (b) and (c), the average transverse momentum of the muons is approximately 25 GeV and 10 GeV, respectively.

3.2.1 Electromagnetic calorimeter

The fine granularity and the charge sharing in the accordion shape electrodes are the main features to consider for identifying the muon energy deposits in the electromagnetic calorimeter (fig. 3.7a). In addition to the muon activity, photons from W / Z final-state radiation are absorbed in this technology, specially in the middle layer, leading to a spread of the deposits roughly up to $\Delta R = 0.05$ (fig. 3.6).

In view of these effects, the standard definition of a cone of 0.05 proved to be particularly suited for the middle layer (em2), where most of the energy is collected. For the first compartment (em1), a bigger spread in ϕ is observed, which suggests the use of different values for $\Delta\eta$ and $\Delta\phi$. Overall, a slight reduction on E_T^{core}

was possible while keeping the same isolation and energy loss performance. An example is given in fig. 3.8, where different possibilities for the first compartment are compared and give the same result.

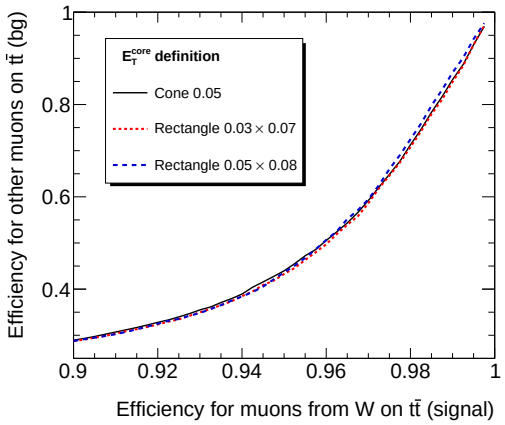

(a) Performance of the isolation variable *etcone*30 on $t\bar{t}$ samples.

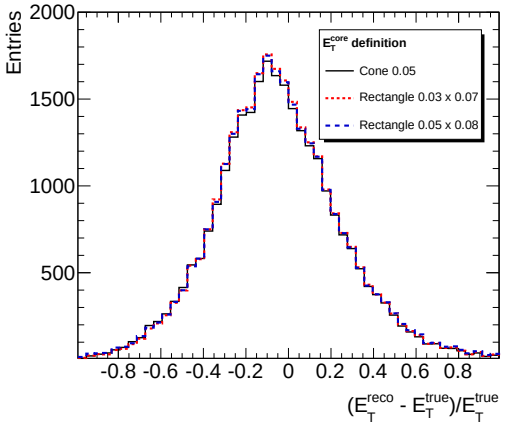

(b) Difference between reconstructed (E_T^{reco}) and true energy deposits (E_T^{true}) from muons of $P_T = 100$ GeV.

Figure 3.8: Isolation performance and energy loss capability with different E_T^{core} definitions for the first layer of the EM calorimeter.

3.2.2 Hadronic End-cap Calorimeter (HEC)

The Hadronic End-cap calorimeter exhibits a much coarser cell granularity than the electromagnetic LAr and a higher RMS noise, around 100 - 300 MeV. Very often the signal left by muons is below the noise threshold, making it difficult to have an accurate measurement of the energy loss.

Nevertheless, in case of large deposits a measurable signal is induced in the crossed cells. As mentioned previously, the non-projective geometry in pseudo-rapidity makes it difficult to identify the cells crossed. For that reason, the new recipe opted for a larger cone of 0.07, in order to take the cell touched by the muon in most of the cases, and also the adjacent cells in case the extrapolation points to the edge of the cell crossed. A cone of 0.05 is slightly smaller than the cell size, and eventually no cell was considered for E_T^{core}. The new definition and the impact on the isolation performance are shown in fig. 3.9.

3.2.3 Tile calorimeter (TileCal)

Unlike the Hadronic End-Cap, the Tile calorimeter exhibits relatively low RMS noise, ranging from 30–50 MeV per cell, for approximately the same calorimetric

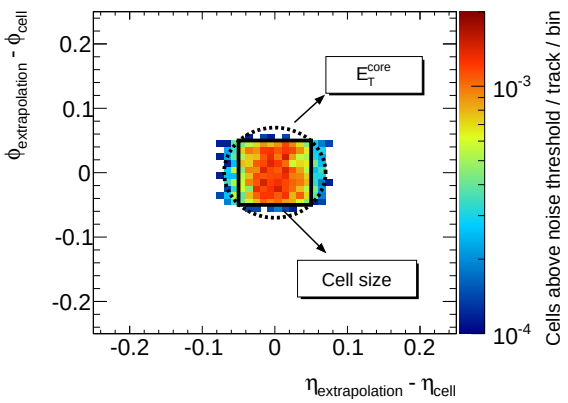

(a) Probability of having a cell above the threshold around the extrapolation point in the $\eta - \phi$ plane. Also shown are the cell size and the new E_T^{core}definition.

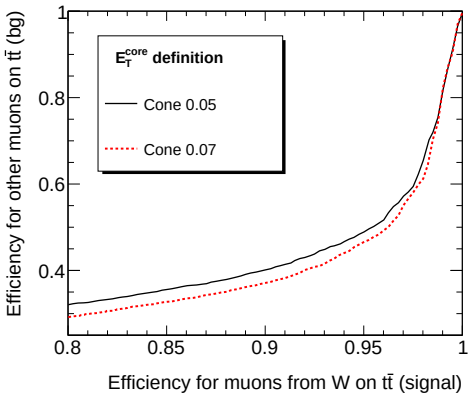

(b) Performance of the isolation variable *etcone*30 on $t\bar{t}$ samples for two E_T^{core} definitions: cones of $\Delta R = 0.05$ (solid line) and 0.07 (dashed line).

Figure 3.9: Spread of the energy deposits around the extrapolation point for muons of $P_T = 100$ GeV and isolation performance of the Hadronic End-Cap Calorimeter.

depth. Muon deposits are usually above the noise thresholds, and they might be shared by two or even three cells in pseudo-rapidity due to the non-projective geometry (fig. 2.13).

Three strategies were tested to overcome this issue: using the full tile geometry to determine the cells crossed by the track; considering the two hottest cells around the track in η; or rectangles with sides that compensate for the cell geometry. This feature was illustrated in fig. 3.2: for both cones and rectangles, the number of cells included depends on the extrapolation position with respect to the center of the cell. One can imagine the situation where the cone radius or the sides of the rectangle exceed the cell size by less than 50%. If the extrapolation points close to the center, only the touched cell is considered. Once it starts to reach the edge of the cell, the adjacent one is also taken.

A comparison between some of the methods is shown in fig. 3.10b for the second compartment using muons with $P_T = 100$ GeV. The old definition of a cone with $\Delta R = 0.05$ is clearly insufficient, while the cells crossed give a better agreement between measured and true energy deposits. The use of two cells in pseudo-rapidity reduces further the tails and gives some improvement in the isolation performance. This recipe was adopted for the layer, while for the first and the third ones, rectangles were chosen, as illustrated in fig. 3.11.

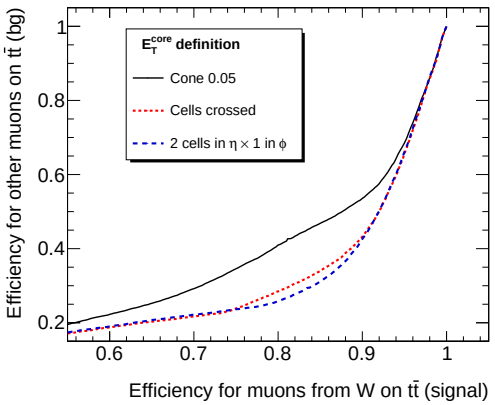

(a) Performance of the isolation variable *etcone*30 on $t\bar{t}$ samples.

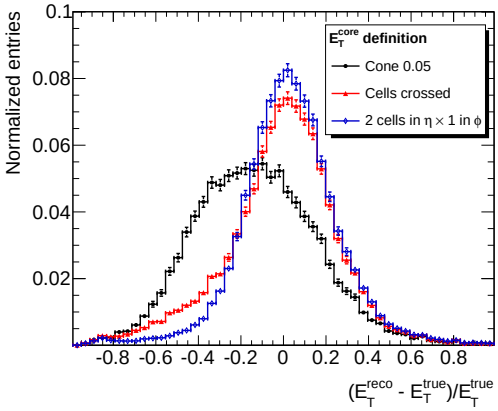

(b) Difference between reconstructed (E_T^{reco}) and true energy deposits (E_T^{true}) from muons of $P_T = 100$ GeV.

Figure 3.10: Isolation performance and energy loss capability with different E_T^{core} definitions for the second layer of the TileCal.

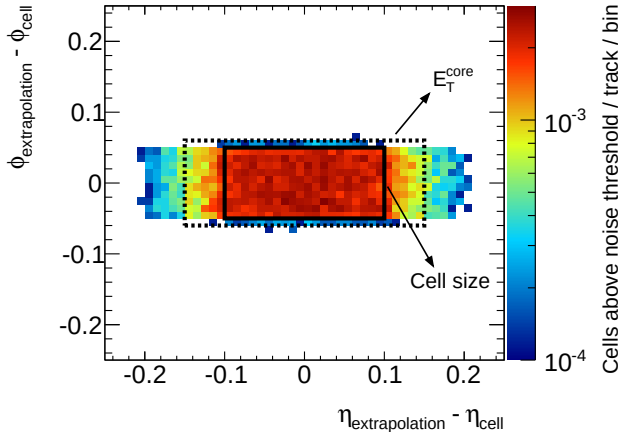

Figure 3.11: Distance in the $\eta - \phi$ plane between extrapolation and cells above the noise threshold on the third layer of the TileCal for muons of $P_T = 100$ GeV. The colors indicate the probability of having a cell above the threshold in each bin. Also shown are the cell size and the new E_T^{core} definition.

3.3 Summary and implications of the new E_T^{core} definition

The new "recipe" for E_T^{core} was defined comparing the isolation performance and energy loss capabilities varying the region associated to the muon energy deposits. Overall, both quantities pointed to the same definition, suggesting that the muon activity should be as much as possible excluded from the activity around the track.

One exception was the middle layer of the electromagnetic calorimeter, where the choice was driven by the presence of final-state radiation from leptonic decays of vector bosons. The selected configuration is summarized in table 3.1.

The minimal cell content was chosen in case of similar performance, to preserve the energy loss from large noise fluctuations and to reduce the sensitivity to pile-up – minimum bias events on top of the hard-process under investigation. This aspect was studied as part of the robustness checks for the new definition. The isolation performance and energy loss capability were also assessed. These features are described in the following subsections.

Table 3.1: New E_T^{core} definition in terms of cones in ΔR, rectangles in $\Delta\eta \times \Delta\phi$ or a fixed number of cells in $\eta \times \phi$ (for the second layer of the TileCal). Also quoted is the typical number of cells taken in $\eta \times \phi$, which depends on the position given by the track extrapolation.

Calorimeter	E_T^{core} **type**	E_T^{core} **definition**	**Cell content** ($\eta \times \phi$)
EM calorimeter			
Presampler	rectangle	0.025×0.06	1 (or 2) $\times$ 1
Sampling 1	rectangle	0.03×0.07	1×1 up to 5×2
Sampling 2	cone	0.05	3×3
Sampling 3	cone	0.03	1×2 up to 2×3
Tile calorimeter			
Sampling 1	rectangle	0.06×0.08	1 (or 2) $\times$1
Sampling 2	number of cells	2×1	2×1
Sampling 3	rectangle	0.15×0.06	1 (or 2) $\times$1
Hadronic end-cap calorimeter			
Samplings 1-4	cone	0.07	1×1 up to 2×2

3.3.1 Robustness

The new "recipe" for the E_T^{core} definition, described in the previous section, increased significantly the region used to account for muon energy losses in the hadronic calorimeters. And since it was studied for $t\bar{t}$ samples with a particular configuration of *TrackInCaloTools*, several checks were made to ensure that this did not imply a higher sensitivity to the change of the parameters of the tool and the presence of pile-up. Figure 3.12a shows how the activity in the calorimeter is increased with pile-up for a luminosity of 10^{33} cm^{-2} s^{-1}, which results in degradation of the isolation performance.

Nonetheless, as can be seen in fig. 3.12b, the new definition exhibits the same sensitivity to pile-up as before, and the loss in performance cannot be recovered with the change of the noise threshold used to collect the cells. Moreover, the recipe proved to be stable on other configurations and with another Monte Carlo sample containing both isolated and non-isolated muons: $Zb\bar{b} \rightarrow \mu\mu + X$. Picking different isolation variables (*etcone*20 or *etcone*30), changing the noise threshold from 3.4 to 2σ and considering or not cells with negative energies did not affect the chosen parameters for the E_T^{core} definition.

A summary of the robustness tests for new recipe is listed in the following:

- The same definition for E_T^{core} is found to be the optimal for other configurations of the tool, such as different noise thresholds (2σ and 3.4σ as shown in fig. 3.12b) and the use or not of cells with negative energies.
- Two different physics samples, $t\bar{t}$ and $(Z \rightarrow \mu\mu)b\bar{b}$, were tested and yield the same recipe for E_T^{core}.
- The use of different isolation variables, *etcone*20 or *etcone*30, does not suggest any change in the recipe.
- The loss of performance under pile-up conditions is not increased with respect to the previous core energy definition.

3.3.2 Improvement in the isolation performance

The redefinition of the way the muon energy deposits are considered had as one major objective the improvement in the isolation performance. This was observed for $t\bar{t}$ samples and in the Higgs to 4-lepton analysis. The strategy used by the latter is to apply a cut on the isolation of the 4-muons selected to form the Higgs candidate, requiring a minimum value for the ratio between the variable *etcone*20 and the muon transverse momentum. With the new E_T^{core} definition, the rejection of the main reducible background – $(Z \rightarrow \mu\mu)b\bar{b}$ – is increased by a factor close to 2, for the same signal efficiency used in the standard analysis [10]. This is illustrated in fig. 3.13.

3.3.3 Implications for muon energy loss measurements

The optimization of E_T^{core} was also defined in view of the capability of measuring the muon energy deposits in the calorimeter. As a consequence, the new recipe provides a good estimate of this quantity, which was clearly underestimated before.

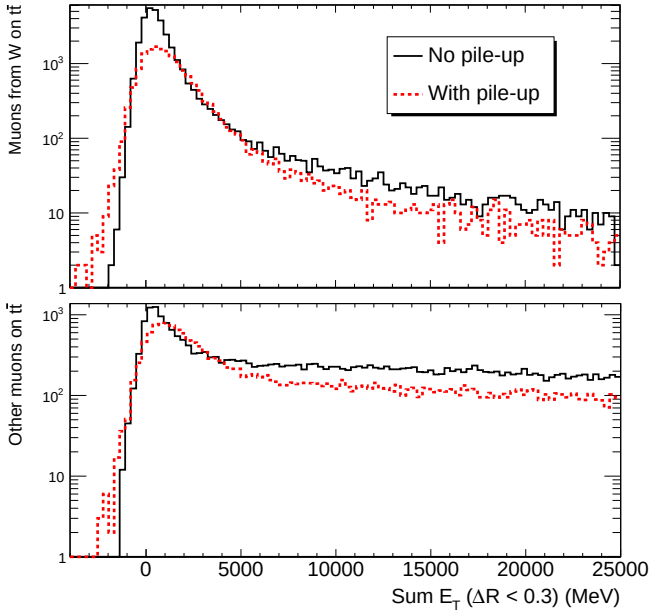

(a) Distribution of the isolation variable *etcone*30 on $t\bar{t}$ samples for muons from W decays (top) and other sources (bottom).

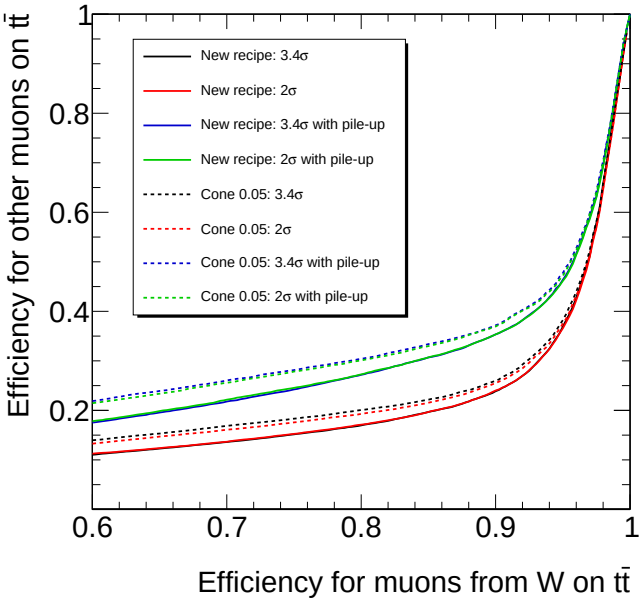

(b) Isolation performance of the *etcone*30 variable, for the old and the new E_T^{core} definitions using different noise thresholds to collect the cells.

Figure 3.12: Effect of pile-up on the isolation variables and associated performance for simulated samples of top-quark pairs. The pile-up is estimated for a luminosity of 10^{33} cm^{-2} s^{-1}.

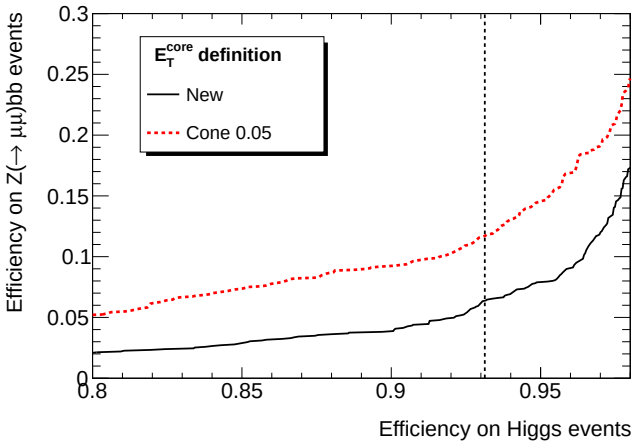

Figure 3.13: Performance of the calorimetric isolation cut (described in the text) for events with the Higgs boson decaying to 4 muons ($M_H = 130$ GeV) and $(Z \to \mu\mu)b\bar{b}$ samples, comparing the old (cone 0.05, dashed line) and the new (solid line) E_T^{core} definitions. The vertical line corresponds to the efficiency used in the standard Higgs to 4-lepton analysis [10]. An improvement of 45% in the background rejection is observed for this signal efficiency with the new definition.

Figure 3.14 shows that for the central region, the difference between the measured and the true energy loss in the calorimeter has an approximate Gaussian shape around zero, with somewhat larger tails. A small excess of negative values is probably related to deposits below the noise threshold and extrapolations that do not follow precisely the path traversed by the track. A Gaussian function was fitted within 2 standard deviations, taking approximately 95% of the data. From the fit one observes a bias of 3% and a resolution around 12% for muons of $P_T = 100$ GeV.

The Hadronic Endcap Calorimeter is not included in the previous measurement since the ratio between the typical energy loss and the noise is below the threshold used by default, pulling the distribution towards negative values. Instead, the distributions for muons of $|\eta| > 1.5$ are shown in fig. 3.15 for the default (3.4σ) and a lower noise threshold (2σ). A small improvement is observed for the new E_T^{core} definition with respect to the old one and with the use of the lower noise threshold. The behaviour for the central region is basically independent of the change in the noise threshold.

Values for $(E_T^{reco} - E_T^{true})/E_T^{true}$ close to -1 correspond to large underestimations of the energy loss and are observed in figs. 3.14a and 3.15. They occur either when most of the touched cells are not included in E_T^{core} or when their energies are below the noise threshold. The latter is expected for the HEC while the former was observed (specially for the TileCal) with the old definition.

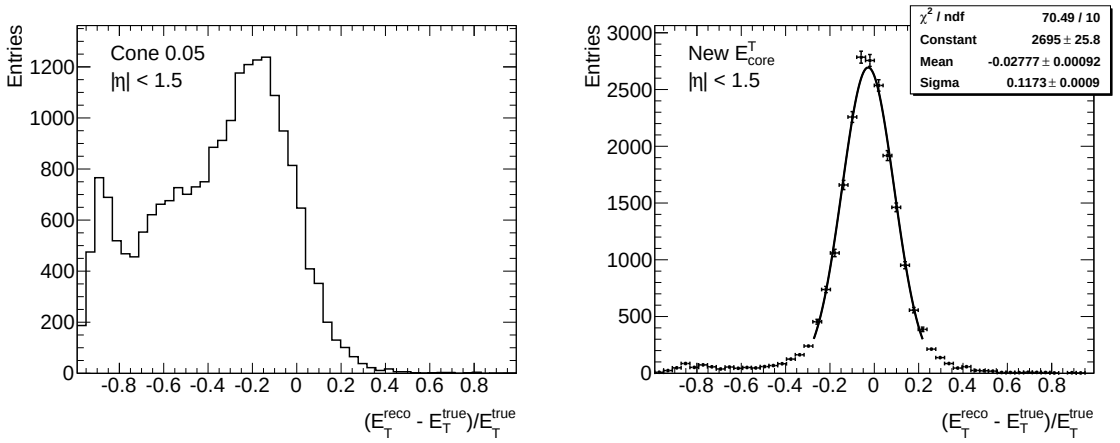

(a) (b)

Figure 3.14: Difference between the reconstructed (E_T^{reco}) and true transverse energy deposits (E_T^{true}) divided by the true value, from muons of $P_T = 100$ GeV and $|\eta| < 1.5$. Comparison between (a) the old E_T^{core} definition and (b) the new one. For the new definition a Gaussian function was fitted within 2 standard deviations.

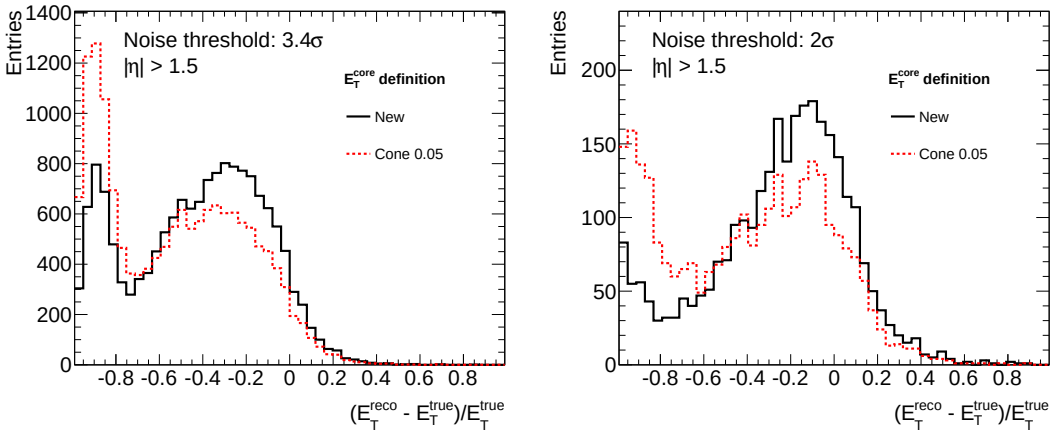

(a) (b)

Figure 3.15: Difference between the reconstructed (E_T^{reco}) and true transverse energy deposits (E_T^{true}) divided by the true value, from muons of $P_T = 100$ GeV and $|\eta| > 1.5$. Comparison between the old E_T^{core} definition and the new one using noise thresholds of (a) 3.4σ and (b) 2σ. The available statistics is lower for plots on the right.

3.4 Perspectives

Several functionalities were included in *TrackInCaloTools* allowing a great level of flexibility for muon isolation and energy loss measurements. The redefinition of E_T^{core} improved considerably the performance of both quantities and the last result opened the possibility of using the calorimeter information to correct for the energy losses[2], specially in the central region. Currently this is not done in all the muon reconstruction algorithms. Studies with cosmic muons were pursued as a validation of the method, and are described in chapter 4.

The isolation studies were performed with Monte Carlo simulated samples and comparisons with first LHC data have started very recently. Remarkable agreement was found on the energy deposited around muons within $\Delta R = 0.2$ and 0.3 on minimum bias events [29]. Studies with muons from W and Z decays should appear shortly. Comparisons of the shape of the isolation variables with Monte Carlo using different E_T^{core} definitions and noise thresholds can be used to validate and if possible improve the results discussed here.

[2]The comparisons up to now were restricted to the energy loss inside the calorimeter volume. Between the ID and the MS, muons also traverse some inert (non instrumented) material and a correction for this effect must be included to use the calorimeter information in muon reconstruction. This aspect will be discussed in the next chapter.

Chapter 4

Studies of muon energy loss with cosmic ray data

Before the first collisions were delivered by the LHC, the ATLAS detector was commissioned with cosmic ray data during several run periods in 2008 and 2009. Hundreds of millions of events were recorded and allowed the study of the performance of nearly all the sub-systems. Each detector element was tested individually after its installation and the combined data taking campaigns involved many and sometimes all sub-detectors.

The commissioning phase included also the trigger, data acquisition, detector control system and reconstruction software. At the same time the full online and offline chains had their behaviour evaluated when exposed to real data, and supported hardware commissioning.

Tracks reconstructed in the Inner Detector or Muon Spectrometer were used for efficiency, resolution and alignment studies among others [30, 31]. A great level of understanding of each system was achieved, permitting studies of their combined performance. Two examples are presented in this chapter, involving the muon energy loss in the calorimeters. In section 4.4, the strategy used for collecting the energy deposits, described in the previous chapter, is evaluated comparing the values to the momentum difference given by the tracking devices. In a second step, described in section 4.5, the effect of the calorimeter correction on the Muon Spectrometer momentum resolution is estimated.

First, a description of cosmic ray events in the ATLAS detector, their reconstruction and the obtained performance are given in section 4.1. Section 4.2 details the event selection for the studies while the method for estimating the energy loss is presented in 4.3.

4.1 Cosmic ray events in the ATLAS detector

Protons are the dominant component of the primary cosmic rays that arrive at the top of the Earth's atmosphere. However, the particles that actually reach the ATLAS underground consist mostly of muons originating from the decay of mesons produced in interactions of the primary cosmic ray.

The location of the ATLAS cavern at 100 m below the surface makes the fluxes from cosmic muons particularly non-uniform. The ones that can traverse the rock between the cavern and the surface lose 30 GeV on average, resulting in a low-momentum spectrum. Most of them, though, arrive through two access shafts located at $z = 13.5$ and -17.7 m, with radii of 9 and 6 m respectively. Figure 4.1 illustrates the position of the ATLAS detector and the shafts in the cavern. As a consequence, cosmic muons have incident angles close to the vertical axis and cross the detector with non-pointing trajectories. Low-momentum particles bend considerably in the toroidal magnetic field and deviate from their original direction.

In contrast, particles from LHC collisions are not only pointing but also synchronous with the accelerator and global experiment clock, with predictable time-of-flights between the different detectors. To cope with the different configuration of cosmic signals, several adaptations were made in the trigger and reconstruction strategies. The main adjustments included the removal of pointing requirements and use of looser criteria for timing and eventually spatial resolution.

Some of the modifications introduced for the reconstruction of cosmic events in the muon system are highlighted in the next subsection. Details are given in ref. [31].

4.1.1 Detection and reconstruction of cosmic muons

Given the normal incidence and the area covered by each sub-detector, the great majority of the events were triggered by the Resistive Plate Chambers, which provide that capability in the barrel part of the Muon Spectrometer. Random triggers as well as calorimeter based triggers were also used. In addition, a dedicated trigger at Level-2 for the Inner Detector allowed the selection of particles traversing its fiducial volume.

The offline reconstruction software was also modified to deal with cosmic ray topologies. Minor changes in the Inner Detector tracking have been made, to remove any assumption on a collision vertex and to be able fit the traversing particle as a full track across both hemispheres in ATLAS. The Muon Spectrometer software had to face specific challenges due to its large volume and the importance of projectivity and timing measurements:

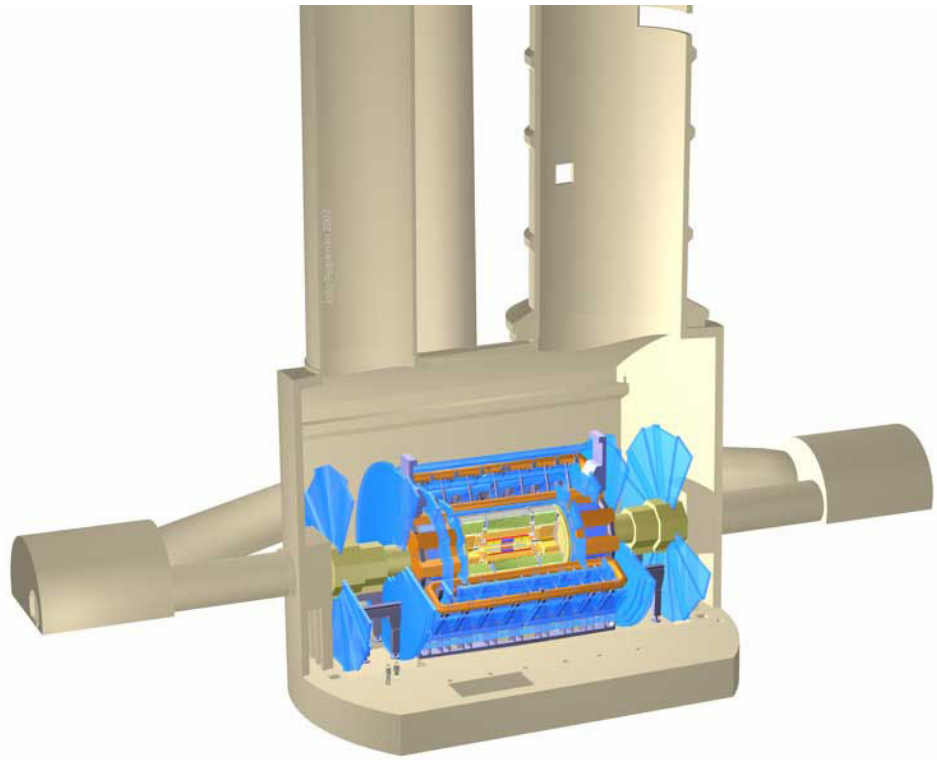

Figure 4.1: Illustration of the ATLAS detector in the cavern, showing the access shafts through which most of the cosmic rays arrive.

- **Pointing requirements.** In collision events, pointing back to the primary vertex is imposed both at the local (chamber) and global (spectrometer) level, when forming segments and tracks. This criterion was relaxed, as the regions of activity normally used to identify muon candidates were considerably enlarged.

- **Calibration and timing.** In the absence of the timing synchronization, a procedure to determine the instant when a muon crossed each chamber was introduced. It relies on the minimization of the hit residuals at the segment level, providing an accuracy comparable with the RPC time measurement when available (around 2 - 4 ns). In any case, the precision associated to the $r - t$ relations is limited, which affects directly the position resolution. As a consequence of the poor calibration, the tolerance for hit to track association and the uncertainty of the hit position were also increased.

- **Alignment conditions.** Another difficulty was the pattern recognition in poor alignment conditions. Alignment corrections were progressively derived, relying mostly on runs without magnetic field, either in the solenoid, the toroid or both. The obtained performance is reported in the following subsection.

The requirements described above are used to ensure very low fake rates in collision events. The clean environment and low hit multiplicity from the cosmic ray events allowed the loosening of the criteria. This strategy was put in place to obtain high efficiency in segment reconstruction in order to debug hardware problems. The increase of the fake segment rate is not considered an issue in these conditions, as most of them are rejected when forming tracks.

4.1.2 Tracking performance

Remarkable results were achieved in terms of tracking performance with cosmic ray data. The Inner Detector was exposed to several million tracks, out of which almost one million crossing the pixels. The alignment techniques were tested, leading to momentum resolutions close to the nominal ones. Analogue procedures were applied to the Muon Spectrometer, combining the optical alignment system and track alignment algorithms. This time only runs with toroid off and solenoid on were used. This field configuration gives nearly straight trajectories in the MS, and the information about multiple scattering can be taken from the momentum measured in the ID. For the top sectors in barrel of the spectrometer, which gather most of the statistics, the performance is below a factor of two away from the nominal values. Given the uncertainties due to timing and calibration, this was an excellent starting point for the first collisions.

To mimic collision events, the reconstructed tracks were split in upper and lower components (also referred to top and bottom) in both systems. This allowed the evaluation of the absolute momentum scale and resolution, taking the difference between the measurements at the perigee. The scale was given by the average value of the top – bottom difference and the resolution by the width of the distribution. The results obtained for the Inner Detector are shown in fig. 4.2. A small deterioration of the absolute momentum scale was observed with the use of the TRT. Caveats in the alignment strategy were identified and corrected in view of these results [32]. More details about the Muon Spectrometer analyses are given in section 4.5, where the influence of the calorimeter correction for the energy loss is evaluated.

4.2 Event selection

4.2.1 Event selection for energy loss studies

The analysis of the muon energy loss relies on and reflects the combined performance of Inner Detector, calorimeters and Muon Spectrometer. For this reason,

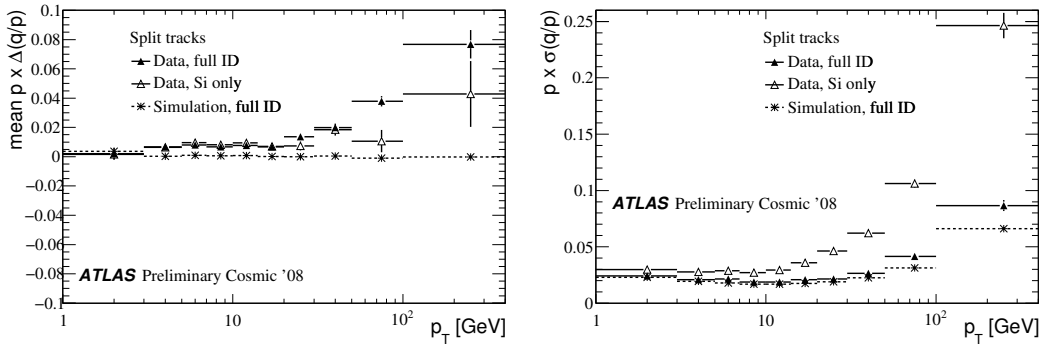

(a) (b)

Figure 4.2: Relative transverse momentum (a) absolute scale and (b) resolution obtained with cosmic ray data for the Inner Detector.

out of the large statistics available from June 2009 data taking period, one run was selected where all the sub-systems were in normal operation modes. About one million events containing Inner Detector tracks were recorded with both solenoid and toroid magnets on.

Strict criteria were applied to select rather pointing trajectories well measured in all tracking sub-systems: Silicon Tracker (SCT) and Transition Radiation Tracker (TRT) in the Inner Detector, Muon Drift Tubes (MDT) and Resistive Plate Chambers (RPC) in the Muon Spectrometer. Most of the results use only events with Inner Detector tracks with momenta between 10 and 25 GeV. In this region the momentum resolution of both systems is below 5%.

The analysis was restricted to tracks crossing the bottom part of the Long Barrel Tile Calorimeter ($-\pi < \phi < 0$ and $|\eta| < 0.65$), to avoid its gap region and to mimic collision events. Table 4.1 shows the full description of the cuts used. The momentum spectrum of the selected tracks (before the momentum cut) is shown in fig. 4.3a.

4.2.2 Event selection for momentum resolution studies

The momentum resolution studies, on the other hand, followed the selection described in ref. [31]. Larger statistics were obtained by including data taken in October 2009, relaxing the cuts on the tracks reconstructed by the Muon Spectrometer, and removing all requirements on the Inner Detector tracks. Out of the 2.3 million events available, 229 thousand were selected with the criteria below.

Exactly one track measured in each MS hemisphere with $|\eta| < 1$ was requested. The separation angle between them at the perigee could not exceed 10 degrees, both

Table 4.1: Selection criteria applied to cosmic-ray events for energy loss studies.

	Cuts	**Events selected**
Initial sample	Events with Inner Detector tracks	1 071 340
Pre-selection	Only one track recorded in the Inner Detector with silicon hits and at least one track recorded in the Muon Spectrometer.	88 594
Inner Detector	Tracks with momentum greater than 5 GeV, within $\|\eta\| < 0.65$, transverse and longitudinal impact parameters below 350 mm and 500 mm respectively, with at least 20 hits in the TRT and 6 silicon hits. Quality cut on the track fit (χ^2 per degrees of freedom < 3).	27 237
Muon Spectrometer	Only one track recorded by Muonboy algorithm in the bottom hemisphere, with at least 3 RPC phi-hits and 17 hits in the MDTs, out of which 7, 5 and 5 in the inner, middle and outer stations respectively. Quality cut on the track fit (χ^2 per degrees of freedom < 5).	11 522
Momentum cut	Momentum measured by the Inner Detector between 10 and 25 GeV (except for figs. 4.3a and 4.5).	4 047

in θ and ϕ. The minimum number of hits in the inner, middle and outer stations was lowered to 6, 4 and 4 respectively. Projectivity requirements on transverse and longitudinal impact parameters were loosen to 1000 mm and 2000 mm. The selection is summarized in table 4.2. The transverse momentum spectrum of the selected tracks is shown in fig. 4.3b.

Table 4.2: Selection criteria applied to cosmic-ray events for momentum resolution studies.

	Cuts	**Events selected**
Initial sample	Events with Inner Detector tracks.	2 299 950
Muon Spectrometer	Only one track recorded by Muonboy algorithm in each hemisphere, with at least 3 RPC phi-hits and 17 hits in the MDTs, out of which 6, 4 and 4 in the inner, middle and outer stations respectively. Transverse and longitudinal impact parameters below 1000 mm and 2000 mm, respectively. Quality cut on the track fit (χ^2 per degrees of freedom < 5). Difference between the azimuthal and polar angles of the tracks ($\Delta\phi$ and $\Delta\theta$) below 10°.	229 469

4.2.3 Monte Carlo simulations

Cosmics ray events were simulated and recorded when the generated tracks crossed specific volumes in the ATLAS detector. An official production was made by the collaboration in 2008 including, among others, muons that crossed the pixel

detector. These samples were selected to have high statistics on projective tracks. They were analysed with the same cuts used for the data and compared to the results on energy loss studies.

More recently, private samples were produced with conditions similar to data taking: updated information about the timing resolutions and newer reconstruction software. Additionally, these samples included the momentum of the generated track at the perigee and at the entrance of the Muon Spectrometer, allowing for a comparison with the reconstructed information. Both the tracking measurements and the energy loss calculation were validated using the "true" information from the tracks.

The available statistics is shown in table 4.3. When compared to 2008 simulations, the 2009 production was made with looser projectivity requirements, which explains the different selection efficiencies observed in the table.

Table 4.3: Available statistics on simulated cosmic ray events, before and after the selection cuts.

	Number of events	
	2008 simulations	2009 simulations
Initial sample	998 634	430 342
After selection cuts (table 4.1)	216 448	29 574
After cuts, within $10 - 25$ GeV	79 401	10 692

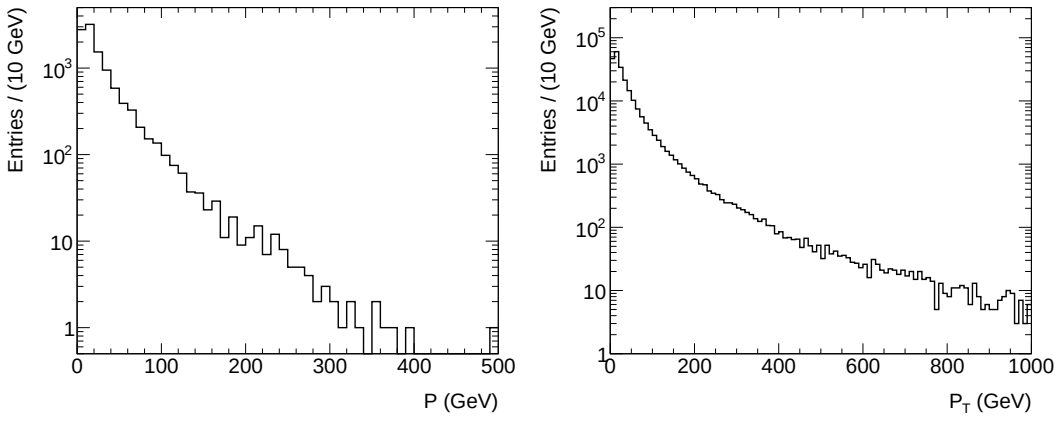

(a) (b)

Figure 4.3: Spectra of (a) the momentum measured in the Inner Detector of the tracks used for energy loss studies (before the momentum cut) and (b) the average transverse momentum $(P_T^{top} + P_T^{bottom})/2$ measured by the Muon Spectrometer of the tracks used for momentum resolution studies.

4.3 Calorimeter energy collection method

TrackInCaloTools was used for all studies, with the loose noise threshold configuration, which accepts cells with energies above twice their noise level. As shown in the previous chapter, a nearly unbiased estimate of the losses inside the calorimeter volume was achieved, without additional corrections to the cell energy. Two main quantities were studied here:

- The energy deposited around the muon candidates, normally used for isolation determinations. In cosmic events they were used to quantify how much of the deposits fall outside the E_T^{core} region.
- The energy deposits associated with the muons. The cells inside the core region were used in the energy loss calculation. Losses in the inert (non-instrumented or dead) material between the ID and the MS are also expected, and thus a correction (E_{dead}) was added. The quantity $\Delta E = E_{calo} + E_{dead}$ was compared to the difference between the momentum measured in the trackers $\Delta P = P_{ID} - P_{MS}$[1].

Corrections for the material between the Inner Detector and the Liquid Argon calorimeter are applied, as well as for the inactive material between the Liquid Argon and the Tile calorimeters, and from the end of the TileCal to the entrance of the Muon Spectrometer. The typical muon energy loss in each of these regions is shown in fig. 4.4.

The ATLAS Tracking Geometry [23] provides the above information in combination with the ATLAS extrapolator. It corrects the momentum of the tracks at each extrapolation step according to the most probable energy loss on the material traversed. Only some iron plates below and above the Tile calorimeter are currently not included in the inactive material description, and should induce losses of less than 40 MeV.

[1] P_{MS} is the measurement at the entrance of the Muon Spectrometer, while P_{ID} is expressed at the perigee; therefore, both ΔP and ΔE represent the energy loss from the perigee to the MS and should have the same value.

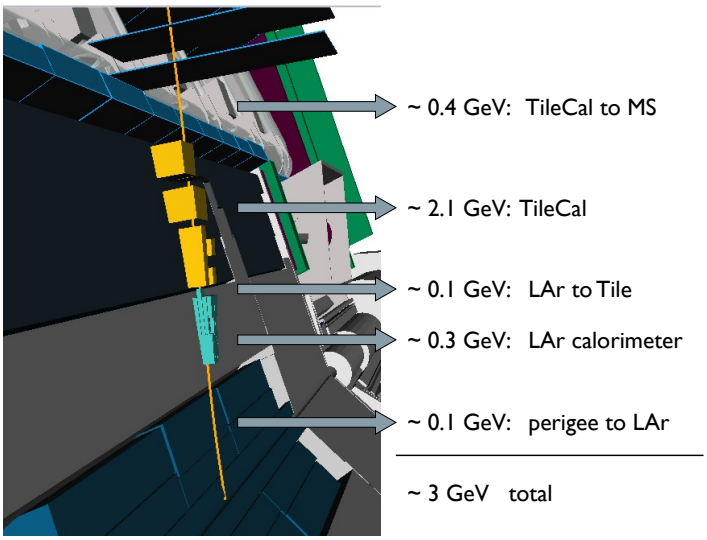

Figure 4.4: Illustration of the typical energy lost by muons traversing the ATLAS detector from the perigee to the MS.

4.4 Results on energy loss studies

4.4.1 Energy deposits around the tracks

A first quantity that was studied was the energy deposited outside the core region. The distance between the extrapolated tracks and the touched cells, shown in fig. 4.5, indicates that most part of the muon activity is concentrated inside the core definition as desired. A small leakage is observed in the phi direction for the second Tile layer. Non-projective tracks crossing the calorimeter might cause this feature. The same effect occurs less frequently in the simulated data, where a higher level of projectivity was ensured by requiring the tracks to cross the pixel detector. Another possibility that goes in the same direction is if the extrapolation does not follow correctly the actual path traversed by the track. Residual misalignments in the Inner Detector and between the ID and the calorimeters can contribute to this effect.

The sum of the transverse energy (Sum E_T) around the tracks within cones of $\Delta R = 0.2$, 0.3 and 0.4, normally employed in isolation studies, was used to quantify the energy outside the core region. The results are shown in figs. 4.6 and 4.7, for data and simulated events, respectively. Negative values are only expected from noise fluctuations, while positive ones can also be caused by deposits outside the E_T^{core} region.

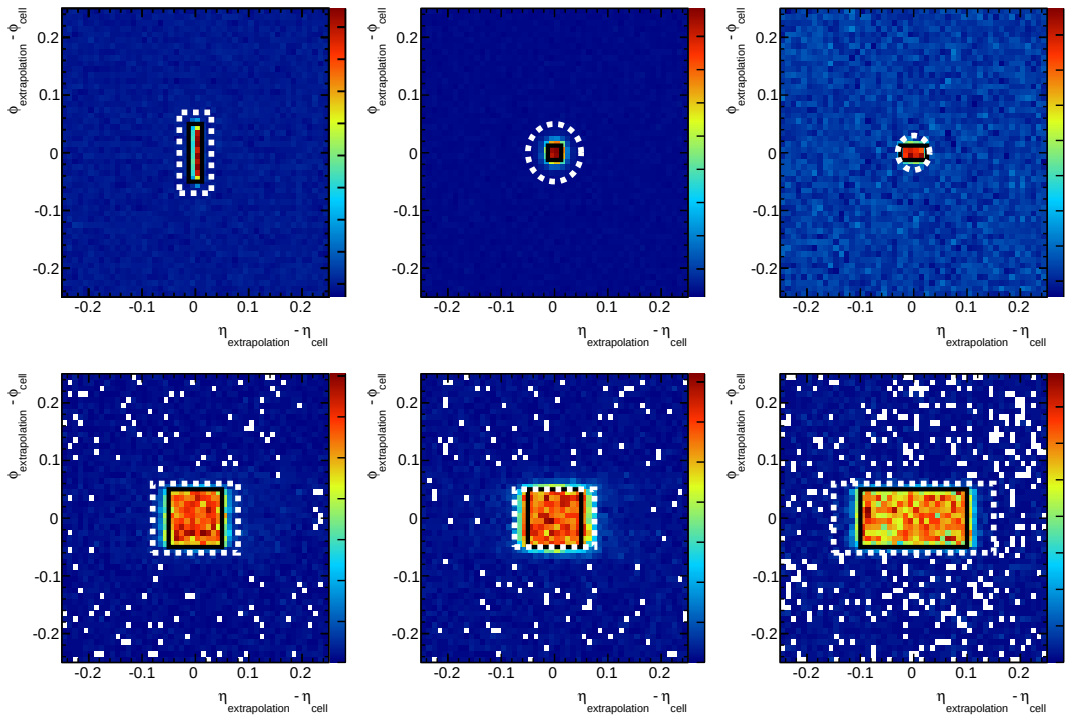

Figure 4.5: Distance between the extrapolated tracks and the cells above the noise threshold on each layer of the EM calorimeter (first row, excluding the presampler) and the TileCal (second row) from 2008 cosmic data. The black solid rectangles indicate the typical cell size and the dashed lines correspond to the core region in each layer. The colors are related to the probability of having a cell above the threshold in each bin.

All the distributions are reasonably centered around zero, with mean values of the order of 100 MeV in the Monte Carlo and 200-300 MeV in the data. The increasing width as the cone size is enlarged indicates that a few cells pass the noise threshold, and this probability augments for larger cones as expected. A small shift towards positive values and some tails on the right-hand side are observed. Again, this effect is less pronounced in the Monte Carlo, where the tracks are more projective and perfect alignment is assumed.

The results indicate that the muon activity in the calorimeters is essentially contained within the core region. Little energy is found outside this area, meaning that the isolation variables are not significantly contaminated by the muon deposits.

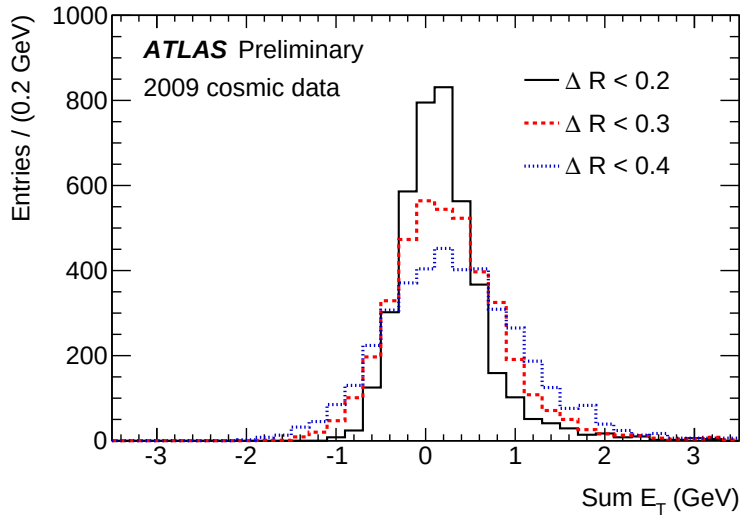

Figure 4.6: Sum of the transverse energy around muon tracks from cosmic-ray events, within $\Delta R = 0.2$, 0.3 and 0.4.

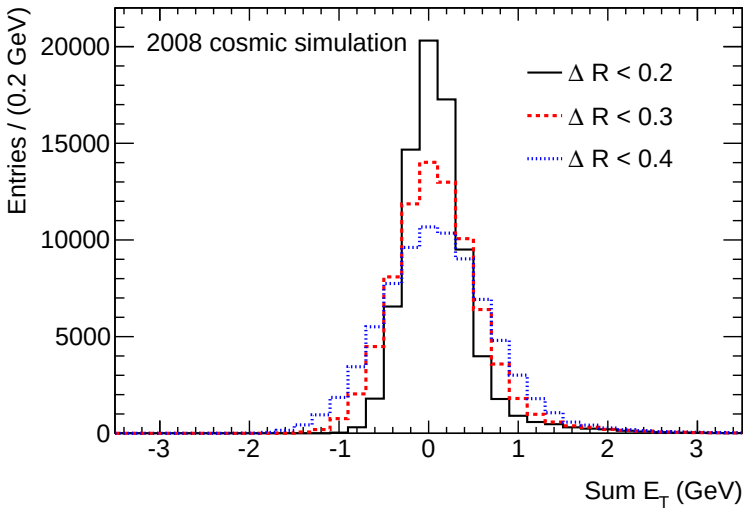

Figure 4.7: Sum of the transverse energy around muon tracks from simulated cosmic-ray events, within $\Delta R = 0.2$, 0.3 and 0.4.

4.4.2 Energy loss and momentum difference between ID and MS

The energy measured in the calorimeter, corrected for the inert material ($\Delta E = E_{calo} + E_{dead}$), was compared with the momentum difference between Inner Detector and Muon Spectrometer tracks ($\Delta P = P_{ID} - P_{MS}$). Results for data and simulations are shown in figs. 4.8 and 4.9, respectively, with the corresponding mean values and RMS listed in table 4.4. The averages are not only consistent with the expected

energy loss of muons in the ATLAS detector which is approximately 3 GeV, but also indicate a remarkable agreement between the quantities both in real and simulated events.

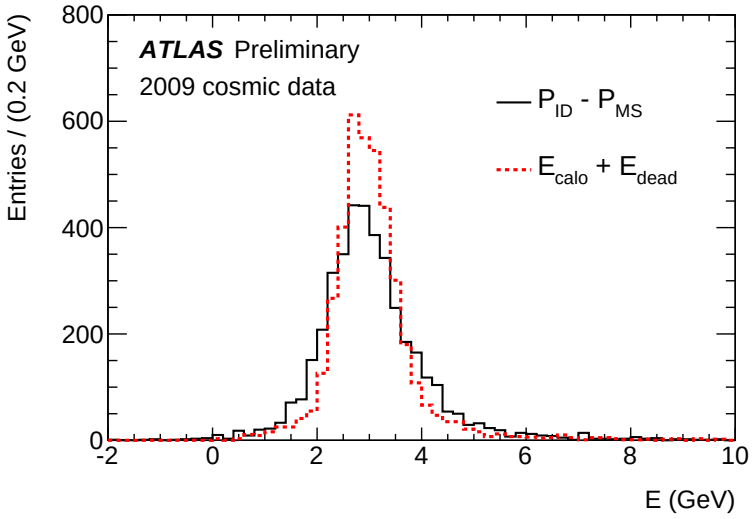

Figure 4.8: Momentum difference between Inner Detector and Muon Spectrometer tracks ($P_{ID} - P_{MS}$) compared with the energy loss measured in the calorimeters (E_{calo}), and a parametrization of the energy loss in the inert material (E_{dead}).

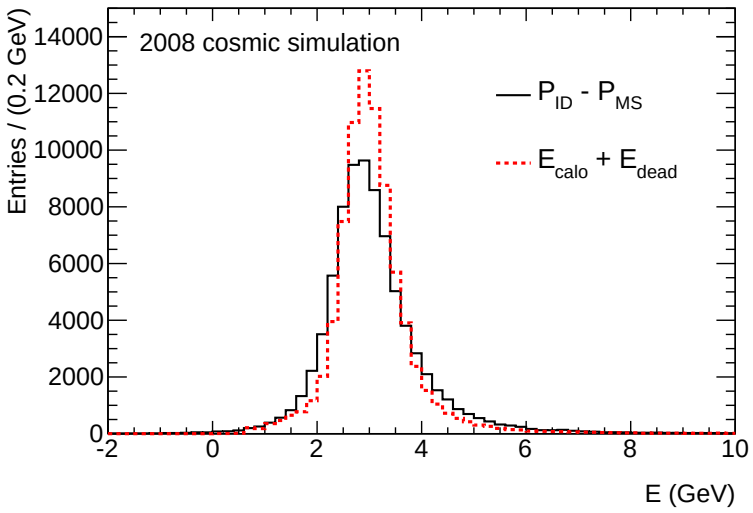

Figure 4.9: Momentum difference between Inner Detector and Muon Spectrometer tracks ($P_{ID} - P_{MS}$) compared with the energy loss measured in the calorimeters (E_{calo}), and a parametrization of the energy loss in the inert material (E_{dead}) on simulated cosmic-ray events.

The difference between the RMS associated to ΔP and ΔE is related to the resolution of each system – trackers and calorimeters –, and exhibits the same behaviour in data and simulation. Although the tracking systems are relatively more precise than the calorimeters, the fact that figs. 4.8 and 4.9 show the difference between their measurements implies that the width of this distribution is larger than the one corresponding to the calorimeter energy. The following estimate supports this argument: the typical momentum of the selected tracks is 16 (13) GeV in the Inner Detector (Muon Spectrometer), measured with a resolution of 2% (4%) [31], while the energy collected in the calorimeters is on average 2.4 GeV, with a precision between 10 and 20% [33].

Table 4.4: Mean value and RMS of the distributions on figs. 4.8 and 4.9.

	Data		**Simulation**	
Quantity	**Mean value** (GeV)	**RMS** (GeV)	**Mean value** (GeV)	**RMS** (GeV)
Momentum difference ($P_{ID} - P_{MS}$)	3.04	1.08	3.06	1.00
Energy measurement ($E_{calo} + E_{dead}$)	3.04	0.85	3.06	0.80

The correlation between the variables is shown in fig. 4.10. No strong dependence is observed in the region below 4 GeV due to the low resolution associated to the measurements. The situation is considerably improved at higher energies. This is specially visible for the simulation plot that has larger statistics. The correlation factors[2] for the full range and these two regions ($E_{calo} + E_{dead}$ below and above 4 GeV) are 0.52 (0.53), 0.14 (0.15) and 0.75 (0.79) for data (simulation), respectively. Higher values for the simulation are explained by the perfect conditions assumed for alignment and calibration.

4.4.3 Comparison between true and reconstructed energy losses

More detailed comparisons were possible using 2009 simulations, due to the presence of information about the true energy loss upstream the Muon Spectrometer. The bias on the momentum determination was evaluated and found to be negligible in the range selected by this study ($10 < P < 25$ GeV). The difference between the

[2]The correlation factor between two quantities is defined as the ratio between their covariance and the product of their standard deviations.

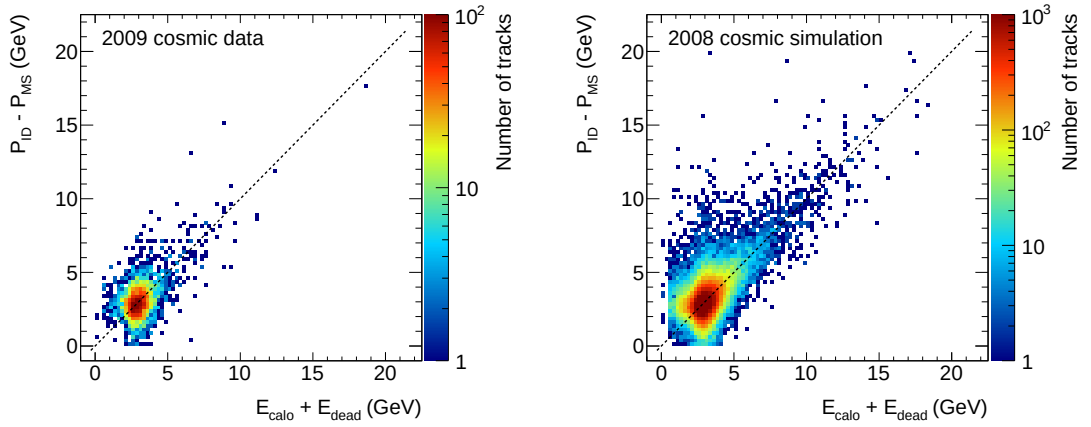

(a) (b)

Figure 4.10: Correlation between the energy loss measured in the calorimeters corrected by a parametrization of the losses in the inert material ($E_{calo} + E_{dead}$) and the momentum difference between Inner Detector and Muon Spectrometer tracks ($P_{ID} - P_{MS}$), for (a) cosmic data and (b) simulations.

simulated and reconstructed quantities is shown in fig. 4.11 and their correlation in fig. 4.12.

Overall, both ΔP and ΔE are in excellent agreement with the true values. Averages close to zero in fig. 4.11 and very good correlation in in the low energy region (up to 10 GeV) of fig. 4.12 are observed. A few events have negative values for the momentum difference due to poor measurements in the Muon Spectrometer. On the other hand, high energy deposits – above 10 GeV – seem to be slightly underestimated by the calorimeter measurement.

4.5 Results on momentum resolution

At high transverse momentum – above 100 GeV – the resolution of the Muon Spectrometer is limited by its spatial resolution and by multiple scattering effects to a lesser extent. Going down to a few tens of GeV, the energy loss fluctuations become the dominant component, given the large amount of material in the ATLAS calorimeters. A parametrization is normally used to correct this effect, but cannot account for the variations around the most probable value. At the same time, the calorimeter measurement was found to be nearly unbiased, both when compared with the true values on Monte Carlo simulations, and compared with the tracking devices on cosmic ray data. Exploring these results, the impact of using the calorimetric information on the muon reconstruction is assessed in the present section.

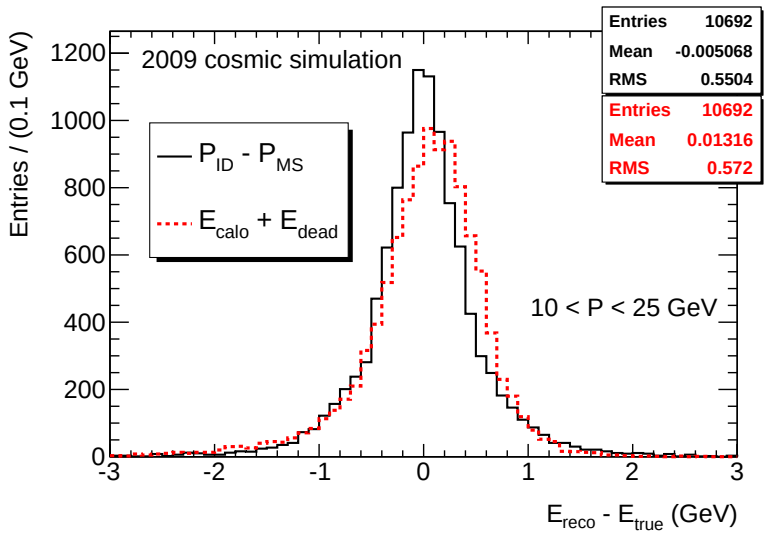

Figure 4.11: Difference between the reconstructed and the true energy loss from simulated cosmic-ray events.

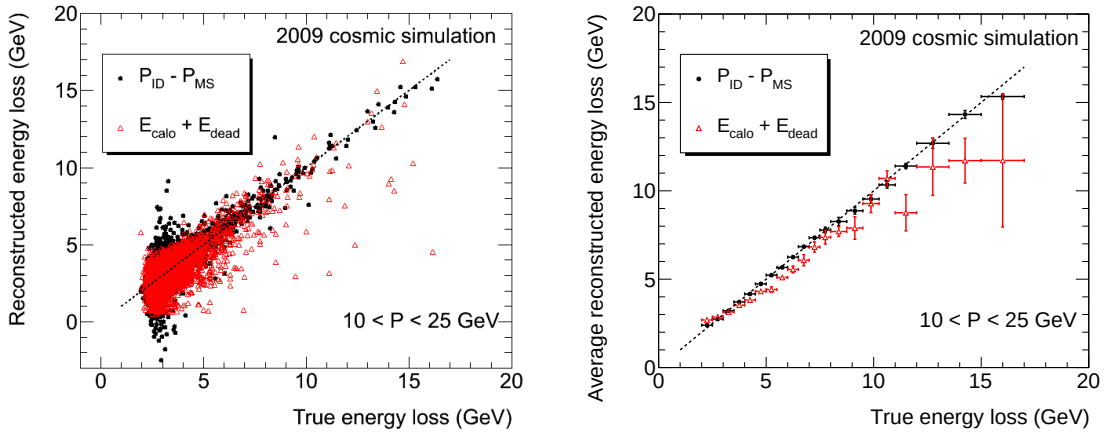

(a) (b)

Figure 4.12: Correlation between the true and (a) the reconstructed energy loss or (b) its average from simulated cosmic-ray events. The dashed lines indicate where both quantities have the same value.

A simple and yet reasonable way to combine the parametrized and the measured energy loss in case of isolated muons was suggested by studies with Monte Carlo samples, mentioned in the previous section. The most probable value for the losses is around 3 GeV, and the fluctuations around the measurement are of the order of 500 MeV (fig. 4.11). For such, a threshold of 4 GeV was chosen, after which the calorimeter information replaces the parametrization. No significant changes are observed when changing this cut from 4 GeV to e.g. 5 GeV. The following relations

are used in those cases to calculate the transverse momenta at the perigee, taking the measurement at the entrance of Muon Spectrometer (P_T^{MS}) for the top and bottom hemispheres:

$$P_T^{top} = P_T^{MS\,top} - (E_T^{calo} + E_T^{dead})\,, \tag{4.1}$$

$$P_T^{bottom} = P_T^{MS\,bottom} + (E_T^{calo} + E_T^{dead})\,. \tag{4.2}$$

In what follows, the effect of this replacement is evaluated. As described in ref. [31], the momentum resolution can be calculated with the so called top – bottom method, by comparing the tracks measured in the upper and lower hemispheres at the perigee. For each pair of tracks, one takes the difference between their transverse momentum divided by the mean value:

$$\frac{\Delta P_T}{P_T} = 2\,\frac{P_T^{top} - P_T^{bottom}}{P_T^{top} + P_T^{bottom}}\,. \tag{4.3}$$

To observe the dependence of the momentum resolution with P_T, the data was divided in 9 bins, between 7 and 1000 GeV. The fraction of events in which $E_{calo\,+\,dead} > 4$ GeV varies from 7% in the first bin, up to 40% and 75% in the last two. The effect of replacing the parametrization by the measurement can be observed in figures 4.13a and 4.13b, for the interval of $20 < P_T < 30$ GeV. The first plot includes all the events while the second one contains only the cases where $E_{calo\,+\,dead} > 4$ GeV, which corresponds to approximately 12% of the statistics.

The method seems able to identify the events which cause the somewhat large tails on the right-hand side when the parametrization is used. Moreover, the measurement corrects this effect making the distribution more symmetric. The next step was to verify if this translates into a gain in momentum resolution.

The functions used to fit the data followed the conventions defined in ref. [31]. The presence of relatively large tails drove the choice for a double-Gaussian with common mean. A Landau function was convoluted to the narrow Gaussian, to account for the energy loss fluctuations. The normalization of the curves was fixed such that 95% of the events were inside the narrow Gaussian at $P_T < 10$ GeV and 70% above.

The results of the fits, with and without the Landau convolution, are shown in figures 4.14 and 4.15, and listed in tables 4.5 and 4.6. The shapes seem to be in reasonable agreement with the data points, with the exception of the pure double-Gaussian fit when using the parametrization. For this combination, χ^2 divided by the number of degrees of freedom (NDF) exceed 30 in the first bins. Values close to

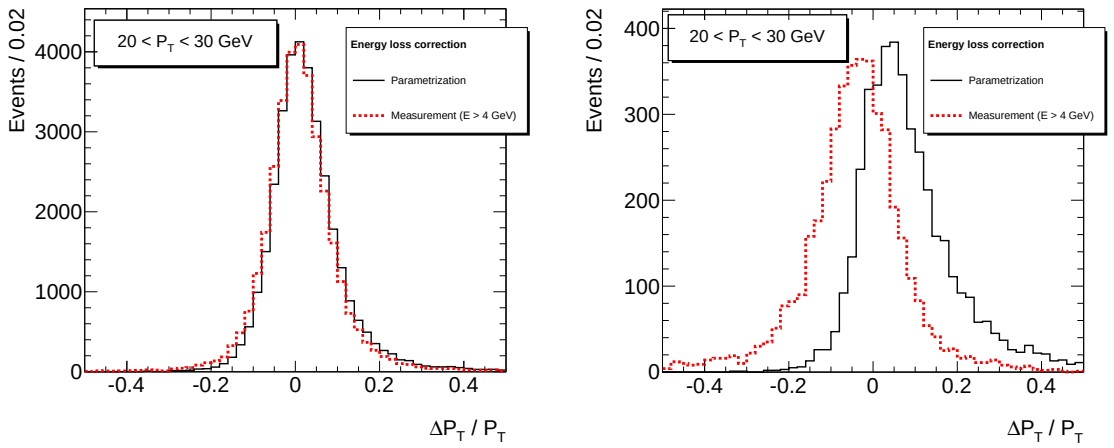

(a) All events. (b) Events with $E > 4$ GeV.

Figure 4.13: $\Delta P_T/P_T$ for the interval $20 < P_T < 30$ GeV, comparing the parametrization (solid line) and the calorimeter measurement (dashed line) for correcting the energy losses.

one are obtained when using the Landau function.

If the measurement is considered, the parameter associated to the Landau is decreased by a factor of two. The fit quality, measured by χ^2 / NDF, is reduced due to some tails on the left-hand side of the plots. It now becomes comparable to quality of the double Gaussian fit, indicating that indeed all distributions are quite symmetric. In summary, the Landau is clearly needed when the parametrization is used alone, but produces a much smaller effect when the measurement is taken.

Still following ref. [31], the resolution was calculated by the sum of the standard deviations of the narrow Gaussian and the Landau, dividing the result by $\sqrt{2}$. The Landau width is added linearly to the narrow Gaussian RMS since the two quantities are strongly correlated. The momentum dependence was derived taking the mean value of P_T in each bin. The results in fig. 4.16 show a clear improvement with the calorimeter correction up to 30 GeV, without any degradation for higher values. A relative gain around 10% was achieved in this region.

This result demonstrates that the calorimeter can provide valuable information for muon reconstruction and could be used to correct the energy loss upstream the spectrometer in case of significant losses. Sophisticated techniques are available to combine the parametrization and the measurement, but due to technical problems they could not be evaluated in cosmic event configuration. The application of this study in collision data is an important perspective opened by the present work.

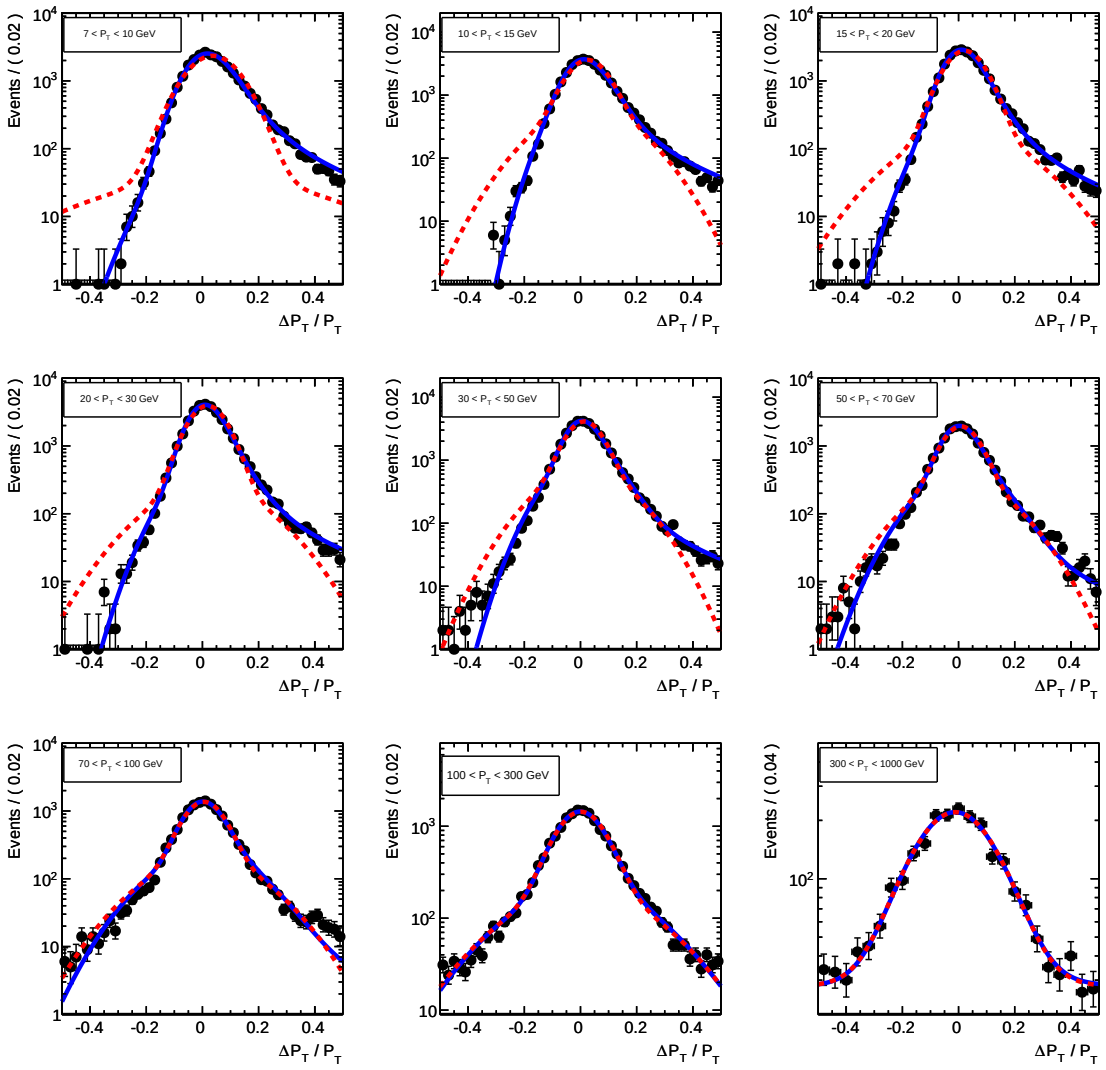

Figure 4.14: Distributions of $\Delta P_T/P_T$ in nine P_T bins. A parametrization is used to correct for the energy losses. A double-Gaussian function (dashed line) and its convolution with a Landau (solid line) are fitted to the data.

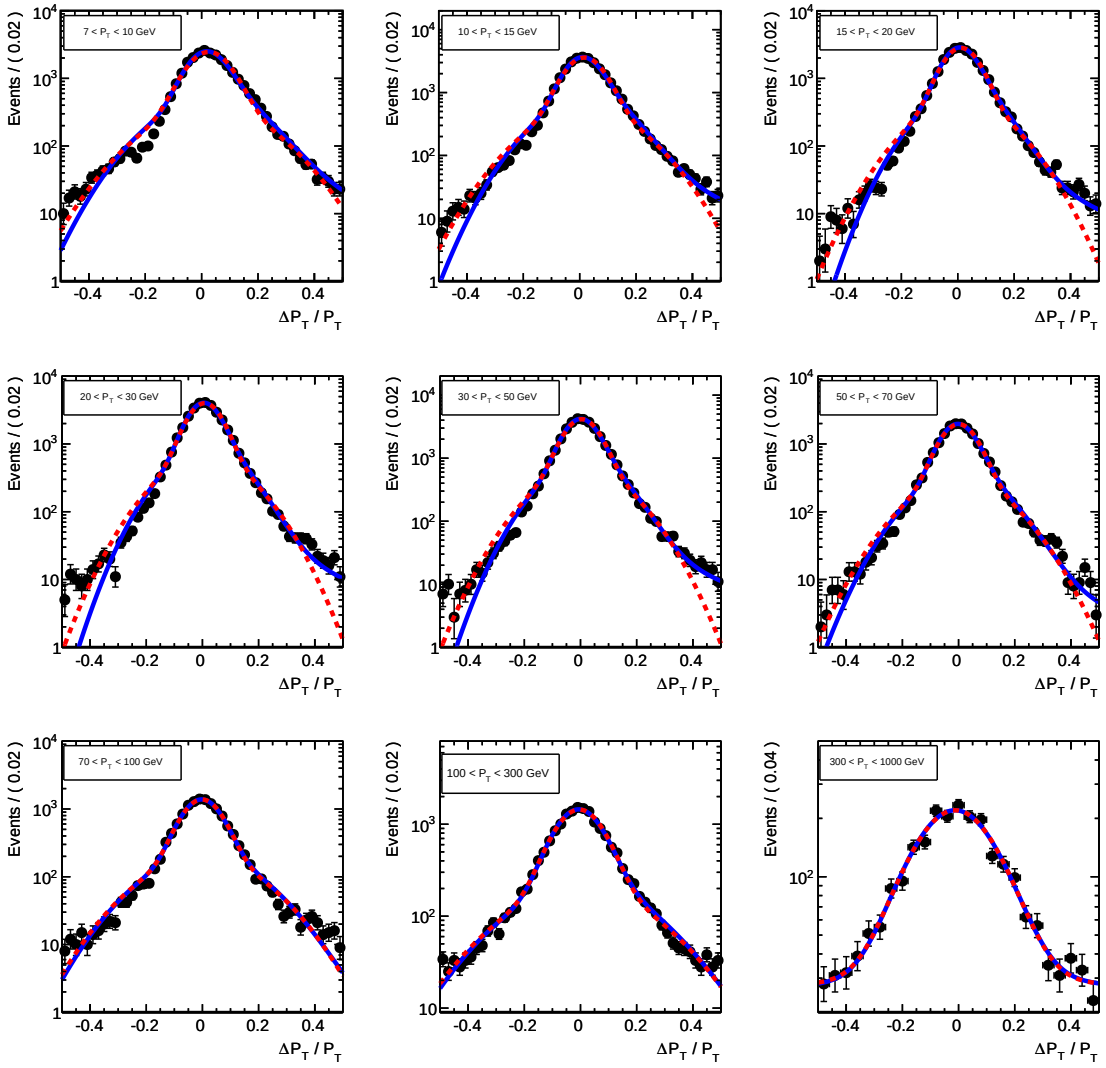

Figure 4.15: Distributions of $\Delta P_T/P_T$ in nine P_T bins. The calorimeter measurement is used to correct for the energy losses. A double-Gaussian function (dashed line) and its convolution with a Landau (solid line) are fitted to the data.

Table 4.5: Parameters of the fits using a double-Gaussian convoluted with a Landau, both when the parametrization and the calorimeter measurement are taken to correct for the energy losses. The width corresponds to the sum of the standard deviations of the narrow Gaussian and the Landau divided by $\sqrt{2}$.

P_T **range**	**Energy loss correction**	Mean	Width	σ_{Landau}	χ^2 / NDF
$7-10$ GeV	Parametrization	0.0003 ± 0.0004	0.0558 ± 0.0007	0.0175 ± 0.0005	1.7
	Measurement	0.0022 ± 0.0005	0.0481 ± 0.0009	0.0104 ± 0.0007	8.4
$10-15$ GeV	Parametrization	0.0005 ± 0.0003	0.0466 ± 0.0008	0.0201 ± 0.0005	2.0
	Measurement	-0.0007 ± 0.0004	0.0434 ± 0.0006	0.0085 ± 0.0005	4.3
$15-20$ GeV	Parametrization	-0.0017 ± 0.0003	0.0446 ± 0.0006	0.0138 ± 0.0004	1.1
	Measurement	-0.0019 ± 0.0004	0.0409 ± 0.0006	0.0071 ± 0.0005	2.7
$20-30$ GeV	Parametrization	-0.0020 ± 0.0003	0.0424 ± 0.0005	0.0110 ± 0.0003	1.4
	Measurement	-0.0021 ± 0.0004	0.0387 ± 0.0005	0.0049 ± 0.0003	4.7
$30-50$ GeV	Parametrization	-0.0034 ± 0.0003	0.0396 ± 0.0005	0.0117 ± 0.0004	2.2
	Measurement	-0.0042 ± 0.0004	0.0395 ± 0.0005	0.0052 ± 0.0003	3.1
$50-70$ GeV	Parametrization	-0.0046 ± 0.0003	0.0410 ± 0.0005	0.0081 ± 0.0002	2.4
	Measurement	-0.0054 ± 0.0006	0.0410 ± 0.0007	0.0041 ± 0.0006	2.0
$70-100$ GeV	Parametrization	-0.0047 ± 0.0004	0.0444 ± 0.0006	0.0058 ± 0.0003	2.6
	Measurement	-0.0036 ± 0.0020	0.0442 ± 0.0014	0.0014 ± 0.0012	2.5
$100-300$ GeV	Parametrization	-0.0048 ± 0.0004	0.0550 ± 0.0006	0.0031 ± 0.0002	1.8
	Measurement	-0.0074 ± 0.0014	0.0549 ± 0.0022	0.0031 ± 0.0028	1.8
$300-1000$ GeV	Parametrization	-0.0085 ± 0.0022	0.0987 ± 0.0027	0.0011 ± 0.0006	0.6
	Measurement	-0.0085 ± 0.0038	0.0989 ± 0.0031	0.0011 ± 0.0010	0.8

Table 4.6: Parameters of double-Gaussian fits, both when the parametrization and the calorimeter measurement are taken to correct for the energy losses. The width corresponds to the standard deviation of the narrow Gaussian divided by $\sqrt{2}$.

P_T **range**	**Energy loss correction**	Mean	Width	χ^2 / NDF
$7-10$ GeV	Parametrization	0.0370 ± 0.0006	0.0615 ± 0.0003	35.7
	Measurement	0.0259 ± 0.0006	0.0497 ± 0.0004	10.1
$10-15$ GeV	Parametrization	0.0256 ± 0.0005	0.0445 ± 0.0003	80.2
	Measurement	0.0168 ± 0.0005	0.0443 ± 0.0003	7.7
$15-20$ GeV	Parametrization	0.0219 ± 0.0005	0.0462 ± 0.0003	34.5
	Measurement	0.0120 ± 0.0005	0.0413 ± 0.0003	6.5
$20-30$ GeV	Parametrization	0.0182 ± 0.0004	0.0439 ± 0.0002	32.2
	Measurement	0.0083 ± 0.0004	0.0390 ± 0.0003	9.4
$30-50$ GeV	Parametrization	0.0136 ± 0.0004	0.0400 ± 0.0003	25.2
	Measurement	0.0047 ± 0.0004	0.0398 ± 0.0003	7.8
$50-70$ GeV	Parametrization	0.0084 ± 0.0006	0.0415 ± 0.0004	6.0
	Measurement	0.0007 ± 0.0006	0.0413 ± 0.0004	2.7
$70-100$ GeV	Parametrization	0.0057 ± 0.0007	0.0448 ± 0.0005	3.2
	Measurement	-0.0016 ± 0.0007	0.0443 ± 0.0005	2.5
$100-300$ GeV	Parametrization	0.0009 ± 0.0008	0.0554 ± 0.0005	2.2
	Measurement	-0.0044 ± 0.0008	0.0553 ± 0.0005	2.0
$300-1000$ GeV	Parametrization	-0.0120 ± 0.0044	0.0987 ± 0.0027	0.6
	Measurement	-0.0120 ± 0.0044	0.0988 ± 0.0028	0.8

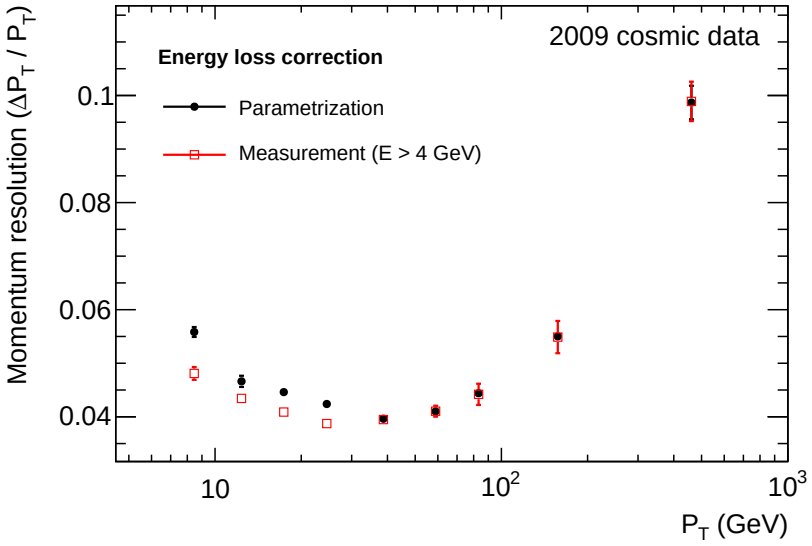

Figure 4.16: Transverse momentum resolution of the Muon Spectrometer, evaluated using the top – bottom method described in the text. Two possibilities for correcting the energy loss are compared: a parametrization (black circles) and the calorimeter measurement (open red squares).

Part II

Higgs boson searches

Chapter 5

The Standard Model and the Higgs boson

A coherent description of the electroweak and strong phenomena was achieved with the development of the Standard Model (SM) of particle physics. It combines the well established electroweak theory of Glashow, Weinberg and Salam with Quantum Chromodynamics (QCD), the fundamental theory of strong interactions. The SM offers an elegant theoretical framework for the characterization of these interactions at the quantum level: it is perturbative at sufficiently high energies and renormalizable due to its gauge invariant formulation.

Moreover, it is able to accommodate basically all the known experimental facts and precise measurements performed in high energy particle colliders over the last decades. It remains however "incomplete". The mechanism for electroweak symmetry breaking that gives masses to the particles was not identified, and the associated particle – the Higgs boson – is still undiscovered.

This chapter gives a very brief overview of the Standard Model and its key ingredients with some attention to the mechanism which predicts the existence of the Higgs particle. These topics are the objects of sections 5.1, 5.2 and 5.3. The state of the art in Higgs searches is reviewed in section 5.4 while the prospects for the near future in terms of discoveries and measurement of its properties are part of sections 5.5, 5.6 and 5.7. Finally, extensions and alternatives to the Standard Model are briefly mentioned in section 5.8.

The Higgs searches in four lepton final states are discussed in the next two chapters after the introduction of some theoretical background in the present one. A complete treatment of these subjects is given in refs. [34–37].

5.1 Electromagnetic, strong and weak interactions

The main elementary constituents of matter are point like spin-$\frac{1}{2}$ particles called fermions. Their dynamics is governed by a relativistic quantum theory. The associated wave function, represented by the four component spinor $\psi(x)$, obeys the Dirac equation:

$$(i\gamma^\mu \partial_\mu - m)\,\psi(x) = 0\,, \tag{5.1}$$

where each ψ component is a function of the space-time coordinates x; γ^μ are Dirac matrices and m is the fermion mass. In the Lagrangian formalism, this equation of motion can be derived from the Lagrangian:

$$\mathscr{L}_0 = i\bar{\psi}(x)\gamma^\mu \partial_\mu \psi(x) - m\bar{\psi}(x)\psi(x)\,, \tag{5.2}$$

where $\bar{\psi}(x)$ is the conjugate of $\psi(x)$. In the context of quantum field theory, ψ represents the fermionic field. After quantization, this field can create and annihilate particles of matter and anti-matter (fermions and anti-fermions).

Up to now the formulation is restricted to a free or non-interacting field theory. Interactions are typically introduced invoking the 'gauge principle'. It states that the underlying physics should be invariant under local phase transformations of the fields. A redefinition of the field of the form $\psi \to \psi' \equiv e^{i\theta(x)}\,\psi(x)$, where $\theta(x)$ is an arbitrary function, should not alter the Lagrangian by more than a total derivative of a function of the coordinates. This is not the case of equation 5.2, since:

$$\partial_\mu \psi(x) \to \partial_\mu \psi'(x) = e^{i\theta(x)}\,\left[\partial_\mu + i\partial_\mu \theta(x)\right]\psi(x)\,. \tag{5.3}$$

The invariance can be restored with the addition of a spin-1 field $A_\mu(x)$, which transforms as $A_\mu(x) \to A'_\mu(x) \equiv A_\mu(x) - \frac{1}{Q}\partial_\mu \theta$, where Q is a constant, under the same $U(1)$ symmetry. Its transformation law allows the cancellation of the last term on the right-hand side of eq. 5.3. If one now replaces the ordinary derivative by the covariant derivative:

$$D_\mu(x)\psi(x) \equiv \left[\partial_\mu + iQA_\mu(x)\right]\,\psi(x)\,, \tag{5.4}$$

the resulting Lagrangian is invariant under $U(1)$:

$$\mathscr{L} = i\bar{\psi}(x)\gamma^\mu D_\mu \psi(x) - m\bar{\psi}(x)\psi(x)\; = \mathscr{L}_0 - QA_\mu(x)\bar{\psi}(x)\gamma^\mu\psi(x)\,. \tag{5.5}$$

The gauge principle has generated the second term of eq. 5.5, which couples the fermion with the vector field A_μ. The dynamics of the latter is governed by the Maxwell's equations if the kinetic term $-\frac{1}{4}F^{\mu\nu}\,F_{\mu\nu}$ is added to the Lagrangian, with $F^{\mu\nu} = \partial^\mu A^\nu - \partial^\nu A^\mu$. The strength of the interaction is proportional to Q, which can be interpreted as the charge of the electron. The quantization of this Lagrangian leads to the theory of Quantum Electrodynamics (QED), which is in excellent agreement with experimental data. The fields are identified with the electron and a gauge boson – the photon. The photon is massless, and a mass term of the form $M^2 A_\mu A^\mu$ was not introduced to preserve gauge invariance.

Quantum Chromodynamics (QCD)

QCD, the theory of strong interactions, explains the existence of a multitude of particles classified as *mesons* and *baryons* – such as pions and protons – by combinations of elementary fermions called *quarks*. Quarks are electrically charged and also carry a new quantum number, color charge. There are three colors (conventionally noted as red, green and blue) such that the baryons and mesons are colour-singlet combinations of qqq or $q\bar{q}$, respectively.

The interactions among the quarks are derived invoking the gauge principle for a $SU(3)$ symmetry. We notice that there are six different quark flavours, which will be labeled by the subscript f. Starting with the free Lagrangian for a quark triplet of a given flavour, $q_f^t = (q_f^{red}\ q_f^{green}\ q_f^{blue})$:

$$\mathscr{L}_0 = \sum_f \bar{q}_f \left(i\gamma^\mu \partial_\mu - m_f\right) q_f \,, \tag{5.6}$$

one is forced to introduce gauge bosons – called *gluons* – to preserve the gauge invariance. The Lagrangian becomes:

$$\mathscr{L}_{QCD} = \mathscr{L}_0 - g_s G_a^\mu \sum_f \bar{q}_f^\alpha \gamma_\mu \left(\frac{\lambda^a}{2}\right)_{\alpha\beta} q_f^\beta - \frac{1}{4} G_a^{\mu\nu} G^a_{\mu\nu} \,. \tag{5.7}$$

The strength of the interaction is g_s, which is universal for all the quark flavours. The second term includes $SU(3)$ matrices λ_a and represents the interaction between the quarks and the gluon field G_a^μ. The kinetic term for the gluons is the third one, with $G_a^{\mu\nu} = \partial^\mu G_a^\nu - \partial^\nu G_a^\mu - g_s f^{abc} G_b^\mu G_c^\nu$, where f^{abc} are the $SU(3)$ structure constants. There are eight gluons which also carry color charge due to the non-abelian nature of the group. This gives rise to self-interactions between them and is behind the existence of bound-states instead of free quarks (quark confinement).

The electroweak theory

Weak interactions are behind a variety of phenomena like beta decay, decays of charged pions and muons, scattering of neutrinos – neutral and nearly massless fermions – on nuclei, among others. Some of the experimental facts that helped constructing a theory of weak interactions are the following:

- The decays of charged pions, muons and neutrons are governed by a universal strength that involves left-handed (right-handed) fermion (anti-fermion) chiralities[1].
- These decays are identified with charged current interactions: transitions between down and up-type quarks (like $d \to u$) or between charged leptons – like electrons or muons – and the corresponding neutrinos. There are different types (flavours) of neutrinos, one associated with each charged lepton.
- Although neutrinos do not have electric charge, they interact via neutral currents, which can also involve charged fermions. Neutral currents conserve flavour, implying that there is no transition between charged leptons like $\mu \to e\gamma$. Those interactions also distinguish between the different chiralities of the fermions, unlike the electromagnetic interaction.

Electromagnetic and weak phenomena are described in an coherent framework requiring a gauge symmetry group $SU(2)_L \otimes U(1)_Y$. The subscript L refers to left-handed fields. The $U(1)$ symmetry does not correspond to the electromagnetic interaction but it is related to it as it will be shown. Its parameter Y – called hypercharge – is connected to the electric charge by a relation which also involves the charge associated with $SU(2)$, called weak isospin.

The electroweak interactions dictate how the particles of matter are organized. Leptons that only interact electroweakly, and quarks that also interact strongly are grouped in three families with increasing mass:

Leptons:	**Quarks:**
$\begin{pmatrix} \nu_e \\ e \end{pmatrix}, \begin{pmatrix} \nu_\mu \\ \mu \end{pmatrix}, \begin{pmatrix} \nu_\tau \\ \tau \end{pmatrix}$	$\begin{pmatrix} u \\ d \end{pmatrix}, \begin{pmatrix} c \\ s \end{pmatrix}, \begin{pmatrix} t \\ b \end{pmatrix}$

[1] Chirality is a property of the field defined by the operator γ^5, which is formed by the product of Dirac matrices so that it anti-commutes with all the others. In case of massless particles the chirality corresponds to the helicity: fermions with right-handed (left-handed) helicity are the ones that have the spin pointing in the same (opposite) direction of the momentum. For anti-fermions this convention is reversed.

The leptons on the upper row are the neutrinos, each one associated with the electron, muon and tau that occupy the lower row. The neutrinos are chargeless while the other leptons have charge $= -1$. The quarks appear in three different colors and carry fractional charge: $+\frac{2}{3}$ for the up (u), charm (c) and top (t) and $-\frac{1}{3}$ for the down (d), strange (s) and bottom (b). Anti-particles for each of the fermions are also included.

This doublet structure illustrated above accommodates the left-handed chiral fields while the right-handed partners transform as singlets under $SU(2)_L$. Right-handed neutrinos do not exist in the minimal version of the theory, only charged leptons, up and down-type quarks.

The interactions among the particles can be derived from the gauge principle. The gauge symmetry implies the existence of two coupling constants – g and g' – and four gauge fields: W^a_μ (with $a = 1, 2, 3$) and B_μ. Taking for instance a quark family given by:

$$\psi_1(x) = \begin{pmatrix} u \\ d \end{pmatrix}_L , \qquad \psi_2(x) = u_R \, , \qquad \psi_3(x) = d_R \, , \tag{5.8}$$

with R referring to right-handed fields, the associated Lagrangian can be written under the form:

$$\mathscr{L}_{EW} = \sum_{j=1}^{3} i\bar{\psi}_j(x)\gamma^\mu D_\mu \psi_j(x) - \frac{1}{4} W^a_{\mu\nu} W^{\mu\nu}_a - \frac{1}{4} B^{\mu\nu} B_{\mu\nu} \, , \tag{5.9}$$

where the covariant derivative D_μ is expressed as:

$$D_\mu \, \psi_j(x) = \left[\partial_\mu - ig \frac{\sigma_a}{2} W^a_\mu \delta_{1j} - ig' \frac{Y_j}{2} B_\mu \right] \psi_j(x) \, . \tag{5.10}$$

Here σ_a are the Pauli matrices, Y_j is the hypercharge and $\delta_{ij} = 1$ for $i = j$ and 0 otherwise. The second term, associated with $SU(2)$ transforms only left-handed fields (ψ_1) while the last term, associated with $U(1)$, acts on both chiralities. Moreover:

$$W^{\mu\nu}_a = \partial^\mu W^\nu_a - \partial^\nu W^\mu_a + g \, \epsilon_{abc} \, W^\mu_b \, W^\nu_c \, , \tag{5.11}$$

$$B^{\mu\nu} = \partial^\mu B^\nu - \partial^\nu B^\mu \, . \tag{5.12}$$

Combinations of the first two components of W^i_μ are associated with two charged vector bosons:

$$W_\mu^\pm = W_\mu^\dagger, W_\mu = \frac{1}{\sqrt{2}}\left(W_\mu^1 \mp i W_\mu^2\right) . \tag{5.13}$$

The remaining component W_μ^3 mixes with B_μ via the Weinberg angle θ_W in such a way to form two neutral bosons: the photon and the Z.

$$\begin{pmatrix} W_\mu^3 \\ B_\mu \end{pmatrix} = \begin{pmatrix} \cos\theta_W & \sin\theta_W \\ -\sin\theta_W & \cos\theta_W \end{pmatrix} \begin{pmatrix} Z_\mu \\ A_\mu \end{pmatrix} . \tag{5.14}$$

Again, the non-abelian group symmetry predicts the existence of interactions between the gauge bosons. There are triple gauge couplings and vertices involving four bosons, always with the presence of a W pair.

This Lagrangian describes charged and neutral interactions associated with weak decays, such as the phenomena mentioned in the beginning of the section. It incorporates QED and self-interactions between the gauge bosons. Nevertheless it is in strong disagreement with experimental facts. The $W^\pm$, the Z and the fermions are massive objects, and mass terms for any of these particles violate explicitly the gauge symmetry.

5.2 The Higgs mechanism

The contradiction pointed out in the last section left the theorists with a difficult question: should one brutally add the mass terms to the Lagrangian and abandon gauge invariance with the nice properties associated such as renormalizability, or is there an alternative to generate masses without breaking the symmetry explicitly?

The answer is yes and came from the work of Higgs, Englert, Brout and others on the mechanism of spontaneous symmetry breaking. One introduces a doublet of complex scalar fields $\Phi(x)$ and a scalar potential $V(\Phi)$ given by e.g.:

$$\Phi(x) = \begin{pmatrix} \phi^+(x) \\ \phi^0(x) \end{pmatrix} \tag{5.15}$$

$$V(\Phi) = \mu^2 \Phi^\dagger\Phi + \lambda\left(\Phi^\dagger\Phi\right)^2 . \tag{5.16}$$

The Lagrangian that includes this potential is invariant under $SU(2)_L \otimes U(1)_Y$ transformations. The existence of minima is guaranteed by taking $\lambda > 0$. The usual choice $\mu^2 > 0$ gives a mass term for Φ and implies a trivial minimum of the

potential at $\Phi = 0$. If one chooses $\mu^2 < 0$ on the other hand, the minimum obeys the condition:

$$\langle 0 \left| \Phi \right| 0 \rangle = \begin{pmatrix} 0 \\ \frac{v}{\sqrt{2}} \end{pmatrix} , \text{ with } v \equiv \sqrt{-\frac{\mu^2}{2\lambda}} > 0 , \tag{5.17}$$

where the ground state of ϕ^+ was chosen to be zero for the electric charge to be conserved.

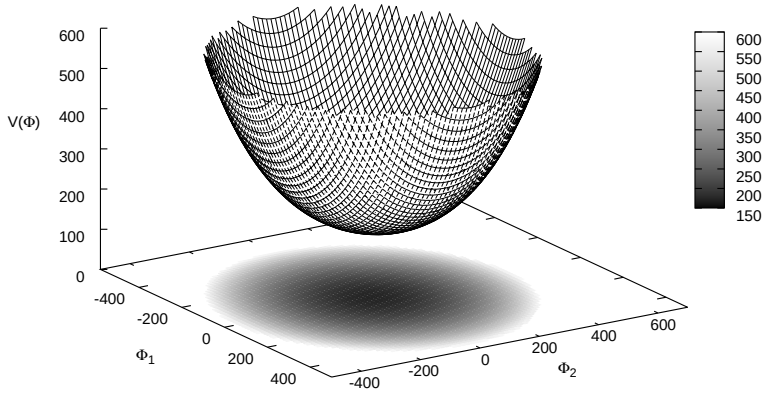

(a) $\mu^2 > 0$.

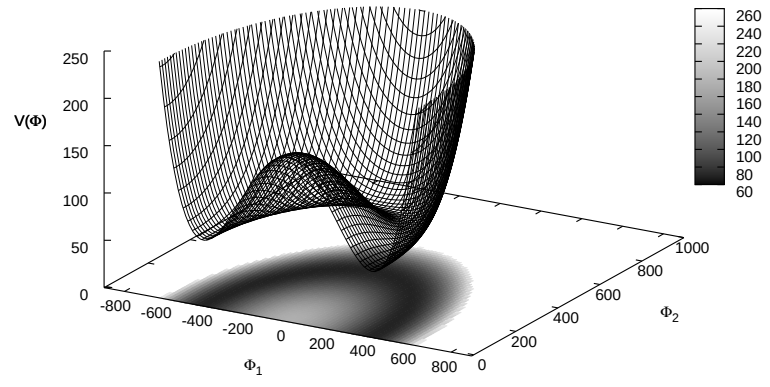

(b) $\mu^2 < 0$.

Figure 5.1: Illustration of the Higgs potential for a scalar field $\Phi = \phi_1 + i\phi_2$ with $\mu^2 > 0$ and $\mu^2 < 0$.

Although the Lagrangian remains invariant under $SU(2) \otimes U(1)$, the choice of a particular value for the ground state breaks the symmetry. This is illustrated in fig. 5.1: the potential on fig. 5.1b is symmetric under rotations, but any minimum chosen is not. One now has to develop the theory around a point of minimum, so that the scalar doublet can be written in terms of real fields as following:

$$\Phi(x) = \frac{1}{\sqrt{2}} e^{i\frac{\sigma_a}{2}\theta_a(x)} \begin{pmatrix} 0 \\ v + H(x) \end{pmatrix} . \tag{5.18}$$

The local $SU(2)$ invariance of the Lagrangian allows any choice of the fields $\theta_i(x)$. In particular, taking $\theta_i = 0$ in the so-called unitary gauge, the kinetic term of the scalar field, using the covariant derivative from equation 5.10, becomes:

$$(D_\mu \Phi)^\dagger D^\mu \Phi \to \frac{1}{2} (\partial_\mu H) (\partial^\mu H) + (v + H)^2 \left[\frac{g^2}{4} W_\mu^\dagger W^\mu + \frac{g^2}{8 \cos^2 \theta_W} Z_\mu Z^\mu \right] . \tag{5.19}$$

We have obtained a kinetic term for a scalar field, interactions between the scalar and the gauge bosons and mass terms for the gauge bosons given by:

$$M_W = M_Z \cos \theta_W = \frac{1}{2} g v . \tag{5.20}$$

Out of the four degrees of freedom introduced by the scalar doublet, three were absorbed by the longitudinal components of $W^\pm$ and the Z, and the remaining one is the Higgs particle, with a mass $M_H = \sqrt{-2\mu^2} = \sqrt{2\lambda} v$. All that came from the spontaneous symmetry breaking and the field redefinition in the unitary gauge.

Moreover, mass terms for the fermions (f) that would violate the gauge symmetry are now allowed by the scalar doublet and its charge conjugate. In the unitary gauge they take the form:

$$\mathscr{L}_Y = -\frac{1}{2} (v + H) \lambda_f \bar{f} f . \tag{5.21}$$

The couplings between fermions and the Higgs boson λ_f are arbitrary. They are related to the fermion masses via $m_f = \lambda_f \frac{v}{\sqrt{2}}$ which are free parameters of the theory.

5.3 The Standard Model

Combining the electroweak theory with the Higgs mechanism and QCD, one obtains a model that describes strong and electroweak interactions. The gauge symmetry group behind it is $SU(3)_C \otimes SU(2)_L \otimes U(1)_Y$. The first one is associated with the color charges of quarks and gluons while the other two are related to weak left-handed isospin and hypercharge. The electroweak symmetry is spontaneously broken into the electromagnetic $U(1)_Q$ with the introduction of the scalar field. These are the ingredients of the Standard Model.

The result is the existence of four intermediate vector bosons mediating the electroweak interactions: the photon (γ), $W^{\pm}$ and Z. After symmetry breaking, the photon remains massless while the others acquire masses which are predicted by the theory given some experimental input (e.g. the vacuum expectation value of the scalar field v and the electroweak couplings as in eq. 5.20). Their experimental values are listed in table 5.1. The gauge sector is completed by 8 gluons (g), mediators of the strong interactions. The scalar sector is represented by the Higgs boson. The Higgs potential and self-interactions are governed by the quadratic and quartic coefficients associated to λ (or μ).

Table 5.1: Properties of the vector bosons of the Standard Model. The experimental values for the masses of the W and Z bosons were extracted from ref. [38].

Boson	Mass (GeV)	Electric charge	Associated interaction
γ	0	0	electromagnetic
Z	91.1875 ± 0.0021	0	weak
$W^{\pm}$	80.399 ± 0.023	± 1	
g	0	0	strong

The Yukawa sector complements the model, with quarks and leptons acquiring masses through the same mechanism as the gauge fields. This time the masses are free parameters, and their values are listed in table 5.2.

Actually, the quark mass eigenstates do not correspond to the eigenstates of the weak interaction. The quark doublets depicted in the previous section are in fact mixtures of the mass eigenstates through a 3×3 unitary matrix named after Cabbibo, Kobayashi and Maskawa (CKM). This mechanism introduces three mixing angles between the quark flavours and a phase that allows for the violation of charge conjugation and parity (CP). Reference [35] gives a full description of this effect.

Table 5.2: Properties of the quarks and leptons of the Standard Model. Only upper limits are given for the masses of the neutrinos, although there is strong experimental evidence that they are massive [26].

Quark		Mass	Electric charge
up	(u)	1.1 to 3.3 MeV	+2/3
down	(d)	3.5 to 6.0 MeV	-1/3
charm	(c)	$1.27\,^{+0.07}_{-0.11}$ GeV	+2/3
strange	(s)	$105\,^{+25}_{-35}$ MeV	-1/3
top	(t)	$171.3 \pm 1.1 \pm 1.2$ GeV	+2/3
bottom	(b)	$4.20\,^{+0.17}_{-0.07}$ GeV	-1/3

Lepton		Mass	Electric charge
electron	(e)	0.511 MeV	-1
e-neutrino	(ν_e)	< 2 eV	0
muon	(μ)	105.7 MeV	-1
μ-neutrino	(ν_μ)	< 0.19 eV	0
tau	(τ)	1777 MeV	-1
τ-neutrino	(ν_τ)	< 18.2 eV	0

Putting all together, one finds that the SM has 18 free parameters: 9 fermion masses, 4 CKM parameters, 3 couplings and 2 parameters for the scalar sector. It is more convenient to translate the last five of them into quantities precisely measured experimentally. The QCD coupling was well determined from Z decays in e^+e^- collisions, and thus it is typically expressed at the Z mass: $\alpha_s(M_Z)$. The other ones can be replaced by the fine structure constant α, measured for instance from the quantum Hall effect [26], the Fermi coupling constant G_F that governs the muon decay, the mass of the Z boson M_Z determined at LEP and SLD, and the Higgs mass M_H which is the only unknown.

Essentially any physical observable can be calculated using this set of parameters. Uncertainties below the percent level can be achieved including loop corrections, given that the Standard Model is renormalizable at all orders in perturbation theory. The result of a calculation is a clear prediction of the model, and extensive tests were performed with many observables. They include the measurement of the W mass and total width, the total and partial widths of the Z boson, asymmetries in its decays from e^+e^- collisions and others (see refs. [37–40] for detailed reviews). No serious discrepancies were observed at the per mille level, and the conclusion is that the SM describes the data up to the highest energies achieved experimentally.

The Higgs particle remains the missing piece and its mass the only unknown parameter of the model. Next section discusses the constraints on the Higgs mass both from the theoretical point of view and from the experimental side, reviewing the limits set by LEP and the Tevatron.

5.4 Constraints on the Higgs boson mass

Theoretical constraints

Extending the validity of the Standard Model beyond the energies for which it has been tested imposes some limits on the Higgs mass. The first example is the $W^+W^- \to W^+W^-$ scattering, which involves the quartic gauge coupling and exchanges of Z, γ and eventually the Higgs. If the Higgs is too heavy or does not exist, the yield of this process at high energies grows proportionally to s, the square of the center of mass energy. Unitarity is violated unless some new physics appears at the scale of around 1 TeV, or if the Higgs is lighter than approximately 800 GeV.

A stronger upper limit is given by the triviality bound. Assuming that the scalar sector of the SM is a ϕ^4 theory, it remains valid as long as the Higgs quartic coupling is finite. As this coupling is expected to increase with energy, a cut-off Λ must be set, after which some new physics takes over. If the SM is restricted to the electroweak scale (10^3 GeV), the Higgs could have masses up to 1 TeV. On the other hand, if its validity extends up to 10^{16} GeV, masses above $M_H = 200$ GeV are not allowed.

Finally, a lower limit is set by the vacuum stability bound. If again one considers the Higgs self-couplings but this time with a low mass Higgs, loops with fermions and gauge bosons must be included. The most important one involves the top quark and contributes with a negative sign. If M_H is too low, the sign of quartic term in the scalar potential is flipped and there is no minima anymore. As the theory cannot be developed from an unstable vacuum, M_H is required to lie above a certain value depending on the cut-off Λ. For the same scales mentioned above:

$$\begin{aligned} \Lambda \sim 10^3 \text{ GeV} &\Rightarrow M_H \gtrsim 70 \text{ GeV}\,, \\ \Lambda \sim 10^{16} \text{ GeV} &\Rightarrow M_H \gtrsim 130 \text{ GeV}\,. \end{aligned} \tag{5.22}$$

Combining all these effects, the theoretical limits on the Higgs mass are represented in fig. 5.2.

Direct searches

The most stringent limit comes from direct searches of Higgs boson at LEP [41]. Operating near the Z mass, the initial phase of the collider excluded the mass range below 65.2 GeV. The upgraded LEP2 increased the center of mass energy up to 209 GeV, looking for the Higgs produced from off-shell Z boson decays. The

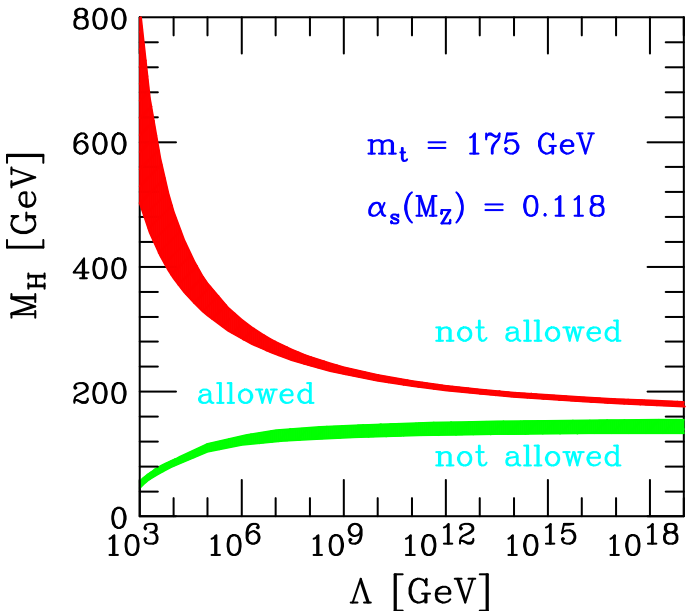

Figure 5.2: Theoretical limits on the Higgs boson mass from the triviality (upper bound) and vacuum stability arguments (lower bound), as a function of the cut-off Λ. Extracted from ref. [37].

process $e^+e^- \to Z^* \to HZ$ is illustrated in fig. 5.3.

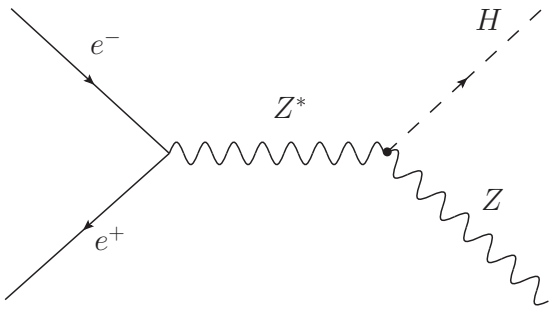

Figure 5.3: Feynman diagram of the dominant production mechanism of the Higgs boson at LEP2.

An excess of events close to $M_H = 116$ GeV created great expectations close to the end of LEP operations, but was not enough to claim a discovery. The final analyses reduced the significance of this signal from 2.9σ to 1.7σ. The exclusion limit for $M_H < 114.4$ GeV was set at 95% confidence level (CL), compared with the expected limit at 115.3 GeV, as shown in fig. 5.4.

Higgs searches have also been conducted at the Tevatron. Essentially two regions are distinguished for the searches, according to the dominant decay modes. The decay modes of the Higgs boson and its production in hadron colliders will be discussed in section 5.5. In the low mass region ($M_H < 130$ GeV), the Higgs decays

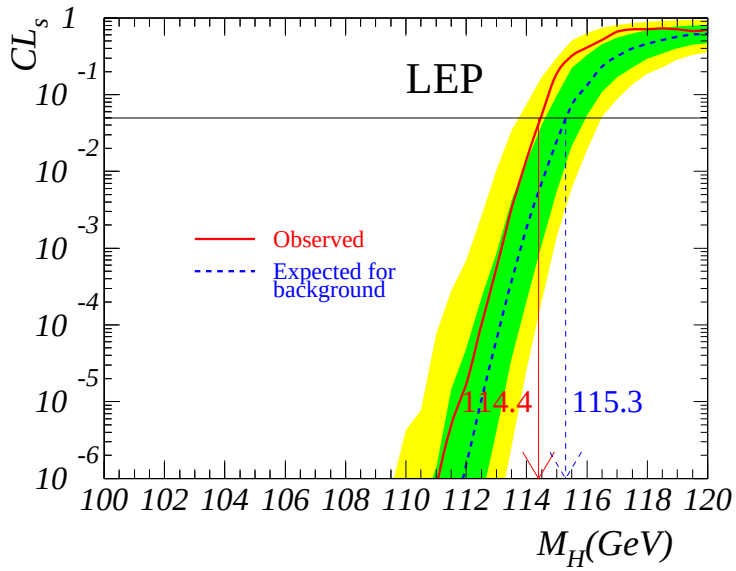

Figure 5.4: Confidence level of signal plus background hypothesis on the Standard Model Higgs boson searches at LEP. Masses below 114.4 GeV, defined by the intersection of the horizontal line at $CL_s = 0.05$ with the observed curve are excluded at 95% CL. Extracted from ref. [41].

mainly to $b\bar{b}$. Associated production with vector bosons, similar to the one used at LEP, is required to fight the overwhelming QCD backgrounds. In the high masses ($M_H > 130$ GeV), the decay to a pair of W bosons takes over and all the production channels can be explored.

Recently, the Tevatron started to reach the sensitivity for exclusion close to $M_H \approx 2M_W$. The region between 162 and 166 GeV was excluded at 95% CL [42] in March 2010. With improved analyses and more statistics, the result was updated in July 2010 [43] and the exclusion was extended to the regions between 100 and 109 GeV, and between 158 and 175 GeV, as shown in fig. 5.5. Some authors, however, argue that these limits should be revised, as the uncertainties involved in the signal cross section are larger than the ones used in these results [44].

Indirect limits from electroweak precision data

Electroweak precision data offer a very powerful check of the internal consistency of the SM. Given its remarkable accuracy, the data is sensitive to energy scales beyond the ones achieved experimentally, as high mass particles contribute to the observables via quantum loop corrections. The Higgs boson, for instance, enters in the one-loop corrections to the W mass, illustrated in fig. 5.6. Although the Higgs contribution is logarithmic and much smaller than the component associated to the

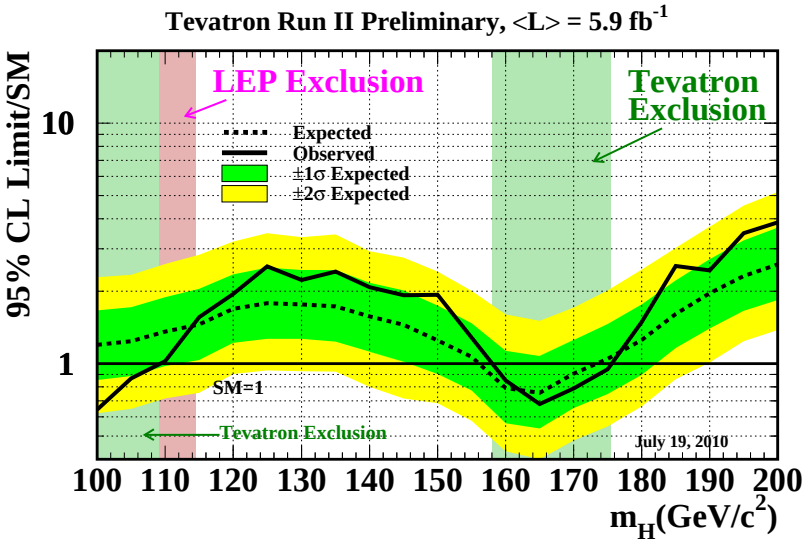

Figure 5.5: Observed and expected 95% CL upper limits on SM Higgs boson production at the Tevatron. Masses between 100 and 109 GeV, and between 158 and 175 GeV, for which the observed curve lies below 1, are excluded at 95% CL. Extracted from ref. [43].

top quark, the data is precise enough to constraint this parameter.

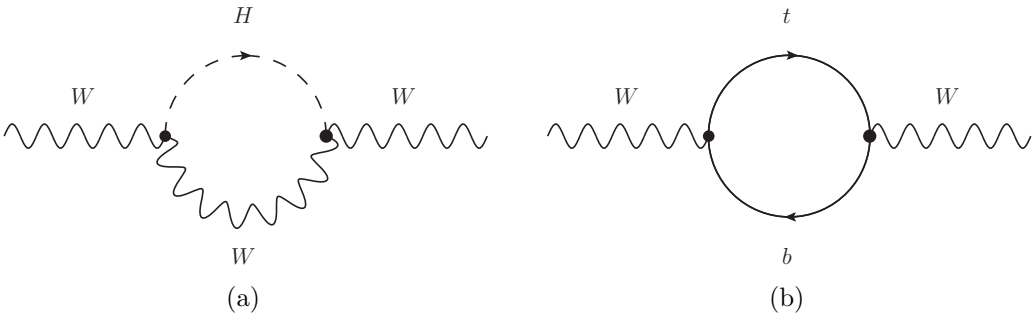

Figure 5.6: One-loop diagrams for the contributions to the W mass involving (a) the Higgs boson and (b) the top quark.

Stringent limits are set from a global fit using all the observables, historically by the LEP Electroweak Working Group [38] and more recently using the GFitter toolkit [40, 45]. Both groups produce results either ignoring or including the direct searches at LEP and the Tevatron. The values for GFitter are the following [45], using the Tevatron results from July 2010:

$$\text{Electroweak precision data only:} \qquad M_H = 84.2^{+30.3\,[+75.0]}_{-23.3\,[-41.9]}\ \text{GeV}\,,$$

$$\text{Including direct searches:} \qquad M_H = 120.6^{+17.0\,[+34.3]}_{-5.2\,[-6.2]}\ \text{GeV}\,,$$

where the errors are quoted at 1σ $[2\sigma]$ level. The results are illustrated in fig. 5.7, and are very similar to the ones obtained by LEP group. The data clearly favours a low mass Higgs boson, with $M_H < 151.5$ GeV at 95% CL (156.0 GeV at 99% CL) [43].

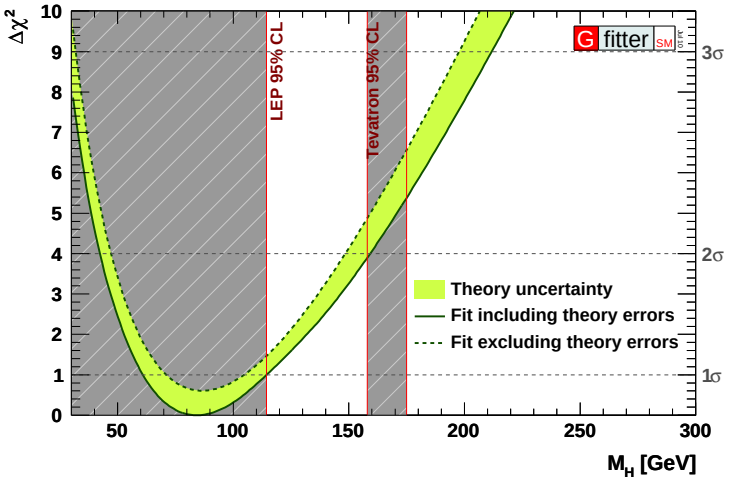

(a) Electroweak precision data only.

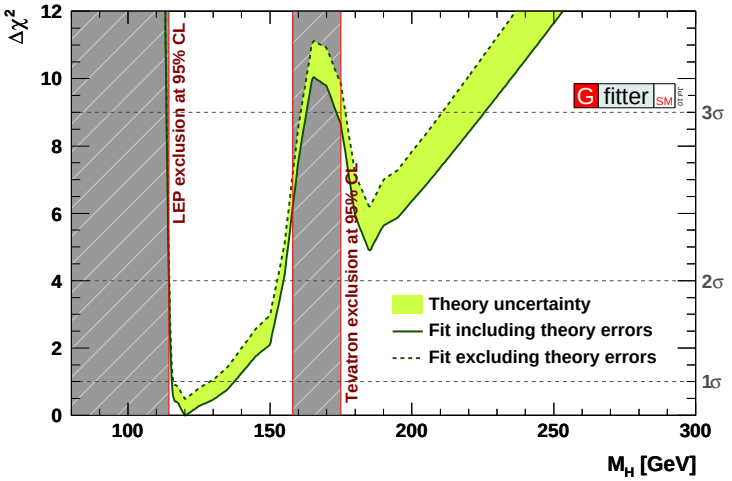

(b) Including direct searches.

Figure 5.7: $\Delta\chi^2$ of a global fit with electroweak precision data as a function of the Higgs mass, without and with the inclusion of direct searches. Extracted from ref. [40].

5.5 Higgs decay modes and production in hadron colliders

5.5.1 Decay modes and total width

Strong limits on the Higgs boson mass were set by theoretical arguments, direct searches at LEP and the Tevatron, and electroweak precision data. Nonetheless, M_H remains the only unknown parameter of the SM. All the Higgs boson properties are completely determined once this value is fixed.

In particular, the decay modes to fermions, gauge bosons and decays involving virtual loops are known to next-to-leading order (NLO) or better. At tree level, the Higgs couplings are proportional to the mass of the particles (m_f/v for fermions and M_V^2/v for $V = W, Z$) and thus it tends to go to the heaviest particles kinematically accessible. Figure 5.8a shows the branching fractions as a function of M_H.

In the "low mass" region ($M_H \lesssim 130$ GeV), $H \to b\bar{b}$ is the dominant mode, with branching ratios (BR) around 50% – 75%, followed by $H \to \tau^+\tau^-$ with BR $\approx 5\%$ to 7%. Decays to massless particles – gluons and photons – proceed through a loop of heavy fermions and/or gauge bosons with the major contribution coming from the top quark in the gluon channel and the W boson in case of photons.

For $130 \lesssim M_H \lesssim 180$, decays to a pair of gauge bosons take over, usually with one of the Ws or Zs still off-shell (noted by the '$*$' superscript). The branching ratios are better determined by including contributions from 4-body decays (both $V^* \to ff$), as shown in fig. 5.9. Close to $M_H = 130$ GeV, $H \to WW^*$ becomes the dominant mode and is almost exclusive when it turns on-shell, for $2M_W < M_H < 2M_Z$. Meanwhile, $H \to ZZ^*$ remains suppressed by the virtual Z and has its relative importance reduced.

The "high mass" range ($180 \lesssim M_H \lesssim 1000$ GeV) is completely dominated by vector bosons, with $H \to WW$ entering with BR $\sim 2/3$ and $H \to ZZ$ with BR $\sim 1/3$. While the latter involves two identical particles (ZZ), the former includes two different ones ($W^\pm W^\mp$), which justifies the factor of 2 between them. Decays to a pair of top quarks open around $M_H \gtrsim 350$ GeV and contribute at most with 20%. While the partial width of this process grows with M_H, the vector boson one is proportional to M_H^3.

The total width (Γ_H), shown in fig. 5.8b, is also a reflex of the previous statement. The Higgs is very narrow at low masses, with $\Gamma_H < 10$ MeV at $M_H = 130$ GeV. With the increase of the vector boson decay yields, the width rises quickly to near 1 GeV at $M_H = 180$ GeV and becomes comparable to the Higgs mass for a heavy

scalar ($M_H \gtrsim 500$ GeV), although such masses are highly disfavoured by electroweak precision data.

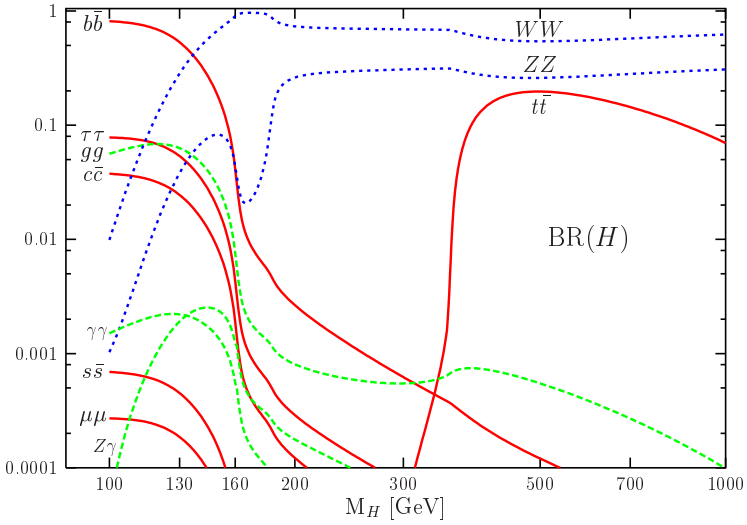

(a)

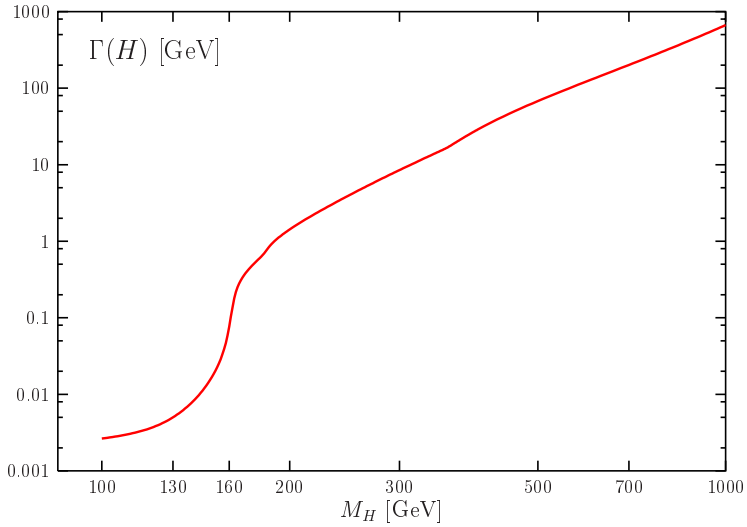

(b)

Figure 5.8: (a) Branching ratios and (b) total width of the SM Higgs boson as a function of its mass. Extracted from ref. [46].

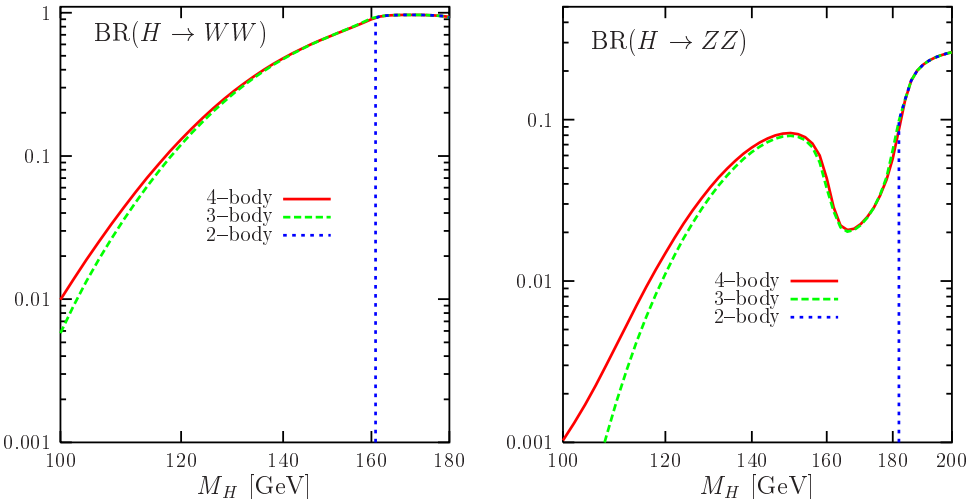

Figure 5.9: Contributions of the 2, 3 and 4-body decays to the $H \to WW$ and $H \to ZZ$ branching ratio. Extracted from ref. [37].

5.5.2 Production in hadron colliders

Both at the Tevatron and LHC, the Higgs is produced through four main channels, depicted in fig. 5.10 and discussed below.

- **Gluon fusion** (also called gluon-gluon fusion) is the dominant one, mediated by a top quark loop and a b-quark loop to a lesser extent. This process receives huge contributions from higher order QCD corrections, with NLO increasing the total cross section by $\sim 70\%$ ($\sim$100%) at $\sqrt{s} = 14$ TeV (1.96 TeV) [47] and NNLO giving extra 30% (50%), while electroweak (EW) corrections are at the percent level [48]. The uncertainties on the total values are not a consensus among the theorists, varying from 10% to 40% depending on the prescription used for their calculation.

- **Vector boson fusion** (VBF) is the sub-leading mode at the LHC, with the Higgs produced in association with two quarks. The quarks are expected to give rise to very energetic jets located in the forward regions, with a big rapidity gap between them. This is a powerful weapon against QCD backgrounds and will be explored in some final states. Higher order effects (QCD + EW) have a modest contribution, increasing the cross section by approximately 5 - 10% [49].

- **Associated production with W or Z bosons** is the same process used at LEP, this time initiated by $q\bar{q}$. The decays of the vector bosons to leptons (including neutrinos) provide good trigger and help reducing QCD backgrounds.

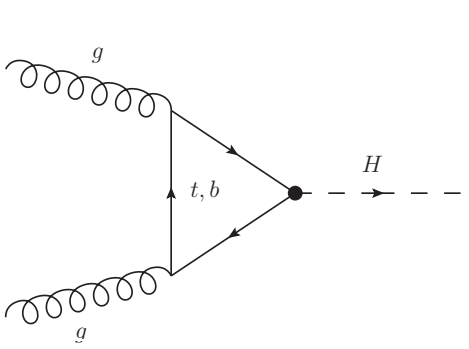

(a) Gluon fusion.

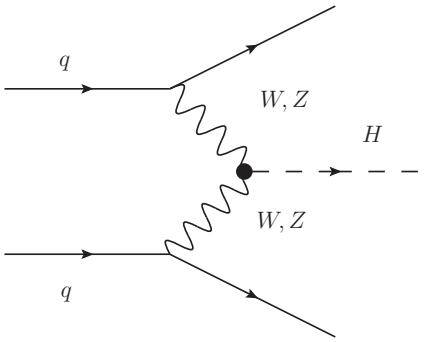

(b) Vector boson fusion.

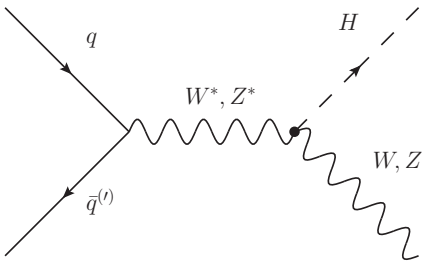

(c) Associated production with W or Z bosons.

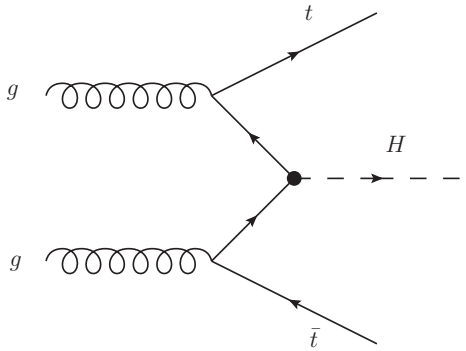

(d) Associated production with top quarks.

Figure 5.10: Main production modes of the Higgs boson at hadron colliders.

It is the second most important production channel at the Tevatron and used to be the most sensitive search mode. Recently it became more attractive at the LHC with the revival of $H \to b\bar{b}$ that will be discussed in the next section. The K-factors[2] (QCD + EW) vary around 30% with uncertainties at the percent level [49].

- **Associated production with top quarks** can be initiated by a pair of gluons or quarks, the Higgs being radiated from a quark line in the latter case. The low yields restrict the interest of this mode to decays that cannot be accessed otherwise, as used to be the case of $H \to b\bar{b}$. This matter will be discussed shortly.

The cross section of of each component as a function of the Higgs mass is shown in fig. 5.11 for $\sqrt{s} = 14$ TeV. Their relative contribution is not the same in both accelerators due to the increase of gluon-gluon cross section with the center of mass

[2]The K-factor is the ratio between higher and lowest order cross sections. e.g. σ_{NLO}/σ_{LO}.

energy, and the presence of valence anti-quarks in $p\bar{p}$ collisions. The subject of the production cross sections is currently being addressed at the LHC Higgs Cross Section Working Group, with a kick-off meeting held in April 2010. This group shall provide the guidelines that will be used in Higgs searches at ATLAS and CMS, discussed in the next section.

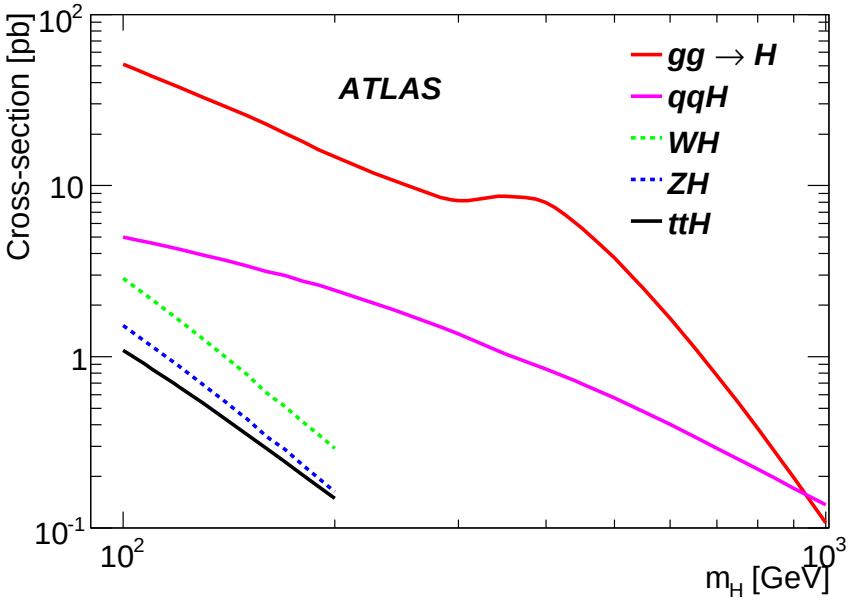

Figure 5.11: Next-to-leading order cross sections for the dominant modes of the production of a SM Higgs at $\sqrt{s} = 14$ TeV, as a function of its mass. Extracted from ref. [50].

5.6 Higgs searches at the LHC

With more than 7.5 fb^{-1} recorded by each experiment (CDF and D0) by May 2010, mature analyses and possibilities for improving the sensitivity, the Tevatron is able to increase the exclusion regions and eventually find evidence at 3σ level for a SM Higgs in the coming years.

The definite answer, however, should be given by the LHC, which can achieve similar results with less data, due to the higher center of mass energy. ATLAS and CMS were designed to either exclude or discover the Higgs at 5σ level with a few tens of fb^{-1} in the whole mass range. The reach of the first LHC run at a center of mass energy of 7 TeV and 1 fb^{-1} is probably restricted to an increase of the LEP and Tevatron exclusion windows. The LHC can probe masses beyond the present limit given by the Tevatron and eventually find hints of the Higgs existence. Some

results will be presented in the end of the section.

The upgraded accelerator running at $\sqrt{s} \approx 14$ TeV is needed for discovery. This section reviews the expected sensitivity of the SM Higgs at the LHC, briefly discussing the analyses considered by ATLAS at $\sqrt{s} = 14$ TeV. Details can be found in ref. [50], while CMS results are reported in ref. [51].

Ideally one would like to use all the combinations between initial and final states on Higgs searches. The overwhelming backgrounds from QCD processes and the low yields for Higgs production restrict the analysis channels to only a few. Efficient trigger require either the presence of leptons or photons, or at least large missing transverse energy and high-P_T jets. Distinctive signatures are also needed in the offline analyses. The most important ones are gauge bosons decaying to leptons, but forward jets and b-quarks can be of great help.

The most interesting decay modes ($H \to b\bar{b}$, $\gamma\gamma$, $\tau^+\tau^-$, WW and ZZ) are briefly discussed in the following. A summary of the accessible production modes, the mass range covered and expected significance of each of them is given in table 5.3. Other decays, involving a pair of gluons or c-quarks are completely swamped by the hadronic activity and cannot be assessed. $H \to t\bar{t}$ and $H \to \mu^+\mu^-$ have low yields, and would need huge luminosities to be distinguished from the $t\bar{t}$ and $\mu^+\mu^-$ continuum backgrounds.

- $H \to b\bar{b}$ has the highest branching ratio at low masses[3]. On the other hand it suffers from huge QCD backgrounds, many orders of magnitude above the signal. The situation of this final state changed considerably in the last few years. Absence of an efficient trigger already excluded both gluon fusion and VBF, leaving the associated production with vector bosons or top quark pairs as the only possibilities. The first one was considered impractical for discoveries before the work on jet substructure associated with a boosted Higgs, described in ref. [52]. Combining leptonic decays of vector bosons ($W \to \ell\nu$, $Z \to \ell\ell$ and $Z \to \nu\nu$, with $\ell = e, \mu$) these techniques now provide expected significances close to 4σ for $\mathscr{L} = 30$ fb^{-1} at $M_H = 120$ GeV [53]. At the same time, $t\bar{t}H$ disappeared from the list of sensitive channels. A complex final state and difficulties with combinatorial backgrounds, given the large number of jets, greatly jeopardize this analysis. Recent developments have also improved the situation. Work on the VBF associated with a photon also seems promising, but higher integrated luminosities are required. All the analyses rely on the identification of b-quarks (b-tagging), which is expected to reject light jets up to factors of 100 for 50% efficiency.

[3]Following section 5.5, low Higgs masses refer to $M_H < 130$ GeV unless stated otherwise.

- $H \to \gamma\gamma$, despite its very low branching ratios of $\mathcal{O}(10^{-3})$, is one of the most important channels in the low mass range. It has a very distinctive signature with two isolated very energetic photons forming a narrow invariant mass peak. The associated resolution on the Higgs mass is around $1-2$ GeV. Jet rejection factors above 10^3 on photon identification greatly reduce the di-jet and γ+jet backgrounds. QCD production of two photons is nearly irreducible. All production modes can be explored, with higher signal over background for associated production modes and higher yields on gluon fusion. A relatively large number of events is expected after selection cuts: 25 for the signal (at $M_H = 120$ GeV) and almost 1000 for the background within the signal mass window per fb^{-1}. This provides a robust method for extracting the signal significance from the data using fits on the side-bands[4].

- $H \to \tau^+\tau^-$ has the second highest branching fraction at low masses. The final states depend on the tau decays: 42% of the time both taus decay hadronically, in 46% of the cases one goes to hadrons and the other one to an electron or a muon, and the remaining 12% are fully leptonic modes. The fully hadronic channels are very challenging and require data-driven methods to study the QCD multijet background, while semi-leptonic and leptonic ones can more easily lead to a discovery at LHC using the vector boson fusion production mode. The tau products in the central region and tagging jets from VBF in the forward part of the detector are a rare topology for QCD events. A central jet veto is explored, although it might be very sensitive to multiple interactions within the same LHC bunch crossing (pile-up). Gluon fusion and W/Z associated analyses, on the other hand, do not seem feasible at ATLAS nor CMS while CDF and D0 have recently shown some results for these modes [54, 55].

  Neutrinos in the final state prevent the full reconstruction of the event and the Higgs mass is calculated using the collinear approximation[5]. Resolutions around 30% on M_H are obtained [56]. The main background after the selection cuts is $Z \to \tau\tau$, with an invariant mass peak close to the signal for $M_H \lesssim 130$ GeV.

- $H \to WW$ with both $W \to \ell\nu$ has the highest potential from $M_H = 2M_Z$ down to 130 GeV, both at the Tevatron and at the LHC. This is a direct

[4]Side-bands are regions were no signal contribution is expected. From the fits one can quantify the amount of background in the signal region.

[5]The collinear approximation assumes that the visible decay products of the tau follow the same direction of the latter. Details about the method are given in ref. [56].

consequence of the large branching ratios and rather clean signature. The presence of two high-P_T isolated leptons and large missing transverse energy provides efficient trigger and great reduction against QCD processes. The dominant backgrounds are WW and $t\bar{t}$ with real leptons and neutrinos in the final state. They can be distinguished from the signal using the jet activity and the angle between the leptons. For the signal, the charged leptons tend to go together given the scalar nature of the Higgs and the chirality of the neutrinos.

Initially, only the $e^{\pm}\mu^{\mp}$ channels were considered [10]. But the angular correlation and requirements on missing transverse energy or momentum offer ways to reduce the $Z \to \ell\ell$ background in the analyses with the leptons of the same flavour [57]. All the production modes can be explored, but an exclusive VBF analysis can further improve the signal over background ratios. In this mode, with the Higgs associated with two jets, final states with one W decaying to hadrons were also studied but suffer from the uncertainties on the background yields.

Back to the leptonic decays, no narrow invariant mass peak can be reconstructed. The signal significance is extracted either through likelihood ratios using the discriminant variables or via simple event counting. This mode alone has exclusion potential already in the first LHC run.

- $H \to ZZ$ can cover a wide mass range, and offers possibilities with the Zs decaying to charged leptons, neutrinos or b-quarks. Above $M_H = 2M_Z$, final states involving only electrons and muons are the 'gold-plated' modes, leading to a narrow peak on top a relatively smooth background. Their reach can go down to 120 GeV, except in the region close to $2 \times M_W$, where the Higgs decays almost exclusively to W bosons. $H \to 4\ell$ analyses will be discussed in detail in chapter 6. For higher masses (above roughly 200 GeV) $H \to ZZ \to \ell\ell\nu\nu$, $H \to ZZ \to \ell\ell b\bar{b}$ and to a lesser extent $H \to ZZ \to \ell\ell\tau\tau$ can increase the yields of $H \to 4\ell$ searches and help in exclusion or discovery.

Clearly one would like to combine the information from the various independent channels, on one hand to increase the overall sensitivity and on the other hand to provide a single measurement of the signal significance. A detailed statistical treatment for the combination of the most relevant ones in ATLAS ($H \to \gamma\gamma$, $H \to \tau^+\tau^-$, $H \to WW \to e\nu\mu\nu$ and $H \to ZZ^* \to 4\ell$) was studied and is described in ref. [50]. It follows a frequentist approach that includes systematic uncertainties by use of the *profile likelihood ratio*, outlined in appendix B.

Table 5.3: Accessible production modes, mass ranges and expected significance at $\sqrt{s} = 14$ TeV and $\mathscr{L} = 30$ fb^{-1} in ATLAS for the main Higgs boson decay modes.

Decay mode	**Accessible production modes**	**Mass range covered**	**Expected significance at $\mathscr{L} = 30$ fb^{-1}**
$H \to b\bar{b}$	Boosted W / $Z + H$	~ 120 GeV	3.7σ
$H \to \gamma\gamma$	All	$\lesssim 140$ GeV	$\sim 4 - 5\sigma$
$H \to \tau^+\tau^-$	VBF	$\lesssim 140$ GeV	5σ at 115 GeV, 3.2σ at 140 GeV
$H \to WW \to e\nu\mu\nu$	All	130 – 190 GeV	Above 5σ
$H \to ZZ \to 4\ell$	All	120 – 500 GeV	Above 5σ, except around 120 and 160 GeV ($3 - 4\sigma$ in these regions)

This study is only valid for integrated luminosities of at least 2 fb^{-1}. The expected significance as a function of the integrated luminosity is shown in fig. 5.12.

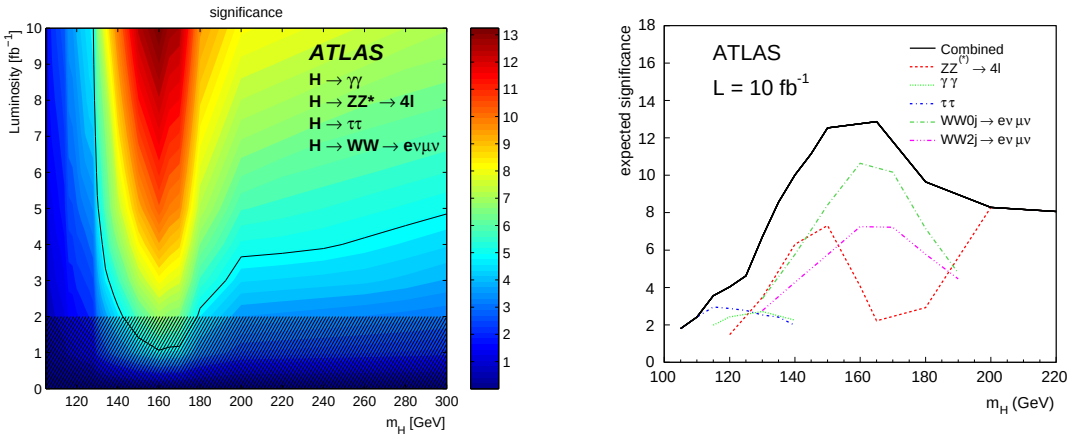

(a) Expected significance as a function of Higgs mass and integrated luminosity. The thick curve represents the 5σ discovery contour (not valid for the hatched area, where $\mathscr{L} < 2$ fb^{-1}).

(b) Expected significance of each channel and their combination (thick line) at $\mathscr{L} = 10$ fb^{-1} as a function of the Higgs mass.

Figure 5.12: Expected significance of a SM Higgs at $\sqrt{s} = 14$ TeV in the ATLAS experiment. Extracted from ref. [50].

Expected results for the first LHC run were extracted for a combination of $H \to \gamma\gamma$, $H \to WW$ and $H \to ZZ$ [58]. They assume a center of mass energy of 7 TeV and $\mathscr{L} = 1$ fb^{-1}. Simulated samples were produced expecting a run at $\sqrt{s} = 10$ TeV, and had to be extrapolated by scaling the cross sections by the ratios at the two center of mass energies, having checked that the event selection efficiencies are stable between

the two energies. The statistical method used for the combination is essentially the same employed in $\sqrt{s} = 14$ TeV analysis. The 95% CL upper bound on the Higgs production cross section are shown in fig. 5.13, normalized to the SM expectations. For masses between 135 GeV and 188 GeV, the curve is below 1, meaning that the Higgs can be excluded at 95% CL. This result is fully dominated by the $H \to WW$ searches, which cover alone the range $140 - 185$ GeV.

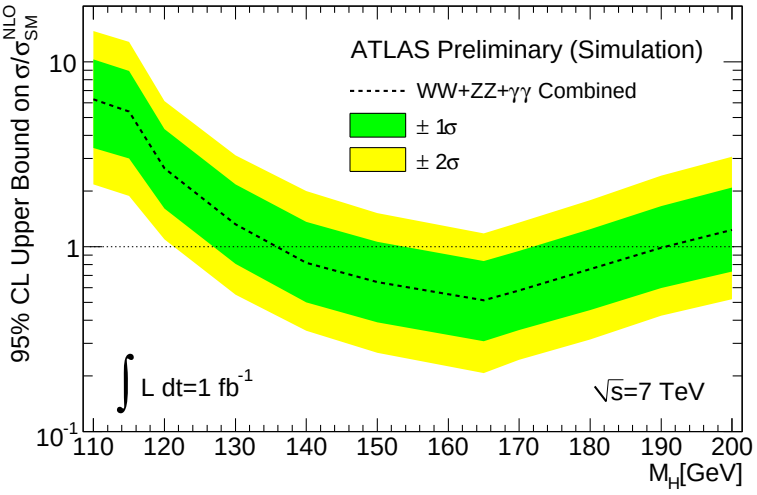

Figure 5.13: Expected upper bound on the Higgs boson production cross section normalized to the NLO Standard Model cross section, assuming 1 fb^{-1} of integrated luminosity collected in 7 TeV collisions. The green and yellow bands represent the range in which the limit is expected to fluctuate. Extracted from ref. [58].

5.7 Studying the Higgs properties

The observation of a resonance is a major goal but only the beginning of a program on Higgs physics. The next step is a confirmation that this resonance is indeed responsible for the electroweak symmetry breaking. A complete test of the Standard Model involves the measurement of the Higgs mass, width, quantum numbers (charge, spin, CP) and couplings.

The LHC experiments have the capability not only of discovering the Higgs but with high integrated luminosities may also look into some of its properties. Detailed studies were performed for the ATLAS Technical Design Report [59] based on $\mathscr{L} = 300$ fb^{-1}. Compared to the current expectations the significances were quite optimistic for many channels. The luminosities also look far in the future, and thus only a general picture is briefly given in this section.

The Higgs mass can be determined rather precisely from di-photons or four lepton final states. Relative errors below 1% are achievable up to 400 GeV for luminosities of a few tens of fb^{-1} [10, 51]. The increase of the natural width limits the precision on M_H for higher masses. The width itself can only be measured in this region, where it becomes comparable to the detector resolution. This time, $H \to ZZ \to 4\ell$ is the only relevant mode.

Determination of the spin and the CP quantum number is very challenging at the LHC. The observation of $H \to \gamma\gamma$ would exclude a spin-1 resonance. Some hints are given by the angular distribution of the tagging jets in vector boson fusion, independently of the Higgs decay channel [60]. While the SM predicts a flat $\Delta\phi$ distribution, additional couplings between the Higgs and the gauge bosons produce a sinusoidal shape where the position of the maxima is determined by the Higgs CP numbers. Otherwise, $H \to 4\ell$ again is useful via the virtuality of one Z (the Z^* mass distribution is sensitive to the spin) and the angle between the planes defined by the Z products, which can distinguish a scalar from a pseudoscalar.

The couplings and decay rates can be assessed primarily through ratios of cross section times branching fractions between pairs of channels. Decay modes involving vector bosons are the most promising ones, with precisions from 15% to 60% expected for $\mathscr{L} = 30$ fb^{-1} [61]. Measuring the couplings to fermions depends on high luminosities and the feasibility of separating the $H \to b\bar{b}$ and $H \to \tau^+\tau^-$ signals from the QCD backgrounds.

Finally, the Higgs self-couplings must be determined to characterize the scalar potential. They intervene in double or triple Higgs production, but unfortunately the cross sections at the LHC are quite low, three to four orders of magnitude below $gg \to H$.

5.8 Beyond the Standard Model

All the discussions up to now were done in the context of the Standard Model, usually assuming the existence of a single Higgs boson. Even if the SM is very successful in explaining basically all the data in particle physics experiments, it has some clear limitations. Going beyond particle experiments, the SM does not include gravity, has no candidate for dark matter – which should be four times more abundant than the ordinary one – and does not explain the baryon asymmetry in the universe.

From the theoretical point of view, the number of free parameters – 18 – is considered excessive and from the mass of the electron ($\sim$0.5 MeV) to the top-

quark mass (~ 173 GeV) there are more than five orders of magnitude. Including the neutrinos, which should be massless in the SM, the mass range goes to down to milli-electron-volts. The model offers no explanation for these parameters nor for the fact that $\mu^2 < 0$, in order to generate the spontaneous symmetry breaking. The mechanism clearly distinguishes strong and electroweak interactions and no real unification between them exist, as the evolution of the three SM coupling constants does not lead to a common crossing point at a high energy scale.

Above all those there is the hierarchy problem that involves the Higgs boson. Unlike the other logarithmic divergences found in the SM when including higher order corrections, the Higgs mass has a quadratic one. The contributions from fermions and bosons at one-loop are represented in fig. 5.14. Introducing a cut-off Λ, above which the Standard Model is not valid any more, the physical mass M_H becomes the difference between a 'bare mass' and an expression proportional to Λ^2. If this cut-off is placed at scales where the other three interactions should be unified ($\sim 10^{16}$ GeV), one must arrange for a cancellation of more than 10 digits to obtain $M_H < 1$ TeV. This very unnatural fine-tuning is viewed as a strong motivation for the appearance of new physics effects, likely in the TeV scale.

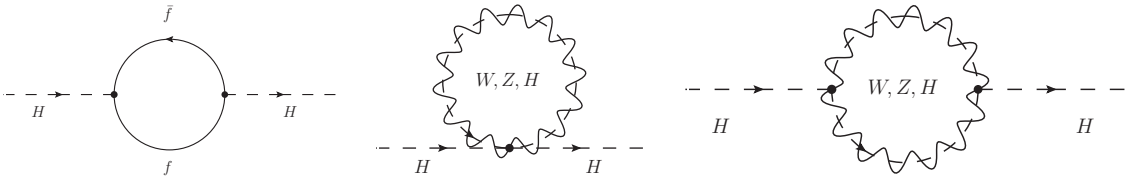

Figure 5.14: Feynman diagrams for the one-loop corrections to the Higgs boson mass.

The hierarchy problem is solved for instance in supersymmetric (SUSY) extensions of the SM. With the introduction of a bosonic (fermionic) partner for each fermion (boson), the quadratic divergences are automatically removed as the partners contribute with opposite signs. Moreover, SUSY models usually have a candidate for dark matter and provide a more natural explanation for electroweak symmetry breaking, as μ^2 is positive at a higher unification scale but becomes negative at the electroweak scale when loop corrections are considered.

The most celebrated of them is the Minimal Supersymmetric Standard Model (MSSM). In the general case, it has more than 100 free parameters, but some assumptions can reduce this number to about 10, on top of the SM ones. When it comes to the Higgs sector, the MSSM is an example of a Two Higgs Doublet Model

(2HDM), with the phenomenology defined basically by the ratio of the vacuum expectation values of the two doublets ($\tan\beta$) and one mass. These models predict three neutral Higgses and two charged ones, most of them nearly degenerate in mass. The lightest neutral can be roughly indistinguishable from the SM one, having its mass limited to about 130 GeV in the MSSM. The other two neutrals might also be within the reach of the LHC, and the observation of a charged scalar would be a clear proof of physics beyond the SM.

Detailed studies of the discovery potential of MSSM Higgses have been carried on both by ATLAS and CMS, and are described in refs. [10, 51, 62]. In summary, at least one neutral particle should be found if present and large regions of the parameter space can be covered both for charged and neutral Higgs bosons with a few tens of fb^{-1}. Most of the accessible final states involve tau leptons and b-quarks, as the couplings to vector bosons are reduced proportionally to $\tan\beta$. In this context, the interest of the $H \to 4\ell$ channel, discussed in the next chapter, is restricted. On the other hand, an observation in such final states could help excluding some models.

In many alternatives to the SM, including some MSSM scenarios, the Higgs decays mostly to particles that do not interact in the detector. To trigger on those events, associated production with top-pairs or vector bosons through Higgs-strahlung or VBF is required. The LHC also provides sensitivity to such cases beyond the LEP limits, and could exclude branching ratios (of $H \to$ invisible) below 90% for masses up to 250 GeV [63] if the Higgs couplings to W and Z bosons are similar to the SM ones.

Finally, one should consider the possibility that the Higgs does not exist. Some new dynamics must come up to explain electroweak symmetry breaking and restore unitarity in the VV scattering. Di-boson production can be the key to study its phenomenology. This time one has to exclude all the allowed mass range for a SM Higgs.

Chapter 6

Higgs searches in four lepton final states

Strong motivations exist for Higgs analyses in four lepton final states. At the same time these analyses have great impact on the discovery sensitivity and if a discovery takes place, $H \to 4\ell$ offers several possibilities to study the properties of the Higgs boson.

This chapter details the first one of the two physics analyses studied in this thesis, both related to the searches for a SM Higgs boson in four lepton final states. The present analysis was published by the ATLAS collaboration in ref. [64]: "Expected Performance of the ATLAS Experiment - Detector, Trigger and Physics".

The chapter is organized as following: characteristics of the signal and main backgrounds are discussed in section 6.1, while section 6.2 describes the simulated events used in this study. The analysis strategy is the object of sections 6.3 and 6.4; the discovery potential at $\sqrt{s} = 14$ TeV and different center of mass energies are reviewed in sections 6.5 and 6.6, respectively. Finally, the perspectives for the analyses with first LHC data are mentioned in section 6.7.

6.1 Characteristics of the signal and main backgrounds

The importance of four lepton final states on Higgs searches is partially due to the high branching ratio of $H \to ZZ$. For Higgs masses greater than 120 GeV, decays to a pair of Z bosons are above the 1% level, becoming the sub-leading process for $M_H \gtrsim 160$ GeV and contributing with roughly 1/3 of the branching fraction from 200 GeV on. The Zs then decay to charged leptons, neutrinos or quarks, the latter

ones being hardly accessible due to QCD backgrounds. While both the taus and the neutrinos induce significant amounts of missing transverse energy, events with only electrons and muons can be fully reconstructed.

From the experimental point of view, these are the cleanest signatures available. The excellent transverse energy and momentum resolutions for electrons and muons, discussed in chapter 2, provide narrow invariant mass distributions when reconstructing the Z and Higgs bosons. The Higgs signal can be identified by a peak on a 4-lepton invariant mass spectrum, sitting on top of a relatively smooth background. For $M_H \gtrsim 180$ GeV, $H \to 4\ell$ is the 'golden channel', with the Higgs decaying to two on-shell Z bosons. The main and almost only background in this region is the non-resonant production of Z boson pairs, which is nearly irreducible, possessing the same characteristics as the signal. The leading diagrams for $H \to 4\ell$ and $ZZ \to 4\ell$ are represented in figs. 6.1 and 6.2a, respectively. In both cases, each Z can decay to electrons or muons, leading to three final states: four electrons ($4e$), four muons (4μ) or two electrons and two muons ($2e2\mu$). The last one has twice the yield of each of the other two modes.

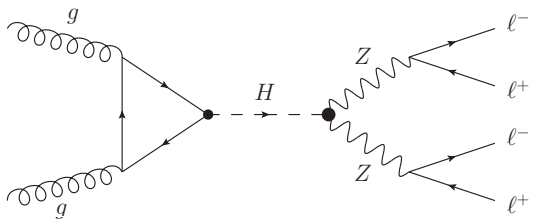

Figure 6.1: Main diagram for Higgs to four lepton production.

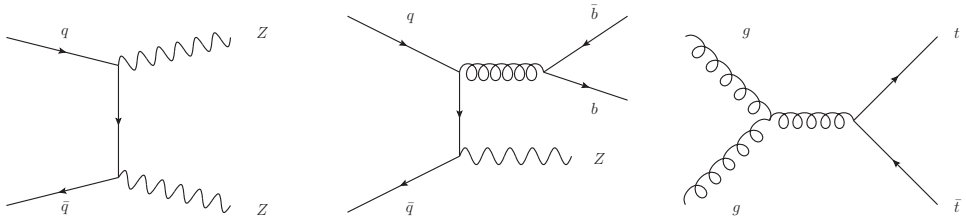

(a) ZZ (b) $Zb\bar{b}$ (c) $t\bar{t}$

Figure 6.2: Some of the diagrams for the backgrounds to $H \to 4\ell$ searches.

While the invariant mass peaks allow for the reduction of non-resonant multi-lepton production, the expected fake lepton rates below 10^{-3} for both electrons and muons limit the number of background processes to be considered. Additionally to ZZ, the most important ones are SM processes which generate four real leptons with high-P_T, such as $Zb\bar{b}$ and $t\bar{t}$, represented in figs. 6.2b and 6.2c. In both cases,

the dominant contribution is from two leptons originating from the leptonic decay of the Z or the Ws, and the other two from decays of the b-quarks. Lepton production from top quark decays is illustrated in fig. 6.3.

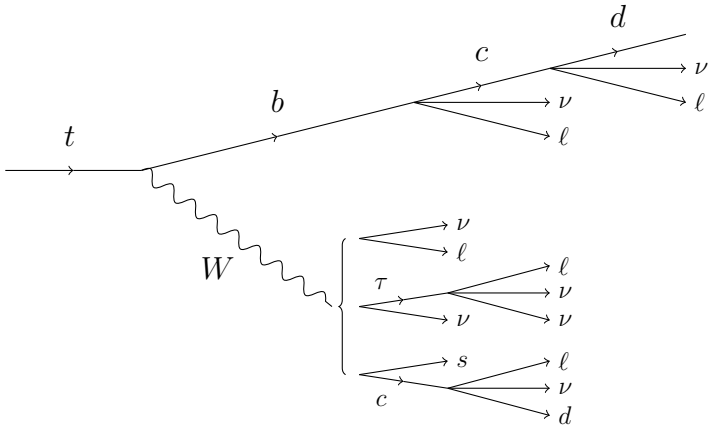

Figure 6.3: Lepton production chains from top quark decays.

Despite the low fake rates, the role of events with three leptons plus a fake one or even two fakes must be carefully evaluated as their cross section can be significantly higher than the ones with four leptons. The list of potentially dangerous processes is thus complemented by WZ and Z + jets, with the Ws and Zs decaying leptonically.

Below $M_H = 2M_Z$, one of the Zs coming from the Higgs is off-shell and decays to low momentum leptons, making the $Zb\bar{b}$ and $t\bar{t}$ backgrounds more harmful. Their yields can exceed the ones for the signal by a few orders of magnitude in this region, imposing additional selection cuts. Apart from the leptons from Ws and Zs, the dominant contribution is expected from semi-leptonic decays of heavy flavour quarks (b and c). Exploiting the hadronic activity around the leptons and the large lifetime of hadrons containing these quarks, both track and calorimetric isolation provide good discriminating power, complemented by impact parameter requirements. Rejection factors above 10 can be achieved with each discriminant, keeping the backgrounds under control. On processes that do not contain vector bosons, the rejection of the isolation cuts is much higher and thus their contribution is negligible.

The challenges related to the analysis arise mainly from two factors. On one side is the low signal cross section. The reduced branching ratio for $Z \to \ell\ell$ ($\sim 3.4\%$) and the presence of four leptons impose ultimate identification efficiencies for both muons and electrons, which can be particularly intricate at low P_T. At the same time, the background yields are known with large uncertainties and some effort will be spend in their understanding with LHC data. These matters are discussed in the next sections.

6.2 Event generation and cross sections for signal and backgrounds

To evaluate the discovery potential of the Higgs boson, a full simulation of signal and background events was performed. For a given process, an event generator was used to calculate the associated cross section and produce a list with the four momenta of the final-state particles emerging from the collisions. The response of the ATLAS detector was then simulated by `GEANT4` using a detailed model of the detector geometry and the underlying physics. The full chain was described in section 2.5.

The event generation should include all the relevant effects to reproduce the collisions: the hard process under consideration (e.g. $gg \to H \to ZZ \to 4\ell$), initial and final-state radiation and the underlying event (multi-parton interactions, etc), followed by parton showering and hadronization. This can be achieved interfacing softwares specialized in matrix-element calculations (for the hard process) with 'general purpose' ones that take care of the fragmentation and the production of final-state particles. The most commonly used for the second task are `PYTHIA` [27] and `HERWIG` [65], the latter one relying on `JIMMY` [66] for the underlying event determination.

Both `PYTHIA` and `HERWIG` also provide leading order matrix-element calculation for many processes. Other generators includes next-to-leading order effects, the case of `MC@NLO` [67] that was used for $t\bar{t}$ generation. This field is in constant development, and one should note that an analysis can hardly be done using the same generator. Either because not all the processes are implemented in a single one or because the physics is better described using a combination of them.

Finally, one must consider that additional interactions might occur in the same bunch crossing that produces the event under study. These pile-up conditions are modeled by mixing simulated minimum bias events and hard scattering processes (e.g. $H \to 4\ell$ events) at the digitization level, to reproduce the expected higher occupancy in the detector. As this generation is very CPU time and memory consuming, only some special samples are normally produced in such configuration. The effect of pile-up is evaluated in section 6.4.5.

6.2.1 Cross sections and generators used

Even if the event generation for some processes is restricted to leading order diagrams, sometimes the cross sections can be calculated at higher order. A way

to include higher order corrections is to use LO event generators and to scale the leading order cross sections using K-factors extracted from analytical calculations of the NLO cross sections. One has to make sure that the impact of the corrections does not go beyond the absolute normalization, modifying the kinematics of the events. Fortunately, these effects are negligible for the leptons arising from the $H \to 4\ell$ signal [68] and this strategy is adopted throughout this chapter[1].

For almost all the processes, filters were applied to select events with at least three and usually four real leptons at generation level. Each of them was required to have $P_T > 5$ GeV and to be within the detector acceptance for electrons and muons ($|\eta| < 2.7$). This procedure is employed to save CPU time, preventing the reconstruction of events that would easily fail the signal selection. An exception is $Z \to \ell\ell$ production where the filter requires only one lepton, in order to evaluate the fake lepton contribution to the expected signal. This aspect will be discussed shortly.

Tables 6.1 and 6.2 summarize the generators used for each signal and background process, the associated cross sections and the corrections applied when necessary. A few details are given in the following list.

Table 6.1: Monte Carlo signal data samples, LO and NLO cross sections, 4-lepton (e, μ) filter acceptance and number of events generated for the analysis (after filtering) as a function of the Higgs mass in GeV (in square brackets). The cross sections in the table include the branching ratio of the Higgs to ZZ^* and $Z \to \ell\ell$, $\ell = e, \mu$.

Process	$\sigma_{LO} \cdot BR\ [fb]$	$\sigma_{NLO} \cdot BR\ [fb]$	Filter acc.	Events
$H[120] \to 4\ell$	1.68	2.81	0.584	40K
$H[130] \to 4\ell$	3.76	6.25	0.633	40K
$H[140] \to 4\ell$	5.81	9.72	0.662	40K
$H[150] \to 4\ell$	6.37	10.56	0.685	10K
$H[160] \to 4\ell$	2.99	4.94	0.704	40K
$H[165] \to 4\ell$	1.38	2.29	0.712	40K
$H[180] \to 4\ell$	3.25	5.38	0.733	40K
$H[200] \to 4\ell$	12.39	20.53	0.753	50K
$H[300] \to 4\ell$	7.65	13.32	0.782	10K
$H[400] \to 4\ell$	6.07	10.78	0.814	40K
$H[500] \to 4\ell$	2.98	5.12	0.842	40K
$H[600] \to 4\ell$	1.53	2.53	0.853	40K

[1]To evaluate the uncertainty in the NLO cross sections, the factorization and renormalization scales were varied independently from $M_H/2$ to $2 \times M_H$ for the signal and from $M_Z/2$ to $2 \times M_Z$ for the $Zb\bar{b}$ background. To determine the uncertainty on the parton distribution functions (PDFs), 40 sets of PDFs from CTEQ6M [69] were used. The total uncertainty is given by the sum of the all the contributions.

Table 6.2: Background samples, generators used, LO cross section (except for $t\bar{t}$, which is NLO), acceptance of the multi-lepton filter (FA). Corrections were applied when some processes were missing in the generation and are identified with a plus (+) sign. The number of events after filtering is given in the last column. For ZZ, $\ell = e, \mu, \tau$ while for the rest $\ell = e, \mu$.

Process	Generator	$\sigma \cdot BR$ [fb]	FA	Evts
$q\bar{q} \to ZZ \to 4\ell$	PYTHIA6.3	158.8 + 47.64 ($gg \to ZZ$)	[4ℓ] 0.219	100K
$gg \to Zb\bar{b} \to 2\ell b\bar{b}$	AcerMC/PYTHIA6.3	52 030 + 8 640 ($q\bar{q} \to Zb\bar{b}$)	[4ℓ] 0.00942	430K
$gg \to Zb\bar{b} \to 2\ell b\bar{b}$	AcerMC/PYTHIA6.3	52 030 + 8 640 ($q\bar{q} \to Zb\bar{b}$)	[3ℓ] 0.147	200K
$gg, q\bar{q} \to t\bar{t}$	MC@NLO/Jimmy	833 000	[4ℓ] 0.00728	400K
$q\bar{q} \to WZ$	Herwig6.5/Jimmy	26 500	[3ℓ] 0.0143	70K
$q\bar{q} \to Z$ inclusive	PYTHIA6.3	$1.5{\cdot}10^6$	[1ℓ] 0.89	500K

- Signal samples were generated for twelve mass points between $M_H = 120$ GeV and $M_H = 600$ GeV (120, 130, 140, 150, 160, 165, 180, 200, 300, 400, 500, 600). Typically 40 thousand events were produced for each mass point; the full numbers are shown in table 6.1.

  The generation was done exclusively with `PYTHIA` at leading order, that includes the full Z/γ^* interference in order to produce off-shell Z bosons. Gluon fusion and vector boson fusion diagrams are considered. The contribution of the other production modes is negligible in the inclusive searches. Higher order (NLO) corrections for the two modes were incorporated through K-factors, determined from analytical calculations using `HIGLU` and `VV2H` [70], respectively.

- ZZ events were produced with `PYTHIA`. Next-to-leading order corrections were calculated with `MCFM` [71] taking into account the dependence on the di-boson invariant mass. The K-factors usually increase with this mass, varying from 1.15 at 120 GeV to 1.8 at 600 GeV. The full numbers can be found in table 3 of ref. [64].

  `PYTHIA` only includes $q\bar{q}$ initiated processes, illustrated in fig. 6.4a. Additional contributions from gluon-gluon diagrams (fig. 6.4b) amount to 30% and were added to the cross section. The resulting cross section is given by the formula:

$$\sigma_{ZZ\to 4\ell} = \sigma^{LO}_{ZZ\to 4\ell} \times [K(M_{ZZ}) + 0.3]\,. \tag{6.1}$$

- $Zb\bar{b}$ is probably the most critical background in terms of the uncertainties on its cross section. Measurements from the Tevatron [72] were compared with NLO calculations through the ratio between events with a Z plus at least one

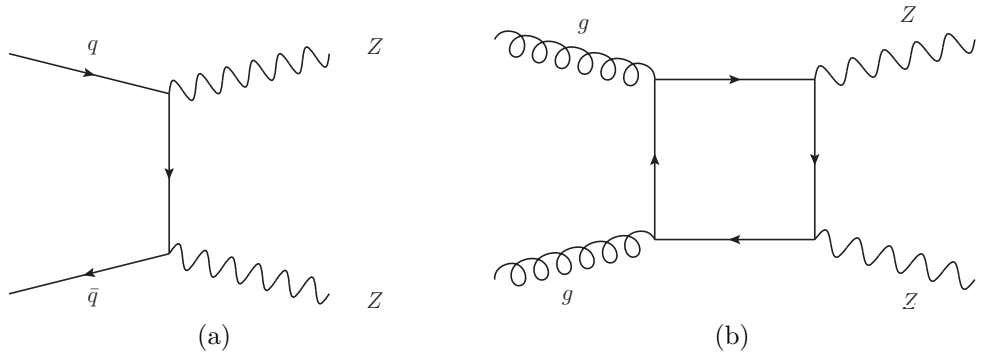

Figure 6.4: Diagrams for ZZ production initiated by (a) $q\bar{q}$ and (b) gluon-gluon.

b-jet and the inclusive Z boson production ($\frac{Z+b}{Z}$). The associated uncertainty is around 20% and the agreement is quite poor. Results from the analysis of the b-jet shape suggest that the fraction of gluon-splitting (fig. 6.5a) for $b\bar{b}$ production is underestimated in `PYTHIA` and `HERWIG`.

In ref. [73] the K-factors for this process are derived as a function of some kinematic variables. One observes large variations (from 1.4 to 2 at $\sqrt{s} = 14$ TeV) in the transverse momentum spectra of b-jets and the Z. This strongly suggests the use of a NLO generator, but this process has not yet been implemented. Scaling the LO cross section remains the best alternative, adopted in $H \to 4\ell$ analyses. The events were generated at LO using `AcerMC` [74] interfaced to `PYTHIA` for showering and hadronization. Only the dominant contribution from gg, shown in fig. 6.5b, is implemented and thus an extra 15% from the $q\bar{q}$ diagram was added to the total cross section. The K-factor of 1.42 was calculated using `MCFM`.

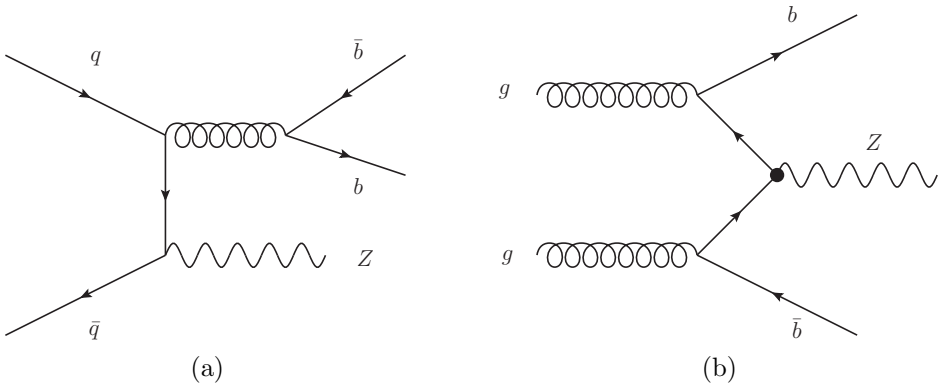

Figure 6.5: Diagrams for $Zb\bar{b}$ production initiated by (a) $q\bar{q}$ and (b) gluon-gluon.

- $t\bar{t}$ was extensively studied at the Tevatron and next-to-leading order generators exist for the process. Here, MC@NLO is used and no correction is needed.

- Inclusive Z production and WZ events were simulated respectively with PYTHIA and HERWIG at leading order. These samples were used to check the fake lepton contribution to the expected signal. The generated events did not survive the analysis cuts that will be discussed in the next sections.

6.3 Analysis strategy: trigger and lepton reconstruction

The uncertainties both on background yields and lepton fake rates motivated the choice for a conservative approach in this analysis. An alternative could be to push the selection efficiencies to the limit to overcome the low signal yields, and adopt multi-variate techniques for signal extraction. Instead, preference was given to cut-based selections including good quality objects reconstructed using the combination of more than one sub-system.

This section presents the guidelines followed up to now in the evaluation of the potential of $H \rightarrow 4\ell$ searches, including the strategies and efficiencies for trigger and lepton reconstruction. Special attention was given to the last point, since the feasibility of this analysis is highly dependent on the efficiencies and fake rates for both electrons and muons. Details about the algorithms were mentioned in chapter 2 and here just the main ideas are re-discussed. The event selection and the statistical methods that are used for extracting the signal significance are described in the next sections. All the optimizations were pursued using signal samples for $M_H = 130$ GeV, where this channel is expected to contribute significantly to the Higgs discovery potential [59] and the presence of all the background processes is important.

6.3.1 Trigger

The response of the trigger to $H \rightarrow 4\ell$ events was evaluated with the simulation of the full ATLAS trigger chain (Level 1, Level 2 and Event Filter). The trigger signatures foreseen for instantaneous luminosities varying from 10^{31} to 10^{33} cm^{-2} s^{-1} were tested, corresponding to the early running up to the highest rates achievable in the first years of LHC operation.

Electrons and muons are excellent signatures against QCD backgrounds already

at the trigger level. Large deposits in the electromagnetic calorimeter and topological coincidence between hits in different layers of muon detectors (RPC or TGC) are used to select regions of interest (ROIs) at Level 1 using programmable energy / momentum thresholds. Fast algorithms run at Level 2 using the full detector granularity around these ROIs. Basic electromagnetic shower shape cuts and matching between clusters and Inner Detector tracks are applied to improve jet rejection and to distinguish between electrons and photons. A simplified muon tracking is performed to obtain better momentum resolution and to reduce fake coincidences. Additionally it allows the combination with ID tracks and discrimination between isolated and non-isolated muons. The Event Filter uses the full detector information and runs basically the reconstruction algorithms described in sections 2.2.5 and 2.3.4 for lepton identification.

The presence of four leptons guarantees a high efficiency output and allows the use of single or di-lepton triggers. The first ones are not expected to be prescaled[2] already with thresholds around 20 GeV, specially if isolation requirements are met in the case of electrons. Di-lepton triggers can run with lower thresholds – 10 (15) GeV for muons (electrons) – combining two leptons of the same or different flavours. They provide an alternative in case the single-lepton ones become saturated.

The trigger efficiencies for a Higgs mass of 130 GeV were verified before and after the event selection, by counting the number of events triggered by a given chain. Efficiencies above 97% for the selected events were obtained in all the three channels. The single lepton triggers with thresholds of 20 GeV for muons and 22 GeV for electrons (with isolation requirements) were chosen for simplicity. The complete results showing the efficiency of each trigger chain can be found in table 4 of ref. [64].

6.3.2 Electron reconstruction

Electrons are identified by large deposits in the Electromagnetic Calorimeter associated with tracks measured in the Inner Detector. A set of cuts on calorimeter and tracking variables is used to classify the objects as *Loose*, *Medium* and *Tight*, providing different purity and efficiency patterns. Additionally one can include isolation requirements, which limits the ratio between the cluster energy and the deposits in the EM and hadronic calorimeters within a cone of $\Delta R = 0.2$ around the electron candidate. The isolation cut value depends on η due to the non-uniform calorimeter geometry and is described in ref. [10]. The expected electron reconstruction efficiencies are shown in fig. 6.6. A drop in performance at low momenta was observed and

[2] A prescale is a random selection of events accepted by the trigger, used in order to reduce the rates of a given trigger signature, usually to cope with the limited bandwidth for event recording.

justified by the loss in the discriminating power of shower shape cuts in this region.

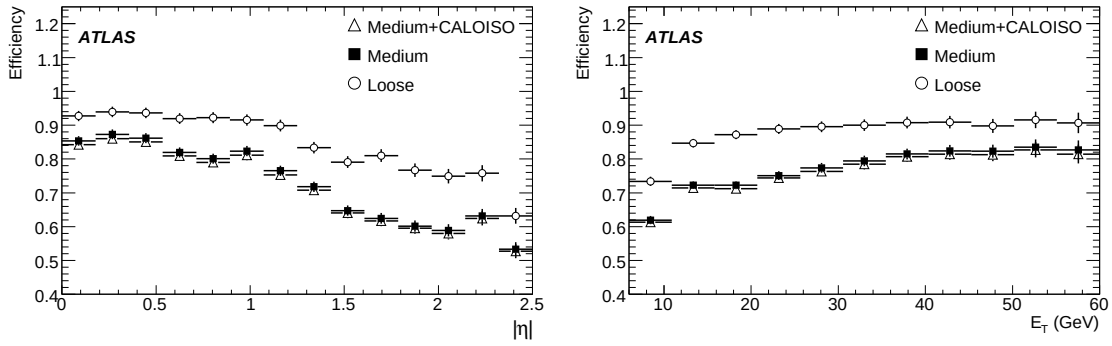

(a) (b)

Figure 6.6: Expected reconstruction efficiencies as a function of (a) pseudo-rapidity and (b) transverse energy for electrons originating from Higgs decays in the $H \to 4e$ channel ($M_H = 130$ GeV). The different definitions mentioned in the text are compared.

The *Loose* definition was the first choice for giving the highest efficiency and was kept in the event preselection, described in the next section. For Higgs masses below 200 GeV, sufficient rejection against electrons from heavy flavour decays was only obtained with *Medium + CaloIso* requirements.

6.3.3 Muon reconstruction

Muon identification relies primarily on the ATLAS Muon Spectrometer. Standalone reconstruction is performed in this sub-system and once the track parameters are expressed close to the interaction point, a combination with Inner Detector tracks takes place. If the combination is successful, the lowest fake rates and best resolutions are achieved for all momenta. The matching efficiency is typically above 95%.

Tagging algorithms were developed to recover the efficiency gaps left by low momentum particles that cannot reach the outer stations of the MS, or regions where this system is not fully instrumented. They associate ID tracks with MS segments and ensure acceptable fake rates. These are the two categories used in the analyses: combined and tagged muons. Standalone ones – only seen by the spectrometer – must be carefully studied with collision data before their inclusion.

The muon reconstruction efficiency is shown in fig. 6.7 as a function of pseudo-rapidity and transverse momentum. The use of tagged muons helps achieving values close to 97%, approximately constant as a function of P_T and subject to some

variations in η due to the MS coverage. In particular, the effect of the gap around $|\eta| \sim 0$ left for the passage of services from the calorimeters, and the transition between barrel and end-cap at $|\eta| \sim 1.2$ are visible.

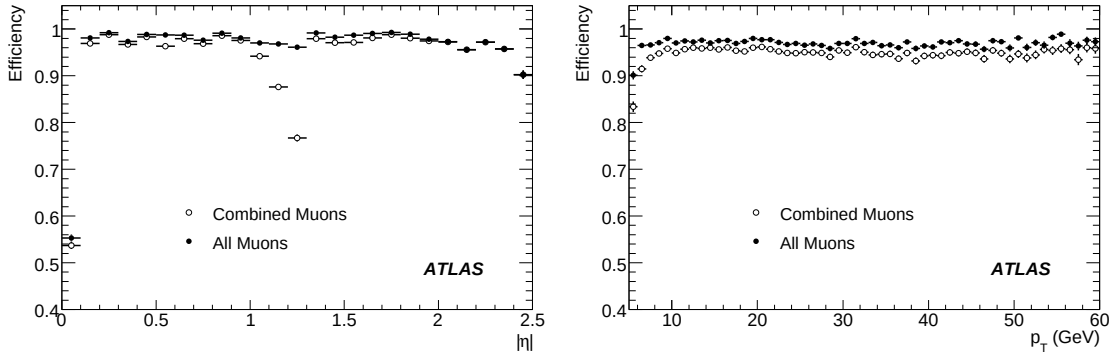

(a) (b)

Figure 6.7: Expected reconstruction efficiencies as a function of (a) pseudo-rapidity and (b) transverse momentum for muons originating from Higgs decays in the $H \to 4\mu$ channel ($M_H = 130$ GeV). Empty (filled) circles show the efficiency for combined (combined + tagged) muons.

6.4 Event selection

Once the trigger and the quality of the reconstructed objects were chosen, the analysis cuts were defined in order to bring the reducible backgrounds below one third of the level of $ZZ \to 4\ell$. This is achieved in three stages: an event preselection with kinematic cuts on the leptons, complemented by background reduction based on isolation and vertexing (impact parameter) requirements, and finally the reconstruction of the Z and Higgs candidates. Each one is detailed in this section and a summary is given in table 6.3.

6.4.1 Preselection

Leptons from on-shell Z bosons are expected to have considerable transverse momentum, while those from the reducible backgrounds are usually softer. This motivates some basic cuts applied on the events passing the triggers. They should contain at least four leptons within $|\eta| < 2.5$ and with $P_T > 7$ GeV, not less than two of those with $P_T > 20$ GeV.

The lepton quality identification criteria described in the previous section are usually enforced at this stage: muons must be either combined or tagged, i.e. recon-

Table 6.3: Summary of the analysis cuts for the $H \to 4\ell$ searches. The two lepton pairs are denoted as $Z1$ and $Z2$. The values of the mass cut on M_{Z2} are defined in table 6.4.

Event Preselection	Four leptons: *LooseElectrons*, combined or tagged muons, with $P_T > 7$ GeV and $\|\eta\| < 2.5$. At least two with $P_T > 20$ GeV.
	Event Selection
Kinematic Cuts	Lepton quality: 2 pairs of same flavour opposite charge leptons. For $M_H \leq 200$ GeV, electrons must satisfy *Medium + CaloIso* criterion. Z, Z^* and Higgs reconstruction: single quadruplet with $\|M_{Z1} - M_Z\| < 15$ GeV (12 GeV for $M_H \geq 180$ GeV), M_{Z2} >15 – 60 GeV, depending on Higgs mass considered.
Isolation and vertexing cuts	Calorimetric isolation for muons ($\Sigma E_T/P_T < 0.23$). Inner detector track isolation for both electrons and muons ($\Sigma P_T/P_T < 0.15$). Cut on maximum lepton impact parameter significance ($d_0/\sigma_{d_0} < 3.5$ for muons, $d_0/\sigma_{d_0} < 6.0$ for electrons).

structed by both Inner Detector and Muon Spectrometer; electrons must satisfy the *Loose* definition for $M_H \geq 200$ GeV and *Medium + CaloIso* for M_H below 200 GeV. The *Medium + CaloIso* requirement is applied when forming the Z candidates.

6.4.2 Background rejection

The large cross sections of the backgrounds compared to the signal clearly demands the use of further selection criteria. The distinction between leptons from vector boson and heavy quark decays is possible through isolation and impact parameter cuts.

Isolation cuts

The hadronic activity around leptons inside jets can be quantified with the tracks reconstructed in the Inner Detector and the transverse energy deposits in the calorimeters. Although the quantities are correlated, the measurements take place in different sub-systems, and thus carry some independent information.

Both calorimetric and track-based isolation were applied as discriminants to all four leptons, muons and electrons. The transverse energy or momenta deposited in a cone in $\eta - \phi$ was used, excluding the contribution of the lepton under consideration. The performance for different cone sizes was evaluated in the case of muons (fig. 6.8)

and a conservative choice was made for $\Delta R = 0.2$. At the same time it provides good rejection power and should be less sensitive to pile-up effects which are discussed later on.

Moreover, the effect of the cut is improved with the relative isolation, defined as the ratio between the isolation energy (or momentum) and the P_T of the lepton (fig 6.9). What explains this feature is the lower momenta of leptons from b and c-jets when compared to the ones originating from $Z^{(*)}$ decays. The cut values were defined in view of a combined efficiency close to 90% and are the following:

Calorimetric isolation:	$\sum E_T(\Delta R < 0.2)/P_T^{\mu} < 0.23$ for muons, enforced at reconstruction stage for electrons.
Track isolation:	$\sum P_T(\Delta R < 0.2)/P_T^{e,\mu} < 0.15$ for both leptons, excluding the lepton P_T ($P_T^{e,\mu}$) from the sum.

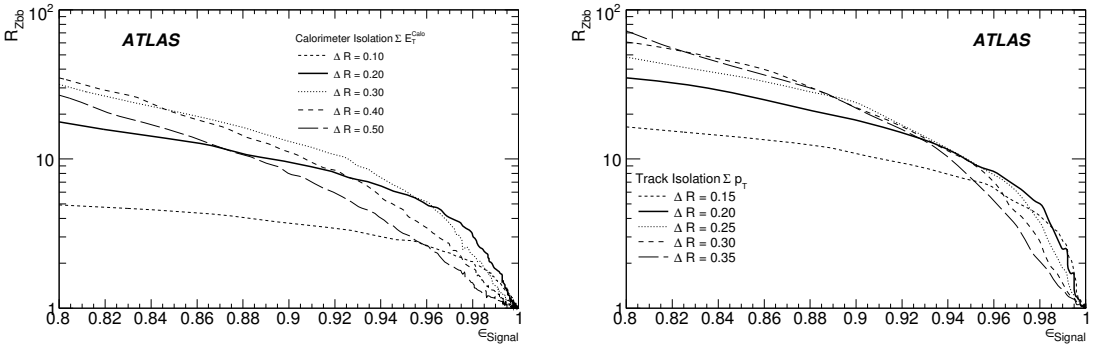

(a) (b)

Figure 6.8: Rejection of the $Zb\bar{b}$ background as a function of the $H \to 4\mu$ ($M_H = 130$ GeV) selection efficiency for different cone sizes used for (a) calorimeter and (b) track isolation.

The associated distributions are shown in fig. 6.10. The signal selection efficiency of each cut is approximately 92% for calorimetric isolation in the $H \to 4\mu$ case, and 97% for track isolation in all the three final states.

The importance of calorimetric isolation for muons in this analysis motivated the studies described in the first part of this thesis. The contribution of the muon deposits to the isolation cone was the limiting factor for this cut. After their re-definition, an improvement in the rejection of the $Zb\bar{b}$ background close to 2 was observed, as discussed in chapter 3. Further studies related to this subject were also performed and should be included in the analyses in the future.

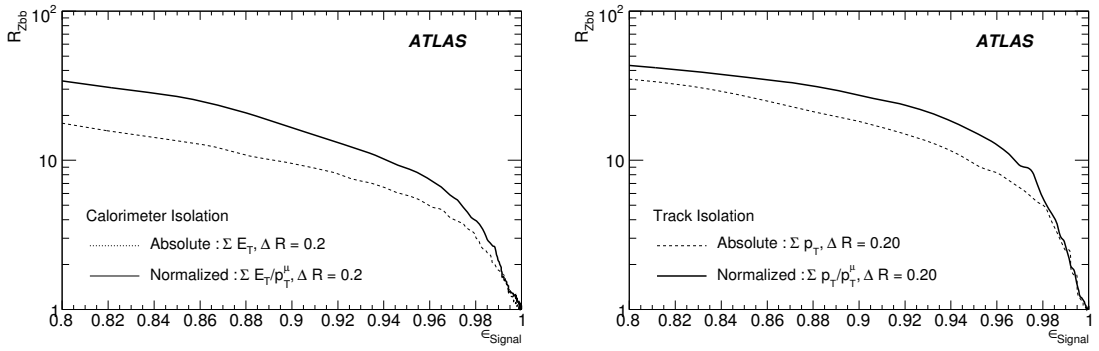

(a) (b)

Figure 6.9: Rejection of the $Zb\bar{b}$ background as a function of the $H \to 4\mu$ (M_H = 130 GeV) selection efficiency using the absolute or the normalized (relative to the momentum of the track) (a) calorimeter and (b) track isolation.

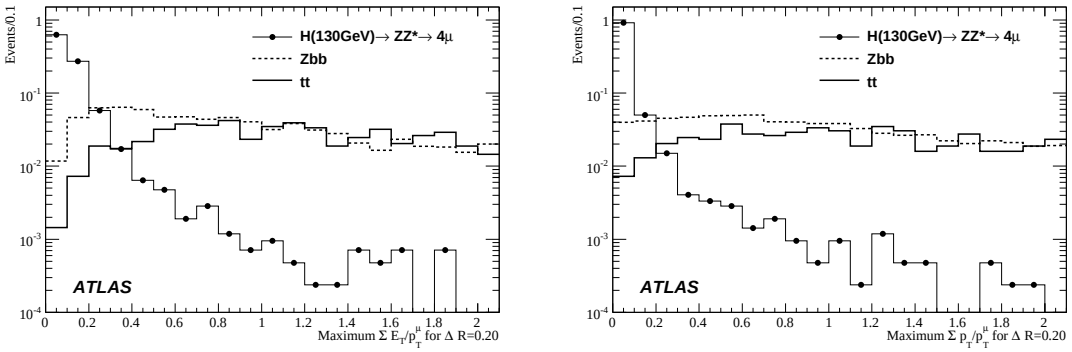

(a) (b)

Figure 6.10: (a) Calorimeter and (b) track isolation distributions for the signal (M_H = 130 GeV), $Zb\bar{b}$ and $t\bar{t}$ backgrounds. The distributions are normalized to unit area.

Impact parameter cuts

Electrons and muons coming from Ws and Zs are produced essentially at the main interaction point while those from b and c-quark decays originate from secondary displaced vertices. This information is used to further reject $Zb\bar{b}$ and $t\bar{t}$ backgrounds.

The approach adopted in the present analysis was the use of the transverse impact parameter significance – defined by the ratio of its absolute value and the associated error ($|d_0|/\sigma_{d0}$) – shown in fig. 6.11. This quantity was required to be below predefined values: 3.5 for muons and 6 for electrons. The difference is explained by the emission of bremsstrahlung photons that limit the accuracy on the electron track reconstruction.

The impact parameter significance is calculated with respect to the primary vertex, fitted using a set of tracks reconstructed in the Inner Detector. This is an attempt to reduce the spread induced by the fluctuations on the vertex position which should be of the order of 15 μm. This strategy ignores the fact that the track under consideration may or may not belong to the fitted vertex.

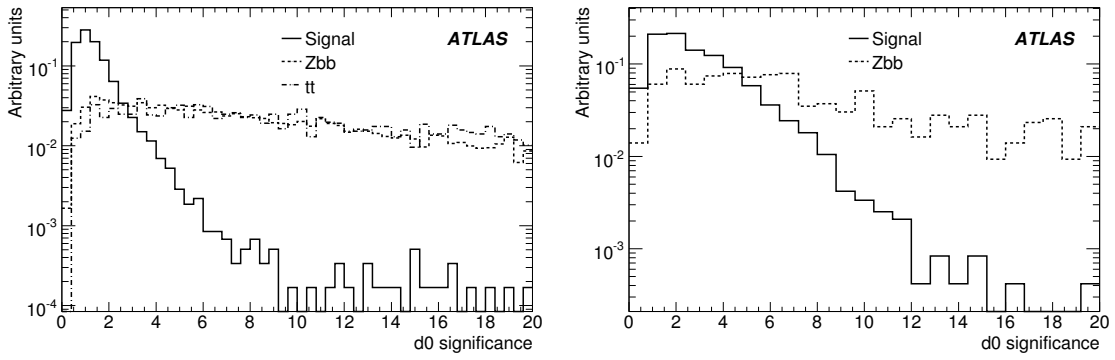

(a) (b)

Figure 6.11: Maximum transverse impact parameter significance for (a) muons and (b) electrons from signal and reducible background events. The distributions are normalized to unit area.

6.4.3 Z and Higgs boson reconstruction

After the leptons are asked to pass the preselection, they are combined into pairs of same flavour and opposite charge. Two pairs are selected to form the Higgs candidate according to the strategy presented in the following.

Lepton pairing and di-lepton mass cuts

The leading pair ($Z1$) is defined as the one whose invariant mass is closer to M_Z from ref. [26]. The physical argument for this choice comes from the Breit-Wigner distribution: the Z is more likely to be found near the pole mass and this method selects the correct candidate in more than 90% of the cases. If there are more than four leptons at this stage, the second pair ($Z2$) is chosen as the combination that gives the highest invariant mass, always with leptons of the same flavour and opposite charge.

Non-resonant di-lepton combinations are rejected with the following cuts: $Z1$ must lie within a window of $\pm$15 GeV centered at M_Z ($\pm$12 GeV for $M_H \geq 180$ GeV) and M_{Z2} must be higher than a certain value that depends on the 4-lepton invariant

mass, varying from 15 GeV at $M_{4l} = 120$ GeV to 60 GeV at $M_{4l} = 200$ GeV. For Higgs masses above 200 GeV, both pairs must be within 12 GeV from M_Z as the contribution from off-shell Z bosons becomes negligible. The cut values were optimized from the signal and background distributions and can be found in table 6.4.

Table 6.4: Mass cuts applied to the reconstructed leading and sub-leading di-lepton pairs, and the Higgs mass resolution values (used to define the signal region).

H Mass (GeV)	$Z1$ mass window (GeV)	$Z2$ mass cut (GeV)	H mass resolution (GeV)		
			$4e$	4μ	$2e2\mu$
120	±15	>15	2.0	1.8	1.9
130	±15	>20	2.2	1.8	1.9
140	±15	>30	2.2	2.0	2.1
150	±15	>30	2.3	2.1	2.2
160	±15	>30	2.4	2.2	2.3
165	±15	>35	2.5	2.4	2.4
180	±12	>40	2.8	2.7	2.8
200	±12	>60	3.9	3.7	3.8
300	±12	±12	8.4	8.4	8.4
400	±12	±12	16.5	17.3	17.2
500	±12	±12	33.8	34.4	32.8
600	±12	±12	52.2	57.2	53.2

Constrained mass fit and reconstructed Higgs boson mass

Whenever the cut on the Z mass window is requested, the lepton pair is assumed to form an on-shell Z boson. The associated mass resolution is improved by applying a constrained fit on both pairs above $M_H = 200$ GeV, and only on the leading pair for lower masses. One tries to minimize a function defined by the convolution of the nominal Z Breit-Wigner distribution and a Gaussian centered at M_Z with σ equal to the experimental resolution (~ 1.7 GeV). The measured momentum (magnitude and directions η and ϕ) of each lepton is allowed to float within the associated error.

This procedure does not introduce significant biases in the mean mass. The bias was evaluated together with the resolution from a Gaussian fit to the four-lepton invariant mass distribution. The results for the three channels are shown in fig. 6.12. When the electrons are included, the distribution has an important tail towards low values due to bremsstrahlung upstream the calorimeter. In the case of muons there is a small component probably due to final-state radiation from Z decays. The shift on the mean reconstructed mass as a function of the input value is shown in fig. 6.13a for M_H up to 180 GeV. All the values are way below the percent level.

The gain in the width of the reconstructed Higgs mass varies from 10 to 17% and is illustrated in fig. 6.13b, in the case of four electrons.

Finally, the Higgs candidate is accepted if the invariant mass of the quadruplet is found within $\pm 2\sigma$ with respect to the input mass. The resolution on the Higgs mass for $H \to 4e$ events is shown in fig. 6.13b, and the values for the other channels are listed in table 6.4.

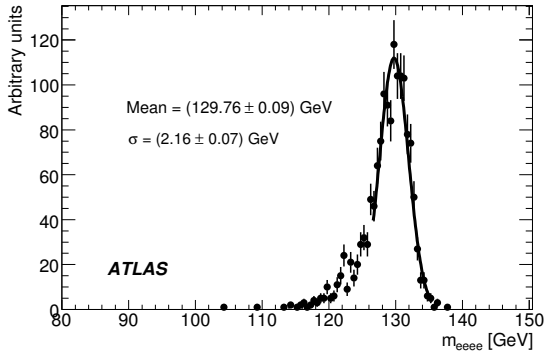

(a) $4e$ channel.

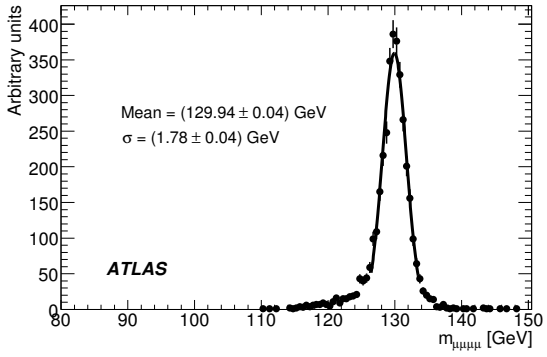

(b) 4μ channel.

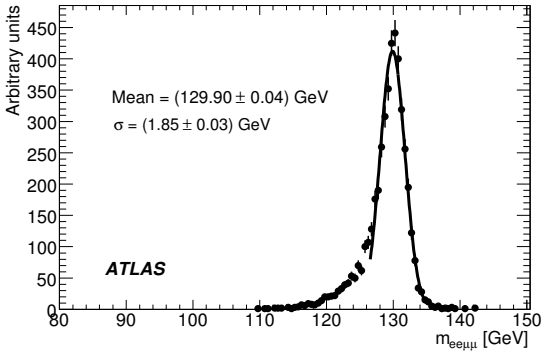

(c) $2e2\mu$ channel.

Figure 6.12: Distributions of the reconstructed invariant mass of the Higgs boson ($M_H = 130$ GeV) after the application of the Z-mass constraint fit. A Gaussian function was fitted to the distributions in order to obtain the mean values and the resolutions, indicated in the figures.

6.4.4 Event selection results

With the set of cuts described above, the reducible backgrounds were kept under control as desired. The fraction of signal and background events selected by each cut are shown in tables 6.5, 6.6 and 6.7. The evolution of the yields along the cut flow in the $2e2\mu$ channel for $M_H = 130$ GeV can be observed in fig. 6.14. The contribution

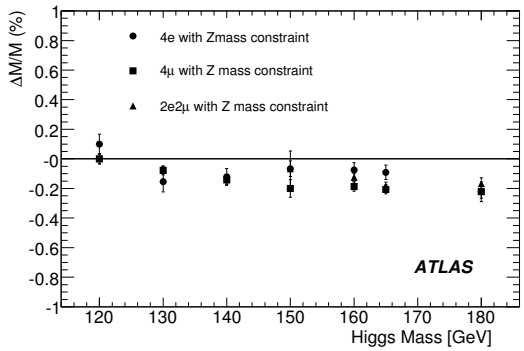

(a) Shift of the mean 4-lepton mass for each of the three decay channels with the Z-mass constraint on the di-lepton mass.

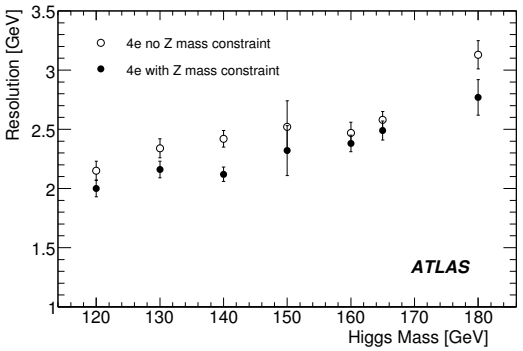

(b) Resolution on the Higgs mass for the $H \to 4e$ channel, with and without the application of a Z-mass constraint fit.

Figure 6.13: Expected (a) shift and (b) resolution on the reconstructed Higgs boson mass.

of $Zb\bar{b}$ and $t\bar{t}$ is well below the irreducible ZZ component. The signal is affected as much as ZZ throughout the analysis, except when it comes to the Higgs mass window cut.

The survival rate of WZ events is negligible, but the situation of Z + jets is more delicate. With the available MC statistics (500 K events), no event passed the lepton quality and P_T cuts. Relaxing some of the lepton quality cuts, such as the calorimetric isolation for electrons, allows a single event to be found in the $4e$ final state at this stage. The level of this background would then correspond to twice the $Zb\bar{b}$ contribution. This is still below the ZZ yield but will need special attention in the future.

Table 6.5: Fraction of $H \to 4\ell$ ($M_H = 130$ GeV) events (in %) selected after each cut for each of the three decay channels.

Selection cut	**Signal**		
	4e	4μ	2e2μ
Trigger	94.7	95.3	95.7
Lepton preselection	57.0	73.8	66.8
Lepton quality and P_T	24.7	60.5	39.7
Z mass cuts	17.1	42.9	27.6
Calo Isolation	17.1	39.5	25.4
Tracker Isolation	16.5	38.1	24.7
IP cut	15.1	36.5	23.2
H Mass cut	12.5±0.3	31.4±0.5	19.2±0.4

In the end, a clear peak is visible on top of the di-boson continuum for an integrated luminosity of 30 fb^{-1}, combining the three analyses ($4e$, 4μ and $2e2\mu$).

Table 6.6: Fraction of events (in %) selected after each cut for the ZZ and $Zb\bar{b}$ background processes. The 130 GeV Higgs mass selection cuts are applied.

Selection cut	ZZ			$Zb\bar{b}$		
	4e	4μ	2e2μ	4e	4μ	2e2μ
Trigger	96.6	96.6	96.6	91.4	91.4	91.4
Preselection	13.8	17.6	31.4	2.6	9.4	12.0
Lepton quality and P_T	7.3	16.0	21.9	$1.1{\cdot}10^{-1}$	2.1	1.7
Z mass cuts	6.9	14.8	20.2	$4.7{\cdot}10^{-2}$	1.1	$8.4{\cdot}10^{-1}$
Calo Isolation	6.9	13.9	19.5	$4.7{\cdot}10^{-2}$	$8.5{\cdot}10^{-2}$	$1.2{\cdot}10^{-1}$
Track Isolation	6.8	13.6	19.2	$1.3{\cdot}10^{-2}$	$3.3{\cdot}10^{-2}$	$4.4{\cdot}10^{-2}$
IP cut	6.2	13.0	17.8	$5.6{\cdot}10^{-3}$	$1.1{\cdot}10^{-2}$	$1.8{\cdot}10^{-2}$
H Mass window	0.05	0.11	0.12	$1.6{\cdot}10^{-3}$	$1.2{\cdot}10^{-3}$	$3.0{\cdot}10^{-3}$

Table 6.7: Fraction of events (in %) selected after each cut for the $t\bar{t}$ background. The 130 GeV Higgs mass selection cuts are applied.

Selection cut	$t\bar{t}$		
	4e	4μ	2e2μ
Trigger	75.1	75.1	75.1
Preselection	1.0	4.7	10.1
Lepton quality and P_T	$6.8{\cdot}10^{-3}$	$7.3{\cdot}10^{-1}$	$5.8{\cdot}10^{-1}$
Z mass cuts	$1.6{\cdot}10^{-3}$	$2.0{\cdot}10^{-1}$	$1.0{\cdot}10^{-1}$
Calo Isolation	$1.6{\cdot}10^{-3}$	$1.6{\cdot}10^{-3}$	$5.4{\cdot}10^{-3}$
Track Isolation	$2.6{\cdot}10^{-4}$	$2.5{\cdot}10^{-4}$	$1.0{\cdot}10^{-3}$
IP cut	$2.6{\cdot}10^{-4}$	$< 6 \cdot 10^{-4}$	$2.6{\cdot}10^{-4}$
H Mass window	$< 6 \cdot 10^{-4}$	$< 6 \cdot 10^{-4}$	$< 6 \cdot 10^{-4}$

The expected four lepton invariant mass spectra before the application of the Higgs mass window cut are shown in fig. 6.15 for four different Higgs mass scenarios: 130, 180, 300 and 600 GeV.

The selection efficiencies for the signal were found to vary as a function of the Higgs mass (fig. 6.16). They increase consistently with the increase of M_H up to 200 GeV, as the Z^* turns on-shell and the average momentum of the leptons is augmented. This is followed by a smooth fall due to the increase of the natural width of the Higgs boson. The presence of low-P_T objects associated with the strict requirements on the electron identification quality are the reasons for the efficiencies ranging from 10 to 21% in the $4e$ channel at low masses. This situation is currently improved and the effect will be visible in the analyses described in section 6.6 and chapter 7. For higher masses this criterion is relaxed and one sees a big jump on the selection rates. The effect on $H \to 4\mu$ is less pronounced, and $2e2\mu$ final states lie in between.

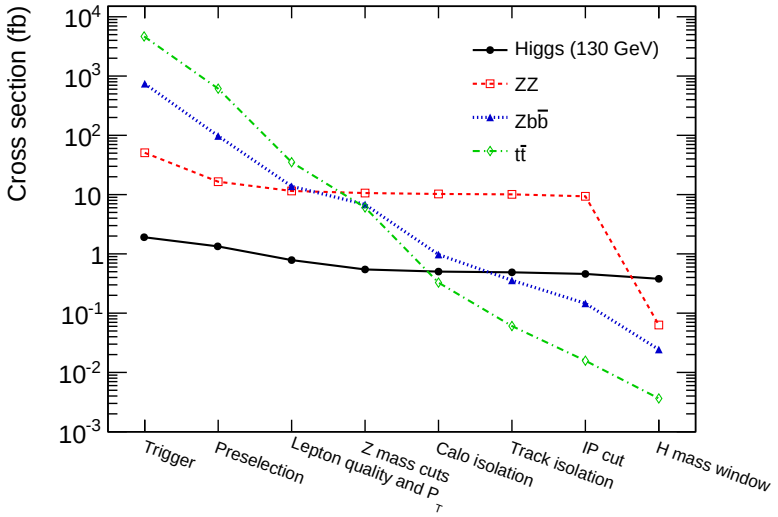

Figure 6.14: Cross sections for the signal and backgrounds after the application of each analysis cut in the $2e2\mu$ channel, in case of a Higgs boson of 130 GeV.

6.4.5 Effect of pile-up and cavern background

Considering an instantaneous luminosity of 10^{33} cm^{-2} s^{-1}, 2.3 events per bunch-crossing are expected at LHC together with additional thermalized slow neutrons and low energy photons escaping from the calorimeters. The performance of all the sub-systems is affected and the impact on this analysis was quantified by studying the losses in the signal selection efficiency for a Higgs mass of 130 GeV. This was the only sample generated in such conditions due to the high CPU time consumption. A safety factor of 5 was adopted for the predicted cavern background (neutrons and photons).

The standard lepton reconstruction was implemented to have a minimal dependence on pile-up. On the other hand the performance of the isolation cuts is reduced due to additional particles coming from pile-up events. The detailed study can be found in ref. [64], and the summary is a 10% loss in the selection efficiency, mainly due to the isolation variables.

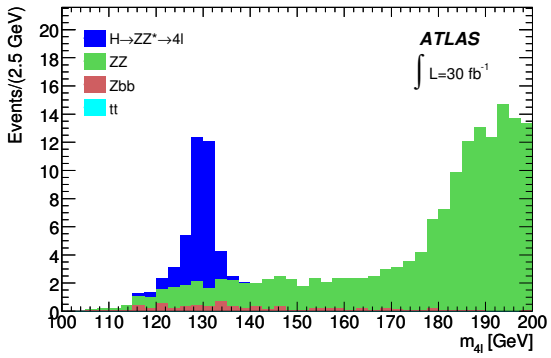

(a) $M_H = 130$ GeV.

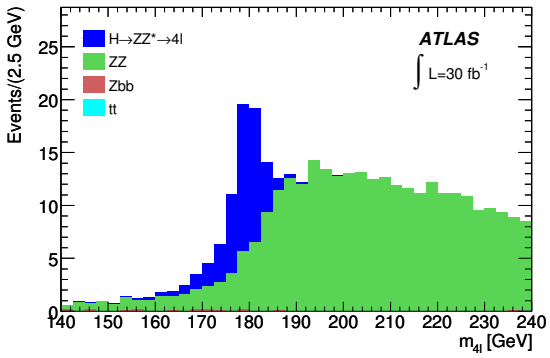

(b) $M_H = 180$ GeV.

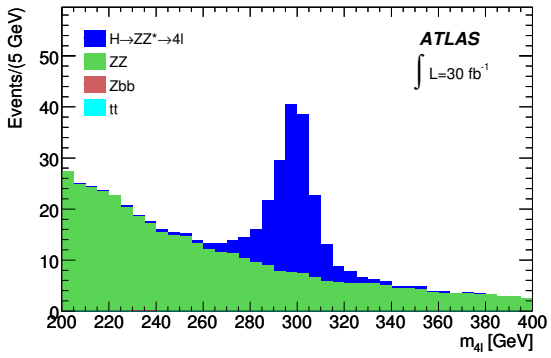

(c) $M_H = 300$ GeV.

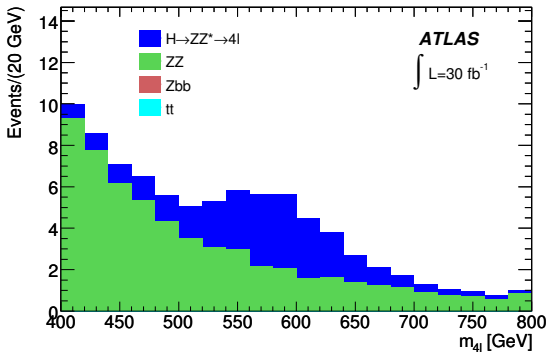

(d) $M_H = 600$ GeV.

Figure 6.15: Reconstructed 4-lepton invariant mass for signal and background processes before the application of the Higgs mass window cut, in the case of a Standard Model Higgs boson with $M_H = 130, 180, 300$ and 600 GeV, normalized to a luminosity of 30 fb^{-1}.

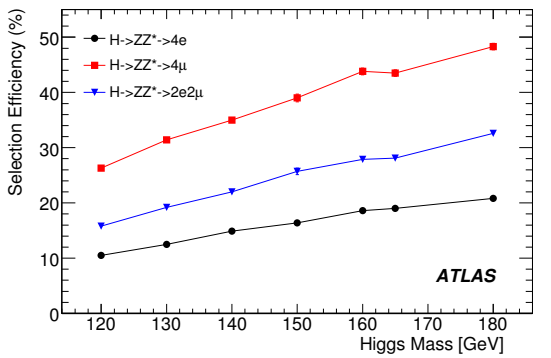

(a) $120 < M_H < 180$ GeV.

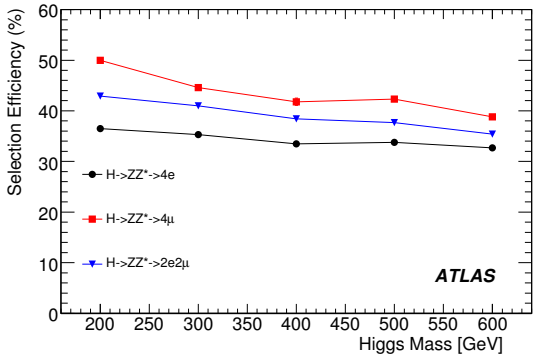

(b) $200 < M_H < 600$ GeV.

Figure 6.16: Signal selection efficiency as a function of the Higgs mass.

6.5 Discovery potential

The discovery of a SM Higgs boson can be claimed once the signal is considered *statistically significant*, which means that it is unlikely to be reproduced by a mere fluctuation of the background. This decision is taken in the context of *hypothesis testing*, outlined in appendix B. Two methods are compared here: the first one uses the Poisson significance, assuming the exact knowledge of the expected yields for the background; the second one includes systematic uncertainties through the profile likelihood. Both are described in the appendix and only the results are quoted in this section, after the definition of the systematics.

6.5.1 Systematic uncertainties

Systematic uncertainties affect directly the expected number of events for the signal and backgrounds. They can originate from the theoretical or the experimental side and are summed quadratically.

An important source of theoretical error is associated to the yield of background processes. It was evaluated by varying the factorization and renormalization scales independently and using different sets of PDFs, as discussed in section 6.2. The obtained values for ZZ and $Zb\bar{b}$ are around 3% and 16%, respectively.

From the experimental point of view, the uncertainties come mainly from lepton reconstruction through the knowledge on the energy scale and resolution, and the lepton identification efficiency. The precision on these quantities was determined by the ATLAS performance groups using simulations, usually under conservative assumptions although some need large amounts of data to be achieved. The effect on the signal and background selection rates was obtained by varying them accordingly.

The reconstructed energies (or momenta) of the leptons were smeared by Gaussian functions to obtain a typical degradation of the order of 10% in the resolution, and a shift of $\pm 0.5\%$ and $\pm 1\%$ for electrons and muons, respectively. Losses in the identification efficiencies were simulated by discarding 0.1% of the electrons and 1% of muons.

The impact on the signal and backgrounds is very similar. Losses of about 3% were observed in the $4e$ channel, while $2e2\mu$ and 4μ modes were affected by 4% and 5%, respectively. The details are given in table 13 of ref [64].

6.5.2 Expected significance

The expected significance using Poisson statistics is obtained by simply integrating the spectra on fig. 6.15 around $M_H \pm 2\sigma_{M_H}$. Figure 6.17a shows the results for each channel and their combination. Except for the combination, the highest significance is obtained in the $2e2\mu$ final state due to the higher yields. It is followed by the 4μ channel, that benefits from better identification efficiency for muons when compared to electrons.

Systematic uncertainties are included only in the profile likelihood estimation, together with a fit on the ZZ continuum. The fit involves ten free parameters in order to well describe the full mass range: the plateau in the low masses and the wide peak when the Zs turn on-shell are fitted almost independently. The motivation for each parameter is discussed in ref. [64]. This procedure intends to extract the di-boson contribution in the signal region through the extrapolation from the side-bands. The resulting uncertainty on the background yields from the fits is below 6% over the full range. The systematic effects discussed in the previous subsection are absorbed by the fit and their impact on the significance is smaller than 4%. The fit behaviour was validated in pseudo-experiments corresponding to integrated luminosities of 30 fb^{-1}. Two examples, for $M_H = 130$ GeV and 180 GeV are shown in fig. 6.18.

Poisson significance and the profile likelihood are compared in fig. 6.17b. The difference between them comes mainly from the knowledge on the background yields, assumed to be perfect in the first case.

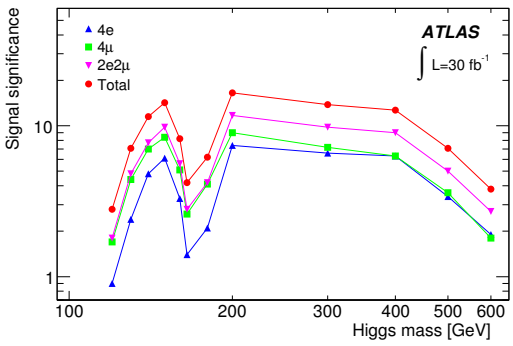

(a) Signal significance (Poisson) for each channel and their combination.

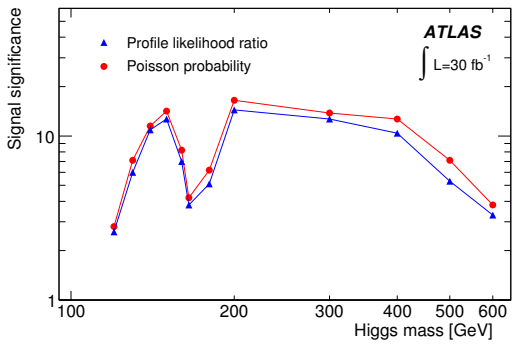

(b) Signal significance computed using Poisson statistics and a profile likelihood that includes systematic uncertainties.

Figure 6.17: Expected signal significance as a function of the Higgs mass for $\sqrt{s} =$ 14 TeV and an integrated luminosity of 30 fb^{-1}.

As a conclusion, the Higgs can be discovered (at 5σ level) with an integrated luminosity of 30 fb^{-1} at $\sqrt{s} = 14$ TeV in the $H \to 4\ell$ channel alone over the range $130 < M_H < 500$ GeV, except for the region around 160 GeV. Significances of about 4σ are obtained in this case, due to the low branching ratios of $H \to ZZ$. The highest sensitivities are verified at $M_H = 150$ GeV and from 200 to 400 GeV, where luminosities of 5 fb^{-1} are already sufficient for discovery [64].

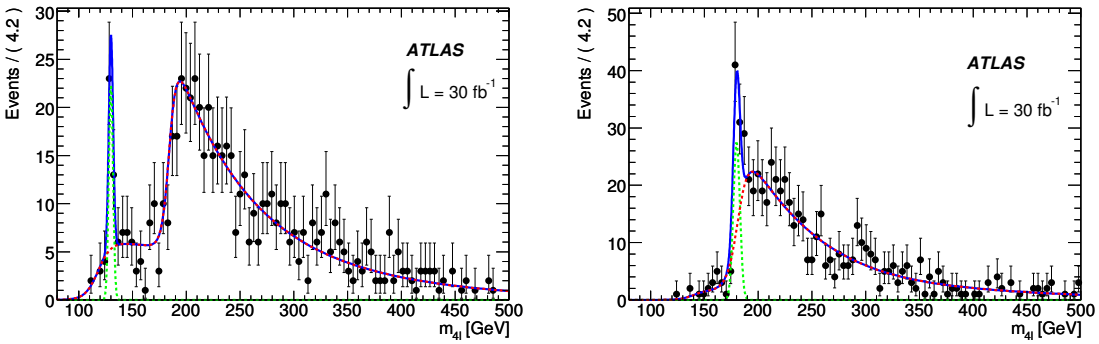

(a) (b)

Figure 6.18: Pseudo-experiments corresponding to 30 fb^{-1} of data in case of (a) $M_H = 130$ GeV and (b) $M_H = 180$ GeV, showing the fits to signal and background.

6.6 Sensitivity at different center of mass energies

In view of the changes in the LHC schedule, this analysis was updated with Monte Carlo samples produced assuming a different center of mass energy: $\sqrt{s} = 10$ TeV. Small modifications in the cut flow were introduced with respect to 14 TeV analyses. Only the obtained results are shown here. The reader is referred to ref. [75] for more information.

In a second step, the results were scaled to the energy of the first physics run ($\sqrt{s} = 7$ TeV). The scaling of the cross sections was validated by a comparison of the kinematic distributions associated to signal and background leptons, to ensure that the cut efficiencies would remain approximately the same. The analyses were done assuming an integrated luminosity of 1 fb^{-1}, achievable by the end of 2011. The ratio of the cross sections for the different center of mass energies for the signal and main backgrounds are shown in table 6.8.

The signal selection efficiencies are shown in fig. 6.19. No significant difference is observed with respect to the previous studies, except for an increase in the yields of the electron channels at low masses. Better cluster to track matching and a tuning

of the values used for the classification (between *Loose*, *Medium* and *Tight*) are behind this effect. The associated identification efficiencies were increased without augmenting the contamination from jets.

Figure 6.20 shows the four lepton invariant mass spectra for the three final states, including different Higgs mass hypotheses: 130, 240 and 500 GeV. The backgrounds are clearly dominated by the $ZZ \to 4\ell$ contribution and the signal peak is easily visible over the full mass range. The expected number of events is of course reduced with respect to 14 TeV analyses due to the lower center of mass energy and integrated luminosity considered (1 fb^{-1}).

Table 6.8: Ratio of the NLO cross sections at $\sqrt{s} = 7$ TeV, 10 TeV and 14 TeV for three Higgs masses (120, 200 and 500 GeV) and the main background processes.

Process	$\frac{\sigma_{\sqrt{s}=7\text{ TeV}}}{\sigma_{\sqrt{s}=10\text{ TeV}}}$	$\frac{\sigma_{\sqrt{s}=10\text{ TeV}}}{\sigma_{\sqrt{s}=14\text{ TeV}}}$	$\frac{\sigma_{\sqrt{s}=7\text{ TeV}}}{\sigma_{\sqrt{s}=14\text{ TeV}}}$
$H[120] \to 4\ell$	0.53	0.52	0.27
$H[200] \to 4\ell$	0.48	0.42	0.20
$H[500] \to 4\ell$	0.37	0.36	0.13
ZZ	0.61	0.65	0.40
$Zb\bar{b}$	0.52	0.66	0.34
$t\bar{t}$	0.43	0.45	0.19
Z	0.66	0.76	0.50

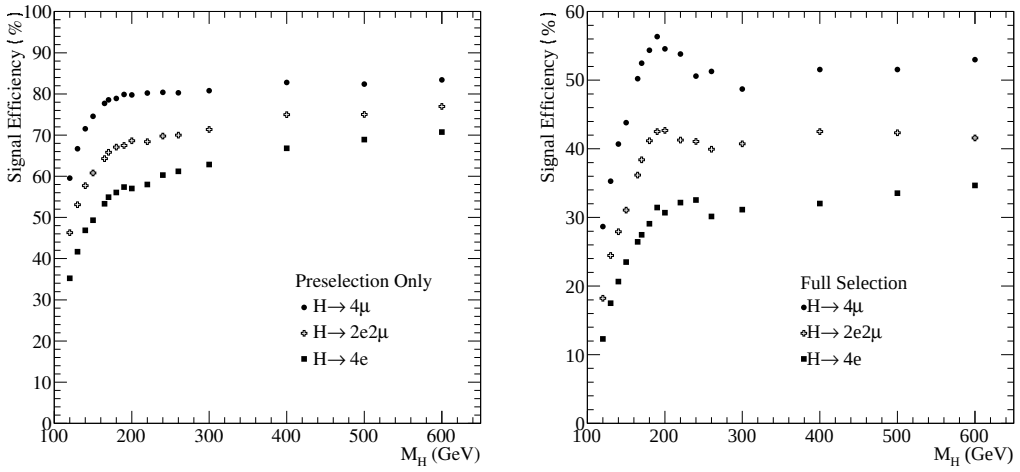

(a) (b)

Figure 6.19: (a) Preselection and (b) selection efficiency for each final state in the Higgs to four lepton channel as a function of the Higgs mass.

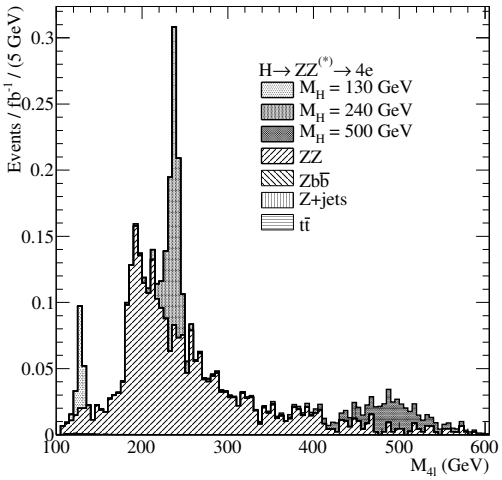

(a) $H \to ZZ^{(*)} \to 4e$.

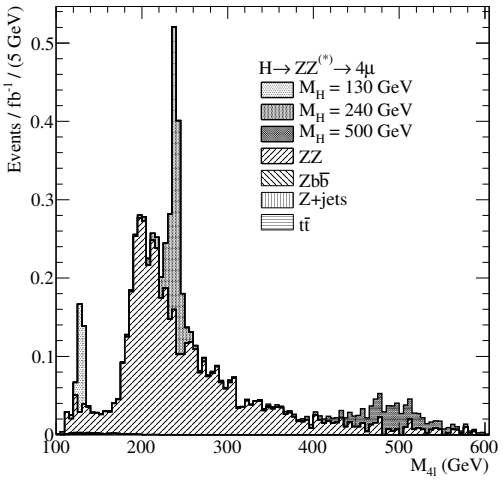

(b) $H \to ZZ^{(*)} \to 4\mu$.

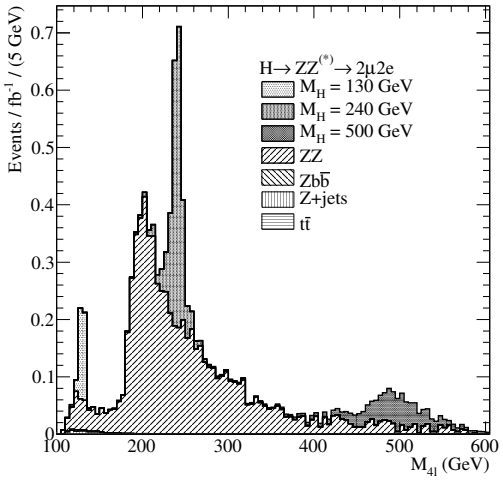

(c) $H \to ZZ^{(*)} \to 2e2\mu$.

Figure 6.20: Four lepton invariant mass distributions after the analysis requirements for the three final states, assuming a center of mass energy of 10 TeV. Different hypotheses for the Higgs mass are included: 130, 240 and 500 GeV.

6.6.1 Exclusion limits

The reduced number of expected events prevents a discovery in this first LHC run. In case no signal is observed, limits can be set on the production cross section normalized to the Standard Model prediction.

This exercise was done to assess the exclusion capability as a function of the Higgs mass. A modified frequentist approach based on the confidence level of the signal hypothesis was used, following the method adopted on Higgs searches at LEP [41]. One calculates the 95% confidence intervals for the number of events to be observed

in case of a SM Higgs boson with a given mass. The ratio R between the lower bounds on this calculation and the actual number of observed events is interpreted in this way: the upper bound for the Higgs cross section $\times$ branching ratio for a given mass is R times the SM prediction. If R is below 1, the Higgs is excluded at 95% CL.

The results for 10 TeV and 7 TeV are shown in fig. 6.21. The systematic uncertainties were found to play a minor role and thus are not included in these calculations. According to the values, no mass range can be excluded by the $H \to 4\ell$ channels alone. They can however contribute to a combination with the other search modes, as shown in fig. 5.13.

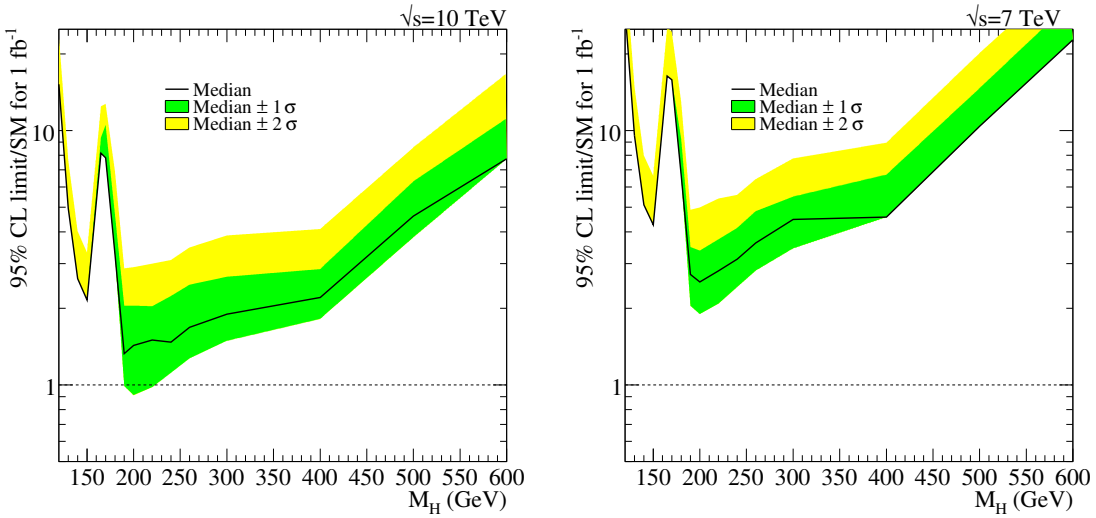

(a) (b)

Figure 6.21: Expected 95% CL upper limits on the Standard Model Higgs boson production in the $H \to ZZ^{(*)} \to 4\ell$ channel as a function of the Higgs mass for (a) $\sqrt{s} = 10$ TeV and (b) $\sqrt{s} = 7$ TeV. An integrated luminosity of 1 fb^{-1} is assumed. The bands indicate the 68% and 95% probability regions in which the limit is expected to fluctuate, in the absence of signal.

6.7 Perspectives

The Higgs searches are a main focus on the ATLAS physics program. The four lepton final states play an important role, being able solely to discover the Higgs boson over a wide mass range with a few tens of fb^{-1} at $\sqrt{s} = 14$ TeV. Section 6.6 discussed the near future of $H \to 4\ell$ searches. In a short time scale, the Higgs cannot be discovered nor excluded in this mode alone.

On the other hand, early data should allow a good understanding of the detector performance and measurements of the background yields. Performance studies have been carried on for the in-situ determination of the lepton reconstruction efficiencies, absolute scale uncertainty and resolution.

In the case of muons, cosmic events have greatly helped on these matters, although the statistics is concentrated in specific regions of the barrel spectrometer. Ultimate results require the reconstruction of Z bosons. Exploiting the very precise mass measurement at LEP and SLD, the calibration of high-momentum objects is totally based on $Z \to \ell\ell$ decays, comparing the reconstructed masses with M_Z.

These decays are also the key for efficiency determinations through a tag-and-probe method: one of the leptons (the tag) is selected with tight cuts while the other (the probe) can be chosen in an unbiased way to give an invariant mass close to M_Z. To quantify the lepton identification efficiency for example, one uses as probes Inner Detector tracks. For the ones that can form Z candidates together with tight leptons, one looks if they were tagged as electrons (muons) by the Electromagnetic Calorimeter (Muon Spectrometer). The efficiency is then given by the ratio $N_{leptons}/N_{tracks}$.

It was stressed in the present chapter that the rather poor knowledge on the yields of $Zb\bar{b}$ and ZZ processes were among the challenges faced by this analysis. Preliminary studies show that the first one could only be measured with a statistical uncertainty of 30% at 1 fb^{-1}. The second one may be determined directly through four lepton events or relying on the ratio to inclusive Z production (σ_{ZZ}/σ_Z) [76]. This ratio is rather well controlled theoretically and $Z \to \ell\ell$ yields will be measured with low statistical errors [77]. This method eliminates the dependence of the cross section on the luminosity uncertainties and reduces the errors on renormalization and factorization scales and on parton density functions. Its feasibility is currently under investigation. The direct quantification of $ZZ \to 4\ell$ should suffer from low statistics in this run, with approximately 9 events expected after the selection cuts for $\mathscr{L} = 1$ fb^{-1}.

An important limitation for $H \to 4\ell$ searches is the low signal yield and thus the associated selection efficiency must be maximized. A set of cuts that provide higher signal selection efficiency is already available and should be refined based on the knowledge about the detector capabilities and characteristics of the background acquired with LHC data.

Still relying on simulations there were improvements between the analyses done at $\sqrt{s} = 14$ and 10 TeV, mainly on the electron reconstruction side. Alternative vertexing requirements were also employed. A common vertex fit to the four leptons,

using the χ^2 of the fit as a discriminant variable proved to be more efficient than the impact parameter cut in the four muon channel. Better handling of calorimetric and track-based isolation were also pursued in the mean time, providing higher background rejection and lower sensitivity to pile-up effects in case of track isolation. The systematic uncertainties associated to these selection cuts (vertexing requirements, track and calorimetric isolation) still need to be included.

A dedicated selection for events where the Higgs decays to two off shell Z bosons was not yet studied and could enhance the sensitivity at low masses, depending on the rejection power of the isolation and vertexing requirements. Again, the optimizations related to this and the other analysis cuts should be studied as the experiment accumulates more data.

Chapter 7

Vector boson fusion analysis in $H \to 4\ell$ final states

The main background in $H \to 4\ell$ searches is the non-resonant production of Z boson pairs with subsequent decays to electrons and muons. The signal selection performed in the inclusive analysis, described in the previous chapter, is at least as efficient for this process as it is for Higgs events and thus it is said to be irreducible.

However, the cuts only deal with the leptonic part of the event, neglecting that the Higgs boson might be produced in association with other particles. While both $H + W/Z$ and $H + t\bar{t}$ have small yields, and would need huge amounts of data to be observed with the Higgs decaying to four leptons, the situation of vector boson fusion is more encouraging. Accounting for approximately 20% (10%) of leading order (NLO) Higgs production cross section, VBF has a distinct signature against other processes: highly energetic jets separated with large rapidity gaps, unlikely to be present in ZZ events. Exploring this fact, an exclusive analysis for this mode could reduce the contribution of the di-boson background.

The interest of this channel goes beyond the background reduction. Vector boson fusion can help characterizing the CP nature of Higgs particle and measuring its couplings to the W and Z, as mentioned in section 5.7. In the intermediate to high mass range, this production mode was mainly studied with the Higgs decaying to WW. The inclusion of another search mode is also beneficial in order to have a more complete picture.

The feasibility of VBF analyses in $H \to 4\ell$ final states was investigated for the first time in ATLAS and is reported in the present chapter. The same samples produced for the inclusive studies were used. They contain the full simulation of the ATLAS detector to signal and background events in collisions at $\sqrt{s} = 14$ TeV. The contribution of the ZZ + jets background was also evaluated.

7.1 Analysis strategy

The combination between the VBF production cross sections and the branching ratios of $H \to ZZ^{(*)} \to 4\ell$ implies very low yields for this channel. The number of expected events before any analysis cuts in the two dominant production modes (illustrated in fig. 7.1) is shown in fig. 7.2, for an integrated luminosity of 30 fb^{-1}.

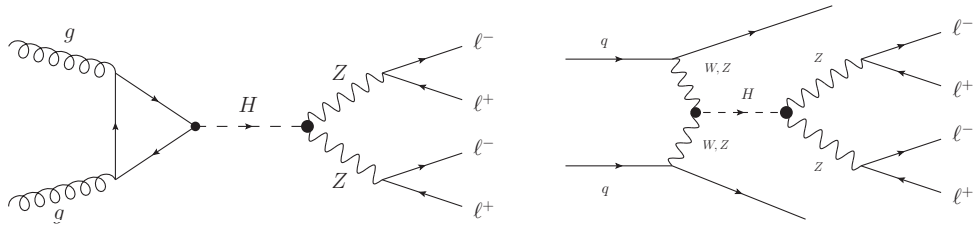

(a) Gluon fusion. (b) Vector boson fusion.

Figure 7.1: Leading order diagrams for $H \to 4\ell$ production.

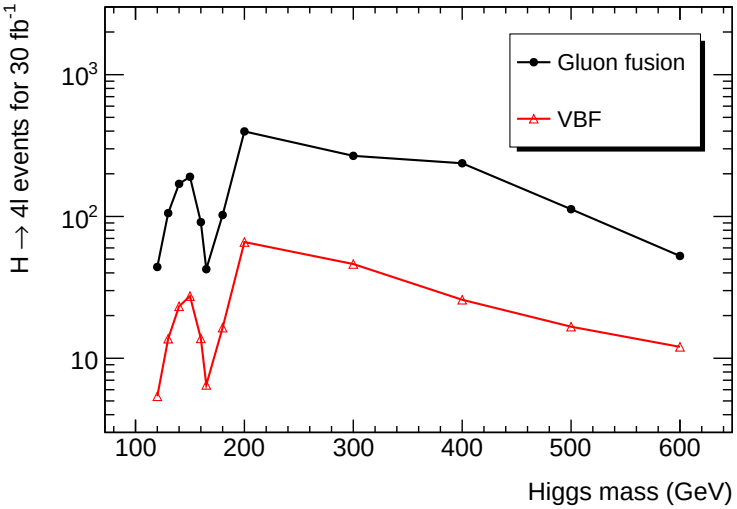

Figure 7.2: Expected number of Higgs boson events produced by gluon fusion and vector boson fusion (VBF) at $\sqrt{s} = 14$ TeV, decaying to 4-leptons with $P_T > 5$ GeV and $|\eta| < 2.7$, for $\mathscr{L} = 30$ fb^{-1}. Next-to-leading order cross sections were used for both processes.

The opening of the on-shell decay to a pair of Zs is behind the great increase observed close to $M_H = 180$ GeV, which also explains the rise of the ZZ background. Right before this threshold, the Higgs decays predominantly to a pair of W bosons, leaving the four lepton channels with very low rates. These two arguments define the region of interest for the present analysis: Higgs masses from 180 GeV and above

are more easily accessible through $H \to 4\ell$, exploring the VBF production mode to reduce the di-boson background that augments in this region.

The starting points of this study were two rather well established analyses in ATLAS: the inclusive $H \to 4\ell$ and the $H \to \tau^+\tau^-$ searches via vector boson fusion production [56]. The simple combination of the two, taking the lepton selection and Higgs boson reconstruction from the first, and jet tagging from the second was used as a guideline. In a first attempt to apply the cuts on forward jets on top of the four lepton selection, approximately 10% of the signal events were kept and only 1% of $ZZ \to 4\ell$. This encouraging result motivated the optimizations pursued here in order to increase the signal yields. Three aspects were identified and are detailed in the next sections:

- Verification of the selection efficiency for VBF events in the inclusive four lepton analysis;
- Study of the efficiency of the forward jet tagging;
- Application of the jet tagging to perform a full VBF $H \to 4\ell$ analysis, optimizing the selections to try to have a few events in the end at $M_H = 180$ GeV with $\mathscr{L} = 30$ fb^{-1}.

7.2 VBF events in the inclusive $H \to 4\ell$ analysis

One contribution from this study to the inclusive analysis was the verification that the proportion between gluon fusion and vector boson fusion events was kept throughout the cut flow. The efficiency of each cut does not vary more than 0.5% between the two modes and the ratio between their yields in the end is basically the same as in the input, both at $M_H = 130$ and 180 GeV. If this turned out not to be the case, a more careful treatment would have to be made for summing the cross sections in the end.

A glance at some basic distributions, shown in fig. 7.3, might suggest otherwise. The Higgs is more central and has a higher transverse momentum in VBF when compared to gluon fusion. One should note that the simulations are done at leading order, and the Higgs P_T in gluon-gluon production comes only from initial and final-state radiation. Next-to-leading order effects might change this picture. The impact on the lepton distributions is smaller and probably this is behind the small differences observed in the selection.

In summary, VBF events are not disfavoured by the standard cut flow, and thus no major changes in the lepton selection are required for the present analysis. The

trigger strategy, in particular, does not need to be modified. Other modifications were introduced to increase the final selection efficiency. They will be discussed in section 7.5, once the jet tagging is defined.

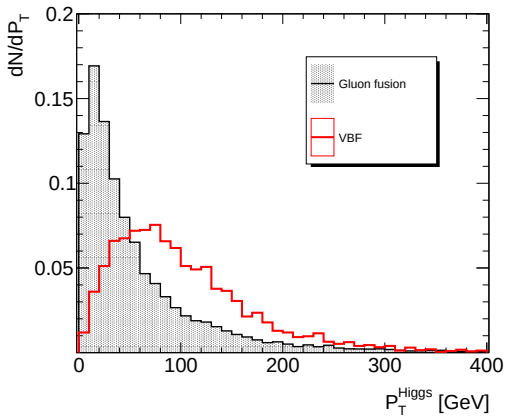

(a) Transverse momentum of the Higgs boson.

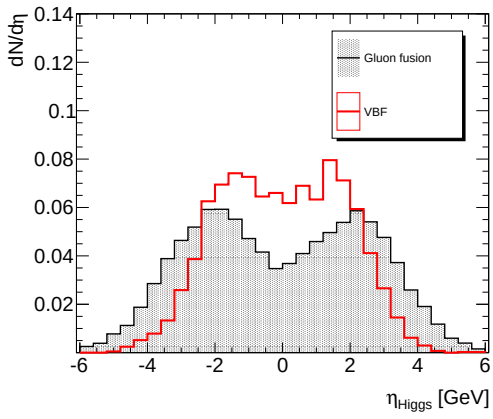

(b) Pseudo-rapidity of the Higgs boson.

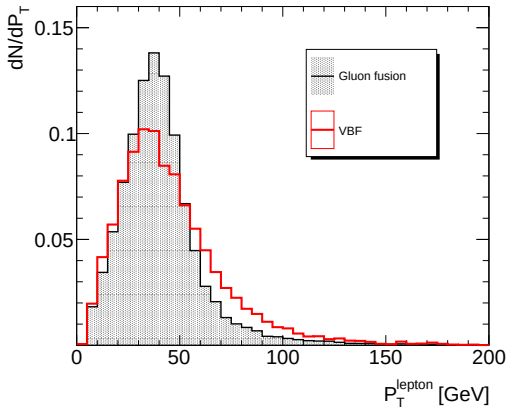

(c) Transverse momentum of the leptons.

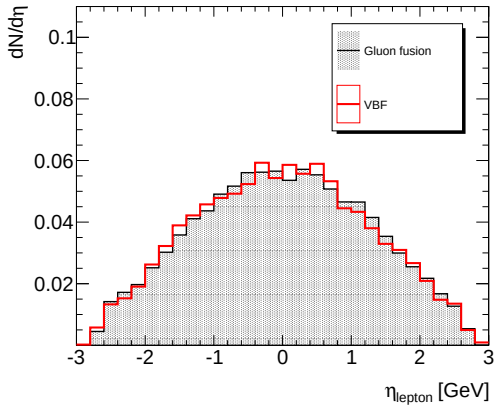

(d) Pseudo-rapidity of the leptons.

Figure 7.3: Kinematic distributions of the Higgs boson and its decay products (leptons) in gluon fusion and vector boson fusion events in the $H \to 4\ell$ samples with $M_H = 180$ GeV.

7.3 Optimizations of jet tagging and selection

The most relevant feature of VBF for this analysis is the presence of two quark-initiated jets with high transverse momentum, usually separated by large rapidity gaps and found in the forward region of the detector. The standard procedure to tag these objects is to select the two jets with the highest P_T in the event. This method was reviewed as part of the optimizations pursued to increase the signal

yields. The choice of the jet algorithm, however, relied on the studies done in the di-tau final states, which are briefly presented in the following. All the optimization studies described in this section used $H \to 4\ell$ samples with $M_H = 165$ GeV.

7.3.1 Choice of the jet algorithm

Different jet algorithms are employed in ATLAS, combining any set of four momentum objects such as calorimeter towers or clusters, tracks and particles from an event generator in the case of simulated events. The most important sub-systems for jet reconstruction are the calorimeters, and the presence of forward jets in vector boson fusion events requires the full detector acceptance. In particular, the use of the forward calorimeters that cover the region of $3.1 < |\eta| < 4.9$ is essential, and the efficiency for jet finding in this part of the detector drove the choice for the jet algorithm and input objects.

An important aspect is that jet and electron reconstruction are completely independent. Therefore, nothing prevents overlaps between them and their removal must be done at the analysis level. This issue will be treated in the next subsection.

Input objects and jet reconstruction

Towers and clusters are the most common inputs for jets. Both are groups of calorimeter cells with the four momentum given by the sum of the energy and momentum components of the cells. Each cell is treated as a massless four momentum object with the direction defined by the vector that connects the interaction point to its center. All the energies are given at the electromagnetic scale and calibration procedures are normally applied only to jets and not to the towers or clusters. The calibration used in this analysis will be discussed shortly.

Calorimeter towers are a projection of all the cells in a fixed grid in pseudo-rapidity and azimuth ($\Delta\eta \times \Delta\phi = 0.1 \times 0.1$). The energy deposited in non-projective cells, or cells that extend beyond the grid-size is divided according to the ratio of the area on each grid element to the total cell surface in $\eta \times \phi$, as illustrated in fig. 7.4. Topological clusters, on the other hand, are an attempt to reconstruct three-dimensional "energy blobs" representing the showers developing for each particle entering the calorimeter. The number of clusters is expected to follow the number of particles in the jet, which is approximately verified. The clustering is seeded by high energy deposits and stops when cells with low signal to noise ratio are encountered in the vicinity of the seed. A splitting algorithm is run afterwards to separate clusters containing more than one local maximum.

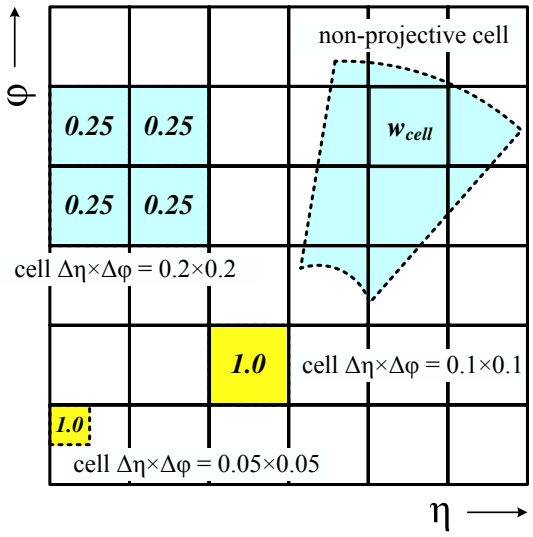

Figure 7.4: Contribution of cells to calorimeter towers on a regular grid of $\Delta\eta \times \Delta\phi = 0.1 \times 0.1$. The numbers illustrate the partition of the cell energy between the towers according to the fraction of its area in each grid element.

Concerning the jet finder, a cone algorithm seeded by high energy deposits ($E_T > 1$ GeV) was the natural choice in ATLAS when this analysis was performed, with fixed cone sizes of $\Delta R = 0.4$ or 0.7. Although no significant differences were observed between the two, the first option was used in $H \to \tau^+\tau^-$ analysis for providing better handle on additional jets in the event. This guideline was followed here.

The clustering algorithms, on the other hand, exhibit very different performance. While the efficiency for finding jets based on topological clusters is almost flat as a function of pseudo-rapidity, the same curve for jets formed out of calorimeter towers shows a big drop in the forward region. This is probably due to the non-projective nature of the FCal. The comparison is shown in fig. 7.5, and motivated the choice in favour of topo-clusters.

Finally, the minimum transverse momentum required for the reconstructed jets was fixed at 20 GeV, like in $H \to \tau^+\tau^-$ searches. It was chosen as a compromise between the reconstruction efficiency, which increases rapidly in this region exceeding 80% close to this value, and the fakes that quickly decrease from almost 50% at $P_T = 10$ GeV to less than 10% for $P_T > 20$ GeV [78]. Both quantities are shown in fig. 7.6.

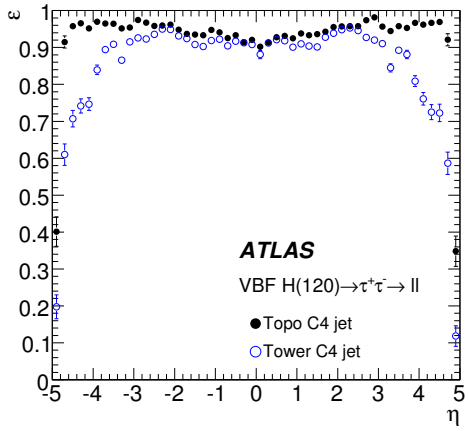

Figure 7.5: Reconstruction efficiencies as a function of pseudo-rapidity for jets from vector boson fusion based on calorimeter towers (open circles) and topological clusters (closed circles) in VBF $H \to \tau^+\tau^-$ simulated events (from ref. [56]).

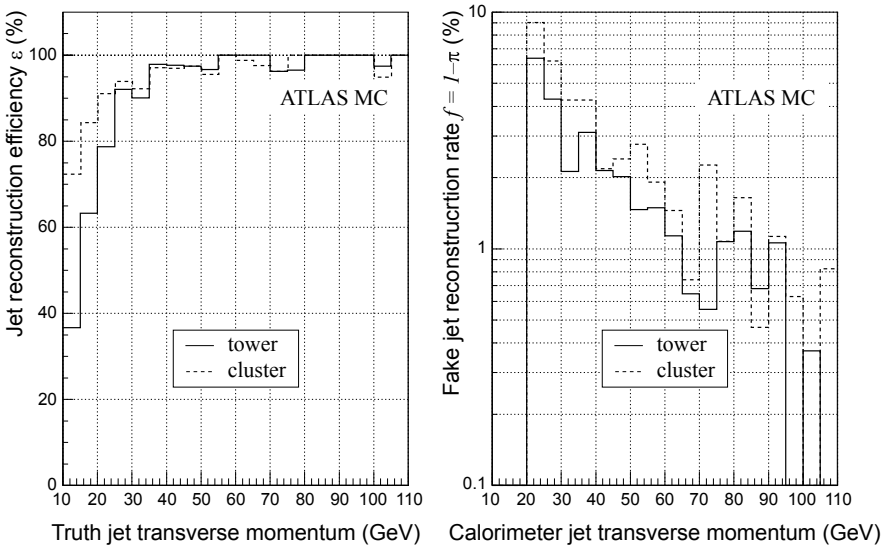

Figure 7.6: Expected efficiencies and fake rates as a function of transverse momentum for reconstructing jets in the forward region ($2.7 < |\eta| < 4.9$) with a cone algorithm of $\Delta R = 0.4$ based on calorimeter towers or topological clusters, in VBF $H \to \tau^+\tau^-$ simulated events (from ref. [78]).

Jet energy calibration

The energy and momentum of the jets are calibrated in two steps. The first one will be outlined here and corrects for detector effects: calorimeter non-compensation[1], noise, losses in dead material and cracks, longitudinal leakage and particle deflection in the magnetic field. After this step the jets are said to be calibrated at the *particle level*, i.e. the jet energy should correspond to the one obtained after running the same jet algorithm over all true momenta of the final-state particles in the event. The second step attempts to reproduce the energy at the *parton level*. It depends on the process under consideration and is required in some analyses for obtaining ultimate precision. They will not be discussed nor applied here. The reader is referred to ref. [10] for more information.

The 'H1 scheme' [79] is usually adopted in the first step of jet calibration. The idea is to weight the energy of each cell according to the associated signal density ρ, defined as the ratio between the cell energy and volume. High energy densities are related to electromagnetic interactions while hadronic interactions are expected to give rise to low density signals in the non-compensating ATLAS calorimeters. A set of weights $w(\vec{x}, \rho)$ that depend on the cell position $\vec{x}$ and energy density was derived from Monte Carlo simulations of di-jet events. Their role is to minimize variations in the calorimeter response as a function of the jet energy (non-linearities) and position (non-uniformities). The final four momentum of the jets is given by the sum of the weighted energies and momenta of the cells:

$$\left(E_{jet}, \vec{P}_{jet}\right) = \sum_{i}^{N_{cells}} w(\vec{x_i}, \rho_i) \left(E_i, \vec{P_i}\right) . \tag{7.1}$$

An alternative scheme called 'local hadron calibration' is also adopted in ATLAS. It exploits the fine granularity of the calorimeters (specially the LArEM) to try to classify the clusters as hadronic or electromagnetic. This time both clusters and jets are calibrated at the hadronic scale again using corrections derived by Monte Carlo. Both methods aim at bringing the uncertainty on the jet energy scale to $\mathcal{O}(1\%)$.

The present study followed the strategy adopted in the $H \to \tau^+\tau^-$ analysis and used jets calibrated by the H1 scheme. A complete description of both methods can be found in ref. [78].

[1] Electromagnetic and hadronic particles of the same incident energy usually induce different amounts of signal in a calorimeter. When their ratio (usually noted as e/π or e/h) differs significantly from one, the calorimeter is said to be non-compensating. The ATLAS calorimeters have $e/\pi \approx 1.5$ [78].

7.3.2 Tagging method for the forward jets

The traditional strategy to associate the two jets with highest transverse momenta to the quarks that generate the vector boson fusion (noted as 'VBF quarks' hereafter) was reviewed. In order to test different tagging methods, reconstructed jets were matched to VBF quarks geometrically, taking the closest jet in ΔR with respect to each quark. The correlation between their transverse momenta, shown in fig. 7.7a, validated this choice. Typically, the jets are found within $\Delta R < 0.1$ from the quarks (fig. 7.7b), but values up to $\Delta R = 0.2$ were accepted to maximize the matching efficiency. Good P_T correlation was still verified for these cases. This cut value is also adopted in jet performance studies in ATLAS (ref. [78]).

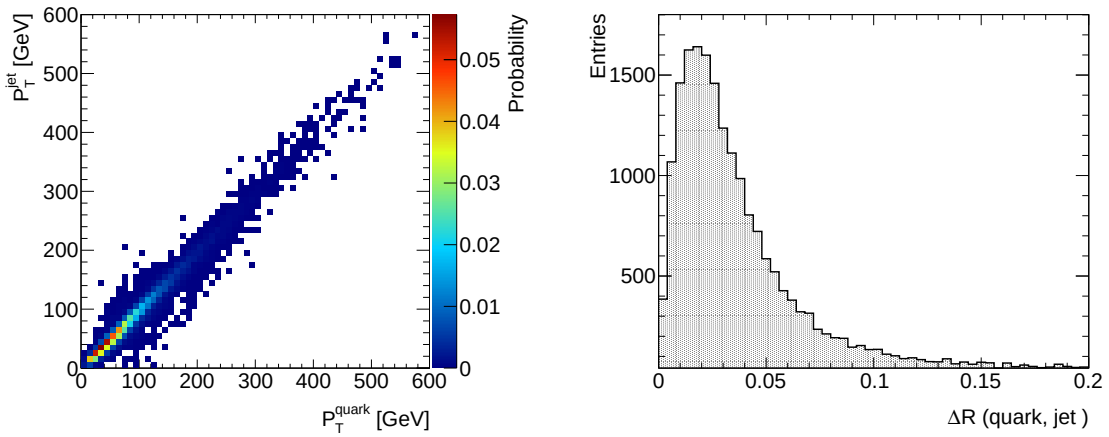

(a) Correlation between the transverse momenta of a VBF quark and the closest reconstructed jet.

(b) Distance between a VBF quark and the closest reconstructed jet.

Figure 7.7: Matching between VBF quarks and the closest reconstructed jets in $H \to 4\ell$ samples with $M_H = 165$ GeV.

Alternative methods to tag the forward jets were compared, always in the four muon channel to avoid the overlap with the electrons from the Higgs decay. The role of the latter ones will be evaluated afterwards. The following strategies were tested, for events where both quarks were matched to jets with $P_T > 20$ GeV:

- Selecting the two jets with the highest transverse momenta in the event.
- The two jets with highest transverse momenta in each hemisphere with respect to $\eta = 0$.
- The two jets with the largest separation in pseudo-rapidity.
- The pair of jets that gives the largest invariant mass.

- The two jets that give an optimal P_T balance with the selected lepton quadruplet.
- The most energetic jet combined with the one that satisfies either of the above criteria (maximum rapidity gap, maximum invariant mass or minimum P_T when combined to the quadruplet).

The highest P_T jets were correctly associated to the quarks in approximately 83% of the cases in the four muon channel. Better performance was obtained by the pair of jets with the largest invariant mass ($\sim 88\%$) or combining the most energetic jet with the one that maximizes the invariant mass of the system ($\sim 90\%$).

A look at the other four lepton final states ($H \to 4e$ and $H \to 2e2\mu$) showed that actually the electrons from the Higgs decay were often reconstructed as jets and corresponded to the highest P_T objects of this kind. These 'overlaps' were removed by discarding the jets close to the electrons selected for the Higgs analysis, i.e. the ones that passed momentum cut, lepton quality and isolation criteria. A minimum distance of $\Delta R > 0.2$ between them was required. This value maximizes the tagging efficiency while minimizing the probability to remove some of the correct VBF jets which happen to be close to the electrons.

Table 7.1 shows the VBF quark association efficiency before and after the overlap removal in all $H \to 4\ell$ final states, for the highest P_T jets and the pair of jets with the highest invariant mass. The efficiencies increased considerably after removing the overlaps specially when the highest P_T jets were used. The remaining discrepancies between electron and muon final states come from the electrons that fail the selection criteria for overlap removal and are identified as jets. Those will not enter the final event selection that will be described in section 7.4.

Selecting the pair of jets with the highest invariant mass proved to be more efficient and less sensitive to the presence of fake jets from electrons when compared to the previous method. Therefore, this strategy was adopted as tagging criteria. Overall, the correct association with the VBF quarks reached almost 85%.

7.3.3 Event selection based on tagged jets

Once the tagged jets were defined, the next aspect to be reviewed was the selection based on their kinematics to reduce the background yields. Normally the transverse momentum of the jets, their rapidity separation and invariant mass are the main discriminants between VBF and other events.

A central jet veto is usually explored, motivated by the fact that the Higgs is a color singlet, which suppresses additional QCD radiation in the event. This is

Table 7.1: Efficiencies (in %) for associating the VBF quarks with the highest P_T reconstructed jets or the pair with the largest invariant mass in each event, before and after removing the jets close to electrons from Higgs decays (overlaps). Only VBF $H \to 4\ell$ events (with $M_H = 165$ GeV) where both quarks were matched to jets with $P_T > 20$ GeV were used.

	VBF quark to jet matching efficiency (%)			
	Before overlap removal		**After overlap removal**	
Mode	**Method**		**Method**	
	Highest-P_T	Invariant mass	Highest-P_T	Invariant mass
$H \to 4\mu$	82.8	88.3	82.9	88.2
$H \to 4e$	12.4	72.6	56.9	81.0
$H \to 2e2\mu$	25.8	78.9	67.8	85.1
All	36.9	79.7	68.9	84.8

especially true for the region between the VBF jets. The cut is very powerful against the background, but its performance is greatly reduced in the presence of pile-up. Due to the absence of pile-up samples both for the signal on Higgs masses above 130 GeV and for the backgrounds, the veto was not applied in this analysis.

In view of the expected low yields for $H \to 4\ell$ channels, the cuts used for instance in the $H \to \tau^+\tau^-$ analysis (mainly the distance between the jets in pseudo-rapidity $\Delta\eta > 4.4$, the invariant mass of the jet pair $m_{jj} > 700$ GeV and the transverse momentum of the jets $P_T^1 > 40$ GeV, $P_T^2 > 20$ GeV) reduce excessively the signal efficiency, keeping approximately 10% of the events. An optimization of the cut values was pursued to increase this rate.

Taking the reconstructed jet pair with the highest invariant mass in each event, the distributions of the kinematic variables for these objects on ZZ events, Higgs production via gluon fusion and vector boson fusion were compared. In addition to the discriminants used in $H \to \tau^+\tau^-$ searches, the distance between the jets in azimuth ($\Delta\phi$) and the rapidity of the forward-most jet (max $|\eta|$) were explored. Only the events with at least two jets of $P_T > 20$ GeV and separated from the electrons used in the analysis (with $\Delta R > 0.2$) were considered. For VBF events, the selection was restricted to the jets correctly associated to quarks in this optimization phase.

Figure 7.8 shows the distributions obtained for the three processes. One notes that while ZZ and Higgs production through gluon fusion have similar patterns, a clear separation is observed with respect to vector boson fusion. The discriminating power of each variable was determined from the selection efficiency for VBF Higgs production and ZZ events, and is shown in fig. 7.9.

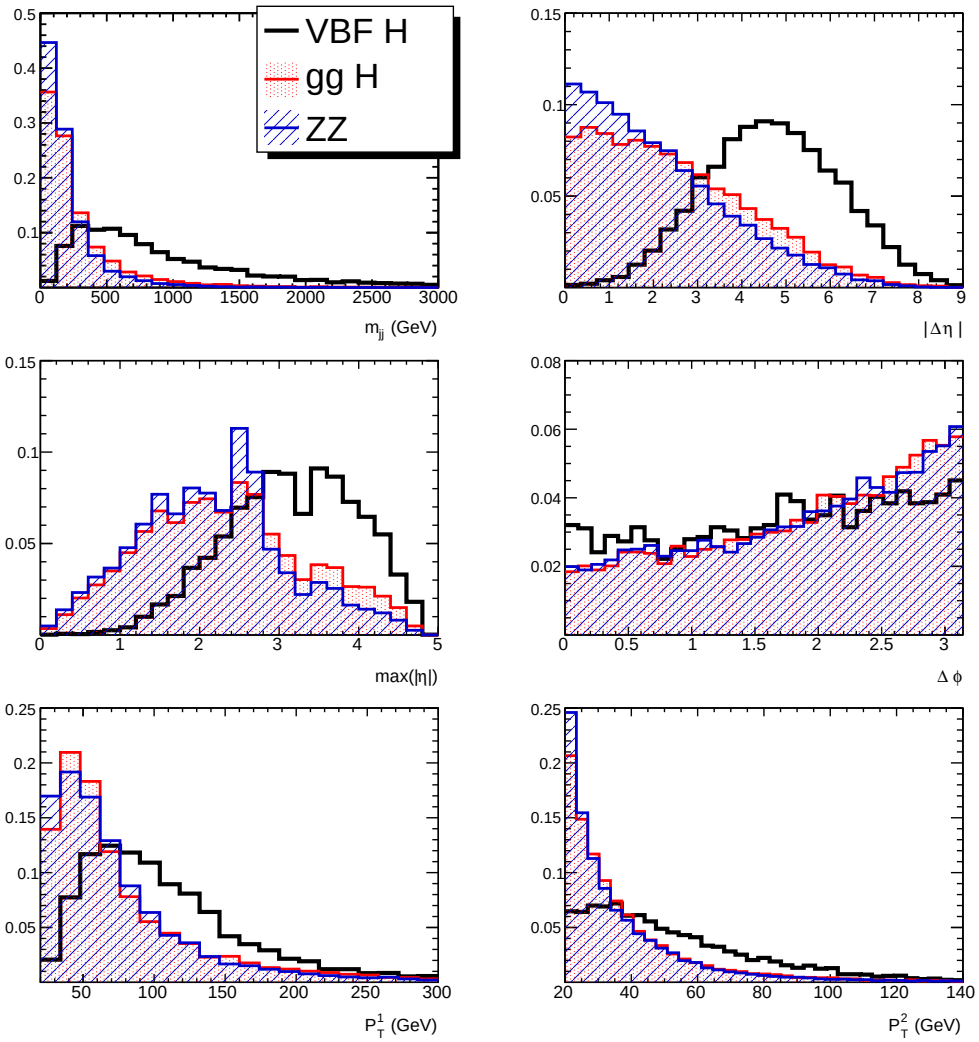

Figure 7.8: Normalized distributions of the discriminant variables (described in the text) used in jet tagging selection, for ZZ events and Higgs events produced through vector boson fusion (VBF H) and gluon fusion ($gg\,H$) with $M_H = 165$ GeV.

Even if the selection of the jet pairs was based on their invariant mass, this quantity appears to be the most performant in the background rejection. The rapidity gap between the jets, one of the remarkable characteristics of VBF, is also very useful in the distinction between the processes. Surprisingly, some of the VBF jets were found at low rapidities, while the other processes contain some very forward ones, reducing the discrimination of the maximum value of $|\eta|$. The excess of jets at $|\eta| \sim 2.5$ in the background comes from the electron contamination (after the overlap removal). The distribution of $\Delta\phi$ in the background is driven by the maximization of the invariant mass of the pair, which prefers back-to-back jets. The signal distribution, in turn, is flat due to the CP quantum numbers of the Higgs boson as discussed in section 5.7. Both this variable and the transverse momenta

of the jets do not provide much information for the signal selection. Finally, one should note that the quantities are highly correlated (the linear correlation factors vary from 30% to 80%) as they are all connected to the jet kinematics.

An optimal rejection curve was derived using the *Toolkit for Multivariate Data Analysis with ROOT* (TMVA) [80] for the combination of the selections on the invariant mass and the rapidity gap between the jets. It followed a cut-based approach as in the inclusive analysis and the results are shown in fig. 7.10. The use of multivariate methods and the addition of the other variables seems to improve the discrimination by reducing the background by around 10%. One notes that separating the two Higgs production mechanisms is more difficult than rejecting di-boson events. The contamination from gluon-gluon events is considered beneficial for the discovery potential of $H \to 4\ell + 2$ jets channel. On the other hand, an exclusive VBF analysis would require a lower signal selection efficiency.

The working point was chosen at a efficiency of 84% for vector boson fusion, with a rejection factor around 6 against ZZ, as shown in table 7.2. The corresponding cuts are $m_{jj} > 300$ GeV and $\Delta\eta > 2.5$. Additionally, the table shows that the rate of events containing at least to jets is significantly lower in the four muon channel for both ZZ and Higgs production via gluon fusion. Again, this indicates that some electrons from Z decays fail the selection for overlap removal and are identified as jets. They will be suppressed by the lepton selection criteria described below.

Table 7.2: Efficiencies (in %) of jet tagging, jet selection for the tagged events and their product in all final states and only 4μ final state for VBF H, $gg\,H$ and ZZ ($M_H = 165$ GeV). The jet tagging includes the overlap removal described in the previous section and keeps only the pair of jets with the highest invariant mass. For VBF events only the jets associated with quarks are considered.

Cut	**Description**	**Efficiency (%)**					
		VBF H		$gg\,H$		ZZ	
		All final states	4μ only	All final states	4μ only	All final states	4μ only
Jet tagging	2 jets with $P_T > 20$ GeV	56.5	59.0	41.3	28.4	29.1	20.1
Jet selection	$m_{jj} > 300$ GeV, $\lvert\Delta\eta\rvert > 2.5$	84.0	82.4	24.6	30.2	16.5	18.5
Total	(tagging × selection)	47.5	48.6	10.2	8.6	4.8	3.7

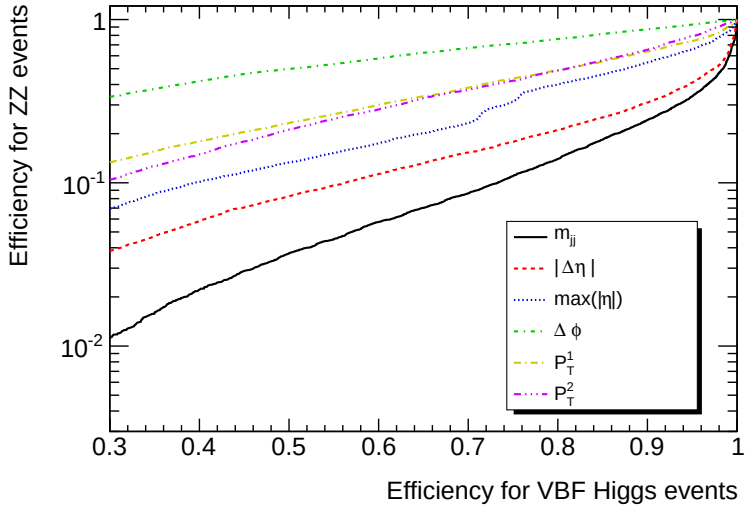

Figure 7.9: Efficiencies of the variables used in forward jet tagging selections on VBF Higgs ($M_H = 165$ GeV) and ZZ events.

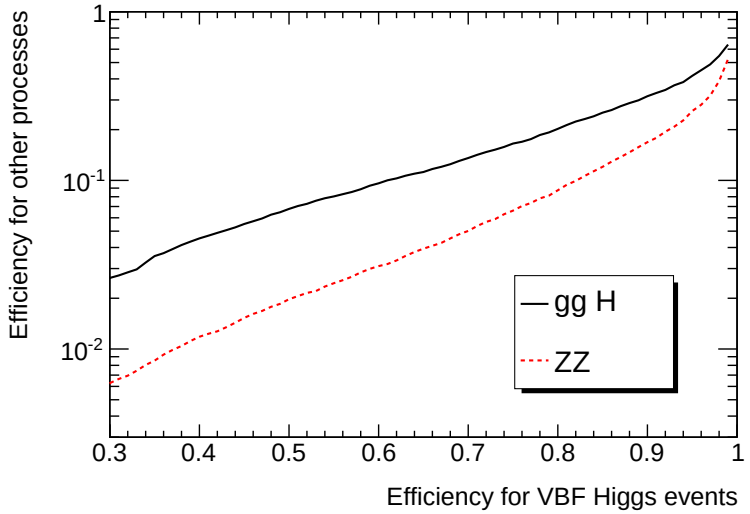

Figure 7.10: Efficiencies of the combined selections on the invariant mass of the jet pair and their rapidity gap in VBF Higgs, gluon fusion Higgs (both with $M_H = 165$ GeV) and ZZ events. The working point was chosen at a signal efficiency near 84%.

7.4 Event selection

The combination of the standard inclusive analysis at $M_H = 180$ GeV with the optimized forward jet tagging would be only slightly above the desired limit of 3 vector boson fusion events expected at an integrated luminosity of 30 fb^{-1}. Since the background should be further reduced by the cuts on the forward jets, an attempt to increase the signal yields without losing the sensitivity was made and is described below. It consisted in relaxing some cuts and allowing more background in the final selection.

At the same time that this study was carried out, an optimization of the electron identification criteria was being evaluated. Later it was adopted as the default method for providing an overall increase of efficiency around 5% for the *Medium* definition, with extra jet rejection power. A preliminary version of these developments was incorporated in the present analysis.

Another change with respect to the inclusive selection concerns the impact parameter requirements for the leptons. This cut removed about 15% of the signal in the inclusive analysis, and was also under review when this result came out. The simplest decision was to remove it temporarily, in order to demonstrate the viability of the VBF analysis with the increase of the signal rates. As will be seen shortly, the yields of the reducible backgrounds still remain well below the levels of di-boson production, and almost irrelevant for this analysis. The summary of the analysis cuts is given in table 7.3.

Table 7.3: Summary of the cuts adopted in the VBF $H \to 4\ell$ analysis. The two lepton pairs are denoted as $Z1$ and $Z2$.

Jet selection	The two jets with the highest invariant mass in the event, satisfying $P_T > 20$ GeV, $m_{jj} > 300$ GeV and $\Delta\eta > 2.5$.
Lepton selection	Four leptons: *MediumElectrons*, combined or tagged muons, with $P_T > 7$ GeV and $\|\eta\| < 2.5$. At least two with $P_T > 20$ GeV.
Kinematic cuts	Two pairs of same flavour opposite charge leptons. Z, Z^* and Higgs reconstruction: single quadruplet with $\|M_{Z1} - M_Z\| < 12$ GeV and $M_{Z2} > 40$ GeV.
Isolation cuts	Calorimetric isolation for muons ($\Sigma E_T/P_T < 0.23$). Inner detector track isolation for leptons ($\Sigma P_T/P_T < 0.15$).

7.5 Expected sensitivity of VBF analysis in $H \to 4\ell$ final states

Contrary to the inclusive searches, this study used leading order cross sections for signal and background processes. The application of K-factors was considered not adequate since the jet kinematics can be modified considerably by the inclusion of higher order effects (when compared to the leading order diagrams used for the generation).

The four lepton invariant mass spectra with and without the application of the jet tagging criteria are shown in fig. 7.11. After the application of the cut, a clear suppression of the ZZ background is observed, and the contribution of VBF events becomes dominant over gluon fusion. The presence of the $Zb\bar{b}$ background is way below the level of ZZ in the inclusive spectrum (fig. 7.11a) as desired, even without the impact parameter requirements. The $t\bar{t}$ background was not considered here since already with the inclusive selection no event was found in the end. The jet selection should reduce it further and therefore its contribution is negligible.

The expected number of events for each Higgs production mode and the main backgrounds is given by the integral of each component in a mass window between 170 and 185 GeV, and is listed in table 7.4. The corresponding significance was determined using Poisson statistics. The inclusive analysis from chapter 6 is also included, using both LO and NLO cross sections for comparison.

When compared to the analysis described in the previous chapter, the present one without the jet selection has lower signal over background ratio (S/B) due to the use of a slightly larger mass window (15 GeV against ~ 12 GeV). On the other hand, this modification contributes to the increase in the signal efficiency, leading to a higher significance.

After the cut on forward jets, almost 6 VBF events can be expected for $\mathscr{L} = 30$ fb^{-1}, with a signal survival probability of 2/3. The cut reduces considerably the yields of all other processes, suggesting that an exclusive VBF analysis in four lepton final states is feasible with integrated luminosities of tens of inverse femtobarns.

Including events produced via gluon fusion, the signal over background ratio was increased by almost one order of magnitude with the jet selection. The associated significance is above 5σ, showing that a Standard Model Higgs boson with a mass of 180 GeV could be discovered in the $H \to 4\ell + 2$ jets channel alone.

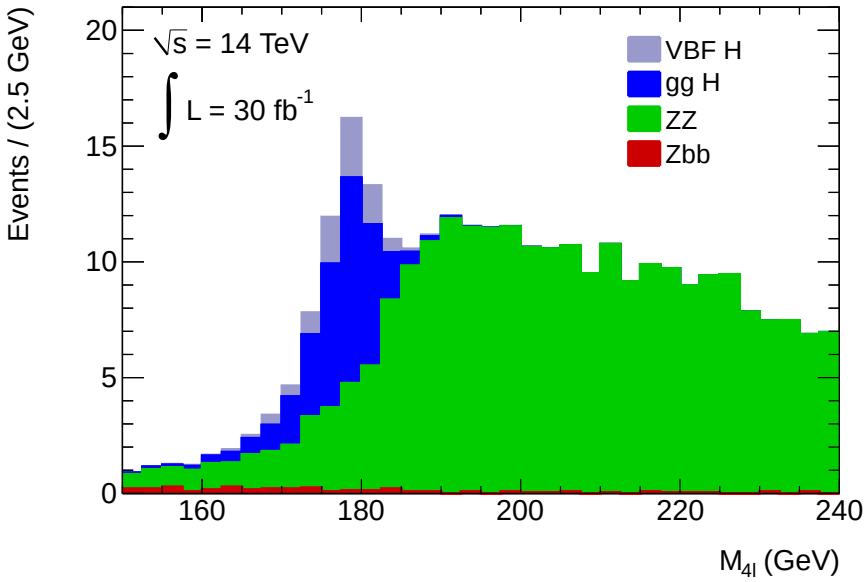

(a) Without forward jet tagging.

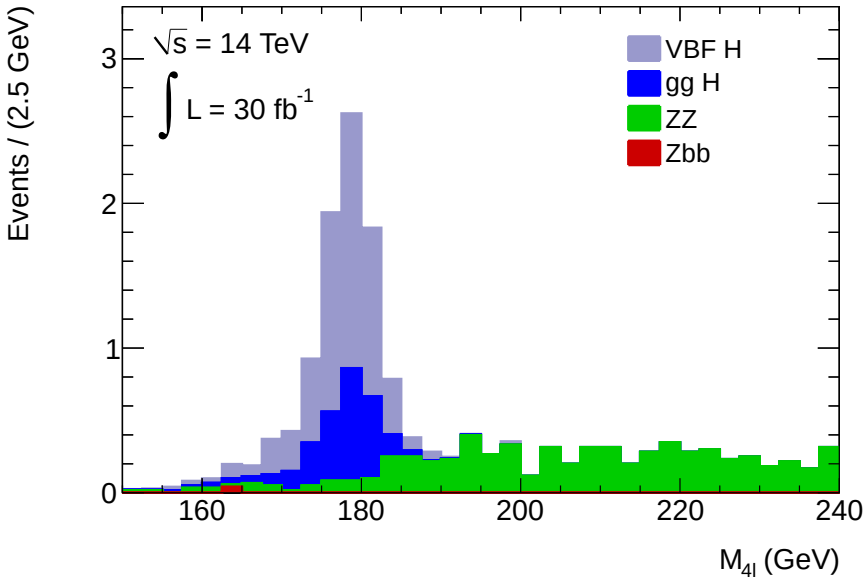

(b) With forward jet tagging.

Figure 7.11: Four lepton invariant mass spectrum after the application of the selection cuts (except for the Higgs mass window) in case of a Higgs boson mass of 180 GeV, normalized to $\mathscr{L} = 30$ fb^{-1}.

Table 7.4: Expected events, signal over background ratio (S/B) and Poisson significance at $\mathscr{L} = 30$ fb^{-1} for the Higgs signal ($M_H = 180$ GeV) and main backgrounds after the full selection. The inclusive analysis described in the previous chapter is compared to the present one using leading order and next-to-leading order cross sections (except when the VBF cut is applied). For the $Zb\bar{b}$ background, 68.3% CL limits were set when no event passed the selection.

	Inclusive analysis		**This analysis without VBF cut**		**This analysis with VBF cut**
Process	**Number of expected events**				
LO or NLO	LO	NLO	LO	NLO	LO
Higgs (gluon fusion)	18.5	34.1	29.5	54.3	2.5
Higgs (VBF)	5.4	5.5	8.4	8.6	5.6
ZZ	17.5	28.1	36.5	58.9	0.8
$Zb\bar{b}$	0.27	0.39	1.0	1.5	< 0.05
S / B					
1.3	1.4		1.0	1.0	9.2
Significance					
5.0	6.2		5.6	7.1	5.4

7.5.1 Contribution of ZZ + jets events

The samples used for this study, generated with `PYTHIA`, only include leading order diagrams. With the exception of vector boson fusion, the jets always originate from the underlying event or initial and final-state radiation. A concern about the accuracy of this description arose due to the low efficiency of the cuts on forward jets ($m_{jj} > 300$ GeV and $\Delta\eta > 2.5$).

It is known that a more realistic simulation of the jet kinematics is obtained by considering final-state partons already in the matrix element calculation. By matching the hard process with the parton evolution, the leading logarithmic contribution from higher order effects are absorbed.

This is done by the `ALPGEN` generator, separating the inclusive ZZ production into the exclusive processes ZZ + N jets, with N $= 0, 1, 2, \ldots$ Moreover, `ALPGEN` includes electroweak diagrams for di-boson production, absent in `PYTHIA`. Some of those are illustrated in fig. 7.12, and constitute irreducible backgrounds for this analysis. Fortunately their contribution is well below the Higgs signal, as shown in ref. [81].

Monte Carlo samples including ZZ + jet events were produced after this analysis

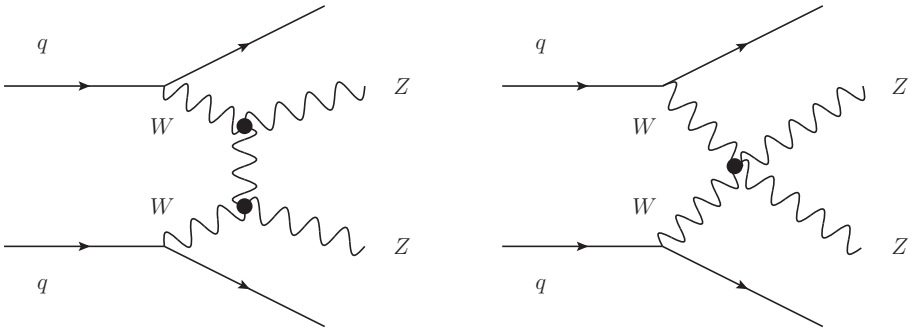

Figure 7.12: Some of the diagrams for electroweak ZZ production.

was completed, at a different center of mass energy: $\sqrt{s} = 10$ TeV. It used ALPGEN interfaced to HERWIG for the parton shower generation. Up to three hard partons were considered, requiring $P_T > 15$ GeV and $|\eta| < 6$ for each of them. Inclusive PYTHIA samples were also produced in this configuration, allowing the comparison between the jet kinematics in the two approaches. The number of events on each sample is listed in table 7.5[2].

Table 7.5: Number of events and ratio between the exclusive and inclusive cross sections of $ZZ \to 4\ell$ Monte Carlo samples ($\sqrt{s} = 10$ TeV) used in the evaluation of the ZZ + jet contribution to this analysis.

Process	**Generator**	$\sigma/\sigma_{inclusive}$	**Events**
ZZ inclusive	PYTHIA	1	86 831
ZZ + 0 parton	ALPGEN	0.56	1 480
ZZ + 1 parton	ALPGEN	0.27	743
ZZ + 2 partons	ALPGEN	0.13	357
ZZ + 3 partons	ALPGEN	0.04	174

The contribution of each exclusive process in the ALPGEN samples is shown in fig. 7.13, weighted by the relative cross sections. Although the statistics is low, a few conclusions could be drawn. In the following, all the quoted errors are purely statistical.

The fraction of events containing two high-P_T jets (above 20 GeV) is increased with respect to PYTHIA, moving from $15.6 \pm 0.1\%$ to $21 \pm 1\%$. Their kinematics, however, is essentially unchanged, as demonstrated by the distributions of the sepa-

[2]Events where any of the Zs decayed to electrons were rejected to avoid the overlaps between the latter ones and the jets.

ration between the selected pair and their invariant mass on figs. 7.14 and 7.15. As a consequence, the efficiency of the cuts on the tagging jets is basically the same: $10.9 \pm 0.3\%$ for PYTHIA against $13.2 \pm 1.6\%$ for ALPGEN. In PYTHIA samples produced at $\sqrt{s} = 14$ TeV, 18.5% of the events with a jet pair in the four muon final state passed the cuts and the fraction of events with at least two jets in this case is 20%.

In summary, despite the low statistics, ALPGEN samples suggest an increase of the ZZ contamination due to the presence of a higher number of jets with $P_T > 20$ GeV. This increase is estimated to be $35 \pm 6\%$ if the same efficiency for the VBF cut ($\Delta\eta > 2.5$ and $m_{jj} > 300$ GeV) is assumed with respect to PYTHIA samples.

If the number of ZZ events after the full selection is augmented accordingly, the significance drops to 5.0σ. Under the hypothesis that the same increase applies for Higgs production via gluon fusion[3], the significance remains at 5.4σ as quoted in table 7.4. A loss in the purity of vector boson fusion signal would be the main consequence, although this could be recovered by using the pseudo-rapidity distribution of the tagged jets or a central jet veto. For such studies, dedicated samples that are currently not available would be needed.

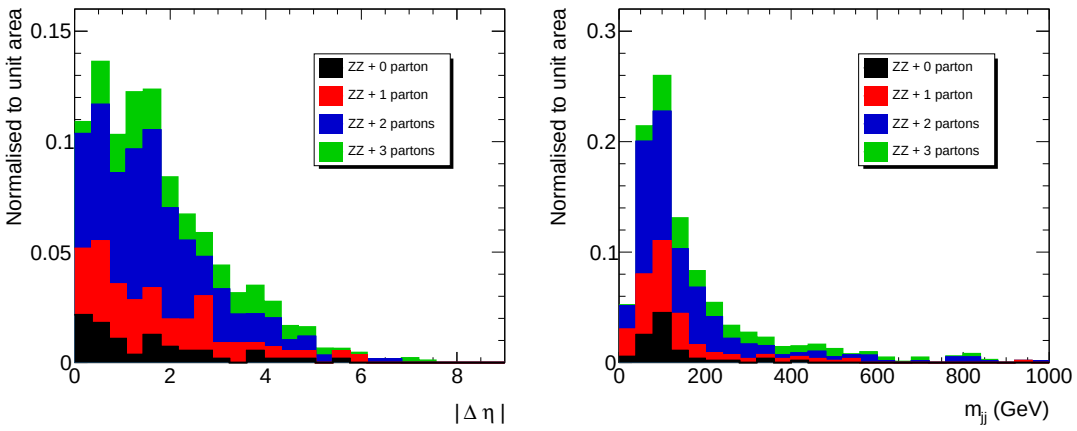

(a) (b)

Figure 7.13: (a) Rapidity gap and (b) invariant mass of the tagging jets on ZZ samples produced with ALPGEN.

[3]In fact the amount of QCD radiation leading to hard jets is expected to be higher in Higgs production via gluon fusion than in ZZ events. This feature is explored in some analyses such as $H \to \gamma\gamma + 1$ jet in ATLAS [10].

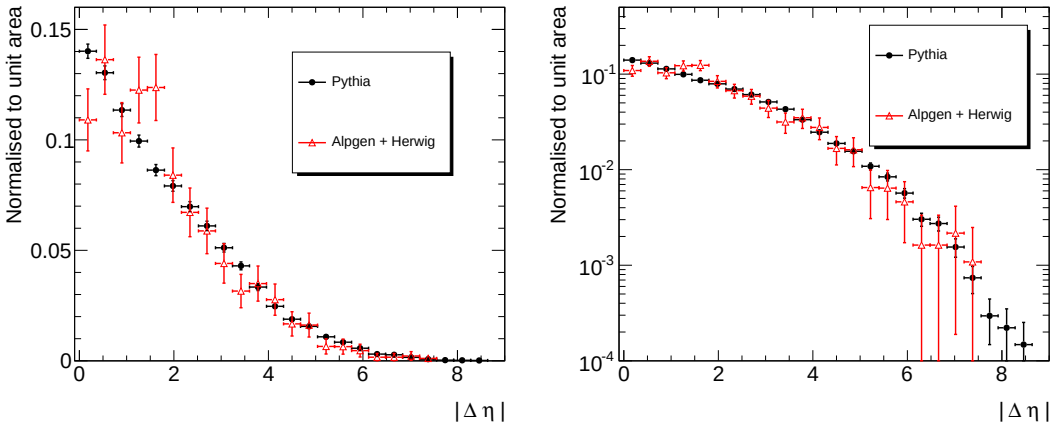

(a) Linear scale. (b) Log scale.

Figure 7.14: Rapidity gap between the tagging jets selected on ZZ samples produced with ALPGEN and PYTHIA.

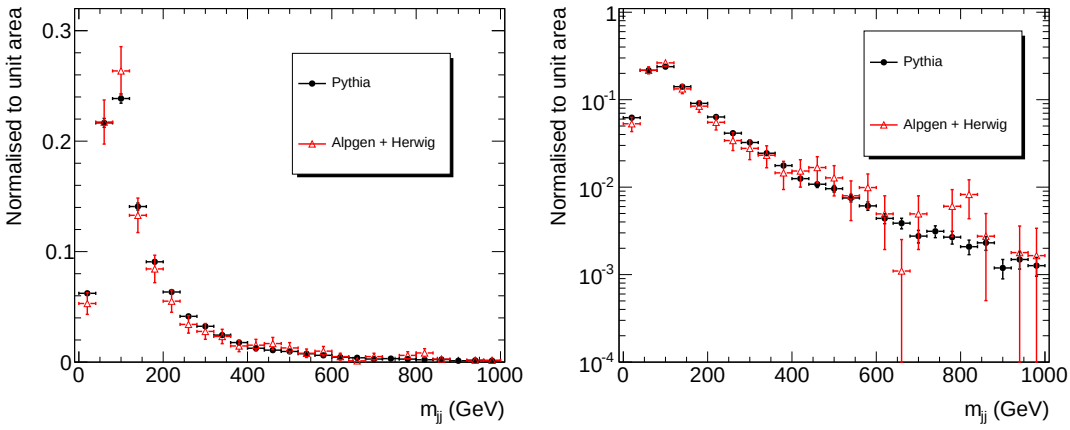

(a) Linear scale. (b) Log scale.

Figure 7.15: Invariant mass of the tagging jets selected on ZZ samples produced with ALPGEN and PYTHIA.

7.6 Conclusions and perspectives

The feasibility of an analysis for Higgs decays to four lepton final states, dedicated to vector boson fusion production was studied for the first time in the ATLAS collaboration. In this mode the Higgs boson is accompanied by two high-P_T jets with large invariant mass and separated by large rapidity gaps. Tagging those jets allows the reduction of the most important background for the inclusive searches, $ZZ \to 4\ell$.

The rates of both the Higgs signal and the ZZ process rise steeply for masses above 180 GeV and thus the interest of the present analysis resides in this mass region. The strategy adopted was to combine jet tagging with the Higgs to four lepton selection cuts, with some modifications to increase the signal yield. For $M_H = 180$ GeV, with a center of mass energy of 14 TeV and integrated luminosity of 30 fb^{-1}, approximately 6 events are expected from VBF Higgs production after the selection cuts and additionally 2.6 from gluon fusion. The background contribution is below one single event. The associated significance exceeds 5σ, indicating that the Higgs could be discovered in this search mode alone.

Optimizations both on the jet tagging and jet selection were performed to achieve this result. Monte Carlo simulated samples produced by the collaboration for the inclusive studies were used. The signal and ZZ background processes were generated with `PYTHIA`. When confronted to samples simulated using `ALPGEN` at a different center of mass energy ($\sqrt{s} = 10$ TeV), some differences were observed in the rate of events containing two jets with P_T above 20 GeV. As a result, the purity of the VBF signal is reduced with the higher survival rates of ZZ and gluon fusion Higgs production after the jet selection cuts. Both processes should be enhanced in such a way that the signal significance is not affected. The jet multiplicity issue needs to be studied with LHC data, and will depend also on the pile-up conditions. This will determine the efficiency of a central jet veto that was not applied in this analysis.

The combination of this exclusive mode with the inclusive analysis was not performed here and should increase the overall Higgs discovery potential. For the first LHC run this channel clearly suffers from the reduced statistics but opens interesting possibilities in the long term LHC running.

Concluding remarks

The search for the Higgs boson is one of the main objectives of the Large Hadron Collider and its general purpose experiments – ATLAS and CMS. The present work focused on two complementary aspects related to these searches and the physics program of the ATLAS collaboration.

Studies of muon isolation and energy loss

In the first part, studies connected to the reconstruction of muons and their use in analyses using simulated data and cosmic-ray events were described. Muons are the cleanest signatures in the hadronic collisions created by the LHC and can be identified by their penetrating power through large amounts of material. On their way from the interaction point to the ATLAS Muon Spectrometer, they undergo multiple scattering and energy losses which must be taken into account in their reconstruction in the spectrometer. Some of the losses occur in non-instrumented material but the major component can be measured by the ATLAS calorimeters. The identification of this component is essential when quantifying the activity around the particle – also known as isolation –, which is directly related to its origin.

The software package that deals with energy loss measurements and muon isolation in the ATLAS calorimeters was redesigned. Optimizing the way to separate the energy deposits associated to the muon itself from the activity induced by the accompanying particles in the production process was the main focus of the developments. Monte Carlo simulations of single muons and physics channels like top-quark pair production and Higgs decays to four muons in the ATLAS detector were used to assess the capabilities of the software in treating these quantities. The following results were obtained:

- The separation between muons issued from Z boson and heavy quark (b and c) decays was greatly enhanced when compared to the previous implementation of the tool. As a consequence, the rejection of the main reducible background

to Higgs analyses in four muon final states – $Zb\bar{b}$ – was almost doubled for the standard signal selection efficiency.

- The reconstructed energy loss after the optimizations was found to be in good agreement with the input values from the simulations, with an associated bias of 2% and a resolution of 11%.

Cosmic-ray events were recorded in the ATLAS detector before the LHC research program was initiated. Millions of muon tracks were analysed, allowing the commissioning of each sub-system and determinations of their combined performance. In this context, the capability of measuring the energy loss by muons that traversed the Inner Detector, the calorimeters and the Muon Spectrometer was extensively studied to validate the optimizations pursued with simulated data mentioned above. The following conclusions were drawn:

- Muon energy losses in the calorimeter are mostly contained in the region used for their measurements (noted as 'core' throughout the thesis). The contamination in the region used for isolation determinations is expected to be minimal.

- Two ways of determining the energy loss by muons traversing the detector were compared: energy deposits in the calorimeter corrected for the losses in inert material, and the momentum difference between the Inner Detector and the Muon Spectrometer measurements. Compatible mean values were found together with correlation factors around 80% in case of large deposits, both in real and simulated cosmic-ray events.

- The transverse momentum resolution of the Muon Spectrometer measurement was improved with the use of the information from the calorimeters on the energy loss. A relative gain around 10% was achieved for tracks with $7 < P_T < 30$ GeV.

The application of the last result on collision events is an interesting perspective opened by this work. Collision data should also allow the validation of the methods and the optimizations pursued for the selection of W and Z bosons using isolation information.

Higgs searches

The discovery potential of the Standard Model Higgs boson in the ATLAS experiment was the object of the second part of this document. Decays to a pair of Z bosons with the subsequent production of electrons and muons through $H \to ZZ \to 4\ell$, known as the 'golden channel', were investigated.

Although constrained by theoretical arguments and experimental data, the Higgs mass M_H is the only unknown parameter of the Standard Model. The search strategy depends highly on this quantity and $H \to ZZ$ is one of the preferred decays, being able to cover almost the full mass range allowed by the present limits.

The sensitivity of the ATLAS experiment to Higgs boson decays to four leptons was evaluated with dedicated simulated samples of the signal and main backgrounds. The samples were produced by the collaboration using the best knowledge about the physics processes and the response of the ATLAS detector, assuming a center of mass energy of 14 TeV for the LHC collisions. Two analyses in these final states were described here:

- Inclusive searches involving all the Higgs production modes with decays to four leptons;
- An exclusive analysis aiming at production through vector boson fusion (VBF) with decays to four leptons, a study done for the first time in the collaboration.

The inclusive searches benefit from higher event rates and should be able alone to discover the Higgs with an integrated luminosity of 30 fb^{-1} at $\sqrt{s} = 14$ TeV in a wide mass range. Significances above 5σ are expected for masses from 130 GeV to 500 GeV, excluding a region around 160 GeV where only evidence at 4σ level can be found and the combination with other channels is required for discovery.

The VBF analysis on the other hand is concentrated on masses of 180 GeV and above, due to the small number of events expected for the same integrated luminosity. In this mode the Higgs is accompanied by two highly energetic quark jets usually found in the forward region of the detector and separated by large gaps in rapidity. Their presence is a distinctive signature against background processes, including the $ZZ \to 4\ell$ production, irreducible in the inclusive searches. An optimized way of exploring the discriminating power provided by the jets was defined, leading to a big reduction of the backgrounds and the Higgs events not coming from vector boson fusion.

The feasibility of this analysis was demonstrated despite the reduced event rates, with expected significances above 5σ and signal to background ratio close to 10. In

summary, a Standard Model Higgs boson with a mass of 180 GeV could be discovered in the VBF $H \to 4\ell$ channel alone at $\sqrt{s} = 14$ TeV with luminosities of 30 fb^{-1}.

In the near future, four lepton final states have little sensitivity to a SM Higgs due the low expected number of events in the first LHC run. This run at $\sqrt{s} = 7$ TeV should provide an integrated luminosity of 1 fb^{-1}, allowing performance studies and measurements related to the most important backgrounds for this channel. A shutdown will follow, in order to prepare the LHC to attain the design center of mass energy and higher luminosities. The final answer about the existence of the Higgs particle shall be given after a few years running this upgraded machine.

Appendix A

Calorimeter response to the passage of muons

Muons lose energy and undergo multiple scattering on their way through the ATLAS detector. The energy loss is subject to important fluctuations mainly because of two factors:

- The amount of material traversed varies considerably as a function of pseudo-rapidity, as shown in fig. 2.10. Some variations are also expected as a function of the azimuthal angle ϕ (e.g. due to front-end electronics and support of the TileCal) but are generally much less important. The average loss in each calorimeter technology and in the non-instrumented (dead) material as a function of $|\eta|$ is shown in fig. A.1 for muons of $P_T = 10$, 100 and 1000 GeV.
- Ionization losses dominate for muon momenta below ~ 100 GeV but the probability of radiative losses increases with the momentum and is above the percent level already for $P \gtrsim 5$ GeV (fig. A.3). This effect induces large tails in the energy loss distribution, thus the reason for the truncation adopted in fig. A.1. This feature can be observed in fig. A.2.

It is clear from fig. A.1 that most part of the losses occur inside the calorimeters. This fact associated to the large fluctuations involved is a strong motivation for the use of the calorimeter measurement for correcting the losses upstream the MS. The study presented in chapter 3 was mainly focused on the selection of the cells affected by muon energy deposits. However, a precise and unbiased determination of the energy loss depends on the interplay between three effects:

- e/μ **factor:** The calorimeter calibration is oriented to electron reconstruction, which is adequate for radiative losses but overestimates the energy deposited

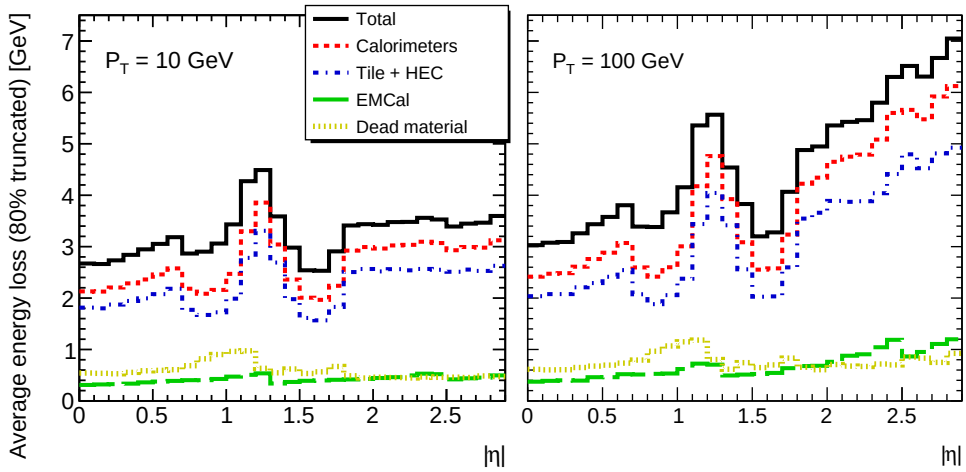

Figure A.1: Average energy loss (80% truncated) from the perigee to the entrance of the ATLAS Muon Spectrometer (total) in the different regions (calorimeters and dead material) for muons of $P_T = 10$ GeV (left) and $P_T = 100$ GeV (right).

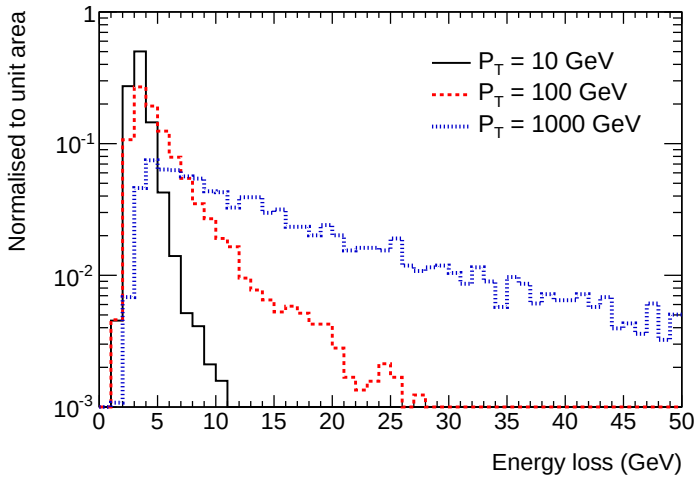

Figure A.2: Energy loss distribution for muons of $P_T = 10$, 100 and 1000 GeV crossing the ATLAS detector from the perigee to the entrance of the Muon Spectrometer.

by ionization. This aspect will be discussed in the next section.

- **Leakage:** Part of the deposits might fall outside the E_T^{core} region if the latter is not sufficiently large or if the extrapolation does not follow correctly the trajectory of the particle in the calorimeter.

- **Noise suppression:** Some cells are rejected by the noise cut which leads to underestimations in the measured energy.

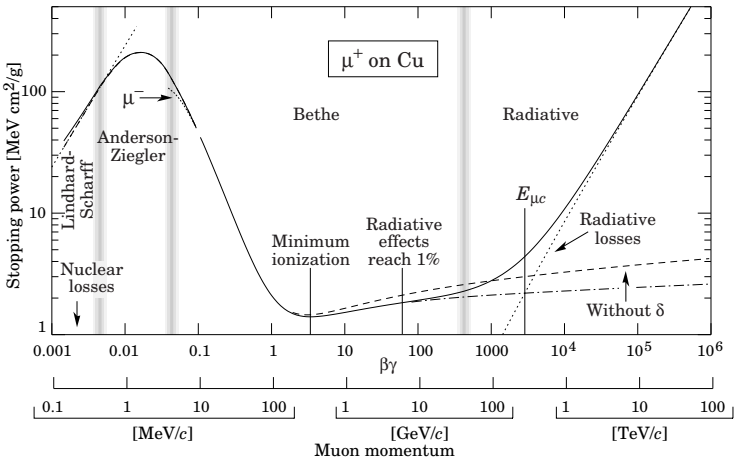

Figure A.3: Energy loss per unit length ($-dE/dx$ or stopping power) of muons in copper, as a function of their momentum. Extracted from ref. [82].

A.1 Cell energy calibration and e/μ factor

The cell energy reconstruction is done at the calorimeter front-end electronics, where the analog signals are sampled and digitized after shaping. An optimal filtering algorithm based on the knowledge of the pulse shape and noise autocorrelation is applied to maximize the signal over background ratio and remove the ADC pedestal. The sum of the ADC counts after filtering corresponds to the amplitude of the signal A, which is related to the cell energy via:

$$E_{cell} = A \cdot C_{ADC \to Q,I} \cdot C_{Q,I \to E} \cdot C_{corrections} \,, \tag{A.1}$$

where $C_{ADC \to Q,I}$ is the conversion between amplitude and charge Q (in the case of the TileCal) or current I (in the case of the LAr), obtained from injecting a known calibration signal and reconstructing the corresponding cell response; $C_{Q,I \to E}$ is the charge or current to energy conversion factor that has been determined from simulations and testbeam results; $C_{corrections}$ corrects for instance differences between the calibration and the physical ionization pulse in the LAr, non-linearities in the photomultiplier response in the TileCal, non-uniformities between the cells and other effects. More details can be found in [24, 25].

The cells are calibrated at the electromagnetic scale, i.e. to give an unbiased measurement of the energy deposited by electrons and photons[1]. Both particles at LHC energies induce electromagnetic cascades through bremsstrahlung and electron-positron pair production. The following processes take place throughout the cascade

[1]The cell calibration does not correct for losses in front of the calorimeter nor from lateral leakage if a small cluster is used. Such corrections are only applied at the cluster level.

development:

- High energy electrons and photons ($\gg$ 1 MeV) induce bremsstrahlung and pair production which in turn result in more electrons and photons with lower energy. The process goes on until the energy threshold for pair production is reached.
- Low energy photons ($\lesssim$ 1 MeV) are absorbed via photoelectric and Compton effects, producing low energy electrons. These two processes occur preferentially in the materials with high atomic number Z that compose the absorbers of a sampling calorimeter.
- Low energy electrons lose a considerable fraction of their energy by ionization and have a short range in the calorimeter. The ionization cross section is proportional to Z/A (A is the mass number) and thus higher for the active material of a sampling calorimeter.

As a consequence, a great fraction of the photons interact in the absorbers, giving rise to electrons that may not reach the active layers. This leads to a very disproportional ratio between the energy deposited in the absorber and in the active material (i.e. a high sampling fraction) in case of electromagnetic showers. The same ratio is smaller for particles that lose energy mainly via ionization such as muons. The relation between the sampling fractions associated to electrons and muons (S_e and S_μ) is usually called 'e/μ factor' [83], such that:

$$\frac{e}{\mu} = \frac{S_e}{S_\mu} < 1\,. \tag{A.2}$$

The calorimeter calibration leads to an overestimation of the energy deposited by ionization. This effect is demonstrated in figure A.4, which shows the ratio between the reconstructed and the true energy losses in the middle layer of the electromagnetic calorimeter. When radiative losses dominate, the ratio is close to one as expected for high energy photons. For pure ionization losses one should find a 'μ/e factor' greater than one, i.e. the inverse of eq. A.2.

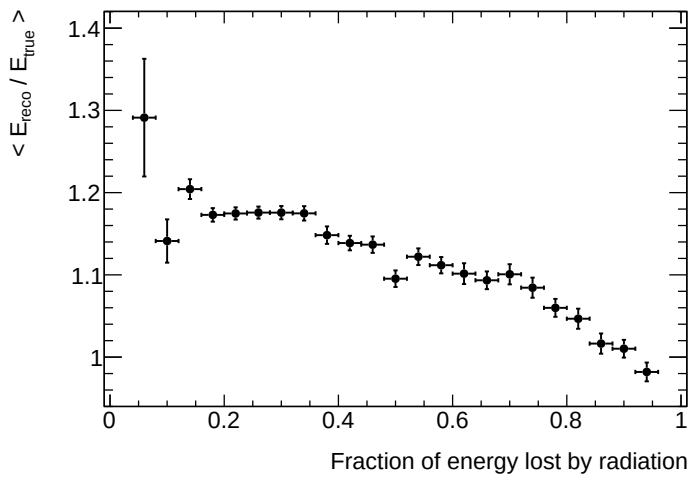

Figure A.4: Average ratio between the reconstructed and the true energy loss in the cells of the middle layer of the electromagnetic calorimeter, as a function of the radiative loss fraction inside the cells. From simulated samples of single muons with $P_T = 100$ GeV.

A.2 Calibration of muon energy loss

The interplay between the three effects mentioned previously (e/μ factor, leakage and noise suppression) determines the bias in the muon energy loss measurement. The bias is defined as:

$$\texttt{bias} = \frac{E_T^{reco} - E_T^{true}}{E_T^{true}}\,, \tag{A.3}$$

and the goal of a calibration process is to minimize this quantity. In view of this definition one expects contributions with positive sign from the e/μ factor and negative ones from the other two effects. Moreover:

- The e/μ factor is valid only for ionization losses, and the associated bias is expected to be maximal for low energy deposits which are not affected by radiative losses.

- The noise suppression and the leakage factor are expected to vary as a function of the energy deposited and the pseudo-rapidity of the muons and cells. Changes in the calorimeter granularity, the noise pattern and the precision of the extrapolation (the Inner Detector loses precision as η increases) justify the η variations. As for the energy dependence, higher deposits are less influenced by noise suppression if they concentrate on one or a few cells. On the other hand, they should affect larger regions and thus be more sensitive to leakage

effects.

Correcting for each component individually is extremely difficult and would need detailed studies using large statistics that are hard to obtain. A simple solution was to use two independent functions to correct for the energy and pseudo-rapidity dependences. The correlation between the two is ignored by this approach. The transverse energy was used for convenience, since this quantity was studied for isolation measurements in chapter 3.

Simulated samples

To cover a large fraction of the energy loss spectrum, simulation samples of single muons with $P_T = 3$, 5, 10, 20, 50, 100, 300, 500 and 1000 GeV were generated with about 10 000 events each[2]. The true and reconstructed energy in each calorimeter cell were kept. *TrackInCaloTools* was used to collect the energy deposits using the optimized E_T^{core} definition described in chapter 3 and a 2σ noise threshold. The following steps were adopted to calibrate the muon energy loss in each calorimeter layer and validate the procedure. All the examples are given for the end-cap section of the middle layer of the electromagnetic calorimeter.

Deriving and applying the calibration

1. For each muon one calculates the bias on the energy measured in the layer according to eq. A.3. The bias as function of the transverse energy is shown in fig. A.5.

2. To calculate the average bias as a function of the transverse energy loss, the sample is divided into several energy bins (fig. A.6). The goal is to have large statistics and relatively small variation of the bias within each bin.

3. The energy dependence of the bias $B(E_T^{true})$, shown in fig. A.7a, is constructed using the average value of E_T^{loss} in each region (x-axis) and the mean value of the bias in each region (y-axis).

4. The values are interpolated using linear (or cubic) splines to have a continuous description of $B(E_T^{true})$.

5. The calibration consists is estimating E_T^{true} for a given E_T^{reco} by inverting eq. A.3. In practice this is done by minimizing the relation:

[2]As a comparison, the standard calorimeter calibration is performed with several million simulated events of single electrons and photons.

$$\chi^2 = \left[E_T^{reco} - E_T^{true} \cdot (1 + B)\right]^2 , \tag{A.4}$$

for E_T^{true}. One uses $E_T^{true} = E_T^{reco}$ as a first guess and the solution is determined iteratively, exploiting the knowledge of the derivatives of the function B from the spline interpolation.

6. One now calculates the bias as a function of η as done in steps 1 and 2. The obtained values are shown in fig. A.8a. Again, an interpolation is used to derive a continuous function $B'(\eta)$.

7. The calibration in η consists in dividing the measured energy by $1 + B'(\eta)$.

Testing the calibration procedure

I. After the calibration step, a new set of values for E_T^{reco} is obtained. One then repeats steps 1 and 2 (step 6) to check the calibration procedure as a function of the measured energy (pseudo-rapidity). The average bias after correction is shown in fig. A.7b (fig. A.8b).

II. The energy resolution σ_{E_T} is estimated from the RMS (or the standard deviation given by a Gaussian fit) in each energy bin after calibration. Its dependence with energy is again obtained by spline interpolation. The results are shown in fig. A.9a.

III. For each combination $(E_T^{true}, E_T^{reco}, \sigma_{E_T})$ one calculates the pull, defined as:

$$\texttt{pull} = \frac{(E_T^{true} - E_T^{reco})}{\sigma_{E_T}} . \tag{A.5}$$

The associated distribution is shown in fig. A.9b. One ideally expects normalized Gaussian distributions (centered at zero with standard deviations equal to one). The energy and pseudo-rapidity dependence are shown in fig. A.10.

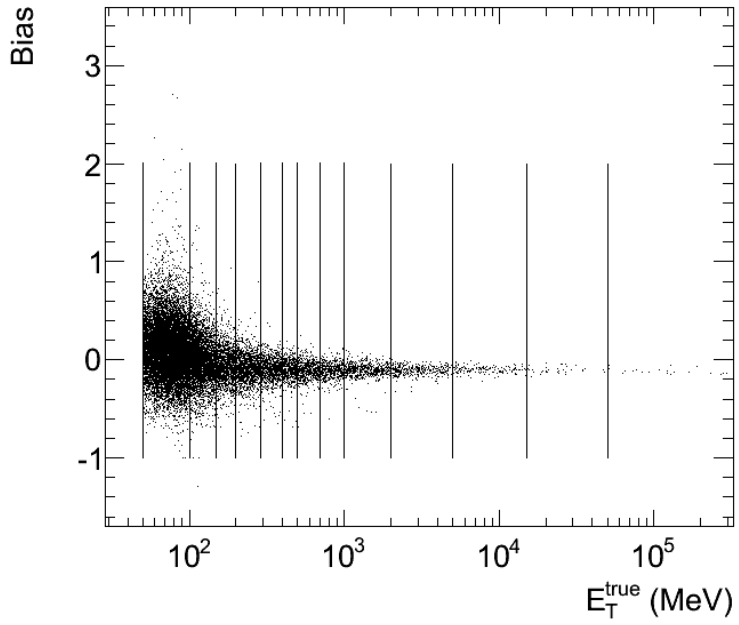

Figure A.5: Bias on the muon transverse energy loss measurement in the middle layer of the LArEM calorimeter as a function of the true transverse energy loss (E_T^{true}). The vertical lines indicate the intervals used in the calculation of the average bias (figs. A.6 and A.7).

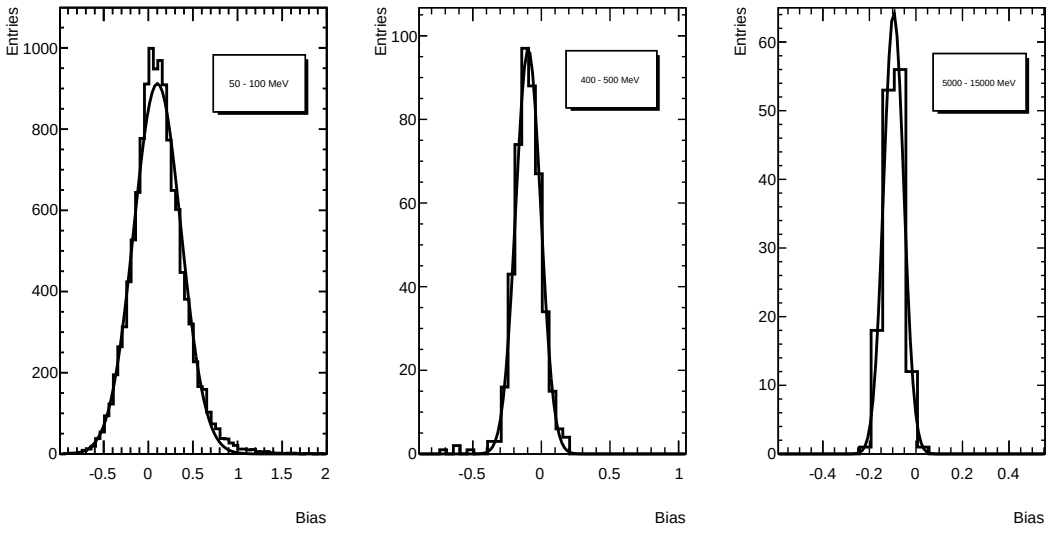

(a) (b) (c)

Figure A.6: Distribution of the bias on the transverse energy loss measurement in the middle layer of the LArEM calorimeter for three intervals of the true transverse energy loss: (a) 50 – 100 MeV, (b) 400 – 500 MeV, (c) 5 000 – 15 000 MeV. The Gaussian fits used to estimate the average bias are also shown.

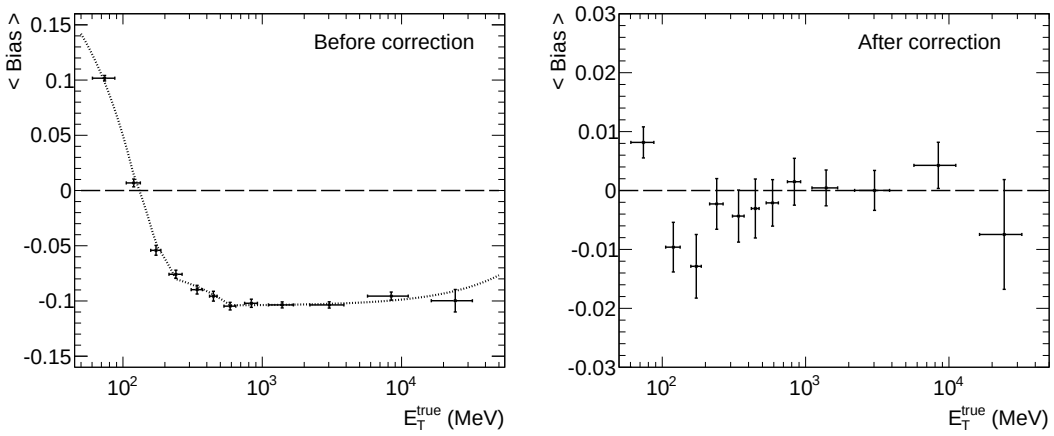

(a) (b)

Figure A.7: Average bias on the muon transverse energy loss measurement in the middle layer of the LArEM calorimeter as a function of the true transverse energy loss (E_T^{true}), (a) before and (b) after the calibration procedure. The dotted line in the left plot shows the interpolation used to describe the bias $B(E_T^{true})$.

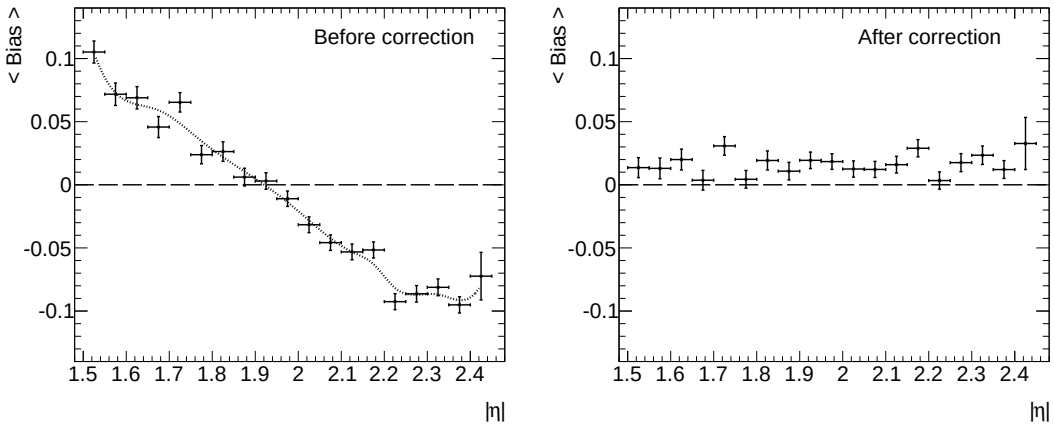

(a) (b)

Figure A.8: Average bias on the muon transverse energy loss measurement in the middle layer of the LArEM calorimeter as a function of the pseudo-rapidity, (a) before and (b) after the calibration procedure. The dotted line in the left plot shows the interpolation used to describe the bias $B'(\eta)$.

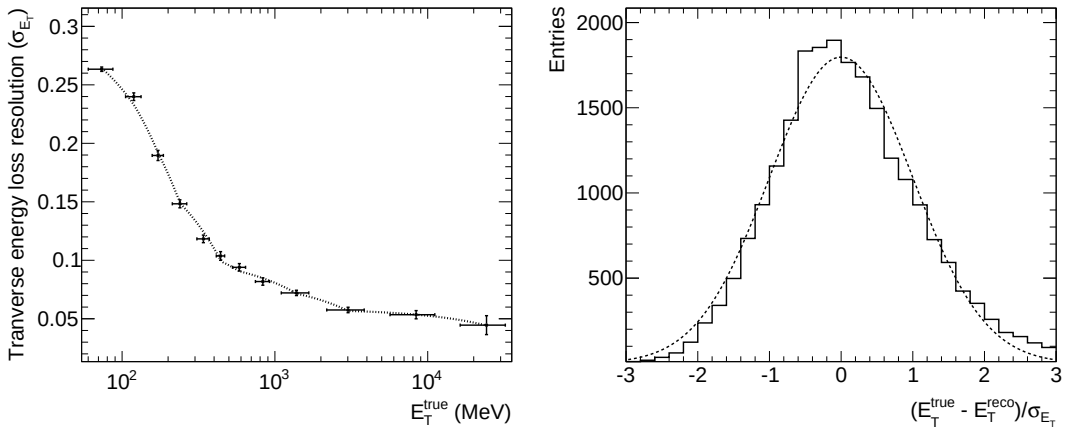

(a) (b)

Figure A.9: (a) Resolution on the measured transverse energy loss in the middle layer of the LArEM calorimeter and (b) the associated pull (eq. A.5). The dashed line on the left plot shows the interpolation used to describe $\sigma_{E_T}(E_T^{true})$. The normalized Gaussian curve (zero mean and standard deviation equal to unit) on the right shows the expected behaviour of the pull distribution.

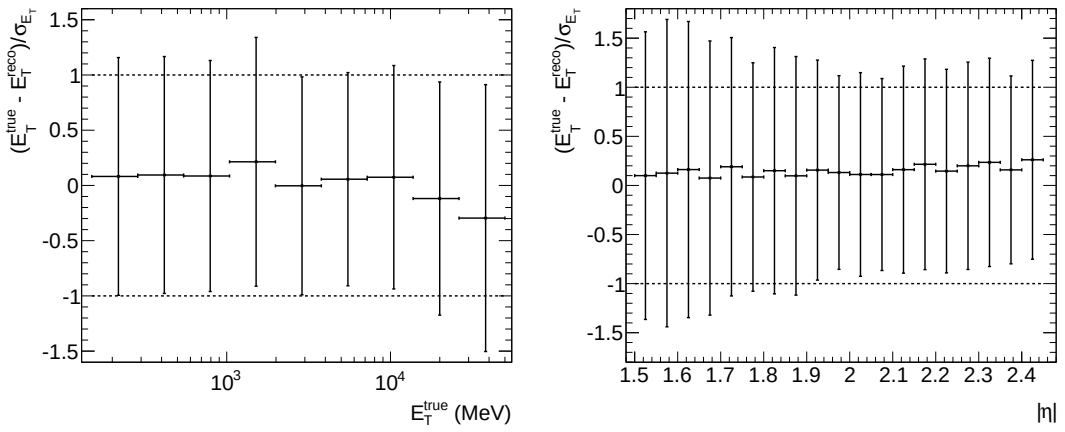

(a) (b)

Figure A.10: Pull (eq. A.5) on the measured transverse energy loss in the middle layer of the LArEM calorimeter as a function of (a) the true transverse energy and (b) pseudo-rapidity. The error bars correspond to the RMS of each bin and the dashed lines at ± 1 indicate the expected behaviour.

Conclusions

The calibration procedure reduces the bias on the energy loss measurement as desired. Typical values before and after the corrections are of the order of 10% and 1%, respectively, as shown in figs. A.7 and A.8.

Both the energy and pseudo-rapidity dependences are treated by simple functions that ignore their correlation. This limitation implies a small degradation of the energy loss dependence after both corrections are applied, with an average bias exceeding 2% in a few regions. Given the simplicity of the present approach and the required precision, the corrections are considered satisfactory.

Preliminary studies indicate that approximately the same precision can be obtained for most part of the calorimeter layers. The noise levels in the HEC and the non-projectivity of the hadronic calorimeters were the main difficulties encountered when applying this method.

One notes that the bias is small in the region were most part of the values are concentrated ($\sim 80 - 200$ MeV in the middle layer of the LArEM). This justifies the fact that nearly unbiased energy loss measurements were found even without the calibration in chapter 3. When moving to higher values, the measurement underestimated the losses and this behaviour is observed here as well.

Appendix B

Hypothesis testing for the discovery of the Higgs boson

B.1 Poisson significance

Considering a scenario where the Higgs boson does not exist, the four lepton invariant mass spectrum after the selection cuts described in section 6.4, is dominated by the ZZ contribution. In a given mass window, the number of events n is expected to follow a Poisson distribution $\rho(n;\bar{n})$, centered at the value given by the cross section times the integrated luminosity, $\bar{n} = \sigma_{ZZ} \times \mathscr{L}$, assuming the reconstruction and selection efficiencies are included in the cross section. The probability p to observe at least N events is then:

$$p(n \geq N) = \sum_{n=N}^{\infty} \rho(n;\bar{n}) \ , \text{ with } \rho(n;\bar{n}) = \frac{\bar{n}^n \, e^{-\bar{n}}}{n!} \, . \tag{B.1}$$

This probability (also called *p-value*) is usually expressed in terms of the statistical significance $\mathbf{Z}$. In particle physics this is defined by the number of standard deviations that give a one-sided area of a standard normal distribution equal to p:

$$p = \int_{\mathbf{Z}}^{\infty} \frac{1}{\sqrt{2\pi}} \, e^{-x^2/2} \, dx = 1 - \Phi(\mathbf{Z}) \, , \tag{B.2}$$

$$\mathbf{Z} = \Phi^{-1}(1-p) \, . \tag{B.3}$$

The relation between $\mathbf{Z}$ and p is illustrated in fig. B.1. The significance can be calculated according to eq. B.3, using the inverse of the cumulative distribution Φ^{-1}.

One then performs a measurement. If the number of observed events N is below

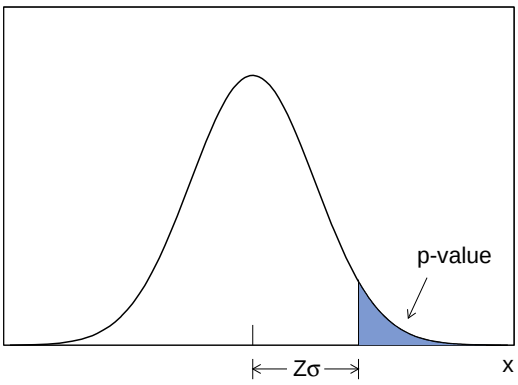

Figure B.1: Illustration of the correspondence between the significance **Z** and the *p-value*. Extracted from ref. [10].

the expectations, there is clearly no evidence of the Higgs signal, and the probability $p(n \geq N)$ should be high. But if the probability is low enough, or in other words, the significance exceeds a predefined value, the background hypothesis is rejected and the discovery is claimed. The convention is to use 5σ, which corresponds to a *p-value* of 2.87×10^{-7}.

Alternatively, the Higgs signal can be included in the expectations, with the cross section predicted by the Standard Model. One can define an interval that contains a certain fraction of the area of the expected curve for the number of events. The convention is to chose a 95% *confidence interval*.

Let us assume that the number of events observed is small, outside this interval. It is very unlikely that it occurs if the signal is actually there. In that case, the Higgs boson is said to be excluded of the mass window under consideration with 95% *confidence level* (CL).

B.2 Profile likelihood ratio

A more sophisticated method, capable of including systematic uncertainties, was chosen to provide input for the combination of the different Higgs search channels. It follows a frequentist approach through the use of the *profile likelihood ratio* [84]. The significance is quantified with the help of a parameter μ that measures the *signal strength*. In the absence of a Higgs boson, $\mu = 0$, and for the Standard Model expectation, $\mu = 1$. Discovery is claimed when the background only hypothesis ($\mu = 0$) is rejected, and limits can be set if the discovery is not realized by the confidence level (CL) associated with the calculated value for μ.

The method is rather generic and can be used not only for Higgs searches. It is

based on the following ideas:

- The main input is the histogram of a discriminating variable, such as the invariant mass spectrum. In case of simple event counting it has only one bin.
- The background shape and yields on the signal region are extracted from Monte Carlo or data regions where no signal is expected (control regions).
- Subsidiary measurements from control regions, in the form of additional histograms, can be used to provide information on the background normalization and eventually its shape.
- The number of events in each bin of the histograms – s_i and b_i for signal and background respectively – is given by integrals of functional forms for signal and the background f_s and f_b that depend on a set of parameters θ (e.g. the mean value and the resolution for a Gaussian peak for the signal and the slope and intercept of a linear distribution for the background on an invariant mass spectrum):

$$s_i = \int_{\text{bin } i} f_s(x\,;\theta)\,dx\,. \tag{B.4}$$

- A likelihood estimator L is constructed as the product of the Poisson probabilities of all N bins of the main input (with n_i entries per bin) and the M subsidiary measurements u_k, as in eq. B.5. Maximizing the likelihood allows the determination of the signal and background shapes and yields.

$$L(\mu,\theta) = \prod_{j=1}^{N} \frac{(\mu\, s_i + b_i)^{n_i}}{n_i!}\, e^{-(\mu\, s_i + b_i)} \prod_{k=1}^{M} \frac{u_k^{m_k}}{m_k!}\, e^{-u_k}\,. \tag{B.5}$$

- Systematic uncertainties are incorporated in the form of probability density functions (*pdf*s) that multiply the likelihood estimator. The *pdf* must contain the information about the best estimation of the parameter and its error (e.g. the calculated signal efficiency and its error). When combining independent channels, common systematics can be included (e.g. the uncertainty on the luminosity or on a background yield).
- The final estimator $\lambda(\mu)$ is the ratio between two likelihoods: the one in the numerator is maximized for a fixed value of the signal strength and the one

in the denominator using a floating value of μ. It quantifies the agreement between the data and a given hypothesis on μ. One actually uses $q = -2 \ln \lambda$ as a test statistics that follows a well-known and simple distribution: χ^2 with one degree of freedom.

Bibliography

[1] L. Evans and P. Bryant, *LHC Machine*, JINST **3** (2008) S08001.

[2] *CERN press releases*, `http://press.web.cern.ch/press/`. PR08.08, PR09.08, PR17.09, PR18.09, PR07.10.

[3] Particle Data Group Collaboration, C. Amsler et al., *Kinematics*, in Phys. Lett. [26], pp. 321 – 324.

[4] ATLAS Collaboration, G. Aad et al., *The ATLAS Experiment at the CERN Large Hadron Collider*, JINST **3** (2008) S08003.

[5] J.-F. Arguin, M. Elsing, and B. Heinemann, *ATLAS Tracking Performance in the Presence of Pile-up*, Tech. Rep. ATL-INDET-INT-2010-001, CERN, Geneva, Feb, 2010.

[6] *ATLAS: Detector and physics performance technical design report.*, vol. 1. CERN-LHCC-99-14, 1999.

[7] *ATLAS liquid-argon calorimeter: Technical Design Report.* CERN, Geneva, 1996.

[8] D. Varouchas and D. Rousseau, *Study of the Higgs boson discovery potential, produced by the vector boson fusion with the ATLAS detector and commissioning of calorimetric transverse missing energy.* PhD thesis, Orsay, France, Universite Paris 11, 2009.

[9] W. Lampl, S. Laplace, D. Lelas, P. Loch, H. Ma, S. Menke, S. Rajagopalan, D. Rousseau, S. Snyder, and G. Unal, *Calorimeter Clustering Algorithms: Description and Performance*, Tech. Rep. ATL-LARG-PUB-2008-002. ATL-COM-LARG-2008-003, CERN, Geneva, Apr, 2008.

[10] ATLAS Collaboration, G. Aad et al., *Expected Performance of the ATLAS Experiment - Detector, Trigger and Physics.* 2009. `arXiv:0901.0512 [hep-ex]`.

[11] *ATLAS muon spectrometer: Technical Design Report.* CERN, Geneva, 1997.

[12] S. Hassani et al., *A muon identification and combined reconstruction procedure for the ATLAS detector at the LHC using the (MUONBOY, STACO, MuTag) reconstruction packages*, Nucl. Instrum. Meth. **A572** (2007) 77–79.

[13] R. Nicolaidou, L. Chevalier, S. Hassani, J. F. Laporte, E. L. Menedeu, and A. Ouraou, *Muon identification procedure for the ATLAS detector at the LHC using Muonboy reconstruction package and tests of its performance using cosmic rays and single beam data*, J. Phys. Conf. Ser. **219** (2010) no. 3, 032052.

[14] *The ATLAS Computing Technical Design Report*. CERN-LHCC/2005-022, 2005.

[15] *ROOT - An Object Oriented Data Analysis Framework*, http://root.cern.ch, 2010.

[16] B. Lenzi, *The Physics Analysis Tools project for the ATLAS experiment*, . Proceedings of the ICCMSE Symposium: Computing in Experimental High Energy Physics, to appear.

[17] *Geant4: A toolkit for the simulation of the passage of particles through matter*, . `http://geant4.cern.ch/`.

[18] *ATLAS computing workbook*, `https://twiki.cern.ch/twiki/bin/view/Atlas/WorkBook`.

[19] K. Bachas and C. Petridou, *Studies of the ATLAS Muon Spectrometer with Test Beam and Simulated Physics Data*. PhD thesis, Aristotle University of Thessaloniki, 2008.

[20] K. Bachas and S. Hassani, *Track based software package for measurement of the energy deposited by muons in the calorimeters of the ATLAS detector*, J. Phys. Conf. Ser. **119** (2008) 042002.

[21] B. Lenzi, R. Nicolaidou, and S. Hassani, *TrackInCaloTools: a package for measuring muon energy loss and calorimetric isolation in ATLAS*, J. Phys. Conf. Ser. **219** (2010) no. 3, 032052.

[22] A. Salzburger, *The ATLAS Track Extrapolation Package*, Tech. Rep. ATL-SOFT-PUB-2007-005. ATL-COM-SOFT-2007-010, CERN, Geneva, Jun, 2007.

[23] A. Salzburger, S. Todorova, and M. Wolter, *The ATLAS Tracking Geometry Description*, Tech. Rep. ATL-SOFT-PUB-2007-004. ATL-COM-SOFT-2007-009, CERN, Geneva, Jun, 2007.

[24] ATLAS Collaboration, *Readiness of the ATLAS Liquid Argon Calorimeter for LHC Collisions*, arXiv:0912.2642 [physics.ins-det]. Accepted for publication in EPJC.

[25] The ATLAS Collaboration, *Readiness of the ATLAS Tile Calorimeter for LHC collisions*, arXiv:1007.5423 [physics.ins-det]. Submitted for publication in EPJC.

[26] Particle Data Group Collaboration, C. Amsler et al., *Review of particle physics*, Phys. Lett. **B667** (2008) 1.

[27] T. Sjostrand et al., *High-energy-physics event generation with PYTHIA 6.1*, Comput. Phys. Commun. **135** (2001) 238–259, 0010017 [hep-ph].

[28] P. Golonka and Z. Was, *PHOTOS Monte Carlo: A Precision tool for QED corrections in Z and W decays*, Eur. Phys. J. **C45** (2006) 97–107, arXiv:0506026 [hep-ph].

[29] *Muon Performance in Minimum Bias pp Collision Data at* $\sqrt{s} = 7$ *TeV with ATLAS*, Tech. Rep. ATLAS-CONF-2010-036, CERN, Geneva, Jul, 2010.

[30] ATLAS Collaboration, P. Ryan et al., *The ATLAS Inner Detector commissioning and calibration*, arXiv:1004.5293 [physics.ins-det].

[31] ATLAS Collaboration, *Commissioning of the ATLAS Muon Spectrometer with Cosmic Rays*, arXiv:1006.4384 [physics.ins-det].

[32] A. Andreazza et al., *ATLAS Inner Detector Track Resolution Measured for 2008 Cosmic Rays Data*, Tech. Rep. ATL-INDET-INT-2010-013, CERN, Geneva, Jun, 2010.

[33] B. Lenzi, R. Nicolaidou, and S. Hassani, *Developments on the software package for calorimetric isolation and energy loss measurements for muons in ATLAS*, Tech. Rep. ATL-SOFT-INT-2009-002. ATL-COM-SOFT-2009-010, CERN, Geneva, Aug, 2009.

[34] F. Mandl and G. G. Shaw, *Quantum field theory; 2nd ed.* Wiley, New York, NY, 2010.

[35] M. E. Peskin and D. V. Schroeder, *An Introduction to Quantum Field Theory; 1995 ed.* Westview, Boulder, CO, 1995.

[36] A. Pich, *The Standard model of electroweak interactions*, arXiv:0705.4264 [hep-ph].

[37] A. Djouadi, *The Anatomy of electro-weak symmetry breaking. I: The Higgs boson in the standard model*, Phys. Rept. **457** (2008) 1–216, arXiv:0503172 [hep-ph].

[38] *The LEP Electroweak Working Group*, http://lepewwg.web.cern.ch/LEPEWWG/.

[39] ALEPH Collaboration, J. Alcaraz, *Precision Electroweak Measurements and Constraints on the Standard Model*, arXiv:0911.2604 [hep-ex].

[40] *A Generic Fitter Project for HEP Model Testing*, http://gfitter.desy.de/.

[41] LEP Working Group for Higgs boson searches Collaboration, R. Barate et al., *Search for the standard model Higgs boson at LEP*, Phys. Lett. **B565** (2003) 61–75, arXiv:0306033 [hep-ex].

[42] CDF and D0 Collaboration, T. Aaltonen et al., *Combination of Tevatron searches for the standard model Higgs boson in the W+W- decay mode*, Phys. Rev. Lett. **104** (2010) 061802, arXiv:1001.4162 [hep-ex].

[43] The TEVNPH Working Group of the CDF and D0 Collaboration, *Combined CDF and D0 Upper Limits on Standard Model Higgs- Boson Production with up to 6.7 fb^{-1} of Data*, arXiv:1007.4587 [hep-ex].

[44] J. Baglio and A. Djouadi, *Predictions for Higgs production at the Tevatron and the associated uncertainties.*, Tech. Rep. CERN-PH-TH-2010-051. LPT ORSAY 10-05., Mar, 2010. arXiv:1003.4266 [hep-ph].

[45] H. Flacher et al., *Gfitter - Revisiting the Global Electroweak Fit of the Standard Model and Beyond*, Eur. Phys. J. **C60** (2009) 543–583, arXiv:0811.0009 [hep-ph].

[46] A. Djouadi, J. Kalinowski, and M. Spira, *HDECAY: A program for Higgs boson decays in the standard model and its supersymmetric extension*, Comput. Phys. Commun. **108** (1998) 56–74, arXiv:9704448 [hep-ph].

[47] M. Spira, A. Djouadi, D. Graudenz, and P. M. Zerwas, *Higgs boson production at the LHC*, Nucl. Phys. **B453** (1995) 17–82, arXiv:9504378 [hep-ph].

[48] A. Djouadi, *The Higgs in the Standard Model: status and expectations*, CERN Theoretical Seminar, `http://indico.cern.ch/conferenceDisplay.py?confId=92290`, April, 2010.

[49] *Inauguration workshop of the LHC Higgs Cross Section Working Group*, `http://james.physik.uni-freiburg.de/ warsinsk/xsfrhiggs/` and presentations therein, April, 2010.

[50] ATLAS Collaboration, G. Aad et al., *Higgs Boson*, in Expected Performance of the ATLAS Experiment - Detector, Trigger and Physics [10], pp. 1197–1511, `arXiv:0901.0512 [hep-ex]`.

[51] CMS Collaboration, G. L. Bayatian et al., *CMS technical design report, volume II: Physics performance*, J. Phys. **G34** (2007) 995–1579.

[52] J. M. Butterworth, A. R. Davison, M. Rubin, and G. P. Salam, *Jet substructure as a new Higgs search channel at the LHC*, Phys. Rev. Lett. **100** (2008) 242001, `arXiv:0802.2470 [hep-ph]`.

[53] ATLAS Collaboration, *ATLAS Sensitivity to the Standard Model Higgs in the HW and HZ Channels at High Transverse Momenta*, Tech. Rep. ATL-PHYS-PUB-2009-088. ATL-COM-PHYS-2009-345, CERN, Geneva, Aug, 2009.

[54] CDF Collaboration, *Search for the SM Higgs Boson using τ lepton*, CDF Note 9248, February, 2008.

[55] D0 Collaboration, *Search for the SM Higgs boson in the $\tau^+\tau^- qq$ final state*, Conference Note 5845-CONF, August, 2009.

[56] ATLAS Collaboration, G. Aad et al., *Search for the Standard Model Higgs Boson via Vector Boson Fusion Production Process in the Di-Tau Channels*, in Expected Performance of the ATLAS Experiment - Detector, Trigger and Physics [10], pp. 1271 – 1305, `arXiv:0901.0512 [hep-ex]`.

[57] ATLAS Collaboration, *Prospects for Higgs Boson Searches using the $H \to WW^{(*)} \to \ell\nu\ell\nu$ Decay Mode with the ATLAS Detector for 10 TeV*, Tech. Rep. ATL-PHYS-PUB-2010-005. ATL-COM-PHYS-2010-185, CERN, Geneva, Jun, 2010.

[58] ATLAS Collaboration, *ATLAS Sensitivity Prospects for Higgs Boson Production at the LHC Running at 7 TeV*, Tech. Rep. ATL-PHYS-PUB-2010-009. ATL-COM-PHYS-2010-373, CERN, Geneva, Jul, 2010.

[59] *ATLAS detector and physics performance. Technical design report.*, vol. 2. CERN-LHCC-99-15, 1999.

[60] T. Plehn, D. L. Rainwater, and D. Zeppenfeld, *Determining the structure of Higgs couplings at the LHC*, Phys. Rev. Lett. **88** (2002) 051801, arXiv:hep-ph/0105325.

[61] M. Duehrssen, *Prospects for the measurement of Higgs boson coupling parameters in the mass range from 110 - 190 GeV*, Tech. Rep. ATL-PHYS-2003-030, CERN, Geneva, Jul, 2003.

[62] B. Lenzi, *MSSM Higgs searches at the LHC*, ATL-PHYS-SLIDE-2010-076. Presented at MCTP Spring Symposium on Higgs Boson Physics, Ann Arbor, Michigan, USA, May, 2010.

[63] ATLAS Collaboration, G. Aad et al., *Sensitivity to an Invisibly Decaying Higgs Boson*, in Expected Performance of the ATLAS Experiment - Detector, Trigger and Physics [10], pp. 1419 – 1450, arXiv:0901.0512 [hep-ex].

[64] ATLAS Collaboration, G. Aad et al., *Search for the Standard Model $H \to ZZ^* \to 4l$*, in Expected Performance of the ATLAS Experiment - Detector, Trigger and Physics [10], pp. 1243 – 1270, arXiv:0901.0512 [hep-ex].

[65] G. Corcella et al., *HERWIG 6.5 release note*, arXiv:0210213 [hep-ph].

[66] J. M. Butterworth, J. R. Forshaw, and M. H. Seymour, *Multiparton interactions in photoproduction at HERA*, Z. Phys. **C72** (1996) 637–646, arXiv:9601371 [hep-ph].

[67] S. Frixione and B. R. Webber, *Matching NLO QCD computations and parton shower simulations*, JHEP **06** (2002) 029, arXiv:0204244 [hep-ph].

[68] H. Liu, B. Mansoulie, J. Purdham, J. Qian, J. Strandberg, and R. Thun, *QCD radiative corrections to the $gg \to H$ cross sections and their potential impact on Higgs searches at the LHC*, Tech. Rep. ATL-COM-PHYS-2009-161, CERN, Geneva, Apr, 2009.

[69] J. Pumplin et al., *New generation of parton distributions with uncertainties from global QCD analysis*, JHEP **07** (2002) 012, arXiv:0201195 [hep-ph].

[70] M. Spira, *HIGLU: A Program for the Calculation of the Total Higgs Production Cross Section at Hadron Colliders via Gluon Fusion including QCD Corrections*, arXiv:9510347 [hep-ph].

[71] R. K. Ellis, *An update on the next-to-leading order Monte Carlo MCFM*, Nucl. Phys. Proc. Suppl. **160** (2006) 170–174.

[72] CDF Collaboration, S.-S. Yu, *Review of Recent Tevatron Jet, W/Z+Jet and Heavy-flavor Production Results*, arXiv:0907.2725 [hep-ex].

[73] F. Febres Cordero, L. Reina, and D. Wackeroth, *W- and Z-boson production with a massive bottom-quark pair at the Large Hadron Collider*, Phys. Rev. **D80** (2009) 034015, arXiv:0906.1923 [hep-ph].

[74] B. P. Kersevan and E. Richter-Was, *The Monte Carlo event generator AcerMC version 2.0 with interfaces to PYTHIA 6.2 and HERWIG 6.5*, arXiv:0405247 [hep-ph].

[75] C. Anastopoulos, O. K. Baker, F. Barreiro, C. Bini, I. Boyko, T. Cuhadar Donszelmann, M. Demichev, F. Dudziak, D. Fassouliotis, L. R. Flores Castillo, J. Hoffman, S. Horvat, P. J. Hsu, L. Iconomidou-Fayard, N. Kerschen, C. Kourkoumelis, T. Lagouri, B. Lenzi, M. Losada, B. Mansoulie, B. Mellado, G. Carrillo-Montoya, N. Morange, R. Nicolaidou, K. Nikolopoulos, A. D'Orazio, E. Paganis, D. J. R. Patarroyo, J. del Peso, E. van der Poel, K. Prokofiev, J. Qian, W. Quayle, D. Rebuzzi, R. Rios, S. Rosati, R. Sandstroem, A. Schaffer, A. di Simone, E. Solfaroli Camillocci, J. Strandberg, R. Tanaka, M. Thioye, C. Wigglesworth, S. L. Wu, and D. Xu, *ATLAS sensitivity prospects for the Standard Model Higgs boson in the decay channel $H \to ZZ^{(*)} \to 4\ell$ at $\sqrt{s} = 10$ and 7 TeV*, Tech. Rep. ATL-PHYS-INT-2010-062. ATL-COM-PHYS-2010-227, CERN, Geneva, Jun, 2010.

[76] J. M. Campbell et al., *Normalizing Weak Boson Pair Production at the Large Hadron Collider*, Phys. Rev. **D80** (2009) 054023, arXiv:0906.2500 [hep-ph].

[77] ATLAS Collaboration, G. Aad et al., *Electroweak Boson Cross-Section*

Measurements, in Expected Performance of the ATLAS Experiment - Detector, Trigger and Physics [10], pp. 747–776, arXiv:0901.0512 [hep-ex].

[78] ATLAS Collaboration, G. Aad et al., *Jet Reconstruction Performance*, in Expected Performance of the ATLAS Experiment - Detector, Trigger and Physics [10], pp. 262–297, arXiv:0901.0512 [hep-ex].

[79] ATLAS Collaboration, G. Aad et al., *Detector Level Jet Corrections*, in Expected Performance of the ATLAS Experiment - Detector, Trigger and Physics [10], pp. 298 – 326, arXiv:0901.0512 [hep-ex].

[80] A. Hoecker et al., *TMVA Toolkit for Multivariate Data Analysis with ROOT*, http://tmva.sourceforge.net/.

[81] B. Jager, C. Oleari, and D. Zeppenfeld, *Next-to-leading order QCD corrections to Z boson pair production via vector-boson fusion*, Phys. Rev. **D73** (2006) 113006, arXiv:hep-ph/0604200.

[82] Particle Data Group Collaboration, C. Amsler et al., *Passage of particles through matter*, in Phys. Lett. [26], pp. 250 – 270.

[83] G. Schlager, C. W. Fabjan, T. Carli, and A. Henriques, *The Energy Response of the ATLAS Calorimeter System.* PhD thesis, Vienna Univ. Technology, 2006.

[84] Particle Data Group Collaboration, C. Amsler et al., *Statistics*, in Phys. Lett. [26], pp. 301 – 310.

Acknowledgements

I must definitely start by thanking my dear supervisor, boss, friend and colleague Rosy Nikolaidou. Thank you very much, Rosy, for all the help during these 3 years and to care about my present and my future. It has been a great pleasure working with you even if I am a bit stubborn sometimes and my working hours are not your preferred ones. I am very glad I met you and we did all this together. I wish you all the best in the months and years to come.

Thanks to all the members of my thesis committee that followed my work, gave me corrections to this manuscript and helped me with many other aspects. To my supervisor Claude Guyot for the nice discussions and corrections to the text; to my *rapporteurs* Vanina Ruhlmann-Kleider and Guillaume Unal who gave me many useful and extremely detailed comments about it; to Abdelhak Djouadi also for teaching me the little I know about Higgs physics; to the Italians Ludovico Pontecorvo and Achille Stocchi who also supported me in many occasions. Thank you Vanina for the nice company at Saclay and for the great course you provided. Thanks Guillaume for the discussions and for explaining to me the mysteries of the calorimeter.

I really enjoyed my staying at CEA Saclay (once things were set). I thank the people of *Service de Physique des Particules* for their *accueil*, in particular Ursula Bassler, Didier Vilanova and the ATLAS Saclay group. Special thanks to Samira Hassani, Philippe Schune, the 'muonboys' (Ahmimed Ouraou, Jean-François Laporte and Laurent Chevalier), the colleagues at CERN and the students (Clément, Eve, Eleni, ...).

Many thanks to the ATLAS colleagues who had the patience to explain to me the (complex) features of the ATLAS detector and to help me with the (amazingly painful) characteristics of the ATHENA framework: Andi Salzburger, David Lopez Mateos, David Rousseau, Irene Vichou, Ketevi Assamagan, Laurent Serin, Sebastien Binet, Sven Menke, the VP1s (Ed, Thomas and Vakho) and many others.

Thanks to the Brazilian, Italian, Greek, Spanish, Portuguese and the few American, Argentinian, French, German, Polish, Scottish and Venezuelan friends who

made me enjoy the life in Paris and in Geneva despite the awful weather. You even made me want more. Thanks to my friends in Brazil as well.

To my mother, father and sister who supported me all the time and came from far to witness his son or brother become a doctor. And to the rest of my family who encouraged me from Brazil and elsewhere. Má, obrigado por descobrir comigo a vida na Europa e compartilhar (ainda que às vezes à distância) muitos dos momentos importantes nesses anos. Letícia, obrigado pelo apoio tão carinhoso e importante no final (ou no começo).

Finally, I thank my ARTEMIS colleagues, specially Chara, Christos, Dinos, Nicolas and Stathes for the nice 'sub-collaboration' in the middle of the big ATLAS jungle. In the name of all of us I thank the European Commission for the (generous) financial support, represented by the holly spirit of Marie Curie and evoked by writing (for the last time) the sentence:

This work is partially supported by the European Commission through the ARTEMIS Research Network, contract number MCRTN-CT-2006-035657.